Imperial College London

PhD Thesis

Methods for Zeeman-Sisyphus Deceleration of Heavy Polar Molecules

---

Gautam Panini Kambhampati

A thesis submitted in partial fulfillment of the requirements
for the degree of Doctor of Philosophy
and the Diploma of Imperial College

in the

Centre for Cold Matter,
Department of Physics,
Faculty of Natural Sciences,
Imperial College London

7 August 2023

Methods for Zeeman-Sisyphus Deceleration of Heavy Polar Molecules

Gautam Panini Kambhampati

Abstract

Zeeman-Sisyphus deceleration (ZS, ZSD) is a method for slowing polar molecules while scattering only a small number of photons when compared with direct laser cooling. It also ensures that molecules are transversely confined by application of transverse magnetic field gradients. It has applications in ensuring that a wider range of molecules, including heavy molecules and those with otherwise unfavourable vibrational branching ratios, can be slowed and confined to within the acceptance of a magneto-optical trap. This work presents results on progress towards a demonstration of ZSD for a CaF molecular beam and towards development of a ZSD scheme for YbF.

First, a helium buffer gas source for CaF is presented. The source produces a beam of CaF moving at $(159 \pm 1)\,\mathrm{m\,s^{-1}}$ and with a molecular flux of $(2.6 \pm 0.1) \times 10^8$ $\mathrm{mol\,sr^{-1}\,shot^{-1}}$. The beam is used to test a ZS decelerator designed for CaF and it is found that molecules are transmitted through the decelerator. A second source, using a neon buffer gas, is also presented. It is shown that the pumping speed of neon by cryogenic adsorptive charcoal pumps is $(3.4 \pm 0.5) \times 10^5\,\mathrm{l\,s^{-1}}$. This is compared to $(1.22 \pm 0.06) \times 10^4\,\mathrm{l\,s^{-1}}$ measured for helium. The higher pumping speed means that the neon source can be run with higher flow rates whilst maintaining a lower chamber pressure, and hence a higher CaF mean free path.

Secondly, a ZSD scheme for YbF is developed and simulations to investigate its dynamics are carried out. The scheme utilises solenoids as a way to increase the physical size of the central bore of the decelerator and makes use of a transverse optical pumping scheme to mitigate the effects of the complex energy level structure of YbF.

For my grandparents: the scientist, the lawyer, the mathematician, and the linguist.

Declaration

I declare that this thesis is my own work. Wherever the work of others is used, the sources are appropriately referenced and acknowledged.

The Zeeman-Sisyphus decelerator discussed in Section 3.3 was designed by Dr Noah Fitch. The decelerator was constructed by Chenfeng Pu. The simulations and field models presented in Chapter 3 are my own work, though the magnetic field data they use was generated by Dr Fitch for preliminary simulations presented in [1].

Gautam Panini Kambhampati

7 August 2023

Acknowledgements

First and foremost I would like to thank Mike Tarbutt, Ben Sauer, and Noah Fitch. Without their help, advice, encouragement, and support none of this work would have been conceivable, let alone possible. Thanks also to Hannah Williams for getting me up to speed and showing me the ropes in the lab when I first started, and to Cameron McGarry for keeping our coffee breaks on schedule and for allowing me to test his background-free imaging scheme on my experiment. My eternal gratitude goes out to Jon Dyne and Dave Pitman, whose brilliant engineering ensured we actually had experiments to work on, and to Sanja Maricic, without whom nothing would ever get done. Finally, thanks to all of CCM for a great three years of working together.

I am grateful to have (in my unbiased opinion) some of the best friends in the world. Firstly, my thanks goes out to my flatmates, Anita Chandran, Emma Watson, and Adam de Bell, for always being willing to lend an ear and for making home life easy when work was challenging. Likewise, thank you to my Covid bubble buddies, Dan Clay and Hilary Lamb, for their excellent company during those long winter lockdowns. Thank you also to Ellie Rose, Zoë Edwards, Rupert Belsham, Maria Woolley, and Arshia Hashemi, for being ever-ready to commiserate, celebrate, or distract with a trip to the theatre, the pub, or with terrible reality TV. And lastly, but most certainly not least, thanks to my oldest friends, Andrew Okenyi, Will Okenyi, and Edward Finn, for always being there. You will never know how grateful I am to have you all in my life.

Thanks also to Ravi Kuchimanchi and everyone else who read this thesis for all their advice and help. It wouldn't have come together without you.

Finally, thank you to my brother, Saatvik, dad, Chandra, and mum, Usha, for everything you have given me and for always supporting me. I love you all very much.

Contents

List of Figures

List of Tables

Chapter 1

Introduction

This thesis is based on research conducted in the Centre for Cold Matter at Imperial College London. The research of the group is principally concerned with the use of cold[1] atoms and molecules to test fundamental physics, investigate the control of quantum systems, and develop quantum technologies. The research presented here focusses on molecules, and polar molecules in particular.

Compared with atoms, molecules have a much richer internal energy level structure, including vibrational and rotational transitions, as well as electronic transitions. This allows for greater experimental flexibility and provides a wide basis for encoding spins and qubits for use in quantum technologies. In addition, polar molecules have a large internal electric dipole moment (EDM). This property provides polar molecules with promising applications in quantum simulation, quantum computing, and the precision measurement of fundamental constants.

However, the complex energy structure of molecules has drawbacks as well as benefits. In particular, electric dipole transitions between vibrational states of a molecule are not necessarily closed, as there are no general vibrational transition selection rules. Laser slowing and cooling typically involves scattering a large number of photons. If the cooling cycle is not fully closed then re-pump lasers are needed to return molecules to the cycle if they fall into a state outside it. As there are no vibrational selection rules in molecules, there are typically a large number of possible vibrational states a molecule can decay into from an excited state. Accordingly, it was thought that the laser cooling and slowing of molecules would be too impractical to implement. However, some molecules have more favourable branching ratios than

[1] As in, for example, [2], 'cold' is defined as $\lesssim 1\,\mathrm{K}$ and 'ultracold' as $\lesssim 1\,\mathrm{mK}$ throughout this work. Atoms and molecules above $\sim 1\,\mathrm{K}$ are 'warm'.

others and the criteria molecules must meet in order to be laser coolable was identified in 2004 [3].

The laser slowing and magneto-optical trapping of molecules is now a well established experimental technique [4], bringing into reach the possibility of exploiting the rich internal structure of molecules in a variety of applications. However, the number of molecules trapped in magneto-optical traps (MOTs) is still small compared with atomic MOTs. There are a variety of reasons for this, but they include the fact that, by the time the molecular beam reaches the MOT, its transverse width is larger than the capture area of the trap, and the fact that cycling many photons will lead to the loss of molecules into unaddressed states, even in molecules with favourable branching ratios. Therefore, there is a need for a slowing technique which slows molecules to within the capture velocity of a MOT in a shorter distance, provides transverse confinement, and which will scatter fewer photons. One possible technique is Zeeman-Sisyphus deceleration, proposed in 2016 [1] and demonstrated in 2021 on a beam of CaOH molecules [5].

1.1 Overview

There are two strands of research presented in this thesis. The first is the application of Zeeman-Sisyphus deceleration (ZS, ZSD) to calcium monofluoride, CaF, with a view to increasing the number of molecules loaded into MOTs of CaF. The second is the development of a ZSD technique for YbF, with a view to making future MOTs of YbF viable.

The remainder of this chapter covers the applications of ultracold molecules in molecular clocks, measurements of the electron's electric dipole moment, quantum simulation, and quantum computation. Then, the theory of magneto-optical trapping is introduced and the need for accepted molecules to be below a certain velocity and within a certain capture area is established. Finally, a variety of techniques for slowing molecular beams are introduced and compared with Zeeman-Sisyphus deceleration.

Chapter 2 covers the key results from molecular and optical physics used in this thesis, including the Born-Oppenheimer approximation. The matrix elements for

the rotational component of the molecular Hamiltonian, the Zeeman effect, and the electric dipole transition are presented.

Following Chapter 2, the thesis focusses first on applications of ZSD to CaF. CaF is used to investigate the dynamics of quantum systems, with the aim of producing a molecular lattice for quantum simulation [6] and computation [7, 8], and molecular clocks for the detection of variations in fundamental constants over time [9]. CaF has favourable vibrational branching ratios, allowing for a large number of photons to be scattered and making laser slowing possible. Research involving CaF molecular beams began with the production of a supersonic beam. This was used to characterise some properties of the first excited state of the molecule in 2008 [10], and in 2011, Stark deceleration [11] was carried out. Later, in 2014, laser cooling and slowing [12] of the supersonic beam was demonstrated. Following this, a cryogenic buffer gas was developed in 2017 [13]. The resulting beam was laser slowed [14] and trapped in a magneto-optical trap (MOT) [15, 16].

Production of a molecular lattice requires magnetically or optically trapping the molecules. To date, progress towards this includes the magnetic trapping and coherent control of molecules in 2018 [17] and the verification of the long rotational coherence time expected in a magnetic trap in 2020 [18]. Sympathetic or evaporative cooling of the molecules has been explored, and atom-molecule collisions within a magnetic trap with a view to this were studied in 2021 [19, 20]. The number of molecules in these traps remains low — on the order of 10^4. To increase this, more molecules need to be within the capture area and below the capture velocity of the MOT. Hence, there is a need for a technique which can slow molecules whilst reducing the transverse size of the molecular beam. Zeeman-Sisyphus deceleration is one such method.

Chapter 3 provides details of the ZSD method, presents details of a ZS decelerator which was constructed, and includes simulations carried out to determine the best experimental configuration for testing the decelerator. Chapter 4 describes the experimental setup, including the vacuum systems, lasers, and optical setup. This chapter also provides various measurements taken to characterise or calibrate different aspects of the experimental setup. Chapter 5 looks at the theoretical and experimental aspects of producing a molecular beam and provides a characterisation of the beam produced using a He buffer gas.

For the ZS decelerator to be tested, molecules need to be detected at the point where the exit of the decelerator will be, whether or not the actual decelerator is present. Once molecules are detected there, it is possible to compare the profile of the molecular beam with and without the decelerator. To that end, some effort was put into attempting to detect the molecular beam around 1 m downstream of the source. Details of these efforts are given in Chapter 6. Chapter 6 also contains details of a neon buffer gas beam, which was trialled in an attempt to reduce the pressure in the vacuum chamber, and results from an experimental trial of the background-free imaging scheme described in [21].

In Chapter 7 the thesis turns to applications of ZSD to YbF. YbF is used in experiments for the precision measurement of the electron's electric dipole moment (eEDM, d_e). A sufficiently high-precision measurement of the eEDM has the potential of discovering new physics or ruling out (or constraining) various theories of beyond-Standard Model physics. Two measurements of the eEDM have been carried out using YbF [22, 23]. Both measurements were conducted using a cold supersonic beam of YbF molecules [24]. It is expected that use of ultracold YbF, either as a beam or trapped in an optical lattice, will provide a higher precision measurement of the eEDM [25]. Progress towards the production of an ultracold YbF beam includes the development of a cryogenic buffer gas source [26] and one dimensional laser cooling of the resulting beam to ultracold temperatures [27]. However, the vibrational branching ratios of YbF are much less favourable than those of CaF, making direct laser slowing unfeasible [28]. Therefore, there is a need for a technique, such as Zeeman-Sisyphus deceleration, which can slow the molecules to within the capture velocity of a MOT with only a few thousand photons scattered.

Chapter 7 presents progress towards developing a ZSD scheme for a beam of YbF molecules. An optical pumping scheme is outlined which differs from the CaF scheme in key ways. The chapter also includes the results of simulations which provide insight into the limitations of such a scheme.

1.2 Applications of Ultracold Molecules

1.2.1 Tests of Fundamental Physics

Modern physics rests on the foundation of two Standard Models: that of particle physics ('the Standard Model'), which is a quantum field theory including all fundamental forces except gravity, and that of cosmology ('the ΛCDM Model'), which is a classical field theory including only gravity. However, it is known that these two models are incompatible with one another. The Standard Model explains only 15% of the matter required by the ΛCDM Model to explain astronomical observations, with the remainder being termed 'dark matter' [29]. Additionally, the Standard Model's prediction of the vacuum energy of the Universe ('dark energy') differs from the value required by the ΛCDM Model to explain the observed expansion of the Universe by a factor of 10^{120} (the 'cosmological constant problem') [30].

Given these problems at the foundation of physics, there is naturally a great deal of interest in theories of beyond-Standard Model physics. There is, accordingly, interest in experimental results which can discover new physics in order to constrain any theories of beyond-Standard Model physics. Two such experiments in atomic and molecular physics are described here.

Detecting Variations in Fundamental Constants

Many models of beyond-Standard Model physics predict that the fundamental 'constants' of the two Standard Models will vary on cosmological timescales. As waiting cosmological timescales to observe this variation is impractical, there is interest in high precision measurements which will be able to observe any change over a more reasonable timescale. Atomic and molecular clocks provide one such measurement [9].

All clocks use some form of oscillation to keep track of time, with one cycle of the oscillation being one 'tick'. The frequency of the oscillation will depend on a physical constant. For example, the frequency of a pendulum clock depends on the local gravitational acceleration, g:

$$f_{\text{pend}} = \frac{1}{2\pi}\sqrt{\frac{g}{L}}, \tag{1.1}$$

where L is the length of the pendulum. The frequency is a dimensionful quantity and so cannot be used to measure g without an external frequency reference. If this frequency reference has a different dependence on g, then the ratio of the frequencies will be a dimensionless quantity which depends on g.

In the case of atomic and molecular clocks, the oscillating system is an electromagnetic wave whose frequency is locked to a specific atomic or molecular energy level transition. These transitions depend on the fine structure constant, α, and the electron-proton mass ratio, μ. Different types of transition have different dependencies on each constant. For example, when expressed in atomic units, the frequency of optical transitions is insensitive to μ, the frequency of hyperfine (microwave) transitions depends linearly on μ, and the frequency of molecular vibrational transitions depends on $\mu^{1/2}$. The dependence on α is more complex and depends on relativistic corrections. In order to properly isolate α and μ, it is advantageous for any such experiment to include molecular clocks.

Since it is the change in the fundamental constants over time that is of interest, the accuracy of the measurement depends on the stability of the frequencies of the clocks used. The measure of this stability for any clock is the fractional frequency uncertainty (FFU): $\frac{\Delta f}{f}$. This is the inverse of the Q-factor. In atomic and molecular transitions the natural linewidth provides the fundamental lower bound on Δf. Therefore, transitions with smaller natural linewidths (i.e., long excited state lifetimes) can provide higher Q-factors, so long as other experimental uncertainties are accounted for. Such transitions are known as 'clock transitions'. As the frequency of transitions in atomic and molecular systems is typically much higher than in any mechanical system, significantly higher Q-factors can be achieved, thus reducing the FFU. For example, the Burgess Clock B, one of the most accurate mechanical clocks ever produced [31], has an FFU of around 1×10^{-7} [32], whereas Caesium atomic clocks can routinely achieve FFUs as low as 1×10^{-16} [9].

As the quantity to be measured is the change in a fundamental 'constant', the value is expected to be very small. Hence, in order to distinguish the result from zero, extremely accurate measurement systems are required. The actual linewidth of an atomic or molecular transition depends on a variety of factors other than the natural linewidth. For example, it can be Doppler broadened due to thermal effects

or power broadened due to the intensity of the pump laser. Cooling the molecules reduces the Doppler broadening, increasing the Q-factor and, therefore, the accuracy of any measurement [33]. Hence, to achieve the highest accuracy, it is important for an experiment of this sort to make use of ultracold molecules.

Electron Electric Dipole Moment

The electric dipole moment (EDM) of a particle is a measurement of the asymmetry of the particle's charge distribution. For a fundamental particle, such as the electron, the EDM vanishes unless both parity and time-reversal symmetry are violated [22, 34]. This property naturally makes the measurement of the EDMs of fundamental particles an area of interest for fundamental physics.

In the Standard Model of Particle Physics, the electron's electric dipole moment (eEDM, d_e) is predicted to have a value of $d_e < 1 \times 10^{-38}\,\mathrm{e\,cm}$. However, in various beyond-Standard Model theories, the eEDM is predicted to be several orders of magnitude larger: in the range $1 \times 10^{-30}\,\mathrm{e\,cm}$ to $1 \times 10^{-26}\,\mathrm{e\,cm}$ [35]. Therefore, a high precision measurement of the eEDM has the possibility of discovering new physics, or ruling out or constraining various theories of beyond-Standard Model physics.

An eEDM measurement is essentially a spin precession experiment [23]. Molecules are prepared in the $|F, M_F\rangle = \frac{1}{\sqrt{2}}\left(|1,-1\rangle + |1,1\rangle\right)$ state. They then pass through a region of electric field where $|1,-1\rangle$ and $|1,1\rangle$ are eigenstates. As the molecule is in a superposition state, a phase difference develops between the two eigenstates:

$$\phi = \frac{\mu B - d_e E_{\mathrm{eff}}}{\hbar} t, \tag{1.2}$$

where E_{eff} is the total effective electric field and t is the time the molecule spends in the region with the external electric field (the interaction time). A small, variable magnetic field, B, is also applied and gives rise to a Zeeman contribution, $(\mu_B/\hbar)\,B$, in the phase. Varying B produces interference fringes in the population of one of the eigenstates. These fringes can be used to determine d_e.

The electric field which needs to be applied varies depending on the internal effective electric field of the molecule being used. Heavy polar molecules have a large

internal effective electric field, on the order of 10–100 GV cm^{-1}. This means that good measurements of the eEDM can be made with smaller external electric fields. With ThO, an electric field of 1 V cm^{-1} is applied [36], with ionic HfF^+, a field of 24 V cm^{-1} is applied [37], and with YbF, a field of 10 kV cm^{-1} is applied [23].

There is a lower limit on the error of the eEDM measurement due to Poisson shot noise, given by [25]:

$$\sigma_{d_e} = \frac{\hbar}{2E_{\text{eff}}t\sqrt{N}}, \tag{1.3}$$

where N is the number of molecules. Present measurements of the eEDM are all consistent with zero, meaning that σ_{d_e} effectively provides an upper bound on the true value. The present state of the art measurements involve room temperature neutral ThO molecules and give an upper limit of 1.1×10^{-29} e cm with 90% confidence [36]. The high precision is achieved by provision of a high molecular flux. However, the molecular state used is metastable in ThO, limiting the interaction time. An alternative method makes use of HfF^+ ions. These have a very large internal electric field. The measurement gives an upper limit of 4.1×10^{-30} e cm with 90% confidence [38]. However, the Couloumb interaction between the ions limits the molecular flux that can be achieved and so places a limit on N.

On the other hand, both long interaction times and high N can be achieved through the use of neutral ultracold polar molecules. It is expected [25] that such an experiment will provide an upper limit as low as 1×10^{-32} e cm, providing information on new physics up to 1000 TeV. This is a far higher energy regime than can be directly probed by collider experiments and so there is a great deal of interest in such experiments.

1.2.2 Quantum Computation & Simulation

Quantum computing and quantum simulation are rapidly developing areas of research which aim to use the properties of quantum systems to solve problems that are difficult or impossible to solve with a classical computer. Whilst quantum simulation aims to

use one quantum system directly as an analogue for another quantum system, quantum computing involves encoding information within a quantum state for processing by the quantum system. Ultracold polar molecules have promising applications in both fields.

Quantum Simulation

There are many physical systems which are difficult or practically impossible to simulate on classical computers, either because the size of the variables needed to run the simulation would occupy too much memory or because the simulation would not complete in a reasonable amount of time. Many of these classically intractable simulations are simulations of quantum systems. It has been shown that it is possible to use the evolution of a controllable quantum system as an efficient simulation of any many-body quantum system [39]. Since a quantum simulator has the ability to efficiently simulate any quantum system, there has been a great deal of interest in producing a working quantum simulator over a wide range of fields, from finding high-temperature superconductors to understanding nuclear matter [6].

Whilst trapped ions are the most well-established candidate for performing quantum simulations at large scale [40], ultracold atoms in optical lattices have provided extremely promising results [41]. This approach allows for gate operations to run in parallel, applied to a large number atoms which have well-specified initial states. Using polar molecules in the place of atoms offers the possibility of simulating long-range interactions, thanks to the electric dipole moments present in molecules. Molecules also have a much richer internal structure, including vibrational and rotational transitions, which provides a wide basis for encoding spins. The prospect of a quantum simulator that makes use of ultracold polar molecules has inspired many proposed applications in the field of quantum magnetism [6].

Quantum Computing

Quantum computing typically involves encoding quantum information into a set of two-level quantum systems known as qubits. The systems are then allowed to evolve under a carefully selected Hamiltonian corresponding to a quantum algorithm. In this way, the quantum information stored in the qubits can be processed in much the same

way that classical information is processed on a classical computer. Ultracold polar molecules make good candidates for qubits as the electric dipole moments makes it possible to implement two-qubit gates with evolution times as short as 1 µs [8].

As well as using qubits, which provide a direct analogue to binary classical computation, it is possible to use higher dimensional quantum systems as 'qudits' [42]. As each qudit can store more information than a qubit, the number of d-level qudits required to encode a given problem is $\log_2 d$ less than the number of qubits. In addition, the extra energy levels present in qudits allow for improved quantum error correction codes. Ultracold dipolar molecules' rich internal structure makes them an excellent candidate for qudit computation, and an implementation of Deutsch's algorithm for CaF or RbCs $d = 4$ qudits has been proposed [7].

1.3 Cooling and Slowing of Molecules

All of the possible applications of ultracold polar molecules outlined in Section 1.2 require holding the molecules in a conservative trap, such as a magnetic trap or a dipole trap. However, production methods for polar molecules generally result in a fast-moving beam. The speed, typically over $100\,\mathrm{m\,s^{-1}}$, means that it is not possible to directly load a conservative trap from the beam. Instead, the molecules must first be confined in a magneto-optical trap (MOT), which can be loaded directly from a molecular beam. The MOT can then be used to cool the molecules so they can be accepted by a conservative trap.

In this section we first examine the mechanics of radiation pressure, before looking at its applications in laser slowing, cooling, and trapping. We also establish the desiderata for a molecular beam by examining the dynamics of a single molecule in a MOT. Finally, we examine the history of molecular slowing and motivate the need for the benefits of a Zeeman-Sisyphus slowing scheme.

1.3.1 Radiation Pressure

Suppose a molecule with momentum $\vec{p} = m\vec{v}$ is in the presence of a laser field, $\vec{\mathcal{E}} = \vec{\mathcal{E}}_0 \cos\left(\omega_{\mathrm{las}} t - \vec{k}\cdot\vec{r}\right)$, which is resonant with a molecular transition of energy $\hbar\omega_0$, as in Figure 1.1. The molecule will scatter photons at a rate, R:

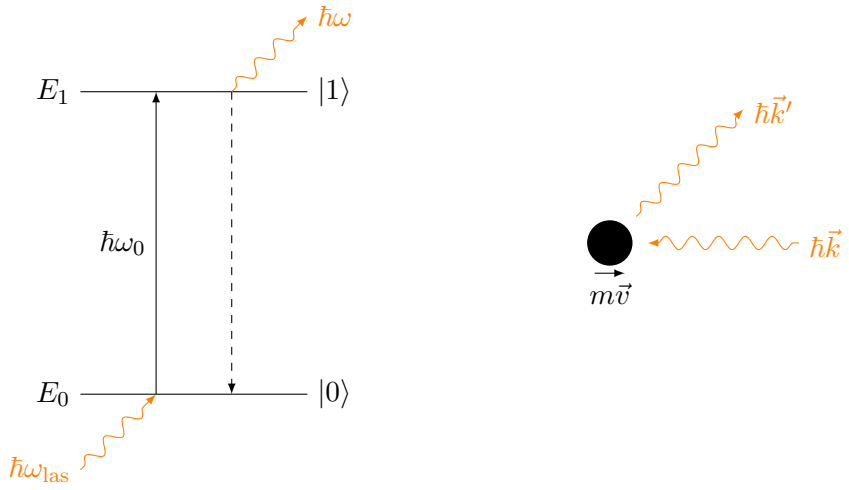

FIGURE 1.1: A two level quantum system with momentum, $m\vec{v}$, eigenstates $|0\rangle$ and $|1\rangle$ and energy eigenvalues E_0 and E_1. The energies are such that $E_0 < E_1$ and $E_1 - E_0 = \hbar\omega_0$. A transition between eigenstates can be driven via an electric dipole coupling with an external laser field of frequency ω_{las}. This results in the 'scattering' of photons.

$$R = \frac{s}{1+s+\delta^2}\,\gamma \qquad s = \frac{\pi hc\gamma}{6\lambda^3} \qquad \delta = \frac{(1-\beta)\omega_{las} - \omega_0}{\gamma}, \tag{1.4}$$

where $1/(2\gamma)$ is the excited state lifetime and $\beta = \frac{\vec{v}\cdot\vec{k}}{c|\vec{k}|}$ is the velocity of the body parallel to the $\vec{k}$-vector of the laser divided by the speed of light. The saturation parameter, $s = \frac{I}{I_{sat}}$, is related to the laser intensity, $I = \frac{1}{2}\varepsilon_0 c\mathcal{E}_0^2$. The intensity of the laser that gives $s = 1$ is defined as the saturation intensity, I_{sat}. Further details on the light-matter interactions are given in Section 2.5.

In addition to carrying energy $\hbar\omega_{las}$, the photons also carry momentum $\hbar\vec{k}$. This means that in every photon scattering event there is a force, the radiation pressure, exerted on the molecule:

$$\vec{F} = -\hbar(\vec{k}' - \vec{k})R, \tag{1.5}$$

where $\hbar\vec{k}$ is the momentum of the inbound photon (a constant of the laser field) and $\hbar\vec{k}'$ is the momentum of the outbound photon. Since the outbound photons are distributed symmetrically, the mean outbound momentum is zero. This means that the average force exerted is:

$$\left\langle \vec{F} \right\rangle = \hbar \vec{k}\ R. \tag{1.6}$$

Due to the Doppler effect, the force exerted will vary with the molecule's velocity parallel to the $\vec{k}$ of the light. The laser frequency can be adjusted to bring the system into resonance with molecules moving at arbitrary velocity, $\beta_0 = v_0/c$:

$$\omega_{\text{las}} = \frac{\omega_0}{1 - \beta_0}, \tag{1.7}$$

so that the detuning parameter, δ, becomes:

$$\delta = \underbrace{\frac{\omega_0}{\gamma\,(1 - \beta_0)}}_{\omega_{\text{las}}/\gamma} (\beta_0 - \beta)\,. \tag{1.8}$$

If the molecule is moving anti-parallel to the light then the velocity will decrease as photons are scattered. As the molecule's velocity reduces, the Doppler shift of the transition will decrease whilst the laser frequency remains constant, and so the force exerted will be reduced. The force exerted on a CaF molecule by a laser resonant with the A–X transition for $\beta_0 c = 145\,\text{m}\,\text{s}^{-1}$ is shown in Figure 1.2.

1.3.2 Laser Slowing and Cooling

The most immediate application of radiation pressure is for slowing down atomic and molecular beams. A CaF molecule will experience a force of around $1.4 \times 10^{-20}\,\text{N}$ from a laser beam on resonance at saturation intensity. Modelled velocity distributions for a CaF beam with initial $v_{\text{out}} = 145\,\text{m}\,\text{s}^{-1}$ and a temperature of 4 K are shown in Figure 1.3. The model includes 606 nm laser light moving anti-parallel to the molecular beam. It can be clearly seen that the modal velocity of the molecules is reduced. Temperature is directly proportional to standard deviation in velocity, $T \propto \sigma_v^2$. Hence, it can also be noted that the longitudinal temperature of the slow molecules is reduced. However, longitudinal cooling implies a transverse heating of

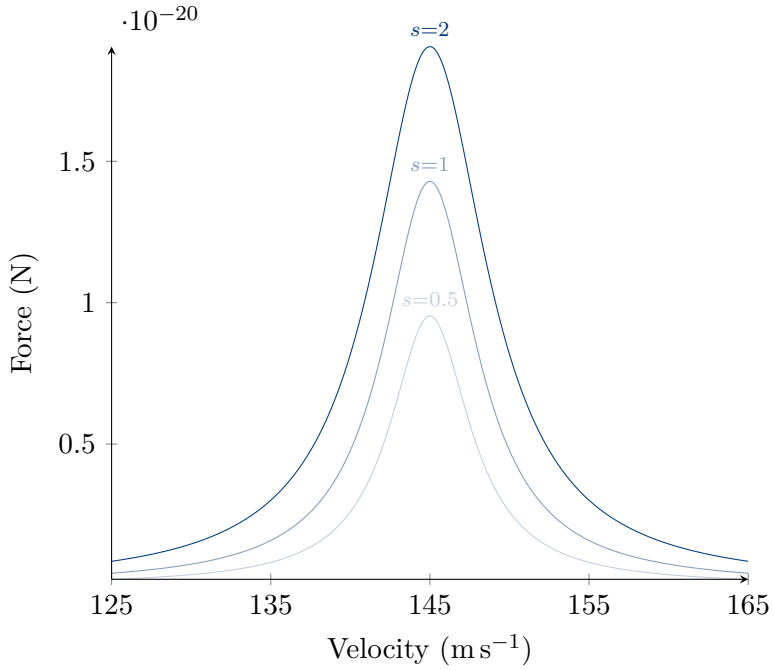

FIGURE 1.2: The force exerted on a CaF molecule by a 606 nm laser resonant with the A–X transition for a molecule moving at $v_0 = 145\,\mathrm{m\,s^{-1}}$ at intensities $s = 0.5$, $s = 1$, and $s = 2$.

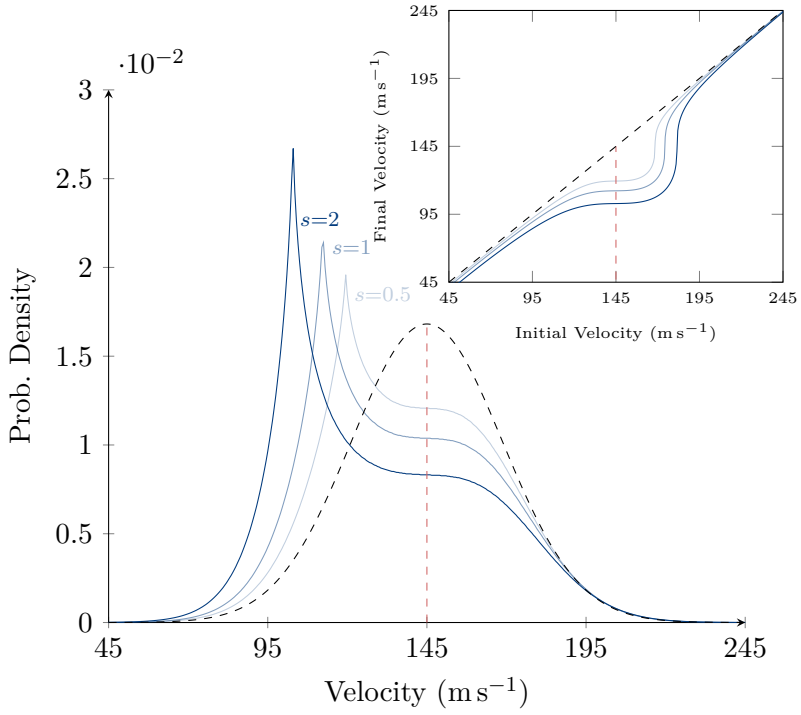

FIGURE 1.3: Modelled final velocity distributions of a CaF beam with $v_{\mathrm{out}} = 145\,\mathrm{m\,s^{-1}}$ and a temperature of 4 K after 80 cm of deceleration by a counter-propagating single-frequency laser on resonance with molecules moving at $145\,\mathrm{m\,s^{-1}}$ at intensities $s = 0.5$, $s = 1$, and $s = 2$. The initial velocity is modelled as a 1D Gaussian distribution (dashed black line). The inset shows the initial and final velocities of individual particles in the beam, with a dashed black line showing the $s = 0$ asymptote.

the molecular beam [43]. Therefore, if nothing is done to confine the beam, the beam intensity will decrease as the molecules spread out transversely.

Any molecule with a component of its velocity anti-parallel to the light will be slowed in that dimension. Therefore, if the laser is arranged perpendicular to a molecular beam then the molecules' transverse velocity will be reduced. To ensure the transverse velocity is reduced regardless of direction, a second laser beam can be arranged anti-parallel to the first (but still perpendicular to the molecular beam). This arrangment is known as transverse laser cooling, and can be used to increase the intensity of a molecular beam. Transverse cooling was first demonstrated for heavy polar molecules in 2010 [44]. Here, a beam of SrF molecules with an initial temperature of 50 mK was cooled to 5 mK by transverse laser cooling.

1.3.3 Magneto-Optical Trapping

As well as slowing, radiation pressure can also be used to trap molecules. Suppose there are two counter-propagating laser fields, $\vec{\mathcal{E}} = \vec{\mathcal{E}}_0 \cos\left(\omega_{\text{las}} t \pm \vec{k}\cdot\vec{r}\right)$, then the force exerted is:

$$\vec{F} = \hbar\vec{k}\,\gamma s \left(\frac{1}{1+s+\left(\frac{(1-\beta)\omega_{\text{las}}-\omega_0}{\gamma}\right)^2} - \frac{1}{1+s+\left(\frac{(1+\beta)\omega_{\text{las}}-\omega_0}{\gamma}\right)^2} \right). \tag{1.9}$$

Although the two lasers have the same red-detuned frequency, $\omega_{\text{las}} < \omega_0$, the molecules see different Doppler shifts from each laser due to the reversal of the k-vector. Only a molecule not moving feels no force in this laser field. If a molecule is moving parallel to $\vec{k}$ then, due to the Doppler shift, the force exerted by the $-\vec{k}$ laser is greater than the force exerted by the $\vec{k}$ laser and so there is a net force. Vice versa for a molecule moving anti-parallel to $\vec{k}$. Since any moving molecule feels a decelerating force, this laser field is called an 'optical molasses'.

That this is a drag-like force can be seen if Eqn. (1.9) is expanded in terms of β. To first order in β, it takes the form of a Stokes' drag, $\vec{F} = -b\beta\hat{k}$, where $\hat{k} = \vec{k}/|\vec{k}|$, and with drag coefficient:

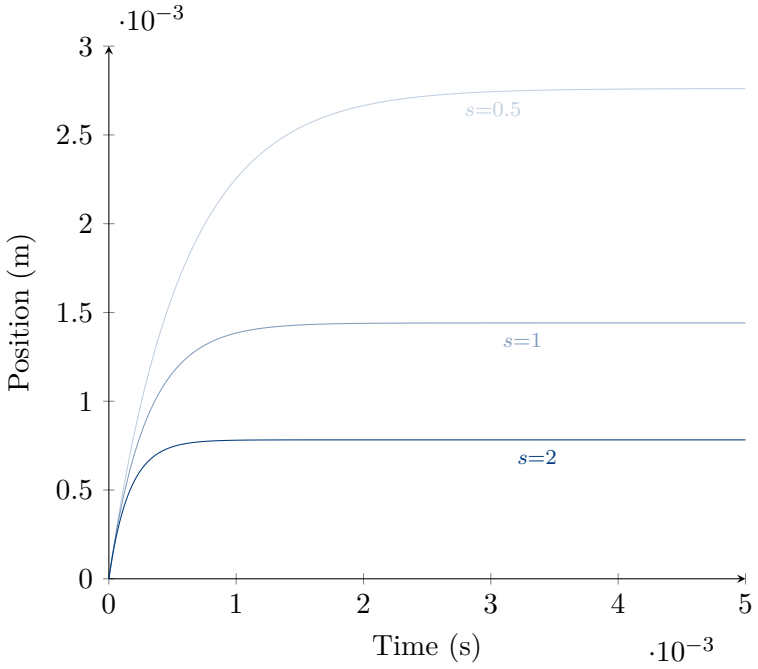

FIGURE 1.4: The position of a CaF molecule moving at $5\,\mathrm{m\,s^{-1}}$ initially at the centre of a 606 nm optical molasses with a red detuning of 5γ, where 2γ is the natural linewidth of the CaF A–X transition, at intensities of $s = 0.5$, $s = 1$, and $s = 2$. The motion of the molecules clearly indicates the molasses are exterting a drag-like force.

$$b = \hbar|\vec{k}|\ \gamma s\ \frac{4(\omega_{\mathrm{las}}^2 - \omega_{\mathrm{las}}\omega_0)}{\gamma^2\left(1 + s + \left(\frac{\omega_{\mathrm{las}}-\omega_0}{\gamma}\right)^2\right)^2}. \tag{1.10}$$

A model of the motion of a single CaF molecule in an optical molasses can be seen in Figure 1.4. The figure shows the motion of a CaF molecule moving at $5\,\mathrm{m\,s^{-1}}$ in an optical molasses with $\omega_{\mathrm{las}} = \omega_0 - 5\gamma$ at three different laser intensities.

Although an optical molasses can bring a molecule to a standstill, a true trap requires a position-dependent restoring force of the form:

$$\vec{F} = -ax\hat{k} - b\beta\hat{k}. \tag{1.11}$$

This can be achieved through the Zeeman effect, which is described in detail in Section 2.4. In the presence of a magnetic field the normally degenerate spin-projection (m quantum number) states split into 'weak field seeking' (WFS) states whose energy

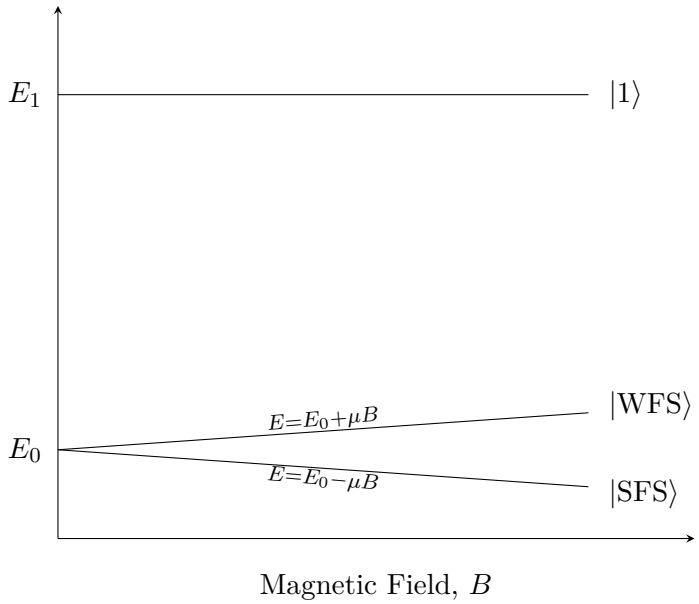

FIGURE 1.5: A modified version of the two-level system shown in Figure 1.1. The ground state is split into a $|\mathrm{WFS}\rangle$ and a $|\mathrm{SFS}\rangle$ state, with different linear magnetic field dependencies. This can be used as a simple model of the Zeeman splitting in the $X^2\Sigma$ state of the CaF A–X transition, in which case, in the high field limit, the magnetic moment equals the Bohr magneton, $\mu = \mu_B$.

increases with magnetic field strength, and 'strong field seeking' (SFS) states whose energy decreases with magnetic field strength. This is shown in Figure 1.5, with WFS states labelled $|\mathrm{WFS}\rangle$ and SFS states labelled as $|\mathrm{SFS}\rangle$.

The polarisations of the two counter-propagating molasses lasers must be chosen such that angular momentum is conserved. If the change in the spin projection, m, quantum number for each of the two transitions is ± 1, then the laser polarisations will then be $\sigma^{\mp}$ [45]. Then the detuning term in the scattering rate becomes:

$$\frac{(1 \pm \beta)\omega_{\mathrm{las}} - \omega_0}{\gamma} \rightarrow \frac{(1 \pm \beta)\omega_{\mathrm{las}} - \omega_0 \pm \frac{\mu A x}{\hbar}}{\gamma}, \tag{1.12}$$

where A is the gradient of the magnetic field ($B = Ax$) and μ is the magnetic moment, which we take to be equal to the Bohr magneton, μ_B, for now. To first order in β and x, the force on the molecule now resembles a damped harmonic oscillator:

$$\vec{F} = -ax\hat{k} - b\beta\hat{k}, \tag{1.13}$$

where $x = \frac{\vec{r}\cdot\vec{k}}{|\vec{k}|}$ and with spring constant:

$$a = \hbar|\vec{k}|\ \gamma s \frac{4\mu A(\omega_{\text{las}} - \omega_0)}{\hbar\gamma^2\left(1 + s + \left(\frac{\omega_{\text{las}}-\omega_0}{\gamma}\right)^2\right)^2}. \tag{1.14}$$

This combination of light and magnetic field is a magneto-optical trap (MOT). Figure 1.6 shows the simulated motion of a CaF molecule in a MOT with $A = 2\,\text{T}\,\text{m}^{-1}$ and $\omega_{\text{las}} - \omega_0 = 5\gamma$. The wavelength of the light is 606 nm and $\gamma/\pi = (8.3 \pm 0.3)$ MHz, as measured for the CaF A–X transition [10]. A more complete model would account for the fact that a real CaF molecule is not a closed two-level system. The multi-level nature of the real molecule gives rise to an effective lifetime, γ_{eff}, and an effective magnetic g-factor, g_{eff}, such that $\mu = g_{\text{eff}}\mu_B$ [46, 47]. The product of these has been measured to be $\gamma_{\text{eff}}g_{\text{eff}} = (0.023 \pm 0.003)\,\gamma$ in an experimentally realised CaF MOT with $A = 0.3\,\text{T}\,\text{m}^{-1}$ and $\omega_{\text{las}} - \omega_0 = 1.5\gamma$ [16].

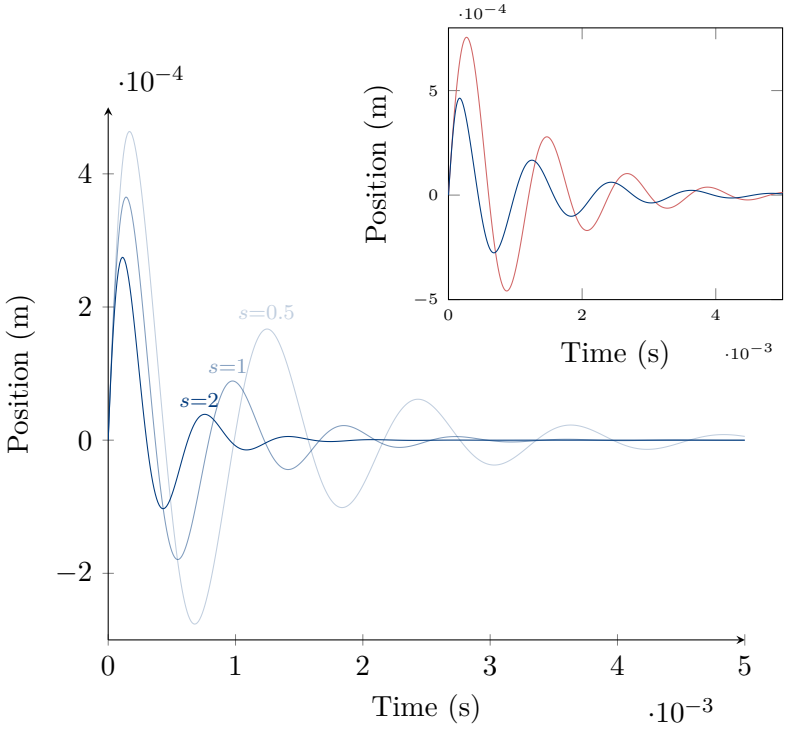

FIGURE 1.6: The position of a CaF molecule moving at $5\,\text{m}\,\text{s}^{-1}$ initially at the centre of a 606 nm MOT with a red detuning of 5γ, where 2γ is the natural linewidth of the CaF A–X transition, at intensities of $s = 0.5$, $s = 1$, and $s = 2$, and a magnetic field strength of $2\,\text{T}\,\text{m}^{-1}$. The inset shows the difference in response between the MOT (blue) and the first-order harmonic oscillator (red) approximation for $s = 0.5$.

Also shown in Figure 1.6 is an example of the motion in a trap equivalent to a first order harmonic oscillator approximation of a MOT. The first-order (harmonic) oscillation frequency is given by:

$$\omega_{\mathrm{MOT}}^2 = \frac{|\vec{a}|}{m} = \frac{4\mu A(\omega_{\mathrm{las}} - \omega_0)s}{m\gamma\left(1 + s + \left(\frac{\omega_{\mathrm{las}} - \omega_0}{\gamma}\right)^2\right)^2}|\vec{k}|, \tag{1.15}$$

and has no dependence on the initial velocity of the molecule. However, the true MOT force depends on velocity, due to the Doppler shift, as can be seen in Figure 1.7. Therefore, the actual oscillation frequency of the MOT also depends on the initial velocity.

Figure 1.7 also shows that the magnitude of the force experienced by a molecule has two maxima and goes to zero as the molecule moves further away from the centre. For a molecule to be captured by the MOT, the work done by the restoring force must be greater than the initial kinetic energy of the molecule. Therefore, above a certain velocity, the restoring force will be too small to prevent the molecule from moving further away from the centre of the MOT. This means that the trap has a certain maximum 'capture velocity', v_{MOT}, which molecules must be decelerated to before entering the trapping region. This effect can be seen in Figure 1.8. v_{MOT} has been measured in an experimentally realised CaF MOT to be $(11 \pm 2)\,\mathrm{m\,s^{-1}}$ [48].

This model includes no position-limit on force, meaning that there is always some velocity for which molecules will experience a significant force, regardless of their position. However, in practice the size of the MOT lasers will provide a limit on the position, regardless of velocity. Together with the limit provided by v_{MOT}, this means that the phase space acceptance of a MOT can be modelled as a parallelogram with base 'length' $2v_{\mathrm{MOT}}$ and perpendicular 'height' given by the size of the laser beam.

Magneto-optical trapping of polar molecules was first demonstrated in 2014 [49]. A beam of SrF molecules was laser slowed from a mean forward velocity of around $135\,\mathrm{m\,s^{-1}}$ to between $50\,\mathrm{m\,s^{-1}}$ and $100\,\mathrm{m\,s^{-1}}$. In all single-frequency laser slowing schemes, the force exterted by the laser drops as the laser is Doppler shifted out of resonance. To mitigate this, the spectrum of the slowing light was broadened so

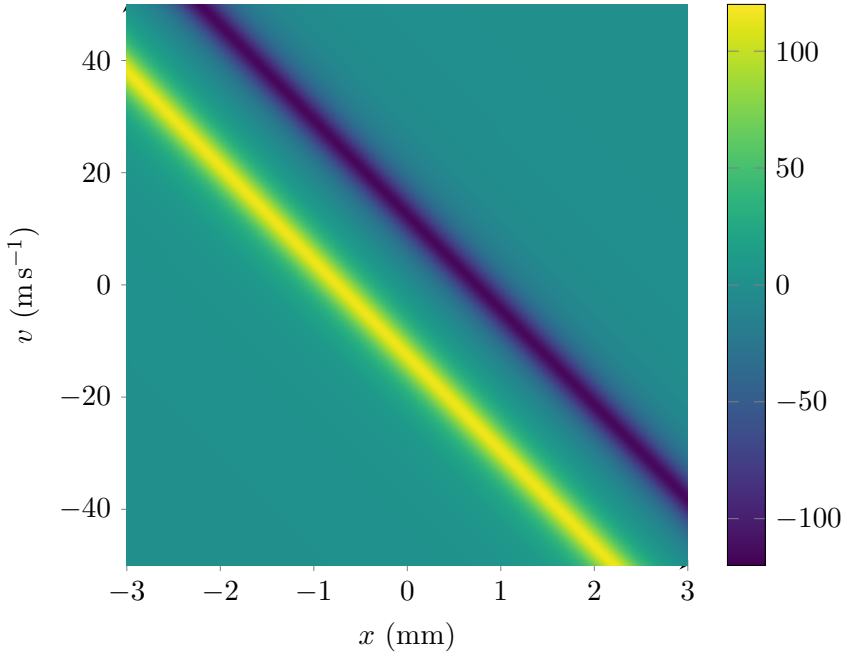

FIGURE 1.7: The force (in $\mathrm{keV\,m^{-1}}$) experienced by a CaF molecule at position x and with velocity v in a 1D MOT of the kind described in Figure 1.6 with laser intensity $s = 2$. For a molecule at $x = 0$ with positive velocity, the force is negative, and vice versa for a molecule with negative velocity. It can be seen that a molecule with too large a velocity will not experience enough force to push it back to the centre and will not be captured.

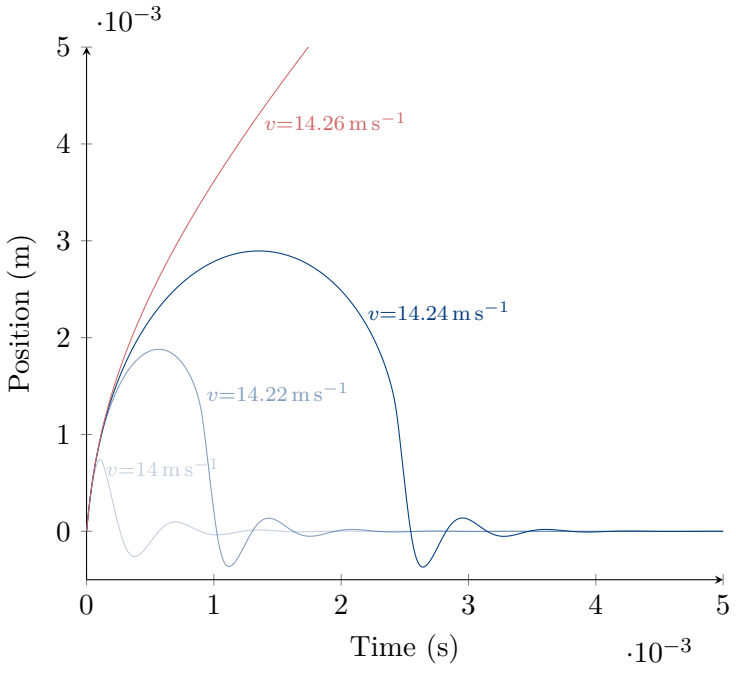

FIGURE 1.8: Oscillations of a CaF molecule in a MOT of the kind described in Figure 1.6 with laser intensity $s = 2$ at four initial velocities: $14\,\mathrm{m\,s^{-1}}$, $14.22\,\mathrm{m\,s^{-1}}$, $14.24\,\mathrm{m\,s^{-1}}$ (blue), and $14.26\,\mathrm{m\,s^{-1}}$ (red). As can be seen, the molecule moving at $14.26\,\mathrm{m\,s^{-1}}$ is not captured by the trap. Additionally, it can be seen that the oscillations become increasingly anharmonic with increasing initial velocity.

that a wider range of Doppler shifts could be addressed. Once slowed, the molecules were loaded into a MOT with $A = 0.0015\,\mathrm{T\,cm^{-1}}$ and a detuning of -1.25γ. The temperature achieved in the MOT was 2.5 mK, which is around the Doppler limit. However, this temperature is still too high for loading a conservative trap. In 2017, heavy polar molecules were cooled below the Doppler limit for the first time [15]. CaF was trapped in a MOT and cooled to 50 µK, a temperature suitable for loading into a magnetic or optical dipole trap.

1.3.4 Methods of Slowing Polar Molecules

Since many promising applications of polar molecules involve first capturing molecules in a MOT, and MOTs have a capture velocity substantially smaller than the $> 100\,\mathrm{m\,s^{-1}}$ velocity of molecular beams, it is necessary to first slow any molecules down before loading them into a MOT.

Laser slowing, described in Section 1.3.2, can be used. However, this is limited by the Doppler effect. As the molecule is slowed, the force exterted drops as the laser is Doppler shifted out of resonance. The force never drops to zero, meaning that a molecule can be slowed to a standstill or even turned around, despite the Doppler shift. However, although a molecule can be slowed indefinitely, it becomes increasingly inefficient to slow down slower molecules with a fixed-frequency laser beam alone. Two ways to resolve this issue are to 'chirp' the laser frequency (that is, change ω_{las} with time) so that the laser is always resonant with the beam as it slows down [14]. The other is to use a broad-spectrum 'white light' laser, so that some component of the laser light is always resonant with the molecular beam [50].

Another commonly used slowing method is Zeeman slowing [51–54]. In this scheme, a magnetic field gradient provided by a solenoid is used to Zeeman shift the transition. In this way, it can be ensured that the molecules always feel a constant force from the slowing laser as they are decelerated. If the molecules start with velocity v_{out} and the Zeeman shift is $\Delta E = \mu B$, then the magnetic field needed to keep the molecules on-resonance is [54]:

$$B(z) = \frac{\hbar k}{\mu} v_{\text{out}} \sqrt{1 - \frac{z}{L}}, \tag{1.16}$$

where L is the length of the decelerator.

Yet another slowing method is Stark deceleration [11, 55, 56]. Instead of making use of radiation pressure, Stark deceleration takes advantage of the Stark effect. This is a change in the molecule's energy in the presence of an electric field, much like the Zeeman effect is for a magnetic field. A molecule in a WFS state passes through an increasing electric field, so increases its internal energy and loses kinetic energy. The field is then switched off, preventing the molecule from regaining that kinetic energy as it exits the field. Thus, a beam can be decelerated by passing it through a series of pulsed electric fields. Stark decelerators have the additional benefit of being able to confine the molecular beam by application of a transverse electric field gradient.

All three of the slowing methods here have drawbacks: laser slowing requires the scattering of many photons, and does not provide any transverse beam confinement, meaning molecules will be lost to unaddressed states and the beam at the end of the deceleration section will be much larger than the capture area of a MOT. Stark deceleration can only slow a small slice of any given molecule beam due to the the timing of the switching of the electric field, limiting the number of molecules which can be effectively slowed. However, through the use of a static periodic magnetic field and optical pumping in a Zeeman-Sisyphus deceleration scheme, it is possible to design a decelerator which can slow an entire beam (rather than just a small slice) whilst also providing confinement via tranverse magnetic field gradients and scattering many fewer photons than laser slowing [1].

Chapter 2

Molecular and Optical Physics

2.1 Molecular Structure

A diatomic molecule is a many-body system which can be considered to consist of two relatively massive centres of positive electronic charge (the two nuclei) and a 'cloud' of much less massive, negatively charged electrons. In addition to the orbital angular momentum of the electrons, $\vec{L}$, the system has two kinetic degrees of freedom. Firstly, the linear motion of the two nuclei relative to the centre of mass, which is denoted by the kinetic energy operator in the centre of mass frame:

$$T_{\text{nuc}} = \frac{-\hbar^2}{2\mu}\frac{1}{\rho^2}\frac{\partial}{\partial\rho}\left(\rho^2\frac{\partial}{\partial\rho}\right), \tag{2.1}$$

where μ is the reduced mass of the two nuclei and ρ is the internuclear distance. And secondly, the rotation of the nuclei about the centre of mass, denoted by the nuclear rotational angular momentum, $\vec{R}$. There are additionally two spin degrees of freedom: that of the electrons, $\vec{S}$, and that of the nuclei, $\vec{I}$.

We can write out the full molecular Hamiltonian schametically as

$$H_{\text{mol}} = T_{\text{el}} + H_{\text{nuc}} + H_{\text{ang}} + V_{\text{en}}, \tag{2.2}$$

where T_{el} is the kinetic energy of the electrons, $H_{\text{nuc}} = T_{\text{nuc}} + B_e\vec{R}^2$, for some constant B_e, is the nuclear Hamiltonian, H_{ang} includes the spins and the various interactions

between the all the angular momenta[1], and V_{en} is the electronic-nuclear interaction potential (i.e., the Coulomb forces between the electrons, nuclei, and electrons and nuclei).

H_{mol} is an operator on the Hilbert space for the joint electronic-nuclear-spin system $\mathcal{H}_{\text{mol}} = \mathcal{H}_{\text{el}} \otimes \mathcal{H}_{\text{nuc}} \otimes \mathcal{H}_{\text{spin}}$. To proceed, we must define a basis that spans $\mathcal{H}_{\text{mol}}$. First, let $\vec{r} = (\rho, \theta, \phi)$ be the internuclear centre-of-mass coordinates. Then, $\{|\vec{r}\rangle \equiv |\rho\rangle \otimes |\theta, \phi\rangle\}$ spans $\mathcal{H}_{\text{nuc}}$. Secondly, define $\{|\epsilon_n\rangle\}$ to span $\mathcal{H}_{\text{el}}$. Finally, the basis spanning $\mathcal{H}_{\text{spin}}$ is the standard spin basis, $|S, I\rangle$, where S and I are the electronic and nuclear spin quantum numbers. Taken all together, $\{|\epsilon_n\rangle \otimes |\vec{r}\rangle \otimes |S, I\rangle\}$ spans the full Hilbert space, $\mathcal{H}_{\text{mol}}$.

Ignoring spin for now, we can expand the 'electronic' portion of the Hamiltonian, $T_{\text{el}} + V_{\text{en}}$ in terms of this basis:

$$T_{\text{el}} + V_{\text{en}} = \int \sum_n E_n^{\text{el}}(\rho) \;\; |\epsilon_n\rangle\langle\epsilon_n| \otimes |\vec{r}\rangle\langle\vec{r}| \;\; \mathrm{d}\vec{r}, \tag{2.3}$$

where $E_n^{\text{el}}(\rho)$ are the expansion coefficients which depend only on the internuclear distance, ρ, for a fixed n. We can also write out an arbitrary solution to the full Schrödinger equation, $H_{\text{mol}} |\psi\rangle = E_\psi |\psi\rangle$, in the same basis:

$$|\psi\rangle = \int \sum_{n'} \psi_{n'}(\vec{r}') \, |\epsilon_{n'}\rangle \otimes \left|\vec{r}'\right\rangle \mathrm{d}\vec{r}'. \tag{2.4}$$

Since $H_{\text{mol}} |\psi\rangle$ can be expanded as:

$$(T_{\text{el}} + V_{\text{en}}) |\psi\rangle + H_{\text{nuc}} |\psi\rangle + H_{\text{ang}} |\psi\rangle \,, \tag{2.5}$$

we begin by expanding out $(T_{\text{el}} + V_{\text{en}}) |\psi\rangle$:

[1] Giving rise to the spin-orbit interaction, Lambda doubling, and the fine and hyperfine structures.

$$(T_{\text{el}} + V_{\text{en}})\,|\psi\rangle = \int \sum_n E_n^{\text{el}}(\rho)\ \psi_n(\vec{r})\,|\epsilon_n\rangle \otimes |\vec{r}\rangle\,\mathrm{d}\vec{r}. \tag{2.6}$$

This expression is difficult to work with due to the dependance of $E_n^{\text{el}}(\rho)$ on ρ, which accounts for relative motion of the electrons and the nuclei. However, if we treat the nuclei as being held fixed a distance, $\tilde{\rho}$, apart, then we can make the substitution $E_n^{\text{el}}(\rho) \to E_n^{\text{el}}(\tilde{\rho})$. Eqn. (2.6) then becomes:

$$(T_{\text{el}} + V_{\text{en}})\,|\psi\rangle \approx \sum_n \left(E_n^{\text{el}}(\tilde{\rho})\,|\epsilon_n\rangle \otimes \int \psi_n(\vec{r})\,|\vec{r}\rangle\,\mathrm{d}\vec{r} \right). \tag{2.7}$$

For notational ease we define $|\nu_n\rangle \equiv \int \psi_n(\vec{r})\,|\vec{r}\rangle\,\mathrm{d}\vec{r}$. Then $|\psi\rangle \approx \sum_n |\epsilon_n\rangle \otimes |\nu_n\rangle$. Since $\int |\vec{r}\rangle\langle\vec{r}|\ \mathrm{d}\vec{r} = \mathbb{1}$ is the identity matrix, the electronic Hamiltonian reduces to $T_{\text{el}} + V_{\text{en}} \approx \sum_n E_n^{\text{el}}(\tilde{\rho})\ |\epsilon_n\rangle\langle\epsilon_n|$. This is the Born-Oppenheimer approximation.

We can now re-introduce spin and re-write the full Schrödinger equation within the Born-Oppenheimer approximation:

$$\begin{aligned} H_{\text{mol}}\,|\psi\rangle &\approx \sum_n \left(H_{\text{nuc}} + H_{\text{ang}} + E_n^{\text{el}}(\tilde{\rho}) \right) |\epsilon_n\rangle \otimes |\nu_n\rangle \otimes |S, I\rangle \\ &= \sum_n |\epsilon_n\rangle \otimes \left(H_{\text{nuc}} + H_{\text{ang}} + E_n^{\text{el}}(\tilde{\rho}) \right) |\nu_n\rangle \otimes |S, I\rangle\,, \end{aligned} \tag{2.8}$$

where the second line follows as $H_{\text{nuc}} + H_{\text{ang}}$ operates on $\mathcal{H}_{\text{nuc}} \otimes \mathcal{H}_{\text{spin}}$ only. As can be seen, $E_n^{\text{el}}(\tilde{\rho})$ behaves as an energy potential in which the nuclei move. The electrons, in turn, are treated as if they move in the potential of a static pair of nuclei. This approximation is good because the electronic mass is so much smaller than the nuclear mass, meaning that the electrons move much faster than nuclei with the same energy.

Since $H_{\text{nuc}} = T_{\text{nuc}} + B_e \vec{R}^2$, for a given n, the nuclear component further splits into radial (vibrational) and angular (angular momentum) parts:

$$T_{\text{nuc}} \left|\nu_{n,v}^{\text{vib}}\right\rangle = E_{n,v}^{\text{vib}} \left|\nu_{n,v}^{\text{vib}}\right\rangle \tag{2.9}$$

$$\left[B_e \vec{R}^2 + H_{\text{ang}}\right] \left|\nu_{n,\{l\}}^{\text{rot}}\right\rangle \otimes |S, I\rangle = E_{n,\{l\}}^{\text{rot}} \left|\nu_{n,\{l\}}^{\text{rot}}\right\rangle \otimes |S, I\rangle \,, \tag{2.10}$$

where v is the vibrational quantum number and $\{l\}$ is the collection of good angular momentum quantum numbers. These may be R and the electronic orbital angular momentum, L, but they also be some combination of these or their projections, depending on which Hund's case the n state falls into. This is considered in Section 2.3.

2.2 Electro-Vibrational Structure

The electronic eigenstates are characterised by two quantities. Firstly, the electronic spin quantum number, S. Secondly, the projection of the electronic orbital angular momentum, $\vec{L}$, onto the intermolecular axis, with quantum number Λ. These are combined into a molecular term symbol, ${}^{2S+1}\Lambda$. Λ is labelled with capital Greek letters:

$\Lambda =$	0,	1,	2,	$\cdots$
Symbol =	Σ,	Π,	Δ,	$\cdots$

by analogy with the S, P, D, etc, of atomic term symbols. The electronic eigenstates can also be labelled by a number, n, in order of increasing energy; though, again, letter symbols are generally used:

$n =$	0,	1,	2,	$\cdots$
Symbol =	X,	A,	B,	$\cdots$

In the case of both CaF and YbF, the lowest three electronic states are known to be [57]:

$$|\epsilon_0\rangle = \left|X^2\Sigma\right\rangle,$$
$$|\epsilon_1\rangle = \left|A^2\Pi\right\rangle,$$
$$|\epsilon_2\rangle = \left|B^2\Sigma\right\rangle.$$

The eigenvalues of these electronic states form a mean field potential for the nuclei to move in, $E_n^{\mathrm{el}}(\tilde{\rho})$. So long as the motion of the nuclei is not large, their effect on the potential they are moving in can be ignored. If we suppose, as an initial assumption, that $E_n^{\mathrm{el}}(\tilde{\rho})$ is a harmonic oscillator, then the energy levels (i.e., the vibrational eigenvalues) will be proportional to $(v+1/2)$, where $v \in \mathbb{N}$. Since $E_n^{\mathrm{el}}(\tilde{\rho})$ is almost certainly not a harmonic oscillator, we can instead consider a series expansion in $(v+1/2)$ [58]:

$$\frac{E_{n,v}^{\mathrm{vib}}}{hc} = \omega_e\left(v+\frac{1}{2}\right) - \omega_e x_e\left(v+\frac{1}{2}\right)^2 + \cdots, \tag{2.11}$$

where, for historical reasons, the (electronic state dependent) constants ω_e, $\omega_e x_e$, $\omega_e y_e$, etc are wavenumbers. These constants are the spectroscopic vibrational constants, and they are determined experimentally.

A candidate function for the acutal potential $E_n^{\mathrm{el}}(\rho)$ which gives such a spectrum to second order in $(v+1/2)$ is the Morse potential [59], which can also be approximated as a harmonic oscillator at low vibrational energies:

$$E_n^{\mathrm{el}}(R) = D_e\left(1-\exp\left(-\sqrt{\frac{\mu\omega_0^2}{2D_e}}(\rho-r_e)\right)\right)^2 \tag{2.12}$$
$$\approx \frac{1}{2}\,\mu\omega_0^2\,(\rho-r_e)^2, \tag{2.13}$$

where μ is the reduced electron-nucleon mass, r_e is the equilibrium internuclear separation, ω_0 is the effective harmonic frequency, and D_e is the molecular dissociation energy. The constants r_e, ω_0, and D_e all depend on the electronic energy level n. The spectrum of the Morse potential is given by [60]:

$$E_{n,v}^{\text{vib}} = \hbar\omega_0 \left(v + \frac{1}{2}\right) - \frac{\hbar^2\omega_0^2}{4D_e}\left(v + \frac{1}{2}\right)^2, \tag{2.14}$$

which means that the Morse potential constants are related to the spectroscopic constants by:

$$\omega_0 = 2\pi c\omega_e \tag{2.15}$$

$$D_e = \frac{hc}{4}\frac{\omega_e}{\omega_e x_e}. \tag{2.16}$$

The spectroscopic constants for the ground and first two excited electronic states of CaF and YbF are known, and the Morse potential for the CaF ground state is given in Figure 2.1.

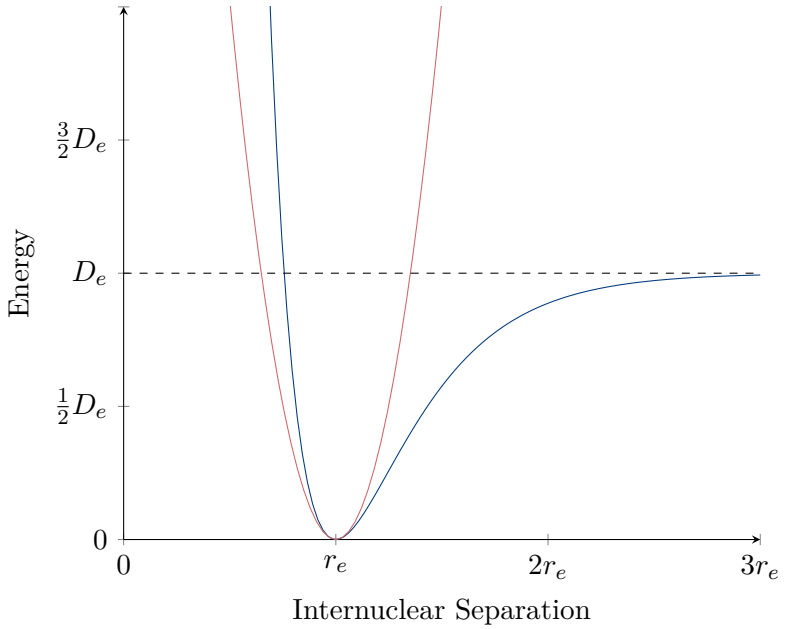

FIGURE 2.1: A Morse potential (blue) with $\frac{1}{2}\mu\omega_0^2 r_e^2 = 8.1D_e$ as in the CaF $X^2\Sigma$ state [57], together with the closest harmonic oscillator approximation (red). It can be seen that a harmonic oscillator is a good approximation for small oscillations about r_e but fails for higher energy vibrations.

2.3 Rotational Structure

The Hamiltonian, $(B_e\vec{R}^2 + H_{\text{ang}})$, for the rotation energy structure of diatomic molecules can be solved for exactly. However, the exact nature of the solution depends on the electronic state as this affects the strength of the spin-orbit interaction (which is located in the H_{ang} term). In particular, we are interested in the case where the spin-orbit coupling is strong, as in the $A^2\Pi$ state, and in the case where $\Lambda = 0$, leading to no spin-orbit coupling, as in the $^2\Sigma$ X and B states. These cases are known as Hund's case (a) and (b) respectively. The Hamiltonians given here largely follow [61] and the matrix elements are given in [61] and [62].

2.3.1 The $X^2\Sigma$ and $B^2\Sigma$ States (Hund's case (b))

In Hund's case (b) there is no spin-orbit coupling (as $\Lambda = 0$). In this scenario, the electronic angular momentum, $\vec{L}$, precesses rapidly about the internuclear axis. Other than Λ, the constants of motion supplying the good quantum numbers are the total orbital angular momentum, $\vec{N} = \vec{L} + \vec{R}$, the electronic spin, $\vec{S}$, and the total non-nuclear angular momentum, $\vec{J} = \vec{N} + \vec{S}$. Additionally, the nuclear spin, $\vec{I}$, and the total angular momentum, $\vec{F} = \vec{J} + \vec{I}$, and its projection onto the lab frame z-axis, M_F, provide good quantum numbers. Hence the basis used to solve the Hamiltonian for this case is:

$$\left\langle N, S, J, I, F, M_F \middle| B_e\vec{R}^2 + H_{\text{ang}} \middle| N', S, J', I, F', M_F' \right\rangle, \tag{2.17}$$

where $S = I = 1/2$ are unprimed because they are fixed.

In order to solve for this matrix element, we must first rewrite the $B_e\vec{R}^2$ term in terms of N. By definition, $\vec{R}^2 = (\vec{N} - \vec{L})^2$. Expanded out, this gives:

$$\vec{R}^2 = \vec{N}^2 + \vec{L}^2 - 2\vec{N}\cdot\vec{L}. \tag{2.18}$$

In molecular frame coordinates $\{x, y, z\}$, $\vec{L} = L_x\hat{x} + L_y\hat{y} + L_z\hat{z}$. Therefore, $\vec{L}^2 = L_x^2 + L_y^2 + L_z^2$. L_x and L_y are related to the angular momentum ladder operators,

$L_\pm = L_x \pm \mathrm{i}L_y$, and so only couple states of differing L^2. Since were are limited to a single electronic state, the matrix elements for these terms are zero. The eigenvalue of L_z is Λ, which is zero. Therefore, the $\vec{L}^2$ term is zero. The $\vec{N}\cdot\vec{L}$ term can be written as $N_z L_z + \frac{1}{2}\left(L_+ N_- + L_- N_+\right)$. Again, the $N_z L_z$ term is zero because $\Lambda = 0$, and the second term only couples states of different L^2, and so is also zero. This leaves $\vec{R}^2 = \vec{N}^2$.

The H_{ang} term of the Hamiltonian contains three angular momentum interaction parts: the electron spin-nuclear rotation interaction, $H_{\mathrm{sri}} = \gamma\vec{N}\cdot\vec{S}$, the nuclear spin-rotation interaction, $H_{\mathrm{nri}} = C\vec{N}\cdot\vec{I}$, and the nuclear-electric spin-spin (i.e., hyperfine) interaction. The latter has two parts characterised by two molecular constants, and these are written in two different ways in the literature:

$$H_{\mathrm{hf}} = b\vec{I}\cdot\vec{S} + c\frac{(\vec{I}\cdot\vec{\rho})(\vec{S}\cdot\vec{\rho})}{\vec{\rho}^2} \tag{2.19}$$

$$H_{\mathrm{hf}} = b_F\vec{I}\cdot\vec{S} - t\left(\vec{I}\cdot\vec{S} - \frac{3(\vec{I}\cdot\vec{\rho})(\vec{S}\cdot\vec{\rho})}{\vec{\rho}^2}\right) \tag{2.20}$$

where $\vec{\rho}$ is the vector pointing along the internuclear axis with magnitude ρ, the internuclear distance. The two sets of constants are related by $b = b_F - t$ and $c = 3t$. The $H_{\mathrm{fci}} = b_F\vec{I}\cdot\vec{S}$ term is called the Fermi contact interaction and the second term, which can be abbreviated $H_{\mathrm{dip}} = t\left(3I_zS_z - \vec{I}\cdot\vec{S}\right)$, is the dipolar hyperfine interaction.

The solutions for the all the matrix elements except H_{dip} can be found using the Wigner-Eckhart theorem, described in chapter 5 of [62], and the additional results given in chapter 7 of [62]. The solutions for H_{dip} require some additional spherical tensor calculus and can be found in chapter 9 of [61]. The solutions used in this work are given in the set of equations Eqn. (2.25.1). The values of the constants are given in Table 2.1 for the CaF $X^2\Sigma$ and $B^2\Sigma$ states and the YbF $X^2\Sigma$ state.

Since B_e is so much larger than the other constants, it is clear that the rotation spacing will dominate the spectrum. The spacing between the energy levels with $\vec{N}$ quantum number N and $N+1$ is $2B_e(N+1)$, which is $\sim 20(N+1)$ GHz for the CaF ground state. The second-order hyperfine structure is given by the various interaction terms which, as can be seen from Table 2.1, will be dominated by the Fermi contact

$$\left\langle \eta \middle| B_e \vec{N}^2 \middle| \eta \right\rangle = B_e N(N+1) \tag{2.21}$$

$$\langle \eta | H_{\mathrm{sri}} | \eta \rangle = \frac{\gamma}{2} \left(J(J+1) - N(N+1) - S(S+1) \right) \tag{2.22}$$

$$\begin{aligned} \left\langle J, \eta \middle| H_{\mathrm{nri}} \middle| J', \eta \right\rangle = C(-1)^{N+S+J+J'+I+F+1} \begin{Bmatrix} I & J' & F \\ J & I & 1 \end{Bmatrix} \begin{Bmatrix} N & J' & S \\ J & N & 1 \end{Bmatrix} \\ \times \left[N(N+1)(2N+1) I(I+1)(2I+1)(2J+1)(2J'+1) \right]^{1/2} \end{aligned} \tag{2.23}$$

$$\begin{aligned} \left\langle J, \eta \middle| H_{\mathrm{fci}} \middle| J', \eta \right\rangle = b_F(-1)^{N+S+J+J'+I+F+1} \begin{Bmatrix} I & J' & F \\ J & I & 1 \end{Bmatrix} \begin{Bmatrix} S & J' & N \\ J & S & 1 \end{Bmatrix} \\ \times \left[S(S+1)(2S+1) I(I+1)(2I+1)(2J+1)(2J'+1) \right]^{1/2} \end{aligned} \tag{2.24}$$

$$\begin{aligned} \left\langle N, J, \eta \middle| H_{\mathrm{dip}} \middle| N', J', \eta \right\rangle = t\sqrt{30} \begin{Bmatrix} F & I & J' \\ 1 & J & I \end{Bmatrix} \begin{Bmatrix} N' & N' & 2 \\ S & S & 1 \\ J & J' & 1 \end{Bmatrix} \begin{pmatrix} N' & 2 & N \\ 0 & 0 & 0 \end{pmatrix} \\ \times \left[S(S+1)(2S+1) I(I+1)(2I+1) \right. \\ \left. \times (2N+1)(2N'+1)(2J+1)(2J'+1) \right]^{1/2} \end{aligned} \tag{2.25}$$

EQUATION 2.25.1: The solutions for the matrix elements of $B_e \vec{R}^2 + H_{\mathrm{ang}}$ in the Hund's case (b) basis. A lack of primes in the quantum numbers indicates the matrix is diagonal in that component and η indicates the remaining quantum numbers not explicitly given.

(GHz)	CaF		YbF
	$X^2\Sigma$	$B^2\Sigma$	$X^2\Sigma$
B_e	10.3	10.2	7.23
γ	0.0397	-1.38	-0.0134
C	2.88×10^{-5}	0	2.04×10^{-5}
b_F	0.123	0.0200	0.170
t	0.0134	0.0167	0.0285

TABLE 2.1: The constants for the angular momentum interaction terms in the Hamiltonians for the CaF $X^2\Sigma$ and $B^2\Sigma$ states and the YbF $X^2\Sigma$ state.

interaction. This will give a spacing on the order of 10^{-1} GHz for the CaF ground state. This can be seen in Figure 2.2 which shows the rotational spectrum for the CaF $X^2\Sigma$ state.

Additionally, since $\vec{J} = \vec{N}+\vec{S}$ and $S = 1/2$, the J quantum number is $J = N\pm1/2$. Then, since $\vec{F} = \vec{J} + \vec{I}$ and $I = 1/2$, the $\vec{F}$ quantum number is $F = J \pm 1/2$. This gives $F \in \{N-1, N, N+1\}$; however, $F = N$ can be achieved by either $N+S-I$ or $N-S+I$. The eigenstates are $|F = N+S-I\rangle \pm |F = N-S+I\rangle$ and we distinguish them by labelled them as $F = N^{\pm}$. These eigenstates are not degenerate in energy, and the N^+ state has higher energy, as can also be seen in Figure 2.2.

2.3.2 The $A^2\Pi$ State (Hund's case (a))

In the $A^2\Pi$ state, the projection of $\vec{L}$ onto the internuclear axis, denoted by the quantum number Λ, is non-zero: $\Lambda = 1$. This means that the electronic spin-orbit coupling term, $\vec{L}\cdot\vec{S}$, is non-negligible. In this case, the components of angular momentum along the internuclear axis are well defined and the good quantum numbers are the projection of the electron orbital angular momentum onto the internuclear axis, Λ, the electron spin, S, and its projection onto the internuclear axis, Σ, the total non-nuclear angular momentum, J, and its projection onto the internuclear axis, Ω, and I, F, and M_F:

$$\left\langle S, \Sigma, J, \Omega, I, F, M_F \middle| B_e\vec{R}^2 + H_{\text{ang}} \middle| S, \Sigma', J', \Omega', I, F', M_F' \right\rangle, \tag{2.26}$$

where, again, $S = I = 1/2$. As before, the nuclear rotation, $\vec{R}$, is not a constant of the motion, so we need to rewrite it in terms of other quantum numbers. Since

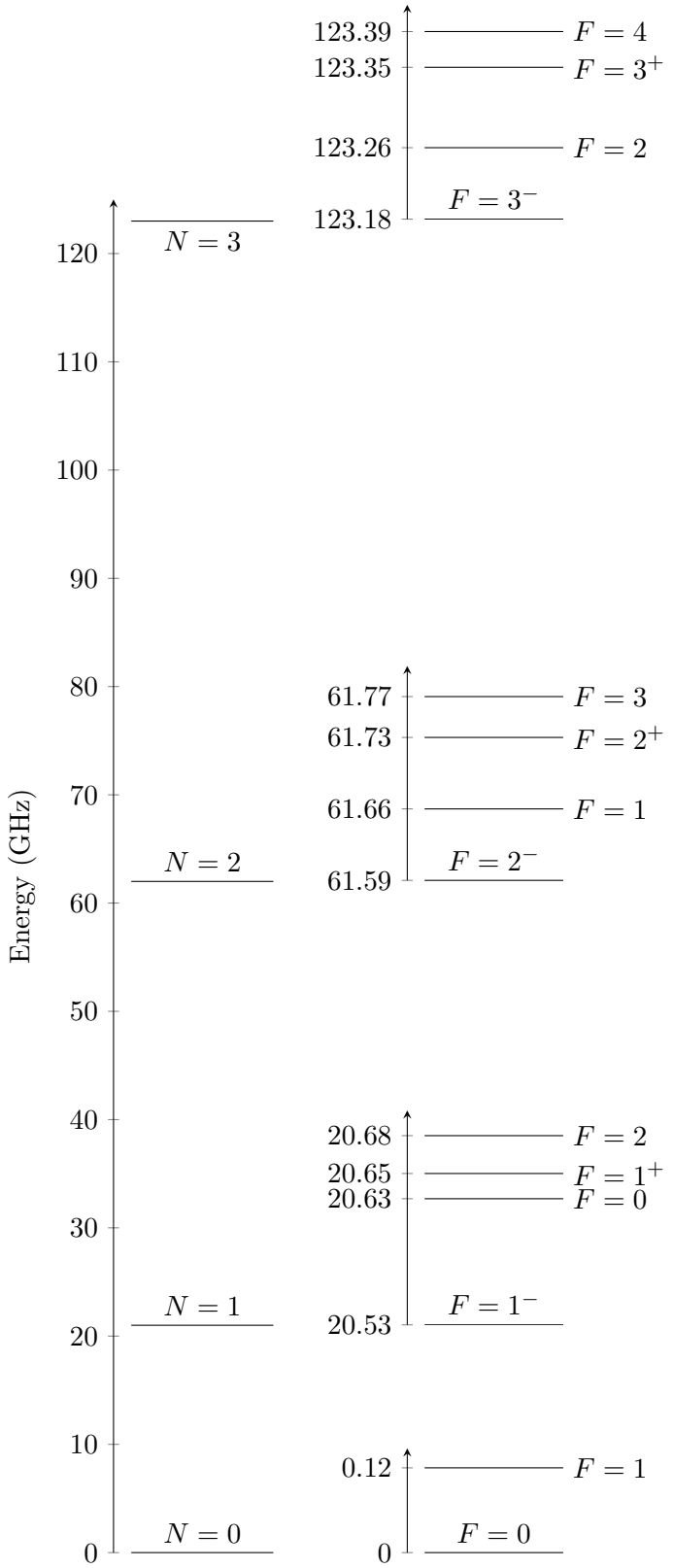

FIGURE 2.2: Rotational energy spectrum for the CaF $X^2\Sigma$ state, for $N = 0$ to $N = 3$.

$\vec{J} = \vec{L} + \vec{S} + \vec{R}$, we can re-write the nuclear rotation term as:

$$B_e \vec{R}^2 = B_e(\vec{J} - \vec{L} - \vec{S})^2. \tag{2.27}$$

This form shows that this term cannot be diagonal in the Hund's case (a) basis, as $\vec{L}$ is not a constant of the motion. However, the matrix elements can now be calculated. Since this term includes a $-2B_e\vec{L}\cdot\vec{S}$ component when expanded, it is helpful to group it together with the spin-orbit interaction term, $H_{\text{soi}} = A\vec{L}\cdot\vec{S}$, as the rotational spin-orbit term, $H_{\text{rso}} = B_e\vec{R}^2 + H_{\text{soi}}$. The matrix elements are given in chapter 9 of [61].

Additional angular momentum interaction terms are the Fermi contact interaction and dipolar hyperfine interaction, as before, and a Λ-doubling term, which gives rise to an interaction between the $A^2\Pi$ state and the $B^2\Sigma$ state:

$$H_{\text{LD}} = \sum_{k=\pm 1} \exp\left(-2ki\phi\right)\left\{-q\mathrm{T}^2_{2k}\left(\vec{J},\vec{J}\right) + (p+2q)\mathrm{T}^2_{2k}\left(\vec{J},\vec{S}\right)\right\}, \tag{2.28}$$

where $\mathrm{T}^2_{2k}\left(\vec{J},\vec{S}\right)$ gives the operator for the $2k$th component of the rank-2 spherical tensor $\vec{J}\otimes\vec{S}$, and likewise for $\mathrm{T}^2_{2k}\left(\vec{J},\vec{J}\right)$. ϕ is an angle around the internuclear z-axis and the exponential term ensures that only states of $\Lambda \pm 2$ are coupled. The final expressions for the $A^2\Pi$ state matrix elements are given in the set of equations Eqn. (2.32.1). As can be seen from this, the H_{LD} matrix elements are not diagonal in Λ, unlike the other components of the $A^2\Pi$ state Hamiltonian. The values of the constants for the CaF $A^2\Pi$ state are given in [63, 64], and for YbF in [65, 66]. The values used for calculations in this work are given in Table 2.2.

From the values of the constants in Table 2.2, it can be seen that the spin-orbit couping term is dominant. The term is diagonal in the Hund's case (a) basis and shifts the energy of each eigenstate by $A\Lambda\Sigma$ (Eqn. (2.29)). Since $\Lambda = \pm 1$ and $\Sigma = \pm 1/2$ and both are good quantum numbers, this causes a splitting of the rotation spectrum into a 'lower spin-orbit manifold', whose energy is shifted by $-\frac{1}{2}A$, and an 'upper spin-orbit manifold' whose energy is shifted by $+\frac{1}{2}A$. This means the spin-orbit splitting

$$\begin{aligned}\left\langle \Sigma,\Omega,\eta\middle|H_{\rm rso}\middle|\Sigma',\Omega',\eta\right\rangle = &\left\{B_e\left[J(J+1)+S(S+1)-2\Omega\Sigma-\Lambda^2\right]+A\Lambda\Sigma\right\}\delta_{\Sigma,\Sigma'}\delta_{\Omega,\Omega'}\\ &-2B_e\left[J(J+1)(2J+1)S(S+1)(2S+1)\right]^{\frac{1}{2}}\\ &\times\sum_{k=\pm1}(-1)^{J+S-\Omega-\Sigma}\begin{pmatrix}J & 1 & J'\\ -\Omega & k & \Omega'\end{pmatrix}\begin{pmatrix}S & 1 & S'\\ -\Sigma & k & \Sigma'\end{pmatrix}\end{aligned} \tag{2.29}$$

$$\begin{aligned}\left\langle \Sigma,J,\Omega,\eta\middle|H_{\rm fci}\middle|\Sigma',J',\Omega',\eta\right\rangle = b_F\sum_{k\in\{\pm1,0\}}&\left\{(-1)^{I+J'+F+S-\Sigma+J-\Omega}\right.\\ &\times\left[S\left(S+1\right)\left(2S+1\right)I\left(I+1\right)\left(2I+1\right)\left(2J+1\right)\left(2J'+1\right)\right]^{\frac{1}{2}}\\ &\left.\times\begin{Bmatrix}J' & I & F\\ I & J & 1\end{Bmatrix}\begin{pmatrix}J & 1 & J'\\ -\Omega & k & \Omega'\end{pmatrix}\begin{pmatrix}S & 1 & S\\ -\Sigma & k & \Sigma\end{pmatrix}\right\}\end{aligned} \tag{2.30}$$

$$\begin{aligned}\left\langle \Sigma,J,\Omega,\eta\middle|H_{\rm dip}\middle|\Sigma',J',\Omega',\eta\right\rangle = t\frac{\sqrt{30}}{2}\sum_{k\in\{\pm1,0\}}&\left\{(-1)^{I+J'+F+S+k-\Sigma+J-\Omega}\right.\\ &\times\left[S\left(S+1\right)\left(2S+1\right)I\left(I+1\right)\left(2I+1\right)\left(2J+1\right)\left(2J'+1\right)\right]^{\frac{1}{2}}\\ &\left.\times\begin{Bmatrix}J' & I & F\\ I & J & 1\end{Bmatrix}\begin{pmatrix}J & 1 & J'\\ -\Omega & k & \Omega'\end{pmatrix}\begin{pmatrix}1 & 2 & 1\\ k & 0 & -k\end{pmatrix}\begin{pmatrix}S & 1 & S\\ -\Sigma & k & \Sigma\end{pmatrix}\right\}\end{aligned} \tag{2.31}$$

$$\begin{aligned}\left\langle \Lambda,\Sigma,\Omega,\eta\middle|H_{\rm LD}\middle|\Lambda',\Sigma',\Omega',\eta\right\rangle = \sum_{k\in\{\pm1,0\}}\delta_{\Lambda',\Lambda+2k}&\left\{\right.\\ &\delta_{\Sigma,\Sigma'}\frac{q}{2\sqrt{6}}(-1)^{J-\Omega}\begin{pmatrix}J & 2 & J\\ -\Omega & -2k & \Omega'\end{pmatrix}\\ &\quad\times\left[(2J-1)(2J)(2J+1)(2J+2)(2J+3)\right]^{\frac{1}{2}}\\ &+(p+2q)(-1)^{J-\Omega+S-\Sigma}\begin{pmatrix}J & 1 & J\\ -\Omega & -k & \Omega'\end{pmatrix}\begin{pmatrix}S & 1 & S\\ -\Sigma & k & \Sigma'\end{pmatrix}\\ &\quad\times\left[J\left(J+1\right)\left(2J+1\right)S\left(S+1\right)\left(2S+1\right)\right]^{\frac{1}{2}}\left.\right\}\end{aligned} \tag{2.32}$$

EQUATION 2.32.1: The solutions for the matrix elements of $B_e\vec{R}^2 + H_{\rm ang}$ in the Hund's case (a) basis.

is equal to A. Given that $\Omega = \Lambda + \Sigma$, each manifold can be characterised completely by the magnitude of the Ω quantum number, with the lower manifold having anti-parallel Λ and Σ, giving $\Omega = \pm 1/2$, and the upper having parallel Λ and Σ, giving $\Omega = \pm 3/2$.

The next most dominant term is the Λ-doubling. This has terms off-diagonal in Λ, coupling states with $\Delta\Lambda = 2$; i.e., coupling together $\Lambda = \pm 1$. This has the effect of coupling together $\Omega = \pm 1/2$ and $\Omega = \pm 3/2$ states in each spin-orbit manifold, making each energy eigenstate a superposition of positive and negative Ω states. This gives rise to a splitting between symmetric and antisymmetric superpositions.

In the case of the $\Omega = \pm 1/2$ spin-orbit manifold in YbF, where the first term of the Λ-doubling (which is diagonal in Σ) is zero, the splitting is $\sim (p+2q)$ for $J = 1/2$ and $\sim 2(p+2q)$ for $J = 3/2$. The actual parity, P, of the state depends on the value of J. For $J = 1/2$ the parity is the same as the symmetry: symmetric eigenstates have parity $+1$ and antisymmetric have parity -1. For $J = 3/2$ the parity is reversed, so symmetric eigenstates have parity -1 and antisymmetric have parity $+1$.

The hyperfine splitting in the YbF $A^2\Pi$ state is 2-3 orders of magnitude smaller than in the YbF $X^2\Sigma$ state, as can be seen from the values of b_F and t. Again, the energy levels in zero magnetic field are degenerate in M_F. The spectrum for the YbF $A^2\Pi$ state is shown in Figure 2.3.

(GHz)	CaF	YbF
B_e	10.4	7.42
A	2.18×10^3	4.09×10^4
b_F	N/A	2.52×10^{-3}
t	N/A	-2.10×10^{-3}
$p + 2q$	N/A	-11.9
p	-1.37	N/A
q	-8.69×10^{-3}	N/A

TABLE 2.2: The constants for the angular momentum interaction terms in the Hamiltonians for the CaF and YbF $A^2\Pi$ states. The hyperfine constants, b_F and t are unknown for CaF $A^2\Pi$, but the hyperfine splitting in the negative parity $J = \frac{1}{2}$ state is known to be (4.8 ± 1.1) MHz [10]. This has also been used to estimate the splitting in the positive parity state as theoretically they should be equal [45].

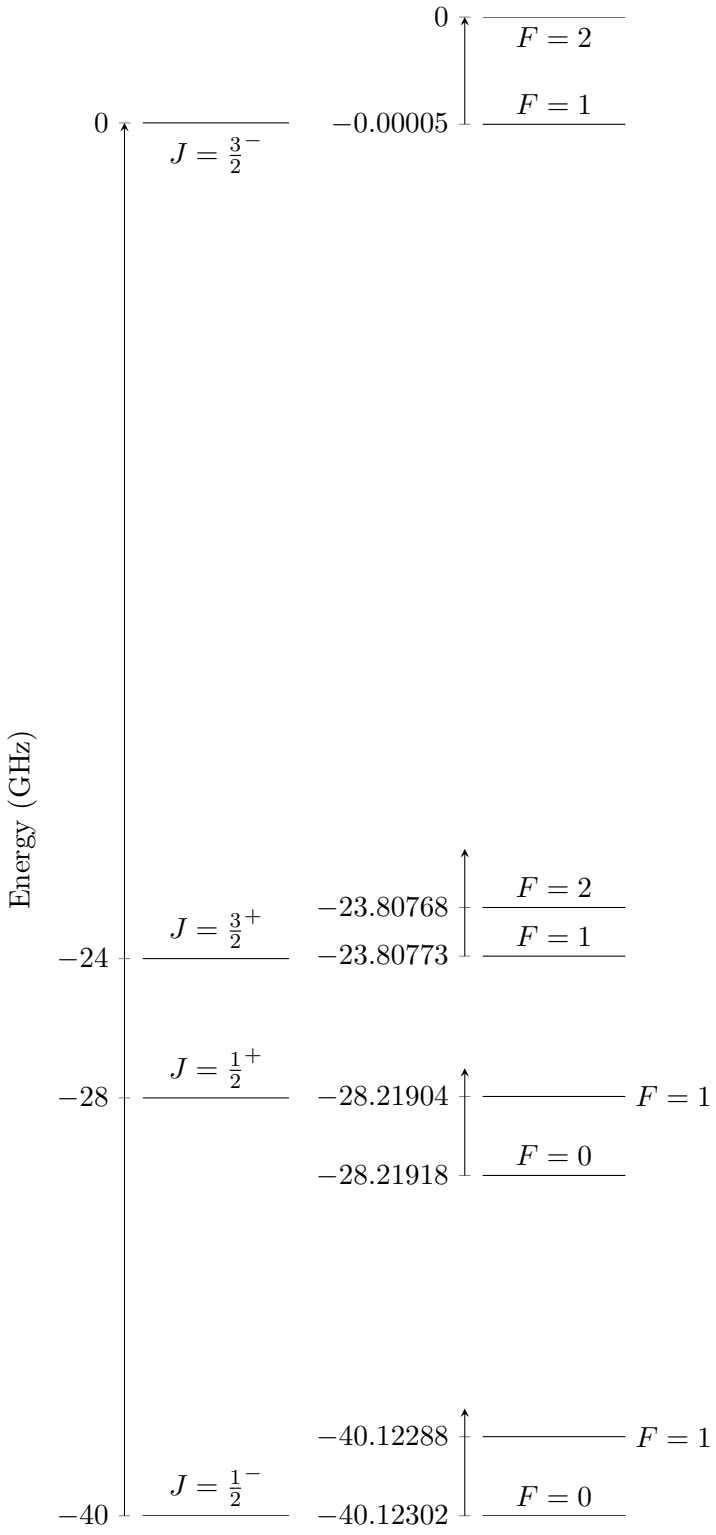

FIGURE 2.3: Rotational energy spectrum for $\Omega = \pm 1/2$ spin-orbit manifold for the YbF $A^2\Pi$ state. The superscript + and − indicate the parity, P, (not symmetry) of the state. Energies are relative to the highest energy state, $\left|\Omega = \pm\frac{1}{2}, J = \frac{3}{2}, P = -1, F = 1\right\rangle$, which has energy $-2.042\,370\,615 \times 10^4$ GHz relative to the electro-vibrational energy.

2.4 The Zeeman Effect

In the presence of a magnetic field, $\vec{B}$, the molecular Hamiltonian gains a field-dependent term:

$$H = H_{\text{mol}} \underbrace{-\vec{\mu} \cdot \vec{B}}_{H_{\text{ZE}}}, \tag{2.33}$$

where $\vec{\mu}$ is the magnetic moment of the molecule. The molecular magnetic moment has contributions from all the angular momenta of the constituents of the molecule:

$$\vec{\mu} = \mu_B \left(g_S \vec{S} + g_L \vec{L} + g_R \vec{R} + g_I \vec{I} \right), \tag{2.34}$$

where the gs are the Landé g-factors, which are at most of order 1. In fact, for both CaF and YbF, $g_S \approx 2$, $g_L \approx 1$, and $g_R \approx g_I \approx 0$ [64, 67]. Thus, while a full treatment of the effect of the Zeeman effect would involve a consideration of the nuclear angular momenta, in practice we can can ignore the nuclear contribution.

If we define the laboratory frame such that $\vec{B} = B_0 \hat{z}$, then H_{ZE} becomes:

$$H_{\text{ZE}} = \mu_B B_0 \left(g_S S_0 + g_L L_0 + g_R R_0 + g_I I_0 \right), \tag{2.35}$$

where $S_0 = \mathrm{T}^1_0 \left(\vec{S} \right)$ is the 0 component of the rank-1 spherical tensor $\vec{S}$, which is equal to the z-component in a Cartesian basis. In the full treatment of the Zeeman effect there are additional perturbation terms which are important for the $A^2\Pi$ state:

$$\begin{aligned} \frac{H'_{\text{ZE}}}{\mu_B B_Z} = {} & g'_l \sum_{k=\pm 1} \exp\left(-2ki\phi\right) \mathcal{D}^{(1)}_{0,-k}(\omega) \mathrm{T}^1_k \left(\vec{S} \right) \\ & + g'^{e}_r \sum_{k=\pm 1} \sum_{P} \exp\left(-2ki\phi\right) (-1)^P \mathcal{D}^{(1)}_{-P,-k}(\omega) \mathrm{T}^1_P \left(\vec{J} - \vec{S} \right) \mathcal{D}^{(1)}_{0,-k}(\omega), \end{aligned} \tag{2.36}$$

where P is the parity, $\mathcal{D}^{(j)}_{m',m}(\omega)$ is a matrix element of the Wigner rotation matrix $R(\omega)$ (see chapter 5 of [61]):

$$\mathcal{D}^{(j)}_{m',m}(\omega) = \left\langle j, m' \middle| R(\omega) \middle| j, m \right\rangle, \tag{2.37}$$

and $\mathrm{T}^1_k\left(\vec{S}\right)$ gives the kth component of $\vec{S}$. In the case of the $X^2\Sigma$ and $B^2\Sigma$ states, $g'_l = g_r^{e'} = 0$, but in the YbF $A^2\Pi$ state, $g'_l = -0.722$ and so the contribution of this term is non-negligible.

Therefore, our total effective Zeeman Hamiltonian is, ignoring negligible nuclear angular momentum terms, and accounting for one of the additional perturbation terms:

$$H_{\mathrm{ZE}} = \mu_B B_0 \left(g_S \vec{S}_0 + g_L \vec{L}_0 + g'_l \sum_{k=\pm 1} \exp\left(-2ki\phi\right) \mathcal{D}^{(1)}_{0,-k}(\omega) \mathrm{T}^1_k\left(\vec{S}\right) \right). \tag{2.38}$$

In the case of the Hund's case (b) basis, $\{N, S, J, I, F, M_F\}$, used for the $X^2\Sigma$ and $B^2\Sigma$ states, $g'_l = 0$, and the electronic orbital angular momentum term can be ignored since $\Lambda = 0$ and the other component rapidly precesses, averaging to zero. The matrix element is given in Eqn. (2.39). In the case of the Hund's case (a) basis, $\{S, \Sigma, J, \Omega, I, F, M_F\}$, used for the $A^2\Pi$ state, the full treatment is required, $\left\langle \Lambda, \Sigma, J, \Omega, F, \eta \middle| \frac{H_{\mathrm{ZE}}}{\mu_B B_0} \middle| \Lambda', \Sigma', J', \Omega', F', \eta \right\rangle$. The matrix element is given in Eqn. (2.40). Figure 2.4 shows the Zeeman effect in the CaF $X^2\Sigma$ and $A^2\Pi$ states.

$$\begin{aligned}\left\langle J,F,M_F,\eta\middle|H_{\mathrm{ZE}}\middle|J',F',M_F',\eta\right\rangle &= \mu_B B_0\; g_S(-1)^{N+2S+J+J'+I+F-M_F+2} \\ &\times \sqrt{S\left(S+1\right)\left(2S+1\right)}\begin{pmatrix} F' & 1 & F \\ -M_F' & 0 & M_F\end{pmatrix} \\ &\times \sqrt{\left(2F+1\right)\left(2F'+1\right)}\begin{Bmatrix} J' & F' & I \\ F & J & 1\end{Bmatrix} \\ &\times \sqrt{\left(2J+1\right)\left(2J'+1\right)}\begin{Bmatrix} S & J' & N \\ J & S & 1\end{Bmatrix}\end{aligned} \tag{2.39}$$

$$\begin{aligned}\left\langle \frac{H_{\mathrm{ZE}}}{\mu_B B_0}\right\rangle &= (-1)^{F-M_F+F'+J+I+1}\begin{pmatrix} F & 1 & F' \\ -M_F & 0 & M_F'\end{pmatrix} \\ &\times \sqrt{\left(2F+1\right)\left(2F'+1\right)}\begin{Bmatrix} J' & F' & I \\ F & J & 1\end{Bmatrix} \\ &\times \sqrt{\left(2J+1\right)\left(2J'+1\right)}(-1)^{J-\Omega}\sum_{k=-1}^{1}\Bigg[\\ &\quad \delta_{\Lambda,\Lambda'}\begin{pmatrix} J & 1 & J' \\ -\Omega & k & \Omega'\end{pmatrix} g_L\Lambda\delta_{\Sigma,\Sigma'} \\ &+ \delta_{\Lambda,\Lambda'}\begin{pmatrix} J & 1 & J' \\ -\Omega & k & \Omega'\end{pmatrix} g_S(-1)^{S-\Sigma}\sqrt{S\left(S+1\right)\left(2S+1\right)}\begin{pmatrix} S & 1 & S' \\ -\Sigma & k & \Sigma'\end{pmatrix} \\ &+ |k|\delta_{\Lambda,\Lambda'-2k}\begin{pmatrix} J & 1 & J' \\ -\Omega & -k & \Omega'\end{pmatrix} g_l'(-1)^{S-\Sigma}\sqrt{S\left(S+1\right)\left(2S+1\right)}\begin{pmatrix} S & 1 & S' \\ -\Sigma & k & \Sigma'\end{pmatrix}\Bigg]\end{aligned} \tag{2.40}$$

Equation 2.40.1: Eqn. (2.39) shows the solution for the matrix elements of the Zeeman Hamiltonian in the Hund's case (b) basis. Eqn. (2.40) shows the same for the Hund's case (a) basis.

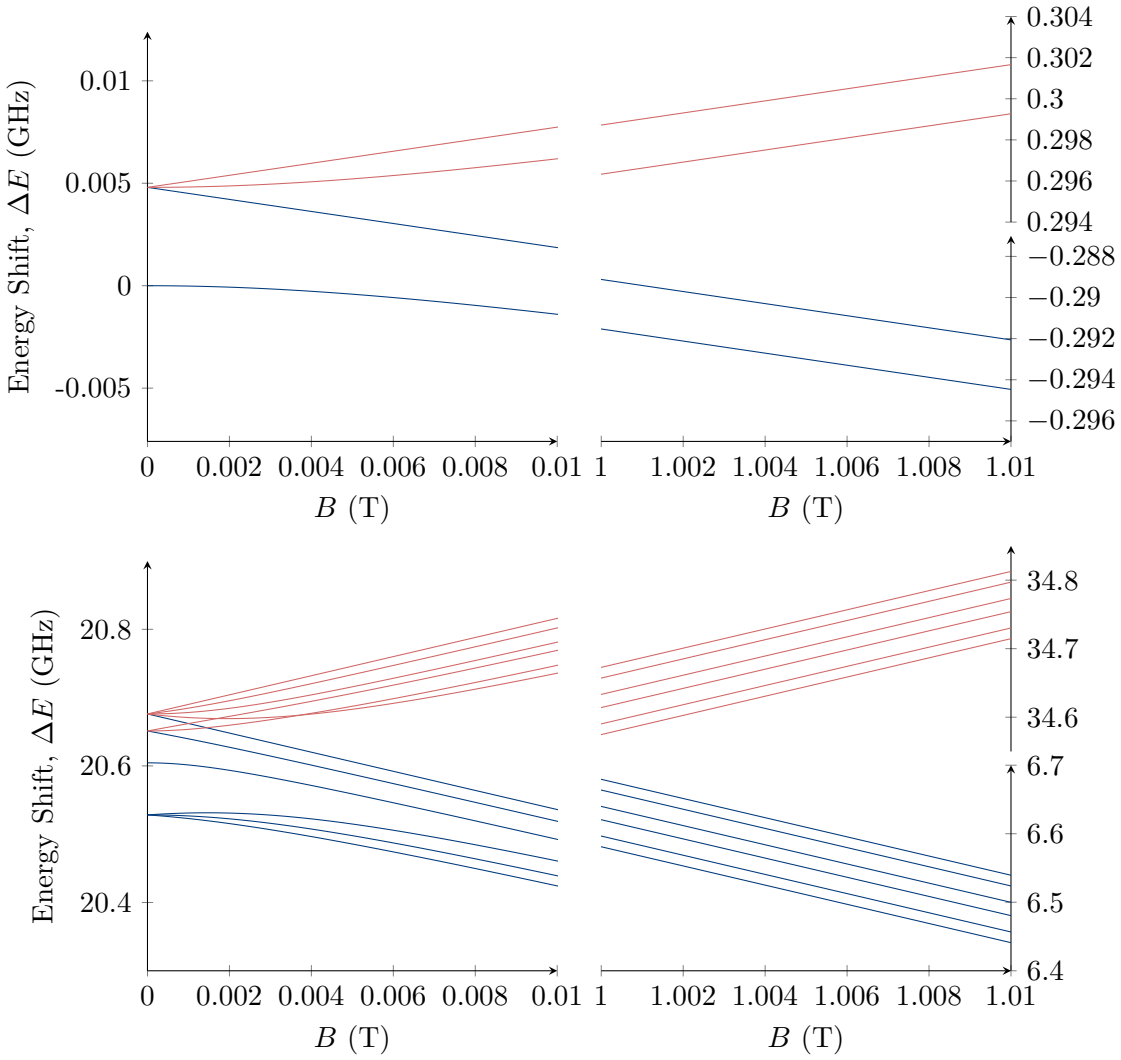

FIGURE 2.4: The sublevels of the CaF $X^2\Sigma(N = 1)$ (below) and $A^2\Pi_{1/2}(J = \frac{1}{2}^+)$ (above) states and their Zeeman splittings. As can be seen, the $X^2\Sigma$ state has six SFS sub-states with a Zeeman splitting of $-14\,\mathrm{GHz\,T^{-1}}$, shown in blue, and six WFS sub-states with a splitting of $14\,\mathrm{GHz\,T^{-1}}$, shown in red. The $A^2\Pi$ state has two SFS and two WFS states, with Zeeman splittings of $\pm 0.29\,\mathrm{GHz\,T^{-1}}$.

2.5 Molecule-Light Interactions

We will be investigating slowing schemes involving laser excitation of the molecule. These will involve either direct momentum transfer from laser photons or optical pumping between selected states of the molecule. Thus, it is important to understand the interaction of the molecule with laser light and calculate the strengths of various transitions.

Suppose the molecule is in the presence of a laser field, $\vec{\mathcal{E}} = \vec{\mathcal{E}}_0 \cos\left(\omega_{\text{las}} t - \vec{k}\cdot\vec{r}\right)$, of frequency ω_{las}, and local intensity $I = \frac{1}{2}\varepsilon_0 c \mathcal{E}_0^2$. The scattering rate between states $|n, v, \eta\rangle$ and $|n', v', \eta'\rangle$ in the rotating wave approximation is given by [68]:

$$R = \frac{\Gamma}{2} \frac{s}{1 + s + 4\left(\frac{\omega_{\text{las}} - (1+\beta)\omega_0}{\Gamma}\right)^2} \left(\sum_{p\in\{\pm 1,0\}} \psi_p \left\langle n, v, \eta \middle| \mathrm{T}_p^1\left(\vec{d}\right) \middle| n', v', \eta' \right\rangle \right)^2, \quad (2.41)$$

where $1/\Gamma$ is the excited state lifetime, ω_0 is the frequency assoicated with the energy difference between the two states, $\beta = v/c$ is the velocity of the molecule divided by the speed of light, and s is the saturation parameter [69]:

$$s = \frac{I}{I_s} = I\left(\frac{\pi h c \Gamma}{3\lambda^3}\right)^{-1}, \quad (2.42)$$

where $\lambda = 2\pi c/\omega_{\text{las}}$ is the laser wavelength. The final sum-squared term of Eqn. (2.41) gives the matrix element of the transition dipole moment, $\mathrm{T}_p^1\left(\vec{d}\right)$. n is the electronic state, v is the vibrational state, and η is the rotational state, and the primes indicate the ground state.

We first deal with the vibrational transitions. From one molecular electronic energy level to the next, the shape of the effective potential, $E_n^{\text{el}}(\tilde{\rho})$, will vary. This results in the vibrational energy levels of the molecule changing for different electronic configurations, meaning that:

$$\left\langle n, v \middle| n', v' \right\rangle \neq \delta_{vv'}\delta_{nn'}. \quad (2.43)$$

$\langle n, v|n', v'\rangle$ is known as the Franck-Condon factor, and for fixed n and n' it forms a matrix, known as the Franck-Condon matrix. For optical cycling, we want to find a transition between two states that is as close to being closed as possible, so that following spontaneous decay the molecule returns to its original state. Therefore, we would like $\langle n, v|n', v\rangle \approx 1$ and $\langle n, v|n', v'\rangle \to 0$ as $|v - v'| \to \infty$. When this is satisfied, only a few vibrational branches need to be addressed for optical cycling to work.

We turn now to the electric dipole transitions. The component, $p \in \{-, 0, +\}$, of the dipole moment corresponds to the polarisation of the light in the spherical tensor basis, such that $\mathrm{T}^1_{\pm}\left(\vec{d}\right)$ gives $\sigma^{\pm}$ polarisation and $\mathrm{T}^1_0\left(\vec{d}\right)$ gives π polarisation. The expansion coefficients, ψ_p, give the complex components of the laser polarisation in this basis such that $\vec{\psi} = \sum_p \psi_p \mathrm{T}^1_p\left(\vec{d}\right)$ is the spherical vector[2] of polarisation.

We choose a frame where the magnetic field is locally parallel to the z-axis, $\vec{B} = B_0\hat{z}$. The laser polarisation in real space is given by $\dfrac{\vec{\mathcal{E}}_0}{|\vec{\mathcal{E}}_0|} \equiv \hat{\mathcal{E}}_0$. The conversion to the spherical tensor basis with π polarisation parallel to the z-axis, $\hat{\pi} = \hat{z}$, follows from the Pauli algebra:

$$\begin{pmatrix} \psi_- \\ \psi_0 \\ \psi_+ \end{pmatrix} = \begin{pmatrix} \sqrt{2} & \mathrm{i}\sqrt{2} & 0 \\ 0 & 0 & 1 \\ \sqrt{2} & -\mathrm{i}\sqrt{2} & 0 \end{pmatrix} \hat{\mathcal{E}}_0. \tag{2.44}$$

Using this we can solve for the matrix elements in Eqn. (2.41) for any arbitrary polarisation. The value of the matrix element is given in chapter 6 of [61] for the case when both the ground and excited eigenstates are Hund's case (a) states, $\eta^{(a)} = \{S, \Sigma, J, \Omega, I, F, M_F\}$ and $\eta^{(a)\prime}$ indicates all angular momentum quantum numbers are primed:

[2] i.e., the rank-1 spherical tensor.

$$\left\langle n,\eta^{(a)}\middle|\mathrm{T}^1_p\left(\vec{d}\right)\middle|n',\eta^{(a)\prime}\right\rangle = \delta_{\Omega,-\Omega'}(-1)^{F-M_F+F'+2J+I-\Omega+1}\begin{Bmatrix} J' & F' & I \\ J & F & 1\end{Bmatrix} \times\sqrt{(2J+1)\,(2J'+1)\,(2F+1)\,(2F'+1)} \times\begin{pmatrix} F & 1 & F' \\ -M_F & p & M'_F\end{pmatrix}\begin{pmatrix} J & 1 & J' \\ -\Omega & \Omega-\Omega' & \Omega'\end{pmatrix}, \tag{2.45}$$

However, the ground state in CaF and YbF is a Hund's case (b) state with quantum numbers $\eta^{(b)} = \{N, S, J, I, F, M_F\}$. The difference is that the case (a) basis replaces N with either Σ or Ω (only one is needed since $\Omega = \Lambda + \Sigma$). Therefore, we can expand $\left|\eta^{(b)}\right\rangle$ in terms of $\left|\eta^{(a)}\right\rangle$ states by summing over Σ [70]:

$$\left|N,\eta^{(b)}\right\rangle = \sum_{\Sigma=-S}^{S}(-1)^{N-\Sigma+\Omega}\sqrt{2N+1}\begin{pmatrix} J & S & N \\ \Omega & -\Sigma & -\Lambda\end{pmatrix}\left|\Sigma,\eta^{(a)}\right\rangle. \tag{2.46}$$

The final matrix elements for the A–X and B–X transitions are given in the set of equations Eqn. (2.48.1). These results are used to calculate the transition intensities and branching ratios shown in Chapter 3 and Chapter 7.

$$\left\langle A^2\Pi,\eta^{(a)}\middle|\mathrm{T}^1_p\left(\vec{d}\right)\middle|X^2\Sigma,\eta^{(b)\prime}\right\rangle = \sum_{\Sigma'=-S'}^{S'}(-1)^{N'-S'+\Omega'}\sqrt{2N'+1}\begin{pmatrix}J' & S' & N'\\ \Omega' & -\Sigma' & -\Lambda'\end{pmatrix} \times \delta_{\Omega,-\Omega'}(-1)^{F-M_F+F'+2J+I-\Omega+1}\begin{Bmatrix}J' & F' & I\\ J & F & 1\end{Bmatrix} \times \sqrt{(2J+1)(2J'+1)(2F+1)(2F'+1)} \times \begin{pmatrix}F & 1 & F'\\ -M_F & p & M'_F\end{pmatrix}\begin{pmatrix}J & 1 & J'\\ -\Omega & \Omega-\Omega' & \Omega'\end{pmatrix} \tag{2.47}$$

$$\left\langle B^2\Sigma,\eta^{(b)}\middle|\mathrm{T}^1_p\left(\vec{d}\right)\middle|X^2\Sigma,\eta^{(b)\prime}\right\rangle = \sum_{\Sigma=-S}^{S}\sum_{\Sigma'=-S'}^{S'}(-1)^{N-S+\Omega}\sqrt{2N+1}\begin{pmatrix}J & S & N\\ \Omega & -\Sigma & -\Lambda\end{pmatrix} \times (-1)^{N'-S'+\Omega'}\sqrt{2N'+1}\begin{pmatrix}J' & S' & N'\\ \Omega' & -\Sigma' & -\Lambda'\end{pmatrix} \times \delta_{\Omega,-\Omega'}(-1)^{F-M_F+F'+2J+I-\Omega+1}\begin{Bmatrix}J' & F' & I\\ J & F & 1\end{Bmatrix} \times \sqrt{(2J+1)(2J'+1)(2F+1)(2F'+1)} \times \begin{pmatrix}F & 1 & F'\\ -M_F & p & M'_F\end{pmatrix}\begin{pmatrix}J & 1 & J'\\ -\Omega & \Omega-\Omega' & \Omega'\end{pmatrix} \tag{2.48}$$

Equation 2.48.1: Matrix elements for the electric dipole transitions between the $X^2\Sigma$ and $A^2\Pi$ states (top) and the $X^2\Sigma$ and $B^2\Sigma$ states (bottom).

Chapter 3

Simulating Zeeman-Sisyphus Deceleration of CaF

3.1 Introduction

Zeeman-Sisyphus deceleration (ZS, ZSD) was first proposed for CaF in 2016 [1] and was recently demonstrated using a CaOH molecular beam [5]. It requires the molecule to have a cooling cycle with a large Zeeman splitting in the ground state, and little to no Zeeman splitting in the excited state, as in Figure 1.5. In a one-dimensional model of the decelerator, the slowing region has a static, periodic magnetic field:

$$\vec{B} = B_0 \sin\left(\frac{2\pi z}{L}\right)\hat{y}. \tag{3.1}$$

If the magnetic field change is adiabatic[1], and the field is large enough that all Zeeman shifts are linear, the corresponding energy splitting of the ground state is $E \propto |\sin(2\pi z/L)|$. The energy of the weak-field-seeking state ($|\text{WFS}\rangle$) will be in phase with $\vec{B}$ and energy of the strong-field-seeking state ($|\text{SFS}\rangle$) will be 180° out of phase. This is shown in Figure 3.1.

A molecule which begins in $|\text{WFS}\rangle$ loses kinetic energy to the field as it moves from $z = 0$ to $z = L/4$. Before it can regain the kinetic energy in the region $L/4 < z < L/2$, it must be optically pumped from $|\text{WFS}\rangle$ to $|\text{SFS}\rangle$, via the excited state, $|1\rangle$. This must happen in the region $0 < z < L/4$. The molecule is optically pumped by a laser

[1] i.e., the frequency of the field change seen by the molecules, $2\pi v_z/L$ where v_z is their forward velocity, is far below the frequency between $|\text{WFS}\rangle$ and $|\text{SFS}\rangle$.

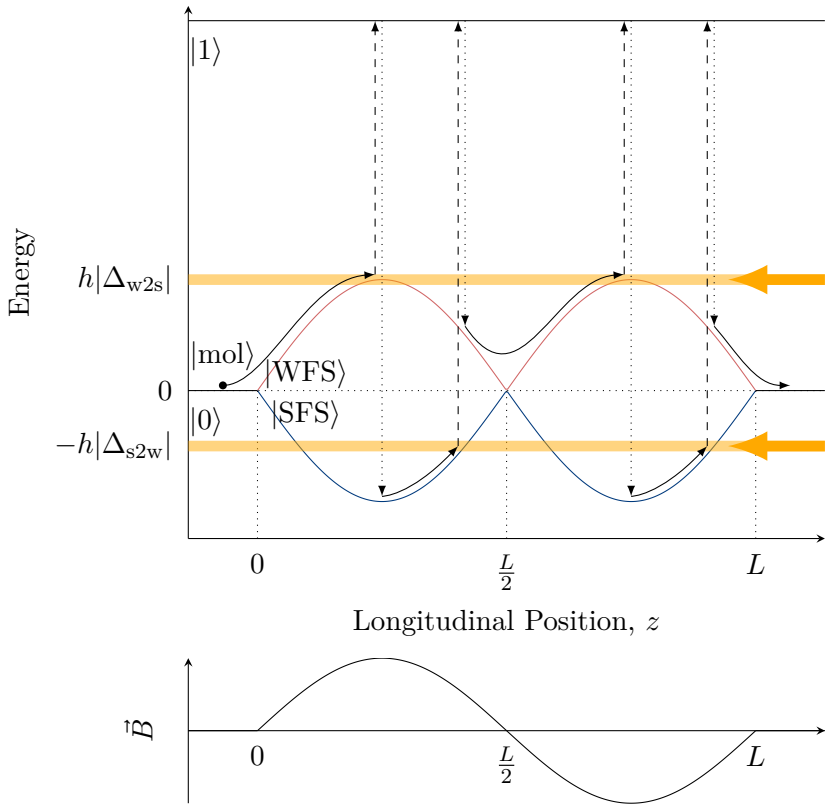

FIGURE 3.1: Schematic of the energy levels of a two-level system with a normally degenerate pair of ground state Zeeman sub-states. The $|0\rangle$ state splits into a weak-field-seeking state $|\text{WFS}\rangle$ (red) and a strong-field-seeking state $|\text{SFS}\rangle$ (blue). Optical pumping is achieved on the transitions $|1\rangle$–$|\text{wfs}\rangle$ and $|1\rangle$–$|\text{sfs}\rangle$ by two lasers (orange) detuned from the $|1\rangle$–$|0\rangle$ transition by $\Delta_{\text{w2s}} < 0$ and $\Delta_{\text{s2w}} > 0$ respectively.

with detuning $-\mu B_0 \leq h\Delta_{\text{w2s}} < 0$ from the $B = 0$ energy of the ground state. The optical pumping will cause the molecule to permanently lose energy $h|\Delta_{\text{w2s}}|$[2].

The molecule will then be in an SFS state with energy $-h|\Delta_{\text{w2s}}|$ and will continue to move towards the field maximum at $z = L/4$. As the molecule will be in an SFS state in a region of increasing magnetic field, it will gain energy. Since it begins with energy $-h|\Delta_{\text{w2s}}|$ and the SFS energy at the field maximum is $-\mu B_0$, the total energy gained in the period from the pumping area to $L/4$ is $\mu B_0 - h|\Delta_{\text{w2s}}|$. Therefore the net energy loss from $z = 0$ to $z = L/4$ is $(-2h\Delta_{\text{w2s}} - \mu B_0)$ or $(2h|\Delta_{\text{w2s}}| - \mu B_0)$. Note that the energy loss is maximised if $h\Delta_{\text{w2s}} = -\mu B_0$, as shown in Figure 3.1.

As the molecule is now in $|\text{SFS}\rangle$, it will now lose energy to the field even though the field is now decreasing. To prevent the molecule gaining energy, it must be pumped

[2]Note that the detuning, Δ_{w2s}, is *negative*, but (relative to the $B = 0$ energy) the corresponding WFS state has *positive* energy, $h|\Delta_{\text{w2s}}|$. The same is true in reverse for the Δ_{s2w} detuning and corresponding SFS state.

to $|\mathrm{WFS}\rangle$ by a laser with detuning $0 < h\Delta_{\mathrm{s2w}} \leq \mu B_0$. The energy lost will be $\mu B_0 - h\Delta_{\mathrm{s2w}}$. The molecule will also gain energy $h\Delta_{\mathrm{s2w}}$ between the pumping point and $z = L/2$. Therefore, the net energy loss between $L/4$ and $L/2$ is $\mu B_0 - 2h\Delta_{\mathrm{s2w}}$. This time, the energy loss is maximised for $\Delta_{\mathrm{s2w}} = 0$. However, $|\mathrm{SFS}\rangle$ and $|\mathrm{WFS}\rangle$ are degenerate at zero field, so the molecule must be pumped at some $B > 0$ ($z < L/2$) to prevent the states mixing. This means that Δ_{s2w} must be strictly greater than zero, by at least enough to ensure the molecule is not excited at $B = 0$ (taking into account the scattering rate of the transition and the laser power and linewidth).

The total energy loss over a half-cycle; i.e., between $z = 0$ and $z = L/2$, is $\Delta\epsilon = -2h(\Delta_{\mathrm{w2s}} + \Delta_{\mathrm{s2w}})$, or $2h(|\Delta_{\mathrm{w2s}}| - |\Delta_{\mathrm{s2w}}|)$. The average force exerted on a molecule over this half-cycle is [1]:

$$\left\langle \vec{F} \right\rangle = -\frac{2\Delta\epsilon}{L}\hat{z}. \tag{3.2}$$

Two photons are scattered per half-cycle and the molecule starts with energy $\frac{1}{2}mv_z^2$. Therefore, if we assume that each photon scatter leads to a perfect spin flip from WFS to SFS or vice versa, the number of photons scattered in order to bring a molecule to rest is:

$$N_{\mathrm{ph}}^{\mathrm{ZS}} = \frac{mv_z^2}{\Delta\epsilon}. \tag{3.3}$$

For direct laser slowing, we can find the lower bound on the number of photons that need to be scattered by ignoring the Doppler effect and assuming a constant laser wavevector $\vec{k}$. The molecule begins with z-momentum mv_z and $\hbar\vec{k}\cdot\hat{z}$ is lost per photon. Defining $|\vec{k}| = \vec{k}\cdot\hat{z}$, this gives:

$$N_{\mathrm{ph}}^{\mathrm{Las}} = \frac{mv_z}{\hbar|\vec{k}|}. \tag{3.4}$$

In reality, the wavelength will need to increase as the molecule slows down in order to maintain resonance. This will decrease $|\vec{k}|$ and so increase the number of photons

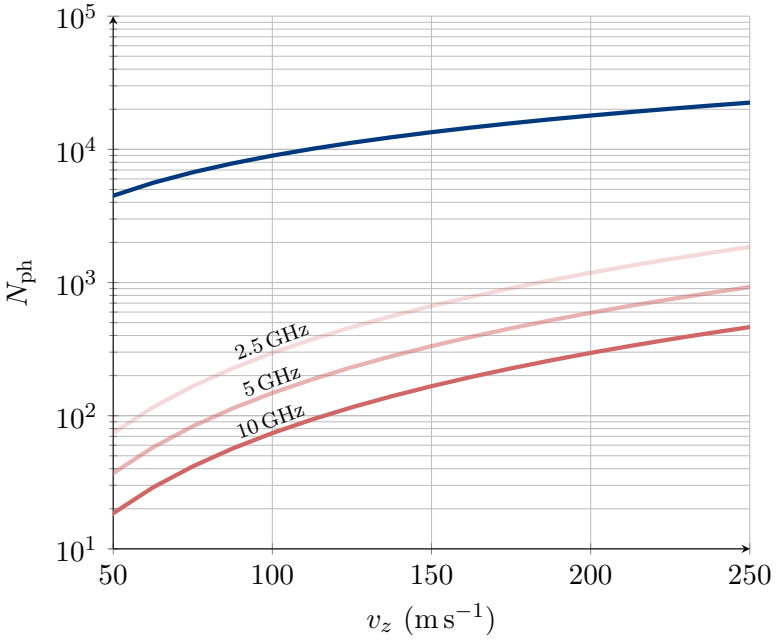

FIGURE 3.2: Number of photons required to be scattered to slow a CaF molecule to a standstill from an initial z-velocity v_z for a ZSD with $\Delta_{\mathrm{w2s}} - \Delta_{\mathrm{s2w}}$ of 2.5 GHz, 5 GHz, and 10 GHz (red) and direct laser cooling on the A–X CaF transition at 606 nm (blue). At $v_{\mathrm{out}} = 150\,\mathrm{m\,s^{-1}}$ to $200\,\mathrm{m\,s^{-1}}$, the ZSD requires two orders of magnitude fewer photons to be scattered. Molecules would have to be travelling in excess of $8.5 \times 10^3\,\mathrm{m\,s^{-1}}$ for direct laser cooling to scatter fewer photons.

that need to be scattered. Hence, $N_{\mathrm{ph}}^{\mathrm{Las}}$ is a lower bound.

Figure 3.2 shows the number of photons which need to be scattered to bring a molecule to rest from v_z for direct laser slowing (blue)[3] and for ZSD at various $\Delta\epsilon$ (red). It can be seen that ZSD requires two orders of magnitude fewer photons to be scattered than the lower bound on direct laser slowing. Molecules would have to be travelling in excess of $8.5 \times 10^3\,\mathrm{m\,s^{-1}}$ for direct laser slowing to scatter fewer photons.

To ensure the cooling cycle is closed, the excited state must be chosen so that the molecule has a high chance of decaying to both $|\mathrm{WFS}\rangle$ and $|\mathrm{SFS}\rangle$. Then, if the molecule begins in $|\mathrm{WFS}\rangle$, it will be optically pumped to $|\mathrm{SFS}\rangle$ (and vice versa), as this will be the only state not in resonance with the laser[4]. The probability of achieving $|\mathrm{WFS}\rangle \rightarrow |\mathrm{SFS}\rangle$ (or vice versa) is the 'spin flip probability' (SFP), and must be close to 1.

Finally, there is a choice to be made regarding the $\vec{k}$-vector of the pumping lasers.

[3] Making the assumption that the Doppler effect can be ignored, so this is a lower bound on the number of photons.

[4] Provided the excited state lifetime is less than the time taken for the molecule to pass through the region where it is in resonance with the pump laser.

One option is to have $\hat{k} \propto -\hat{z}$, so that the laser field is present throughout the slowing region, as in [1]. This 'longitudinal' configuration has the advantage that only two laser beams are required for any number of deceleration stages. However, care must be taken to ensure there are no alternative transitions that may be excited by the lasers at some other magnetic field strength.

Alternatively, two pump lasers per deceleration stage may be placed with $\hat{k} \perp \hat{z}$, as in [5]. This 'transverse' configuration requires more laser beams to be used, but allows molecules with more complex transitions to be ZS decelerated, since laser fields are only present at specific magnetic field strengths. In the case of CaF, the longitudinal method is used. However, some advantages of the transverse method become apparent when YbF is considered, as shown in Chapter 7.

The A–X transition in CaF is a good candidate for ZSD. As shown in Figure 2.4, the $X^2\Sigma$ state has a Zeeman splitting of $\pm 14\,\mathrm{GHz\,T^{-1}}$ and the $A^2\Pi$ state has a much smaller splitting of $\pm 0.29\,\mathrm{GHz\,T^{-1}}$. This splitting will cause the point at which the molecules are pumped to become spread out over a physical region, as the laser comes into resonance with each transition at a different magnetic field strength. If the splitting is small relative to the change in magnetic field strength, this region will be small and the effect can be ignored. In the remainder of this chapter we examine the CaF A–X transition and sub-states in more detail, before providing a description of our implementation of ZSD in the lab. We then examine simulations of ZSD to check the spin flip probability, phase space acceptence, and slowing force.

3.2 The ZS Cooling Cycle in CaF

We consider a ZS scheme as shown in Figure 3.1, where the magnetic field varies periodically between $\sim 0\,\mathrm{T}$ and $\sim 1\,\mathrm{T}$. Figure 3.3 shows the energies of the $A^2\Pi_{1/2}(J = 3/2^+)$, $A^2\Pi_{1/2}(J = 1/2^+)$, $X^2\Sigma(N = 1, \mathrm{WFS})$ (shown in red), and $X^2\Sigma(N = 1, \mathrm{SFS})$ (shown in blue) states. The transitions between $X^2\Sigma(N = 1)$ and $A^2\Pi_{1/2}(J = 1/2^+)$ are known as the the P-branch transitions. The transitions between $X^2\Sigma(N = 1)$ and $A^2\Pi_{1/2}(J = 3/2^+)$ are known as the Q-branch transitions.

The ZSD scheme is shown as a cycle on this plot with black arrows. The molecule begins in a WFS $X^2\Sigma$ state at low magnetic field strength. As it moves to higher

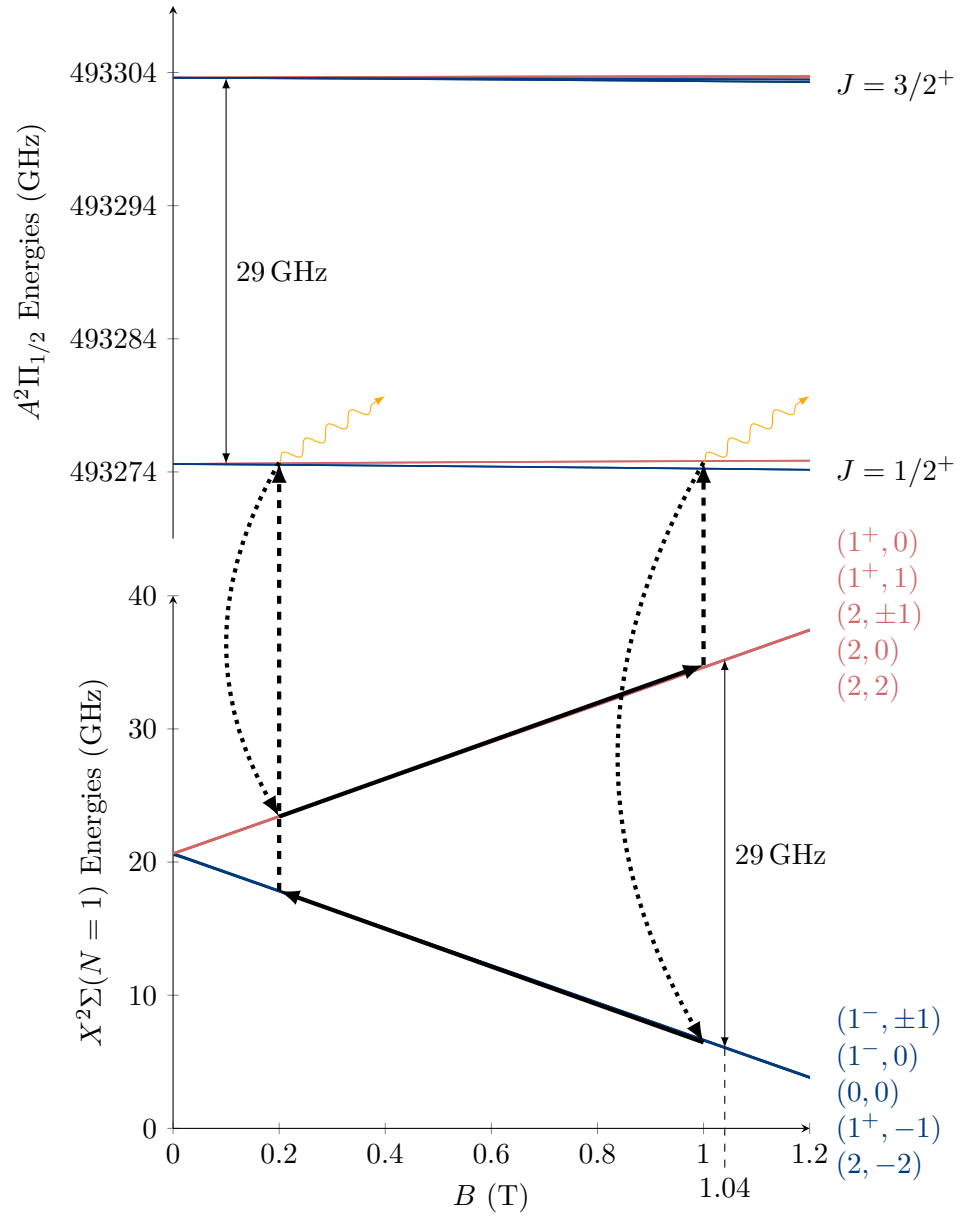

FIGURE 3.3: The energy level diagram for the CaF A–X transition against magnetic field strength. From top to bottom the diagram shows energy levels $A^2\Pi_{1/2}(J = 3/2^+)$, $A^2\Pi_{1/2}(J = 1/2^+)$, $X^2\Sigma(N = 1, \text{WFS})$, and $X^2\Sigma(N = 1, \text{SFS})$. The $X^2\Sigma(N = 1)$ states are also labelled with their (F^P, M_F) quantum numbers. WFS states are coloured in red and SFS states are coloured in blue.
Overlaid is an example ZSD optical pumping scheme with a 'weak-to-strong' laser pumping the $A^2\Pi_{1/2}(J = 1/2^+) - X^2\Sigma(N = 1, \text{WFS})$ transition at $B = 1\,\text{T}$ and a 'strong-to-weak' laser pumping the $A^2\Pi_{1/2}(J = 1/2^+) - X^2\Sigma(N = 1, \text{SFS})$ transition at $B = 0.2\,\text{T}$. The arrows show the path of the molecule.
At 1.04 T the WFS−SFS gap and the $A^2\Pi_{1/2}(J = 1/2^+) - A^2\Pi_{1/2}(J = 3/2^+)$ gap are equal. This resonance means that the frequency of the $A^2\Pi_{1/2}(J = 1/2^+) - X^2\Sigma(N = 1, \text{SFS})$ P-branch transition is equal to the frequency of the $A^2\Pi_{1/2}(J = 3/2^+) - X^2\Sigma(N = 1, \text{WFS})$ Q-branch transition. A 'strong-to-weak' laser in resonance with the P-branch transition at this magnetic field strength would also excite molecules in a WFS state to the $A^2\Pi_{1/2}(J = 3/2^+)$ states on the Q-branch transition.

magnetic field strength it gains energy in its internal state and loses kinetic energy. At $\sim 1\,\mathrm{T}$, the molecule comes into resonance with a laser and is optically pumped to a SFS $X^2\Sigma$ state via a P-branch transition. At the same time, the field gradient switches. The molecule now moves to lower magnetic field strength and so continues to lose kinetic energy. Finally, at a low magnetic field, shown as $\sim 0.2\,\mathrm{T}$ here, the molecule comes into resonance with another laser and is pumped back to a WFS $X^2\Sigma$ state, again via a P-branch transition.

An alternative view of the ZSD scheme can be seen in Figure 3.4. Instead of showing the energy levels, this figure shows the $A^2\Pi_{1/2}$–$X^2\Sigma(N=1)$ transition energies. Each labelled line corresponds to a manifold of different transitions from the various ground (F, M_F) states to the various excited (F, M_F) states. The 'strong-to-weak' (s2w) and 'weak-to-strong' (w2s) lasers are shown in the longitudinal configuration, with non-negligible intensity at all magnetic field strengths.

It can be seen that there is a crossing between transitions at $1.04\,\mathrm{T}$. This is equivalent to the resonance between the WFS$-$SFS gap and the $A^2\Pi_{1/2}(J=1/2^+)-A^2\Pi_{1/2}(J=3/2^+)$ gap shown in Figure 3.3. As long as the magnetic field strength remains below this level ($1.04\,\mathrm{T}$), each laser will be resonant with only one set of transitions. Therefore, no unwanted transitions come into resonance with either laser beam. Additionally, as the CaF $A^2\Pi$ state's Zeeman splitting is small, the spread of the points at which the lasers come into resonance with each transition will be narrow. This can be contrasted with the case for YbF in Chapter 7. Both of these factors make use of the longitudinal scheme viable.

Figure 3.5 shows the transition intensities and branching ratios of the various P-branch transitions; i.e., between the hyperfine sub-states of $A^2\Pi_{1/2}(J=1/2^+)$ and $X^2\Sigma(N=1)$. These are calculated for the high magnetic field limit, which is valid above $0.2\,\mathrm{T}$. Hence, it is valid for the s2w laser beam as well as the w2s laser beam. The transition intensities shown are for π polarised light. As indicated in Eqn. (2.41), the transition intensities relate to the rate that molecules are excited to the A state for a given laser polarisation. The branching ratios give the decay probability from a given $A^2\Pi$ state to one of the $X^2\Sigma$ states, and are normalised to unity per excited state. In order to ensure that the cooling cycle is closed, there must be a non-zero transition intensity between every $X^2\Sigma$ sub-state and at least one $A^2\Pi$ excited state.

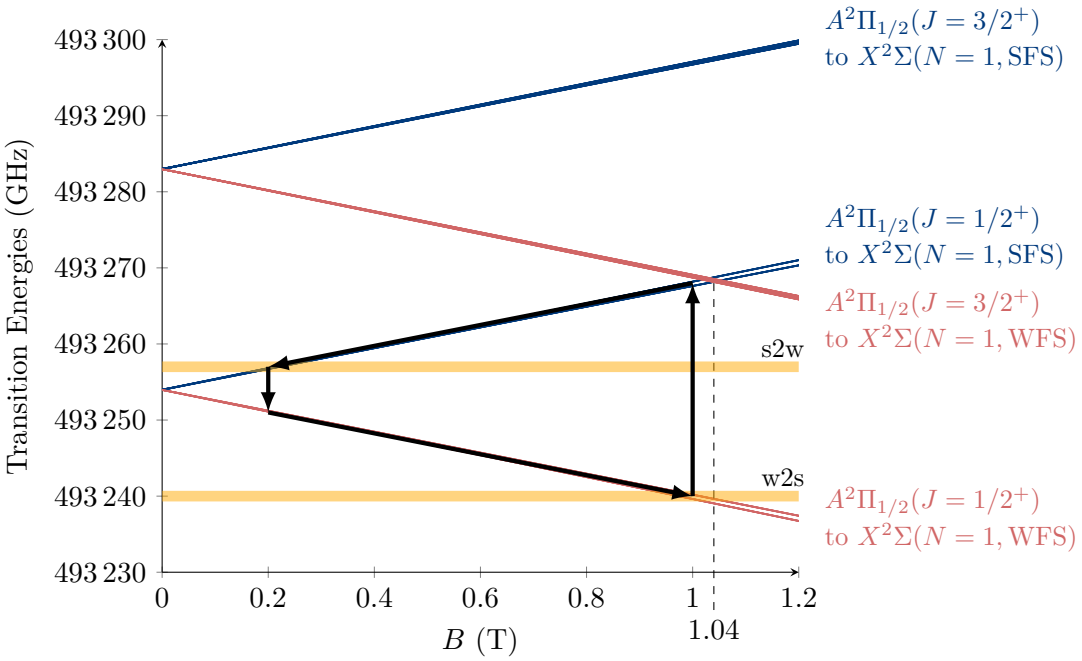

FIGURE 3.4: Transition energies for CaF $A^2\Pi_{1/2}$–$X^2\Sigma(N = 1)$. Overlaid is the same ZSD scheme as shown in Figure 3.3. The 'strong-to-weak' (s2w) and 'weak-to-strong' (w2s) lasers are shown in the longitudinal configuration, with non-negligible intensity at all magnetic field strengths. States are coloured according to whether the ground state is WFS (red) or SFS (blue).

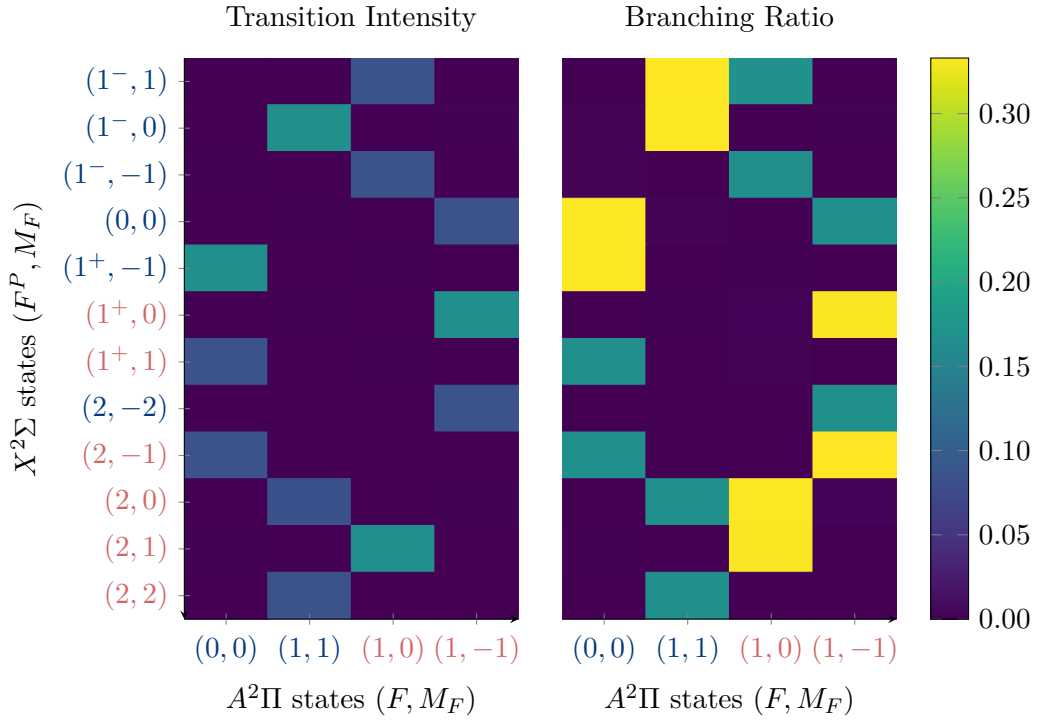

FIGURE 3.5: The transition intensities and branching ratios for the hyperfine sub-states of the $A^2\Pi_{1/2}(J = 1/2^+)$–$X^2\Sigma(N = 1)$ transition. These are calculated in the high magnetic field limit, applicable over 0.2 T. The transition intensities shown are for π polarised light. WFS states are labelled in red and SFS states are labelled in blue.

There must also be non-zero decay probability (branching ratio) from every exited state to at least one WFS ground state and one SFS ground state. It can be seen from Figure 3.5 that these conditions are fulfilled.

3.3 Implementation

A Zeeman-Sisyphus decelerator was designed by the group and built by Chenfeng Pu, a summer student, prior to my arrival. The decelerator was designed to slow CaF molecules over 80 cm. A CAD drawing of the decelerator is shown in Figure 3.6. The magnetic field is generated by a series of stages formed of rings of 12 wedge shaped N52 NdFeB permanent magnets arranged to make approximate Halbach cylinders [71]. The magnetisation of an ideal Halbach cylinder, $\vec{M}$, is:

$$\vec{M} = M_r \left(\hat{i} \cos K\phi + \hat{j} \sin K\phi \right), \tag{3.5}$$

where $K \in \mathbb{N}$, $\phi = \arccos\left(\hat{i} \cdot \hat{j}\right)$, and $\hat{i}$ and $\hat{j}$ are the unit vectors in the plane perpendicular to the axis of the cylinder. The ZSD uses dipole ($K = 2$) and hexapole ($K = 6$) arrays. The dipole arrangement produces a strong magnetic field at the centre of the ring and the hexapole produces a field minimum at the centre. These arrangements are also shown in Figure 3.6.

In the assembled decelerator the stages alternate between hexapole and dipole arrays, with the orientation of the dipole array flipping each time. This produces a periodic magnetic field along the centre of the decelerator. The decelerator is oriented with the central bore along the z-axis (see Figure 4.2). The radius of the central bore is 2.5 mm. The magnetic fields of the individual permanent magnets forming the Halbach arrays had been calculated in Comsol [1] and the resulting fields are shown in Figure 3.7. As can be seen, the decelerator has a peak magnetic field of 1.2 T. The CaF $X^2\Sigma$ state has a Zeeman splitting of $\sim 14\,\mathrm{GHz\,T^{-1}}$, so the upper bound on the energy lost to the field over a single deceleration stage (with $\Delta_{\mathrm{w2s}} = 16.8\,\mathrm{GHz}$ and $\Delta_{\mathrm{s2w}} = 0$) is $6.95 \times 10^{-5}\,\mathrm{eV}$.

Further, it can be seen that the transverse magnetic field in the hexapole (weak field) stages is approximately quartic. This means that molecules in a WFS state will

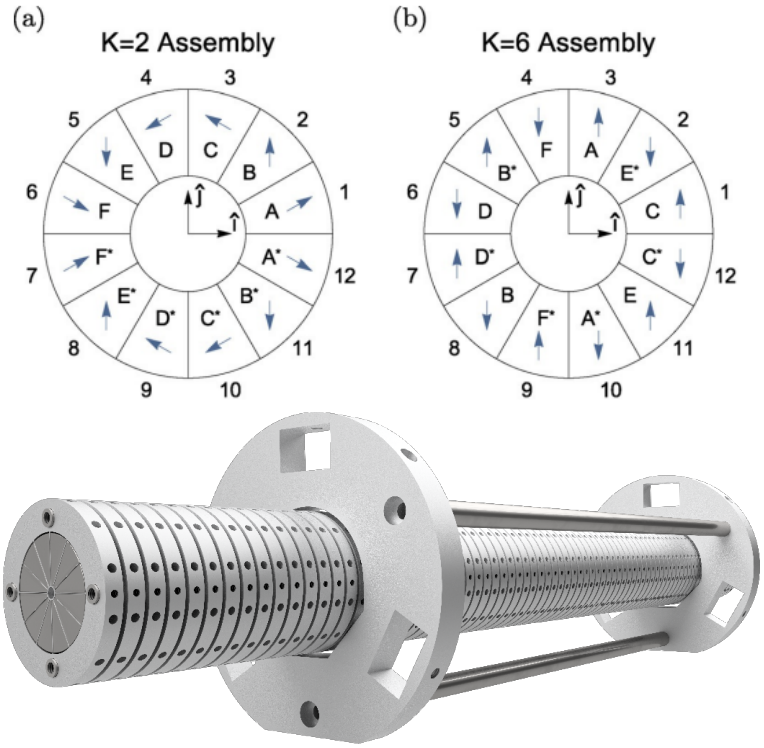

FIGURE 3.6: (top) schematics of the dipole (a, $K = 2$) and hexapole (b, $K = 6$) Halbach arrays producing the strong and weak magnetic field regions respectively. (bottom; to scale, perspective [1]) CAD model of the Zeeman-Sisyphus decelerator, showing the mounting flanges and arrangement of magnets in the first stage.

be guided towards the centre in weak field stages. As discussed in the introduction to this chapter, and seen in Figure 3.1, the molecule will be in a WFS state for at least half the time it is in a weak field stage. In fact, in practice it will always be in a WFS state for more than half the time. Therefore, it is hoped that there will be a net guiding effect. This is shown more clearly in the following simulations.

3.4 Trajectory Simulations

In order to understand the motion of the CaF molecules inside the decelerator, trajectory calculations were carried out. To begin with, we ignore the optical pumping. This means we can model the CaF molecule as a classical particle with the Hamiltonian:

$$H = \frac{1}{2} m_{\mathrm{CaF}} \left(v_z^2 + v_\perp^2 \right) + \mu_{\mathrm{CaF}} B(\rho_\perp, \theta, z), \tag{3.6}$$

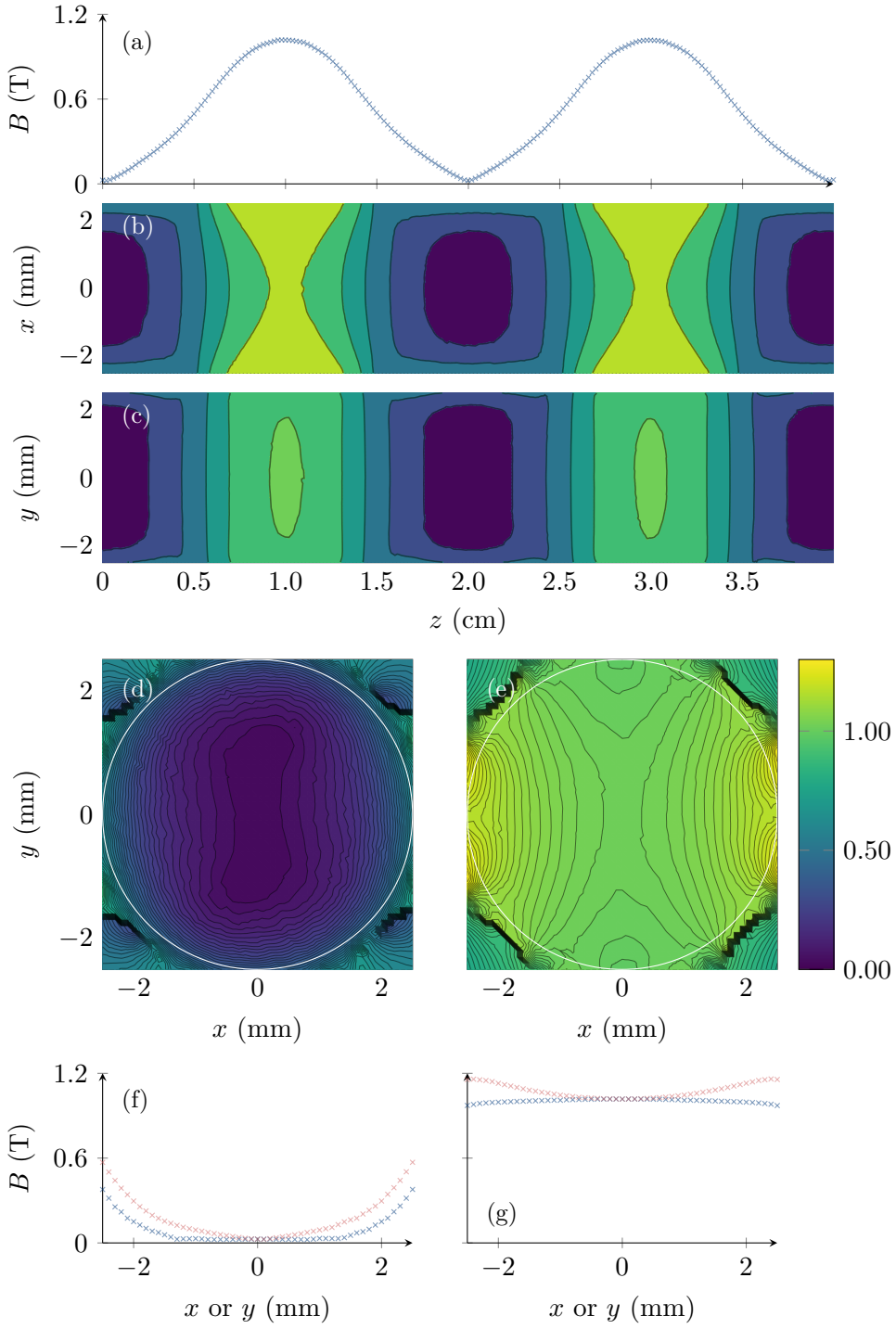

FIGURE 3.7: (a) The magnetic field strength at $(x = 0, y = 0)$ along the z-axis; i.e., along the length of the decelerator. (b-c) A cross section through the decelerator in the (b) x–z plane at $y = 0$ and (c) the y–z plane at $x = 0$, over 5 stages (3 hexapole and 2 dipole), showing the magnetic field strength. (d-e) A cross section through the x–y plane at (d) $z = 0$ (i.e., a hexapole or weak field stage) and (e) $z = 1\,\text{cm}$ (i.e., a dipole or strong field stage). The white circle shows the edge of the central bore of the decelerator. (f-g) The magnetic field strength at (f) $z = 0$ and (g) $z = 1\,\text{cm}$, along the x-axis (red) or y-axis (blue).

where the magnetic moment is $\mu_{\mathrm{CaF}} \approx \mu_B$ for CaF, as shown in Section 2.4. $B(\rho_\perp, \theta, z)$ can be provided by a harmonic oscillator approximation or by linear interpolation of the numerically calculated field shown in Figure 3.7. In the former case, the trajectories can be solved for exactly, and in the latter, time-stepped simulations must be carried out. The results of both methods are given below.

3.4.1 Harmonic Oscillator Approximation

As can be seen from Figure 3.7(f), the transverse field in the weak field region is approximately quartic. However, to begin with, we can approxmiate it as a harmonic oscillator:

$$B = \frac{B_1^{\mathrm{wk}}}{R^2}\rho_\perp^2, \tag{3.7}$$

where $B_1^{\mathrm{wk}} = 0.572\,\mathrm{T}$ in the x-direction and $0.375\,\mathrm{T}$ in the y-direction. The radius of the central bore is $R = 2.5\,\mathrm{mm}$. Since $\mu_{\mathrm{CaF}} \approx \mu_B$, the potential energy of the field-molecule is:

$$V^{\mathrm{wk}} = \pm\frac{\mu_B B_1^{\mathrm{wk}}}{R^2}\rho_\perp^2, \tag{3.8}$$

where the sign is positive for molecules in WFS states and negative for molecules in SFS states.

We take the the transverse field in the strong field stage to be uniform and the longitudinal variation is approximated as a square wave. This means the overall field is approximated as alternating strong and weak stages which are longitudinally uniform. Taking the mean field approximation, a molecule will, on average, experience a transverse force:

$$F_\rho = -\frac{1}{2}\frac{\partial V^{\mathrm{wk}}}{\partial \rho} = \mp\frac{\mu_B B_1^{\mathrm{wk}}}{R^2}\rho_\perp, \tag{3.9}$$

where now the sign is negative for WFS molecules and positive for SFS molecules. For WFS molecules this gives simple harmonic motion with angular frequency:

$$\omega = \sqrt{\frac{\mu_B B_1^{\mathrm{wk}}}{m_{\mathrm{CaF}} R^2}}. \tag{3.10}$$

Taking $m = m_{\mathrm{CaF}}$, this gives $\omega_x = 2.9\,\mathrm{krad\,s^{-1}}$ and $\omega_y = 2.4\,\mathrm{krad\,s^{-1}}$ for the x- and y-directions respectively. If the WFS molecule has a constant forward velocity v_z, its trajectory in this mean field harmonic approximation is:

$$\rho_\perp(z) = \frac{v_\perp(0)}{\omega} \sin\left(\frac{\omega}{v_z} z\right) + \rho_\perp(0) \cos\left(\frac{\omega}{v_z} z\right), \tag{3.11}$$

where $v_\perp(0)$ and $\rho_\perp(0)$ are the initial transverse velocity and position. If the molecule has a forward velocity of $145\,\mathrm{m\,s^{-1}}$, $2\pi v_z/\omega$ corresponds to an oscillation 'wavelength' of 0.37 m. Therefore, in a decelerator 0.8 m long, we can expect a WFS molecule to undergo two full oscillations.

If, on the other hand, the molecule is in a SFS state then its motion is exponential rather than harmonic. The trajectory is:

$$\rho_\perp(z) = \frac{v_\perp(0)}{\omega} \sinh\left(\frac{\omega}{v_z} z\right) + \rho_\perp(0) \cosh\left(\frac{\omega}{v_z} z\right), \tag{3.12}$$

with ω as in Eqn. (3.10). Both $\sinh(\alpha)$ and $\cosh(\alpha)$ are monotonically increasing functions for $\alpha \geq 0$, so this trajectory corresponds to anti-guiding. An SFS molecule intially at $\rho_\perp(0) = 0$ will be anti-guided to the edge of the decelerator bore ($\rho_\perp = R$) after a distance:

$$z(\rho_\perp = R) = \frac{v_z}{\omega} \operatorname{arcsinh}\left(\frac{\omega R}{v_\perp(0)}\right). \tag{3.13}$$

For a CaF molecule travelling at $v_z = 145\,\mathrm{m\,s^{-1}}$ this gives:

$$z(x = R) = (0.035\,\mathrm{m})\,\mathrm{arcsinh}\left(\frac{10.4\,\mathrm{m\,s^{-1}}}{v_\perp(0)}\right) \text{ and} \tag{3.14}$$

$$z(y = R) = (0.043\,\mathrm{m})\,\mathrm{arcsinh}\left(\frac{8.42\,\mathrm{m\,s^{-1}}}{v_\perp(0)}\right) \tag{3.15}$$

in the x- and y-directions respectively. For $v_\perp(0) = 4\,\mathrm{m\,s^{-1}}$ an SFS molecule will be anti-guided to the wall in 6 cm, or 3 half-cycles.

3.4.2 Time-stepped Simulation

For a more realistic simulation, we calculate the trajectories numerically, taking Eqn. (3.6) as our starting point. $B(\rho_\perp, \theta, z)$ was calculated by linear interpolation of the numerically calculated field shown in Figure 3.7. A simulation was carried out with 10^3 molecules distributed uniformly in the transverse plane with $x, y \in [-2.5, 2.5]$ mm, and with a Gaussian velocity distribution with standard deviation $\Delta v_z = \Delta v_\perp = 24\,\mathrm{m\,s^{-1}}$ and mean forward velocity of $v_z = 145\,\mathrm{m\,s^{-1}}$.

An example of the simulated molecular motion in the transverse (x–y) plane can be seen in Figure 3.8. The plotted molecule has $v_z = 129\,\mathrm{m\,s^{-1}}$. The data is fitted with a sine wave, for comparision with the harmonic oscillator model. Over the 10^3 simulations run, the angular oscillation frequency in the x-direction was $\omega_x = (2600 \pm 300)\,\mathrm{rad\,s^{-1}}$ and in the y-direction was $\omega_y = (1200 \pm 500)\,\mathrm{rad\,s^{-1}}$.

Importantly, the guiding effect can be clearly seen in the trajectory simulations. In order for a molecule to be successfully guided, its initial position and velocity must be such that the guiding effect prevents the molecule from hitting the walls of the central bore of the decelerator. These constraints on the initial conditions give the phase space acceptance, which is determined in the next section.

3.5 Phase Space Acceptance

In order to design the experiment, it is important to know what range of positions and velocities the molecules can have at the entrance of the decelerator in order to make it to the exit without hitting the walls. This is the phase space acceptance. Here, we examine the phase space acceptance of WFS molecules in the decelerator with no

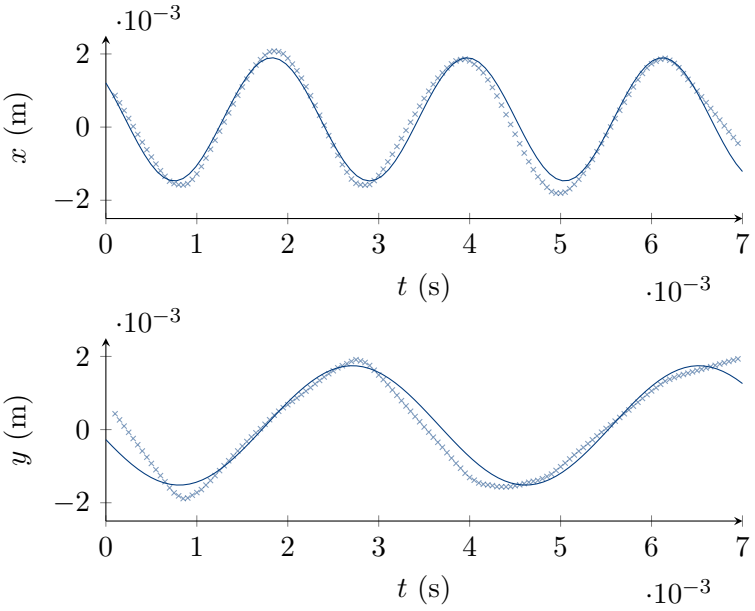

FIGURE 3.8: Simulated motion of a CaF particle in a decelerator with no optical pumping. The trajectories are fitted with sine waves to determine the effective oscillation frequencies, $\omega_x = 2930\,\mathrm{rad\,s^{-1}}$ and $\omega_y = 1650\,\mathrm{rad\,s^{-1}}$.

optical pumping — that is, with the decelerator in 'guiding' mode. The molecules are guided by the transverse magnetic field gradients inside the decelerator, as discussed in Section 3.3 and Section 3.4, but do not lose any energy and are not slowed.

Beginning with the harmonic oscillator approximation of Section 3.4.1, we can rewrite the equation of motion (Eqn. (3.11)) as:

$$\begin{aligned} \rho_\perp(z) &= \psi \sin\left(\frac{\omega}{v_z} z + \phi\right) \\ \psi^2 &= \frac{v_\perp(0)^2}{\omega^2} + \rho_\perp(0)^2 \\ \tan\phi &= \frac{\omega \rho_\perp(0)}{v_\perp(0)} \end{aligned} \tag{3.16}$$

The maximum radial position of the molecule is then ψ, and so the requirement that the molecule doesn't hit the walls is $\psi < R$. The phase space acceptance is the region in phase space (i.e., position-momentum space) that molecules have to lie within at $z = 0$ in order to exit the decelerator. The surface separating the accepted region from the rest of phase space is the separatrix. The phase space we are interested in is two dimensional: $\rho_\perp$–$v_\perp$. Therefore, the separatrix is a line. Given $\psi < R$, the separatrix for the phase space acceptance in the harmonic oscillator approximation

is the ellipse:

$$\frac{m_{\mathrm{CaF}} v_\perp(0)^2}{\mu_B B_1^{\mathrm{wk}}} + \frac{\rho_\perp(0)^2}{R^2} = 1, \tag{3.17}$$

with $\rho_\perp$-axis radius of $\max(\rho_\perp) = R$ and $v_\perp$-axis radius of $\max(v_\perp) = R\omega$. The condition of $\rho_\perp = R$ and $v_\perp = 0$ represents a molecule with no transverse velocity propagating along the edge of the bore without hitting the wall. As the transverse velocity increases, the maximum allowed radial position decreases. This is because (at constant acceleration) it will take more distance to reverse the motion of a molecule moving towards the walls if the molecule is moving more quickly. Therefore, a molecule that starts too near the walls may collide before the guiding takes effect. The separatrix for this model is shown in Figure 3.9 as the white ellipse.

To provide a reference for comparison, we also look at the phase space acceptance of a cylindrical tube with the same geometry as the ZSD but with no magnetic field. This shows the benefit of the transverse guiding of the ZSD scheme. A particle with forward velocity v_z will travel the length of the cylinder, $\mathcal{L}$, in $t = \mathcal{L}/v_z$. If, at $z = 0$, the particle is at transverse position $-R < \rho_\perp < R$, then it must travel no more than

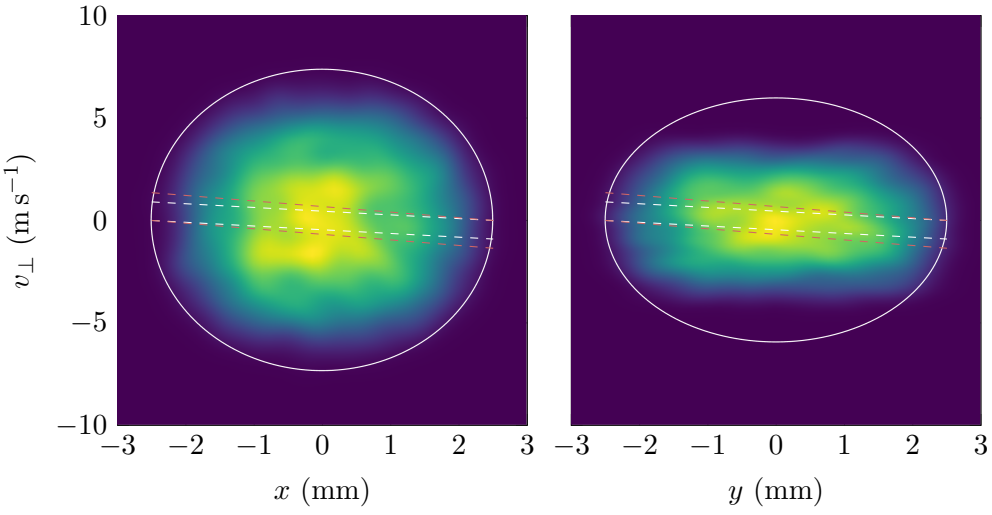

FIGURE 3.9: Density plot showing the distribution in phase space of molecules which are accepted into the decelerator and make it to the end without impacting the walls. The solid white ellipse is the separatrix calculated from the harmonic oscillator model. The dashed lines show the free space acceptance of a cylinder 0.8 m long and 2.5 mm in radius for $v_z = 145\,\mathrm{m\,s^{-1}}$ (white) and $v_z = 217\,\mathrm{m\,s^{-1}}$ (red).

$\Delta\rho_\perp = \pm(R - \rho_\perp)$ in order to not hit the sides of the tube. Therefore, the maximum transverse velocity is $\Delta\rho_\perp/t$:

$$\max(v_\perp) = \frac{\pm(R - \rho_\perp)v_z}{\mathcal{L}}. \tag{3.18}$$

For $\mathcal{L} = 0.8\,\mathrm{m}$ and $R = 2.5\,\mathrm{mm}$, and a particle with $\rho_\perp = 0$ and $v_z = 145\,\mathrm{m\,s^{-1}}$, $\max(v_\perp) = \pm 0.45\,\mathrm{m\,s^{-1}}$. Unlike in the harmonic model, the separatix here depends on forward velocity, v_z. The separatrices for $v_z = 145\,\mathrm{m\,s^{-1}}$ and $v_z = 217\,\mathrm{m\,s^{-1}}$ (i.e., $145\,\mathrm{m\,s^{-1}} + 3\Delta v_z$ for $\Delta v_z = 24\,\mathrm{m\,s^{-1}}$) are shown in Figure 3.9 as the white and red dashed lines. At $\rho_\perp = 0$, the free space $\max(v_\perp)$ is $7\,\mathrm{m\,s^{-1}}$ smaller than the harmonic ZSD model in v_x and $5.6\,\mathrm{m\,s^{-1}}$ smaller in v_y. Thus, the effect of the guiding can clearly be seen in the increased $v_\perp$ acceptance.

To compare the harmonic model with the results from the numerical field calculations, another step-wise trajectory simulation was carried out, this time with 10^5 molecules. The molecules were initially uniformly distributed in phase space over the ranges $x, y \in [-3, 3]$ mm, $v_x, v_y \in [-10, 10]$ $\mathrm{m\,s^{-1}}$, and $v_z \in [160, 161]$ $\mathrm{m\,s^{-1}}$. The initial z position was set to be at the entrance to the decelerator (i.e., the start of the decelerator was $z = 0$). The molecules which reached the end of the decelerator ($z = 0.8\,\mathrm{m}$) without hitting the walls of the central bore were considered to be 'accepted'. The accepted molecules were identified and their initial state (i.e., their state at $z = 0$) in phase space was plotted to find the phase space acceptance. The distribution of initial states of the molecules which were accepted is plotted in Figure 3.9 for both x–v_x and y–v_y.

It can be seen from Figure 3.9 that the molecules accepted in the simulation fit within to the phase space acceptance predicted by the harmonic model. However, there are anharmonic features in the simulation: most clearly, the exclusion of molecules with higher v_y. Both this and the smaller ω_y produced by the simulation are indicative of the harmonic model overestimating the B-field in the y-direction. This can be seen more clearly in Figure 3.10.

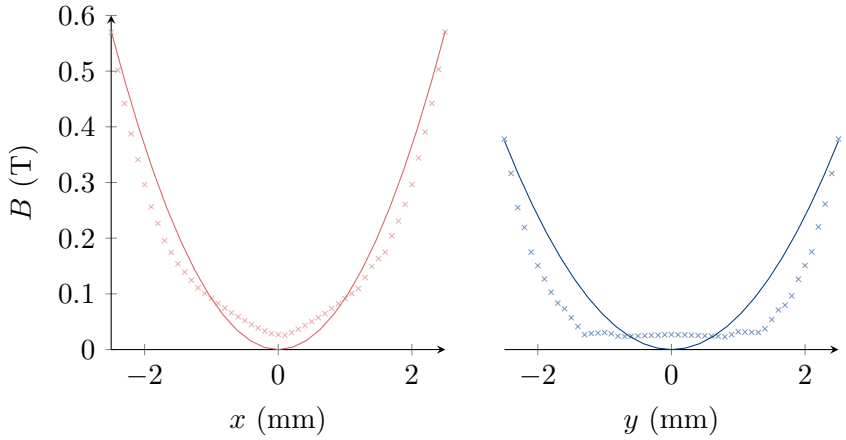

FIGURE 3.10: The harmonic model approximations to the transverse weak field shown in Figure 3.7(f). It can be seen that for the y-axis cross-section in particular the fit is poor, with the magnetic field being overestimated everywhere except for a small region around $y = 0$.

3.5.1 Anharmonic Features of the Phase Space Acceptance

Whilst the harmonic model is useful in order to gain a general understanding of the motion and because it is analytically solvable, it does not reproduce any anharmonic features that can be seen in the time-stepped simulations. We can use a more accurate model of the magnetic field to explore these features. As with the harmonic model, we are only interested in the field strength rather than the field itself. We model the field strength as varying sinusoidally along the z-axis between a transverse strong field, $B^{\mathrm{sr}}(\rho_\perp, \theta)$, and a transverse weak field, $B^{\mathrm{wk}}(\rho_\perp, \theta)$:

$$B(\rho_\perp, \theta, z) = \sin^2\left(\frac{2\pi z}{L}\right) B^{\mathrm{sr}}(\rho_\perp, \theta) + \cos^2\left(\frac{2\pi z}{L}\right) B^{\mathrm{wk}}(\rho_\perp, \theta). \tag{3.19}$$

As the field is not cylindrically symmetric, we model the transverse fields as varying between a known x cross-section, $B_x^{\mathrm{wk}}(\rho_\perp)$ and $B_x^{\mathrm{sr}}(\rho_\perp)$, and a known y cross-section, $B_y^{\mathrm{wk}}(\rho_\perp)$ and $B_y^{\mathrm{sr}}(\rho_\perp)$:

$$B^{\mathrm{wk}}(\rho_\perp, \theta) = \cos^2(\theta) B_x^{\mathrm{wk}}(\rho_\perp) + \sin^2(\theta) B_y^{\mathrm{wk}}(\rho_\perp) + B_0^{\mathrm{wk}}, \tag{3.20}$$

$$B^{\mathrm{sr}}(\rho_\perp, \theta) = \cos^2(\theta) B_x^{\mathrm{sr}}(\rho_\perp) + \sin^2(\theta) B_y^{\mathrm{sr}}(\rho_\perp) + B_0^{\mathrm{sr}}, \tag{3.21}$$

where B_0^{wk} and B_0^{sr} are the field strengths at $\rho_\perp = 0$. $B_x^{\mathrm{wk}}(\rho_\perp) + B_0^{\mathrm{wk}}$ and $B_y^{\mathrm{wk}}(\rho_\perp) + B_0^{\mathrm{wk}}$ are shown in Figure 3.7(f) (red and blue, respectively). $B_x^{\mathrm{sr}}(\rho_\perp) + B_0^{\mathrm{sr}}$ and $B_y^{\mathrm{sr}}(\rho_\perp) + B_0^{\mathrm{sr}}$ are shown in Figure 3.7(g) (again, red and blue, respectively).

We model the transverse weak field as quartic and the transverse strong field as a sixth-degree polynomial (we drop the x and y subscript for convenience here as the equations are the same for both, though the values of the constants are different):

$$B_{x,y}^{\mathrm{wk}}(\rho_\perp) = a\rho_\perp^4 + b\rho_\perp^2 + B_0^{\mathrm{wk}}, \tag{3.22}$$

$$B_{x,y}^{\mathrm{sr}}(\rho_\perp) = a\rho_\perp^6 + b\rho_\perp^4 + c\rho_\perp^2 + B_0^{\mathrm{sr}}, \tag{3.23}$$

This model was fitted to the numerically calculated magnetic field data shown in Figure 3.7 with $B_0^{\mathrm{sr}} = 1.02\,\mathrm{T}$ and $B_0^{\mathrm{wk}} = 0.0290\,\mathrm{T}$ fixed. The fitted models can be seen in Figure 3.11 together with the values of the fit parameters.

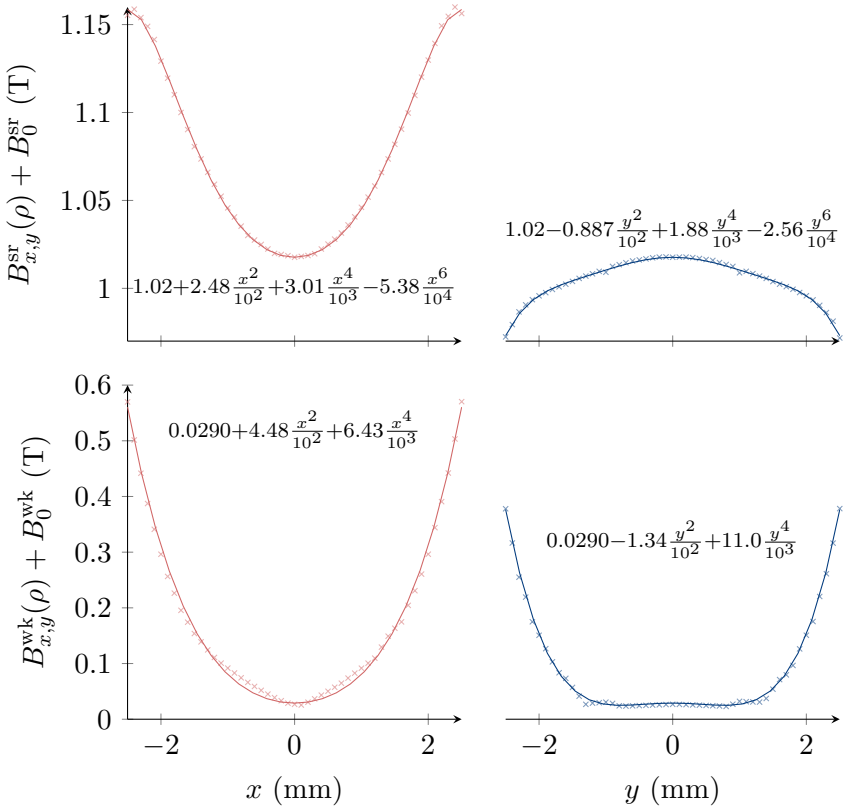

FIGURE 3.11: Anharmonic fits to the transverse fields shown in Figure 3.7(f,g). The strong field profiles (top) have been fitted with sixth-degree polynomials and the weak field profiles (bottom) have been fitted with fourth-degree (quartic) polynomials.

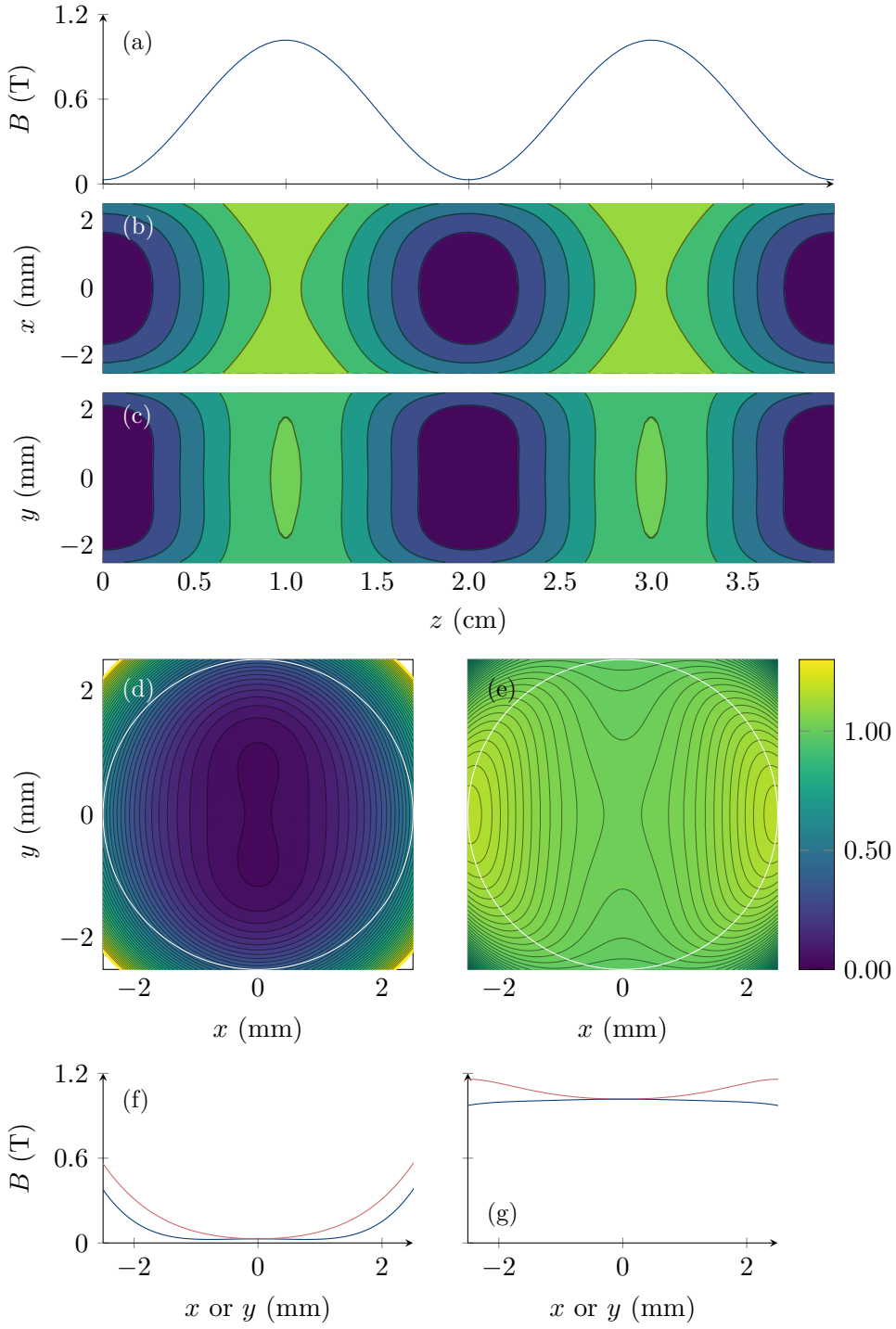

FIGURE 3.12: The anharmonic magnetic field strength model given in Eqn. (3.19). (a) The magnetic field strength at $(x = 0, y = 0)$ along the z-axis; i.e., along the length of the decelerator. (b-c) A cross section through the decelerator in the (b) x–z plane at $y = 0$ and (c) the y–z plane at $x = 0$, over 5 stages, showing the magnetic field strength. (d-e) A cross section through the x–y plane at (d) $z = 0$ (weak field stage) and (e) $z = 1\,\text{cm}$ (strong field stage). The white circle shows the edge of the central bore of the decelerator. (f-g) The magnetic field strength at (f) $z = 0$ and (g) $z = 1\,\text{cm}$, along the x-axis (red) or y-axis (blue).

The resulting field strengths are plotted in Figure 3.12. Compared with the numerically calculated field strengths in Figure 3.7 we can see that the anharmonic model contains the same structural features, and is a better model for the field strength than the harmonic model.

To find the phase space acceptance and separatrix, the mean field approximation was used, so that:

$$\langle B \rangle (\rho_\perp, \theta) = \frac{1}{2} B^{\mathrm{sr}}(\rho_\perp, \theta) + \frac{1}{2} B^{\mathrm{wk}}(\rho_\perp, \theta). \tag{3.24}$$

The Hamiltonian for the molecule is as in Eqn. (3.6). A classical particle's trajectory in phase space will always be a line of constant energy. Since we are operating in the mean field along z, we can ignore the v_z contribution to the Hamiltonian (as this is a constant energy offset). A plot of the mean field in the x–y plane is shown in Figure 3.13. As can be seen, the energy of the mean field monotonously increases towards the edge of the decelerator. Therefore, a particle with total energy less than the Hamiltonian energy at $\rho_\perp = R$ will never touch the walls. The potential is not cylindrically symmetric, and so the energy varies with angle θ. The minimum energy of 6.25×10^{-24} J occurs at $\theta = \pi/2$; i.e., at $(x = 0, y = R)$, also shown in Figure 3.13. The constant energy contour at this energy is the phase space acceptance separatrix.

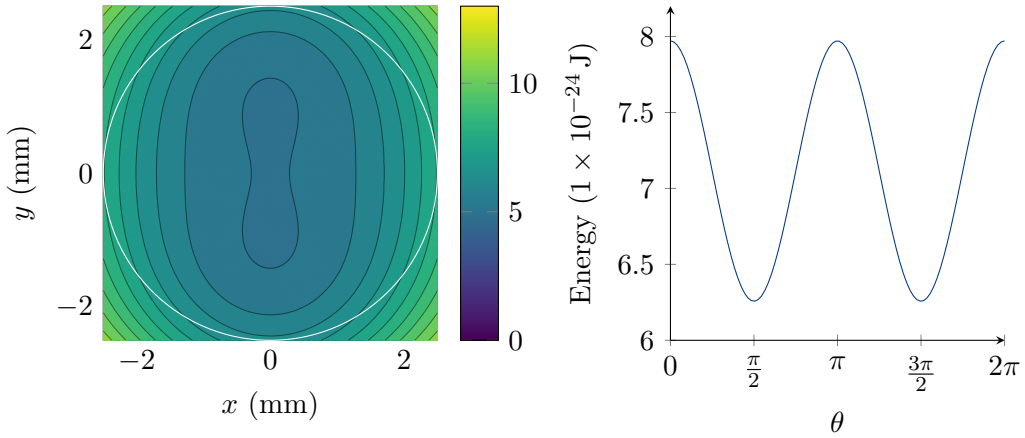

FIGURE 3.13: (left) Contour plot of the Hamiltonian energy for a CaF molecule in the x–y plane with $v_\perp = 0$. The white circle shows the wall of the central bore of the decelerator at $\rho = R = 2.5\,\mathrm{mm}$. (right) The Hamiltonian energy at $\rho = R$ as it varies with cylindrical angle θ.

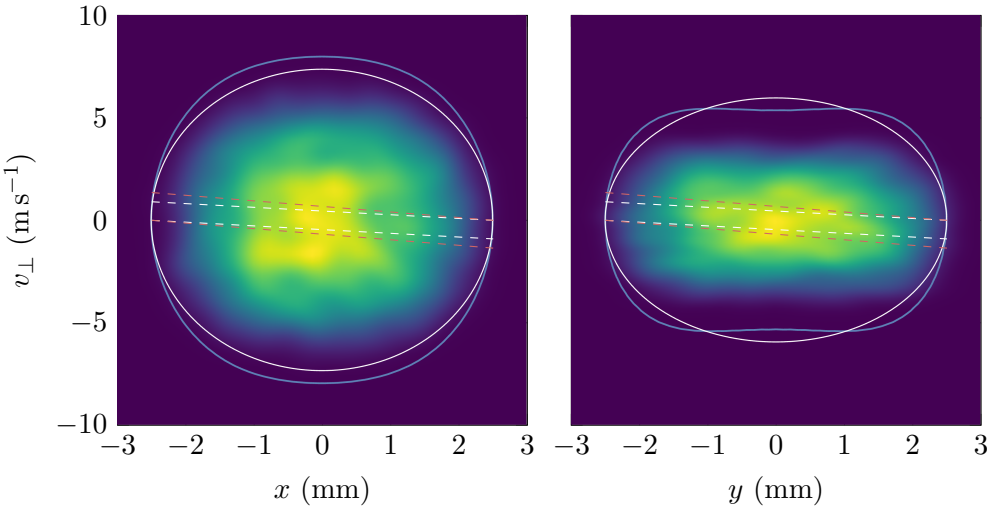

FIGURE 3.14: The phase space acceptance data and harmonic ZSD and free space model separatrices shown in Figure 3.9, together with the addition of the separatrix adjusted for anharmonic features in blue. The anharmonic accounts for the additional $v_\perp$ suppression around $y = 0$.

The separatrices are plotted in Figure 3.14, overlaid on the trajectory simulation distributions from Figure 3.9. As can be seen, the suppression of the v_y phase space acceptance is predicted by this anharmonic field model, though the suppression in the simulations is somewhat larger than predicted. This must be due to the mean field model overestimating the peak magnetic field seen by the average molecule.

3.5.2 Fraction of the Beam Accepted

The simulations so far discussed in this chapter were carried out with the initial z position of the molecules set to be at the entrance to the decelerator (i.e., the start of the decelerator was $z = 0$). However, if this is changed so that there is a gap, Δz, between the starting point of the molecules and the entrance of the decelerator, some molecules will have moved to a radial position too large to be accepted into the decelerator by the time they arrive at the entance.

In a real experimental setup, there must always be such a gap. Therefore, it is useful to know what the reduction in phase space acceptance is as Δz increases. A series of simulations with 10^5 molecules was carried out for different Δz. The molecules were initially uniformly distributed in phase space over the ranges $x, y \in [-3, 3]$ mm, $v_x, v_y \in [-10, 10]$ m s^{-1}, and $v_z \in [160, 161]$ m s^{-1}. The results are shown in Figure 3.15. The number of molecules accepted into the decelerator is reduced

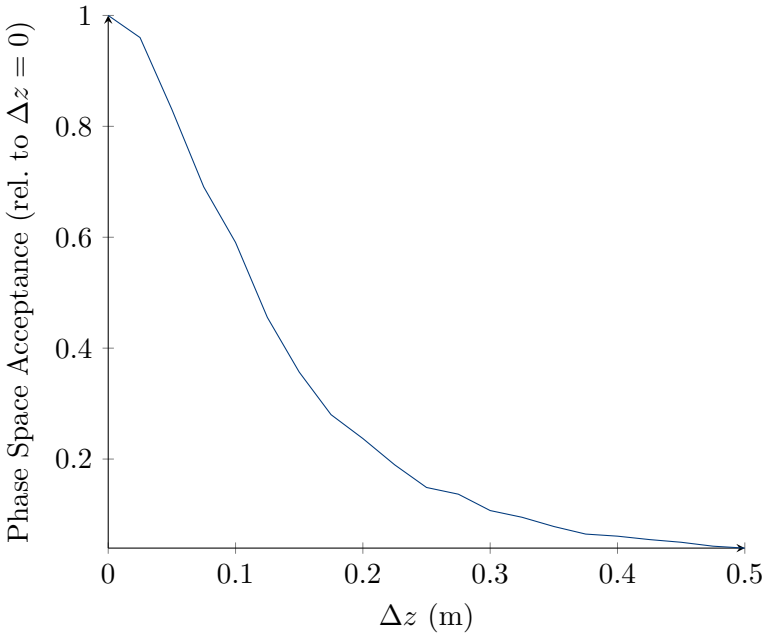

FIGURE 3.15: The fraction of a molecular beam inside the phase space acceptence of the decelerator, for various distances, Δz, of the decelerator from the source, relative to the acceptence at $\Delta z = 0$.

by half at a distance of $\Delta z = 11\,\text{cm}$. It is reduced by another half, to 25%, at $\Delta z = 19\,\text{cm}$.

3.6 Spin Flip Probability

As previously established, a high spin flip probability (SFP) is necessary for the ZSD scheme to work. In order to determine the SFP, trajectory simulations which included optical pumping were carried out.

With the inclusion of transition probabilities derived from the quantum mechanical calculations of Section 2.5, the simulation was now semi-classical. The molecule had a chance of excitation every time-step given by Eqn. (2.41) (see Section 2.5 for more information). The state to which the molecule decayed was given by the branching ratios (see Section 3.2) and the recoil momentum of the photon was accounted for. The time step was now dynamically calculated from the total scattering rate over all excited states $\{n'\}$:

$$\delta t = \frac{1}{1\,\text{s}^{-1} + 100 \sum_{n'} R}, \tag{3.25}$$

with a minimum of 10 ns and a maximum of 1 µs. A small minimum was chosen as too large a time step reduces the simulated probability of excitation below the true value.

A series of simulations was carried out with 100 molecules for a given detuning and each one of the twelve initial $X^2\Sigma$ states. Two single frequency lasers were simulated with the laser powers were set to 75 mW. The free-space flight distance of the molecules before entering the decelerator was set to $\Delta z = 0$. Detunings for molecules starting in WFS states were $\Delta_{\mathrm{w2s}} \in [-20, 0]$ GHz and for molecules starting in SFS were $\Delta_{\mathrm{s2w}} \in [0, 20]$ GHz. The simulations were carried out over two half-stages of the decelerator, from $z = 0$ m to $z = 0.01$ m, as this covered the full range of magnetic fields.

The spin flip probability (SFP) — the probability that a molecule would flip from a WFS state to a SFS state (or vice versa) — was calculated together with the position of the resonance (the z-position at which the flip occurred). The results are shown in Figure 3.16. The resonances occur at slightly different positions due to the hyperfine splitting of the ground state. However, it can be seen that despite not addressing each ground state hyperfine level individually, the spread of positions is very narrow.

The four states with lowest SFP are $(1^+, 0)$ and $(2, 1)$ (WFS, red), and $(1^-, 0)$ and $(1^+, -1)$ (SFS, blue). They are marked with dashed lines. The reason for the low SFP can be seen with reference to Figure 3.5. The two WFS states only have significant transition intensities to the excited WFS states. However, excited WFS states are much more likely to decay to ground WFS states. Therefore, the most likely outcome for any given excitation is a return to a WFS state. The same applies, vice versa, for the two SFS states.

From Figure 3.16 it can also be seen that the CaF molecules only come into resonance with the lasers if the magnitude of the detuning is less than 15 GHz. It can also be seen that the SFP is at a minimum at ±10 GHz, corresponding to a resonance position of 0.6 m. This is because this is the region of greatest longitudinal magnetic field gradient. Therefore, the molecules are at the correct magnetic field strength for a shorter period of time. Since Δ_{w2s} should be maximised and Δ_{s2w} should be minimised, values of $\Delta_{\mathrm{w2s}} = -14$ GHz and $\Delta_{\mathrm{s2w}} = 2$ GHz were chosen for the remaining simulations. This also has the effect of avoiding the area of lowest SFP.

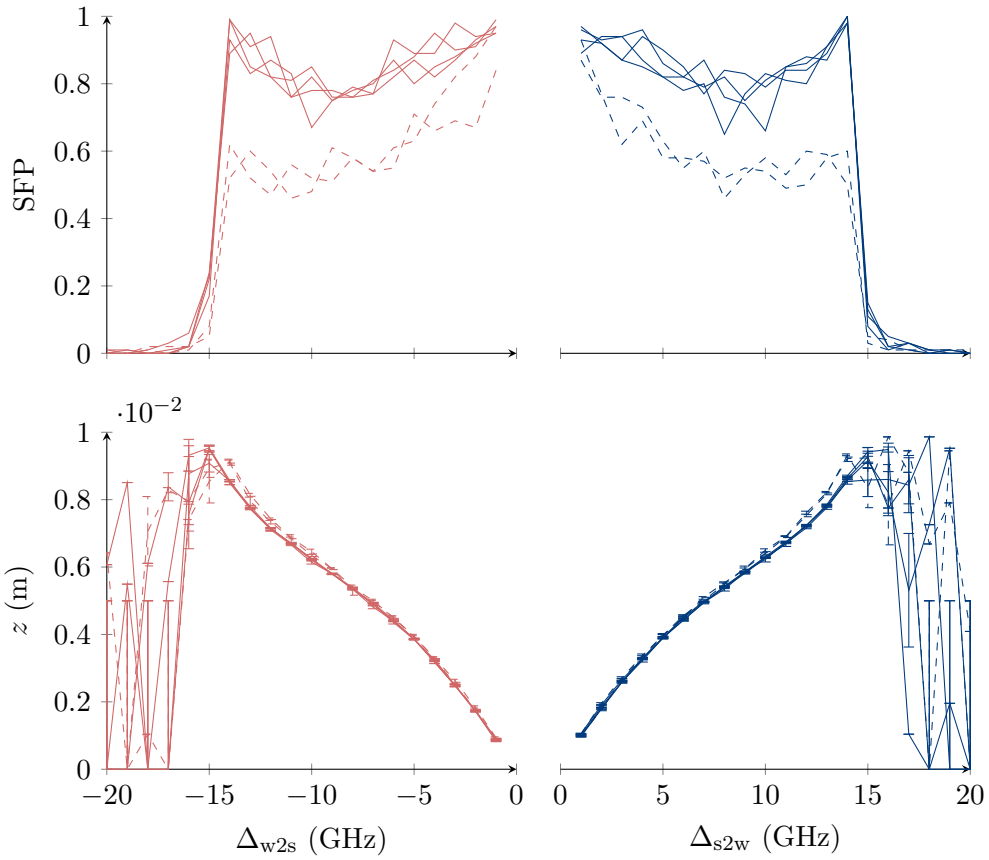

FIGURE 3.16: The spin flip probability (top) and longitudinal position of the resonance (bottom) for molecules initially in WFS states (left, red) and SFS states (right, blue). The x-axis shows either the detuning of the WFS-to-SFS laser, Δ_{w2s}, or the detuning of the SFS-to-WFS laser, Δ_{s2w}. Each line is the mean of 100 molecule simulations per inital state and error bars show standard error. The states marked with dashed lines are $(1^+, 0)$ and $(2, 1)$ (WFS, red) and $(1^-, 0)$ and $(1^+, -1)$ (SFS, blue). It can be seen that the laser never comes into resonance with the molecules outside $\pm 15\,\mathrm{GHz}$.

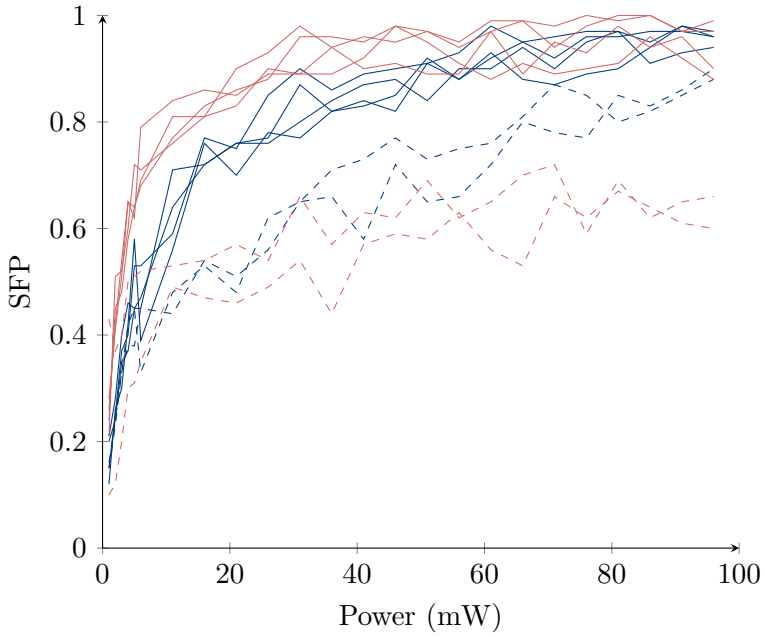

FIGURE 3.17: The spin flip probabilities for molecules initially in WFS states (red) and SFS states (blue) varying with laser power. Each line is the SFP calculated from 100 molecule simulations for a given initial state. The states marked with dashed lines are $(1^+, 0)$ and $(2, 1)$ (WFS, red) and $(1^-, 0)$ and $(1^+, -1)$ (SFS, blue).

A second set of simulations was also run, varying the laser power between 0 mW and 100 mW. The detunings were fixed at $\Delta_{\mathrm{w2s}} = -14$ GHz and $\Delta_{\mathrm{s2w}} = 2$ GHz and 100 molecules were simulated per laser power. The results are shown in Figure 3.17. It can be seen that the SFP saturates around 20 mW. For the remaining simulations, the laser power was fixed to 75 mW.

3.7 Deceleration

As described in the introduction to this chapter, the optical pumping and spin flipping leads to an expected energy change of

$$\Delta\epsilon = 2h(\Delta_{\mathrm{w2s}} + \Delta_{\mathrm{s2w}}) \tag{3.26}$$

per half-cycle (i.e., z to $z + L/2$). This gives $\Delta\epsilon = -1.6 \times 10^{-23}$ J for the optimum detunings found in Section 3.6. If the change in energy is averaged out over the length $L/2$, the approximate energy at a distance z is

$$\epsilon(z) = \frac{2\Delta\epsilon}{L} z + \frac{1}{2} m_{\mathrm{CaF}} \left(v_z^{\mathrm{i}}\right)^2, \tag{3.27}$$

where v_z^{i} is the initial velocity at the decelerator entrance ($z = 0$). Since $\epsilon(z) = \frac{1}{2} m_{\mathrm{CaF}} v_z^2$, this gives a trajectory through z-v_z phase space of:

$$v_z = \sqrt{\frac{4\Delta\epsilon}{m_{\mathrm{CaF}} L} z + (v_z^{\mathrm{i}})^2}. \tag{3.28}$$

Eqn. (3.28) is plotted for five molecules with initial conditions $\{155, 150, 145, 140, 135\}\,\mathrm{m\,s^{-1}}$ in Figure 3.18. The theoretical model is compared with a semi-classical trajectory simulation in Figure 3.19. For the simulation, the lasers had detunings fixed at $\Delta_{\mathrm{w2s}} = -14\,\mathrm{GHz}$ and $\Delta_{\mathrm{s2w}} = 2\,\mathrm{GHz}$, and a power of 75 mW. The difference between the theory and simulation can be explained by the failure of the molecule to spin flip. In the regions where the molecule spin flips regularly (e.g., between 0.6 m and 0.7 m) the trajectory in phase space is parallel to the solution to Eqn. (3.28).

Next, trajectory simulations were carried out using the semi-classical model to test the deceleration effect over a large number of molecules. The lasers had detunings fixed at $\Delta_{\mathrm{w2s}} = -14\,\mathrm{GHz}$ and $\Delta_{\mathrm{s2w}} = 2\,\mathrm{GHz}$, and a power of 75 mW. The free-space flight distance of the molecules before entering the decelerator was set to $\Delta z = 0$. The simulation was setup with an initial molecular distribution as described in Section 5.1.4, with $v_{\mathrm{out}} = 145\,\mathrm{m\,s^{-1}}$, $\Delta v_z = 24\,\mathrm{m\,s^{-1}}$, and was uniform in the transverse plane, with $x, y \in [-2.5, 2.5]$ mm.

To begin with, 10^5 molecules were simulated with $v_{\mathrm{out}} = 145\,\mathrm{m\,s^{-1}}$, $\Delta v_z = 24\,\mathrm{m\,s^{-1}}$ and no transverse velocity, in order to see the pure effect of the slowing without any guiding. The results are shown in Figure 3.20. The initial velocity distribution of the accepted molecules has a mean of $152\,\mathrm{m\,s^{-1}}$ and a standard deviation of $22\,\mathrm{m\,s^{-1}}$. The final velocity distribution has a mean of $120\,\mathrm{m\,s^{-1}}$ and a standard deviation of $35\,\mathrm{m\,s^{-1}}$. This corresponds to an overall average energy reduction of $(1.06 \pm 0.02) \times 10^{-23}\,\mathrm{J}$ per half-cycle (i.e., for every 0.02 m), which is somewhat

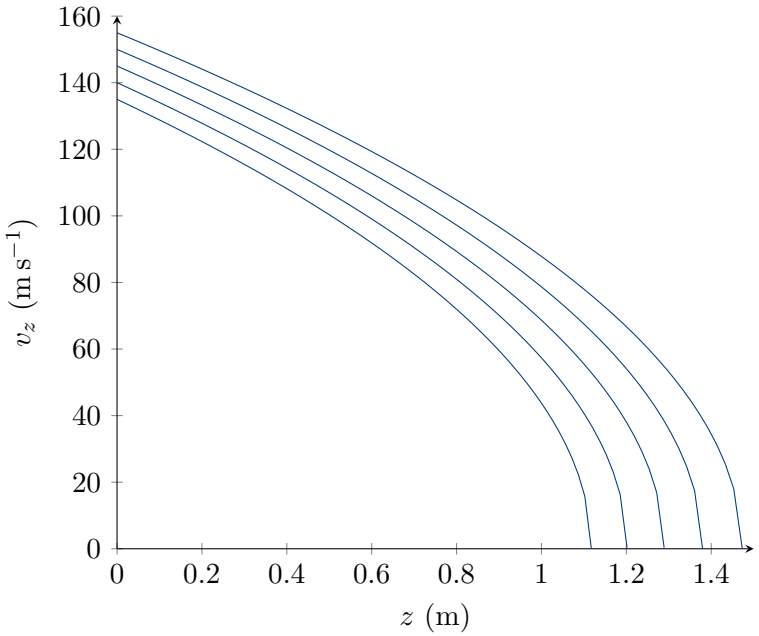

FIGURE 3.18: The theoretical trajectory through the z–v_z phase space of five molecules with different initial velocities, calculated from Eqn. (3.28). It can be seen that for typical molecular velocities a longer ZSD would be required to bring an average molecule to below the capture velocity of a MOT.

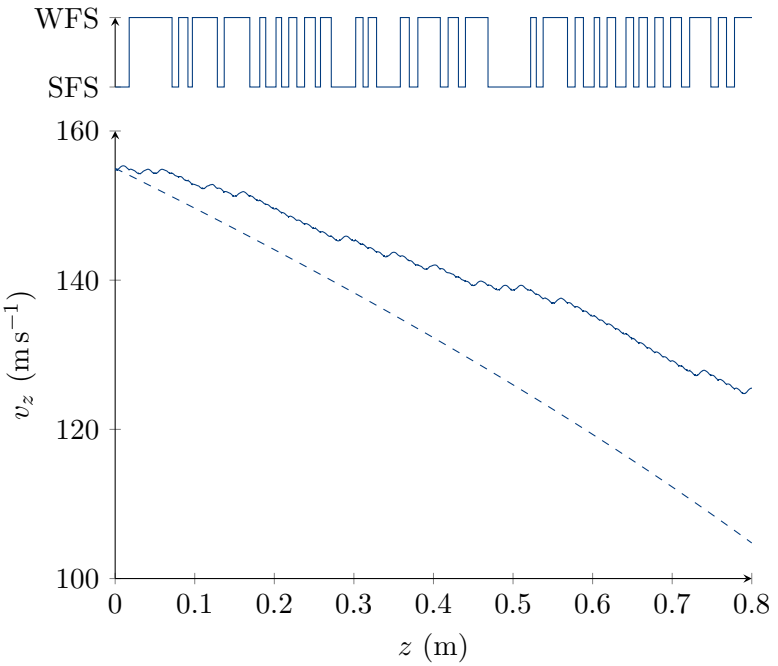

FIGURE 3.19: The trajectory through the z–v_z phase space of a single molecule, together with a plot of the molecule's state. There are some stages where the molecule's spin doesn't flip successfully. This can be seen in both the phase space plot and in the state plot. The dashed line shows the theoretical trajectory calculated from Eqn. (3.28), which assumes perfect spin flipping.

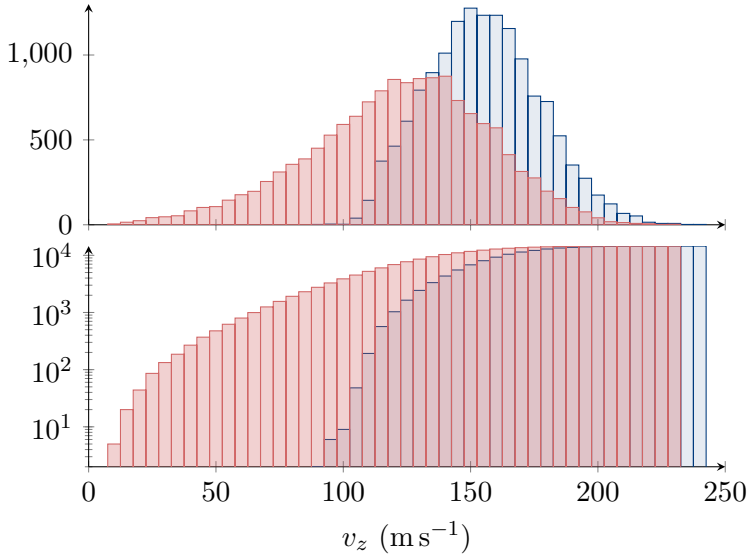

FIGURE 3.20: The initial (blue) and final (red) v_z distributions (top) and cumulative distributions (bottom) for a simulation of 14 502 CaF molecules. The initial molecular distribution had 10^5 molecules with $\Delta z = 0$, $v_{\text{out}} = 145\,\text{m s}^{-1}$, and $\Delta v_z = 24\,\text{m s}^{-1}$. They were uniformly distributed in the transverse plane with $x, y \in [-2.5, 2.5]$ mm but had no transverse velocity. The laser powers were 75 mW and they had detunings $\Delta_{\text{w2s}} = -14\,\text{GHz}$ and $\Delta_{\text{s2w}} = 2\,\text{GHz}$. 4.3% of accepted molecules have a final velocity below $50\,\text{m s}^{-1}$ and 0.08% have a final velocity below $12.5\,\text{m s}^{-1}$.

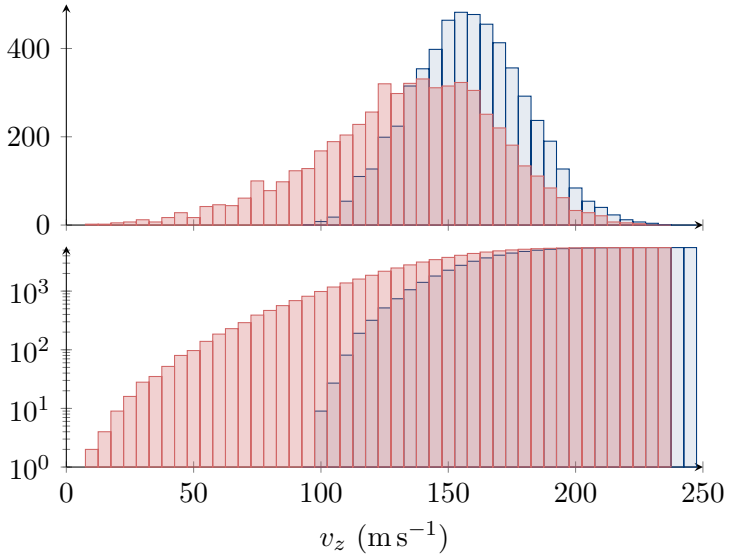

FIGURE 3.21: The initial (blue) and final (red) v_z distributions (top) and cumulative distributions (bottom) for a simulation of 5527 CaF molecules. The initial molecular distribution had 10^6 molecules with $\Delta z = 0$, $v_{\text{out}} = 145\,\text{m s}^{-1}$, and $\Delta v_z = \Delta v_\perp = 24\,\text{m s}^{-1}$. They were uniformly distributed in the transverse plane with $x, y \in [-2.5, 2.5]$ mm, and the transverse velocity distribution was truncated at $\pm 7\,\text{m s}^{-1}$ to avoid wasting computing time. The laser powers were 75 mW and they had detunings $\Delta_{\text{w2s}} = -14\,\text{GHz}$ and $\Delta_{\text{s2w}} = 2\,\text{GHz}$. 2.5% of accepted molecules have a final velocity below $50\,\text{m s}^{-1}$ and 0.07% have a final velocity below $12.5\,\text{m s}^{-1}$.

smaller than the theoretical value of 1.6×10^{-23} J, as expected for a spin flip probability less than unity. 4.3% of accepted molecules have a final velocity below $50\,\mathrm{m\,s^{-1}}$ and 0.08% have a final velocity below $12.5\,\mathrm{m\,s^{-1}}$.

Next, 10^6 molecules were simulated with a more realistic Gaussian transverse velocity distribution with $\Delta v_\perp = 24\,\mathrm{m\,s^{-1}}$. Since the phase space acceptance in velocity was $< 7\,\mathrm{m\,s^{-1}}$, the transverse velocity distribution was truncated at $\pm 7\,\mathrm{m\,s^{-1}}$ to avoid wasting computing time. These results are shown in Figure 3.21. 5527 molecules were accepted by the decelerator. The loss was due to both the initial positions of the molecules and also to the initial transverse velocity. 2.5% of accepted molecules have a final velocity below $50\,\mathrm{m\,s^{-1}}$ and 0.07% have a final velocity below $12.5\,\mathrm{m\,s^{-1}}$.

Both the length of the decelerator and the initial mean forward velocity, v_{out}, affect the number of slow molecules. In order to investigate this, simulations were carried out with varying decelerator length, $\mathcal{L}$, and v_{out}:

$$v_{\mathrm{out}} \in \{110, 120, \cdots, 220\}\,\mathrm{m\,s^{-1}},$$
$$\mathcal{L} \in \{0.8, 1.08, \cdots, 3.6\}\,\mathrm{m}.$$

For a molecule which is within the phase space acceptance of the guiding fields (see Section 3.5), and is always in the correct state to be guided, neither the length nor the forward velocity should affect the acceptance. However, it was found in the trajectory simulations that the acceptance of the decelerator does decrease with increasing decelerator length and does increase with v_{out}. This can be seen in Figure 3.22.

Figure 3.22 also shows the acceptance of a cylinder in free space with no guiding fields, as in Eqn. (3.18). It can be seen that the acceptance of the decelerator does exceed the acceptance of a cylinder in free space, meaning that the guiding is working. However, as already established, the spin-flip probability is not 100%. Therefore, there will be molecules which do not get pumped by the s2w laser and so will be in SFS states whilst passing through the weak field region.

As shown in Eqn. (3.12), molecules in SFS states passing through the weak field region will be anti-guided. A molecule with $v_z = 145\,\mathrm{m\,s^{-1}}$ and $v_\perp = 4\,\mathrm{m\,s^{-1}}$ only

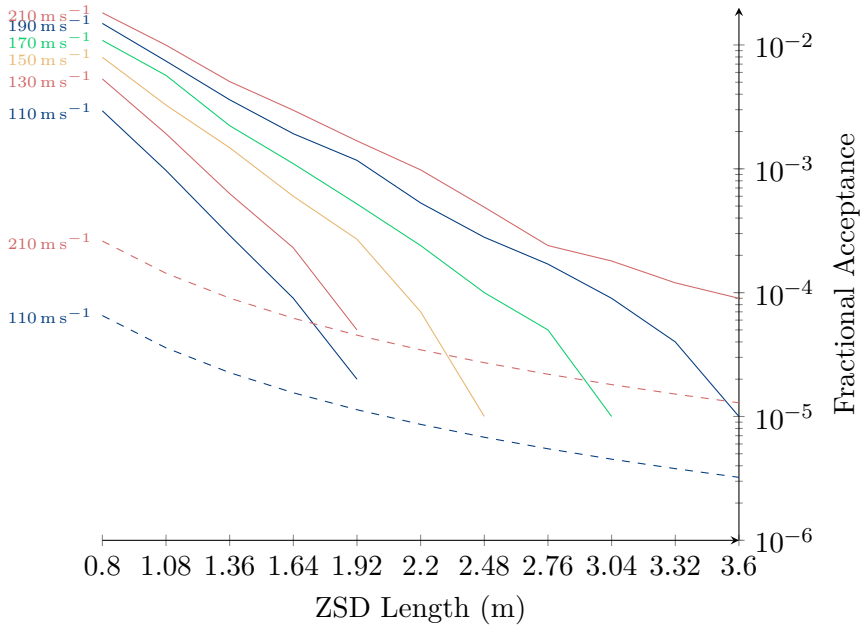

FIGURE 3.22: Fraction of molecules, out of a total of 10^5 simulated, which were accepted by the decelerator. Lines are labelled with v_{out}. The initial molecular distribution is as in Figure 3.21. The dashed lines show the acceptance of a cylindrical tube in free space (i.e., with no guiding). The increased acceptance of the ZSD is due to the effect of the guiding.

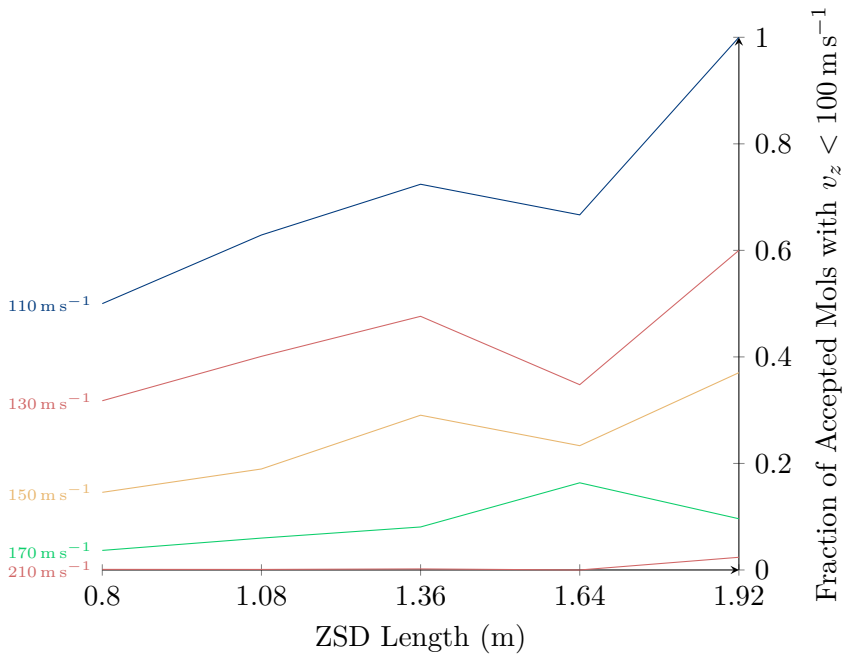

FIGURE 3.23: Fraction of accepted molecules which have a final velocity below $100\,\text{m s}^{-1}$ for beams with various v_{out}. The initial molecular distribution is as in Figure 3.21 with 10^5 molecules.

needs to pass through 3 half-cycles before it hits the wall. As the decelerator length increases, the chance of a molecule passing through this distance in the wrong state increases, leading to reduced acceptance. The effect can be avoided by increasing the SFP by, for example, increasing the laser power.

Of the molecules which are accepted, the proportion of molecules below $100\,\mathrm{m\,s^{-1}}$ increases with decelerator length, as expected. This can be seen in Figure 3.23. Therefore, if the SFP is sufficiently high to ensure molecules are consistently guided and not anti-guided, the ZSD does increase the proportion of molecules which can be accepted by a MOT.

3.8 Outlook

Zeeman-Sisyphus deceleration (ZSD) was introduced as a slowing technique with the potential to slow molecules with fewer photons scattered than direct laser slowing, whilst also providing transverse confinement. In this chapter we examined a ZSD scheme for CaF molecules and its experimental implementation, first introduced in [1].

It was established through trajectory simulations that the decelerator proposed will guide molecules that are in WFS states, and the phase space acceptance for this guiding was established. The dropoff in the percentage of molecules accepted as the gap between the molecular source and the decelerator entrance increases is significant. This impacts the design of any molecular beam experiment for testing the decelerator.

In order for the deceleration to work in a ZSD scheme, the molecules must be reliably optically pumped from WFS states to SFS states, and vice versa. Further trajectory simulations established the spin flip probabilities (SFPs) in the decelerator and it was found that the SFP for four CaF ground states is substantially lower than the others. This impacts the overall number of successful spin flips, reducing the overall deceleration effect, as was established in further trajectory simulations. Failure of a molecule to spin flip also impacts the acceptance, as molecules which remain in SFS states through the field minima of the decelerator are anti-guided.

Nonetheless, the ZSD scheme is predicted to increase the fraction of accepted molecules which are slow and ensure these molecules are transversely confined. At the exit of the decelerator, all accepted molecules are within the capture area of a

MOT. Thus, the number of molecules within the phase space acceptance of a MOT is increased. Next, an experiment was set up to test the decelerator. The experimental setup is described in Chapter 4 and characterisation of the molecular beam produced is given in Chapter 5. Attempts to test the decelerator are then described in Chapter 6.

Chapter 4

Experimental Setup

A CaF molecular beam experiment was set up to test the ZSD scheme simulated in Chapter 3 using the ZS decelerator described in Section 3.3. The apparatus, together with the calibration of various experimental parameters, is described in this chapter.

4.1 Overall Layout of the Experiment

A typical molecular beam experiment consists of a long vacuum chamber with a molecular source at one end. The source produces a beam of molecules which proceeds along the length of the chamber. Various equipment is then set up along the chamber to interact with the molecules. A CAD drawing of the experimental setup and vacuum chamber is shown in Figure 4.1. Sections S_1, S_2, and S_3 have DN250LF ISO flanges, and sections A, B, and C have DN160CF ConFlat flanges. CaF molecules are produced in a 'buffer gas cell' located in S_3. The molecules are produced by ablating a calcium rod in a mixed atmosphere of SF_6 and inert noble gas (helium or neon). This process is described further in Chapter 5. Inlets for helium or neon buffer gas and SF_6 were located on section S_1, together with an electrical feedthrough carrying signals from the temperature monitoring and heaters. Further information on the molecular source is given in Section 4.3.

The coordinate system used throughout this thesis is shown in Figure 4.2. The z-axis is the longitudinal axis of the vacuum chamber. In addition, spherical coordinates with origin at the source, S, located in chamber S_3, and cylindrical coordinates with origin at a detection point D are shown. These are the natural coordinates for describing the molecular beam and the detection light respectively. If cylindrical coordinates centred at S are needed, then $\rho_\perp^2 = x^2 + y^2$ is used as the radial coordinate.

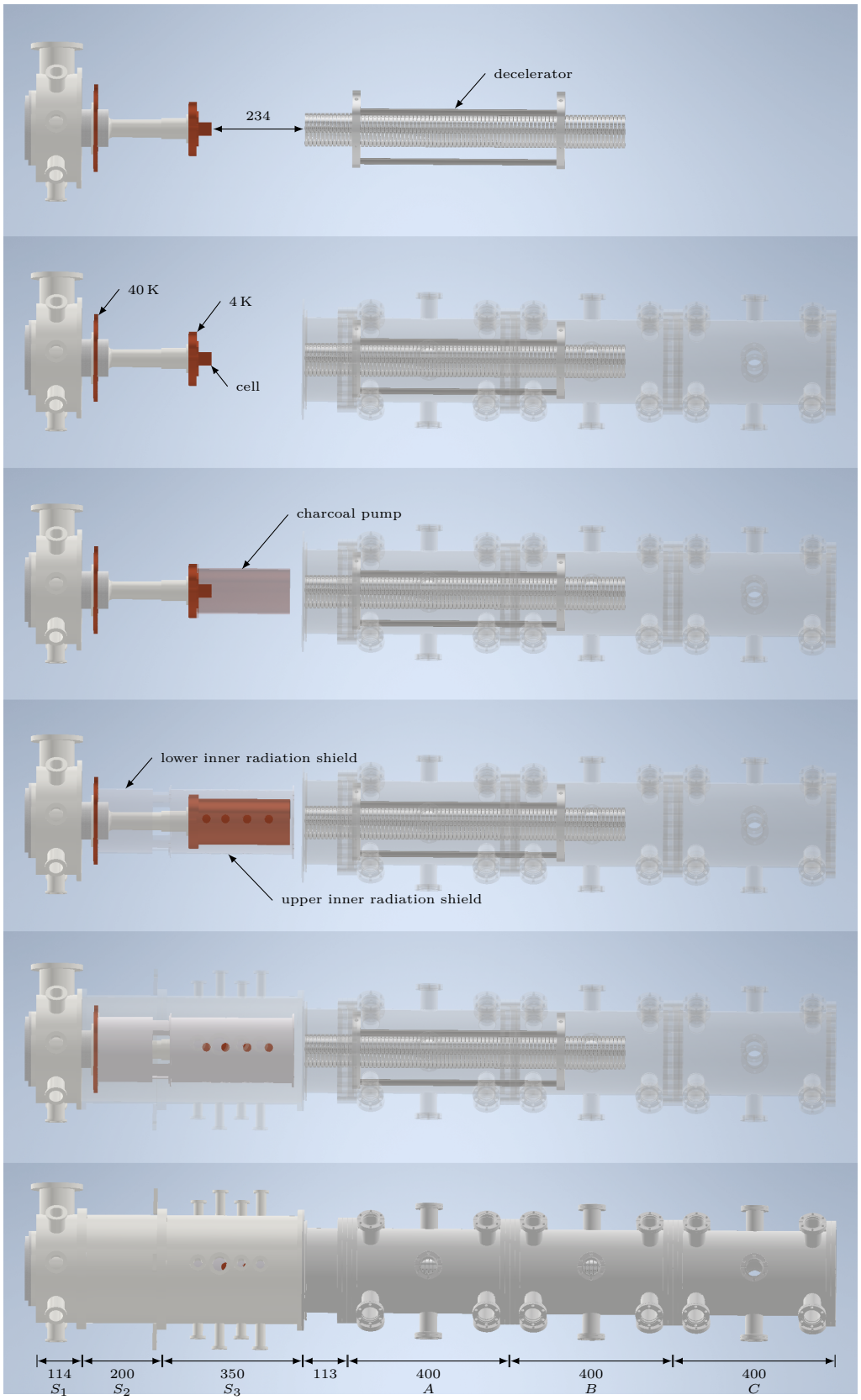

FIGURE 4.1: (mm; to scale; y-z plane) CAD drawings of the experiment showing the various components including the outer vacuum chamber. The sections making up the source portion of the chamber are labelled S_1, S_2, and S_3, while the beamline sections are labelled A, B, and C. The beamline sections can be individually removed in order to alter the length of the chamber.

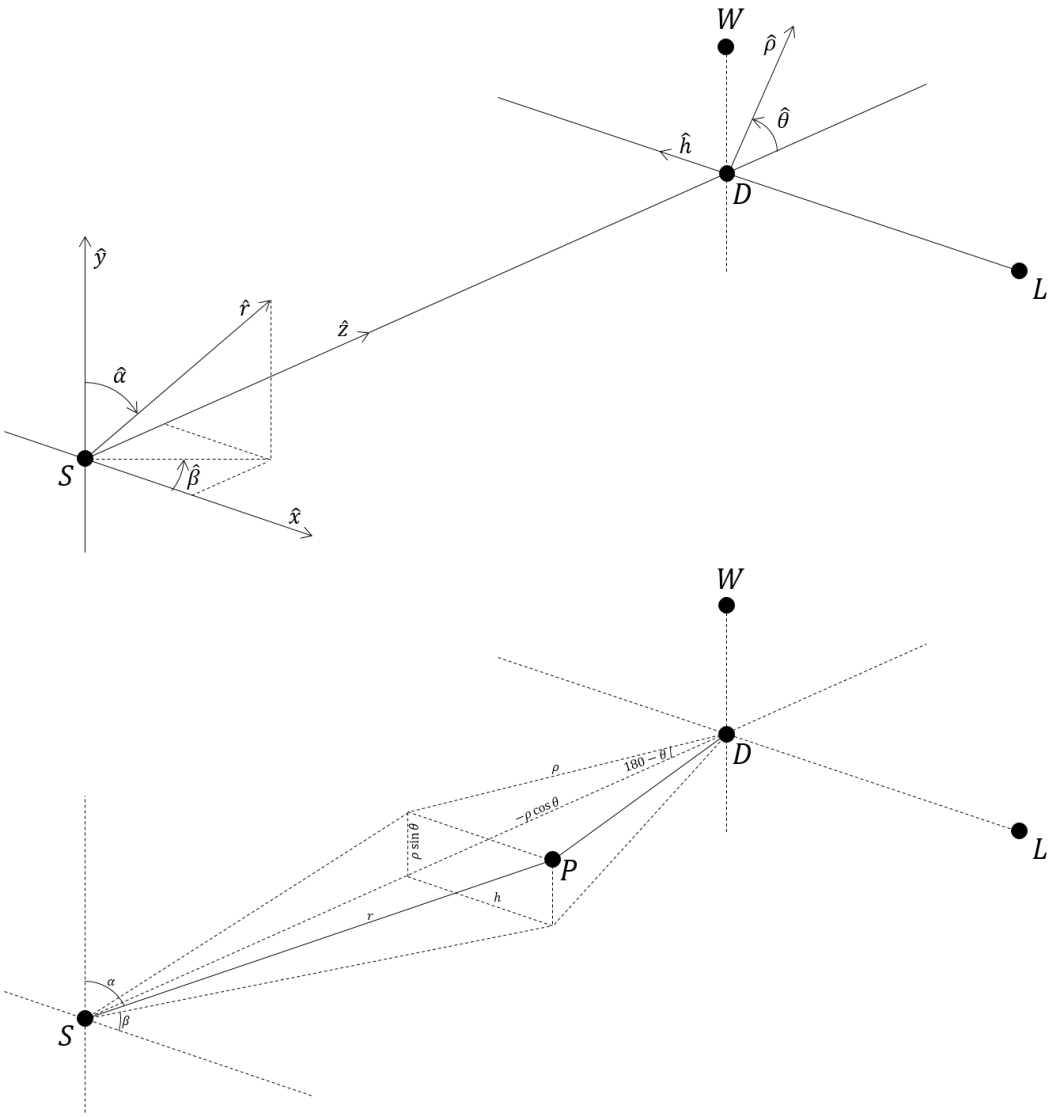

FIGURE 4.2: (top) A diagram showing the two coordinate systems, with the cell outlet, S, detection point, D, detection laser entry, L, and PMT, W, labelled. (bottom) Conversion between the two systems for an arbitrary point, P. Note that this depends on the distance, l, between S and D; e.g., $r^2 = \rho^2 + h^2 + l^2 + 2l\rho\cos\theta$.

Further information on the detection setup is given in Section 4.4. Photographs of the experimental setup can be seen in Figure 4.4.

A Sumitomo F-50 two-stage cryostat was attached to the end of S_1, with the first 40 K stage being located inside S_2 and the second 4 K stage inside S_3. When switched on the cryostat cooled down the two stages to their respective temperatures over the course of six hours. There were two low temperature diode sensors attached to each of the cold stages and a room temperature thermistor attached to the SF_6 line. The temperature readouts during cooldown from room temperature can be seen in Figure 4.3.

SF_6 freezes at around −50 °C. The SF_6 gas line enters the 4 K buffer gas cell through a cut-out. A 3D printed nylon sleeve was used to prevent the SF_6 gas line from coming into contact with the cell and falling below −50 °C. It can be seen in Figure 4.3 that the sleeve does insulate the SF_6 line, but not enough to prevent it from becoming too cold. Therefore, a 220 Ω, 7 W heater was attached to the SF_6 line to prevent it from freezing.

In addition, two 25 W heaters were used to bring the cold stages up to room temperature once the cryostat had been switched off: a 22 Ω heater attached to the 4 K stage and a 5 Ω heater attached to the 40 K stage.

4.1.1 Computer Control

Interface between the physical hardware and the experimental control computer was made via two National Instruments PXI[1] modules and an NI USB-6009 DAQ module. The PXI-6229 Multifunction I/O Module was used to feed in the outputs from the photomultiplier tubes and also to provide an analogue output voltage for controlling a scan parameter (e.g., to be used to control laser frequency). The PXIe-6535 Digital I/O Module was used to output the digital pattern for triggering the ablation laser and starting the data acquisition process. Finally, the USB-6009 DAQ was used to feed temperature and pressure data into the computer and its digital outputs were used to control the cryostat and the heaters.

On the software side, two existing C# applications developed by the group were used. The first was used for monitoring temperature and pressure and controlling

[1] PCI eXtensions for Instrumentation.

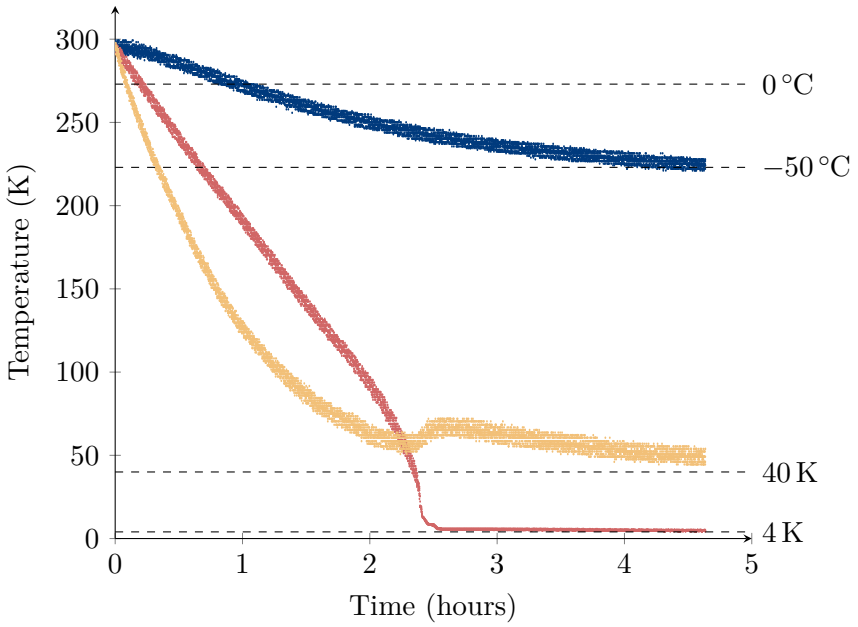

FIGURE 4.3: Chart showing the temperature of the 40 K stage (yellow), the buffer gas cell (red), and the SF_6 line (blue) as the cyrostat cools down from room temperature. As can be seen, even after 4.5 hours the temperature has still not reached a steady state. It can also be seen that even with the insulating sleeve on the SF_6 line, the temperature falls below the lower acceptable limit of −50 °C. Therefore, it is necessary to add an active heater to ensure the line remains above the boiling point of SF_6.

heaters and the cryostat, interfacing with the USB DAQ. The second was for running the experiment, including triggering the ablation laser, varying the scan parameter, and collecting the output from the PMTs. This second application interfaced with the two PXI modules.

4.2 Vacuum Pumps and Gas Flow

The vacuum system consisted of two Oerlikon TMP 361 turbomolecular pumps, which were attached to sections S_1 and B respectively. The pumps were connected to a Leybold Turbovac 90i turbomolecular pump and this was, in turn, connected to a scroll pump. The 90i pump provided a better helium compression ratio than the TMP 361 pumps, which were better for air. The TMP 361 pumps have a helium compression ratio of 6×10^4 whereas the 90i pump has a helium compression ratio of 1×10^9. Two Leybold Ionivac ITR 90 hot cathode ionisation gauges were used to monitor the pressure inside the chamber, with one attached to S_3 and one to C.

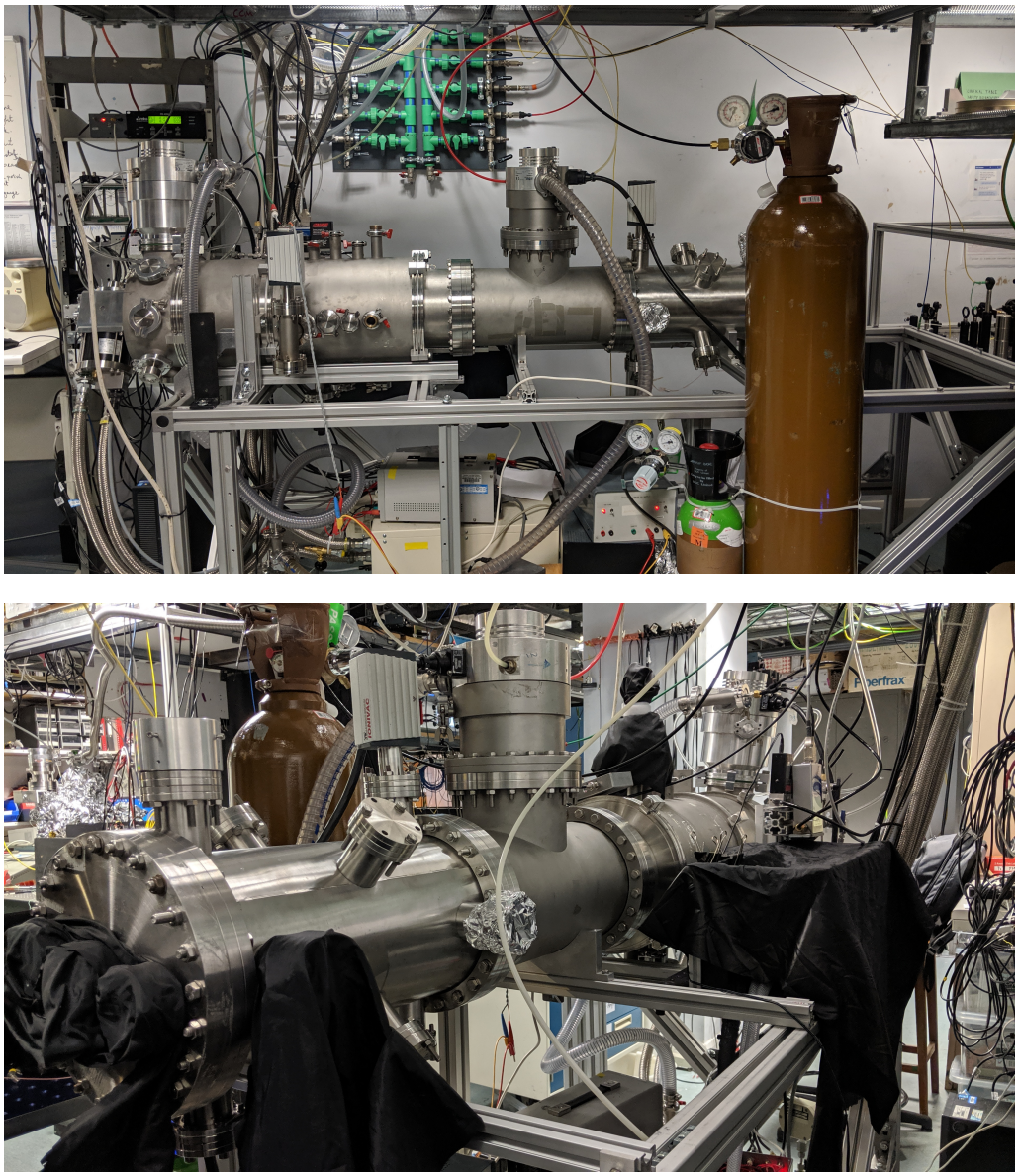

FIGURE 4.4: Photographs of the experimental setup in the lab. Photos are labelled with reference to Figure 4.1. The vacuum chamber is in the 'short' configuration, with section A removed.

The vacuum system achieved typical pressures of 5×10^{-7} mbar when pumping on air alone.

Despite the improved compression ratio of the 90i, the pumping speed of the turbo pumps was still not high enough to cope with the gas load needed to produce a CaF beam. With a helium buffer gas, a flow rate of 0.5 sccm is typical[2]. This corresponds to 84 400 l s^{-1} at 1×10^{-7} mbar. The two TMP 361s had a nominal helium pumping speed of 340 l s^{-1} only. To increase the total helium pumping speed an adsorptive charcoal pump was used. This is typical for cryogenic buffer gas sources.

The charcoal pump uses coconut charcoal adhered to the inside surface of a copper cylinder using Stycast 1266 cryogenic epoxy. When cooled to 4 K, the helium is adsorbed onto the surface of the charoal, trapping it and removing it from the vacuum chamber. Photographs of the charcoal pump are shown in Figure 4.5. Prior to being applied, the charcoal is stored in an unsealed box at room temperature. This means that many of the adsorption sites in the charcoal are likely to be occupied by water from the air. To clear the charcoal and maximise the pumping speed and helium capacity the charcoal was baked prior to installation. The pumping speed of the vacuum system without the charcoal and with both baked and unbaked charcoal was measured and the results are given in Section 4.2.1.

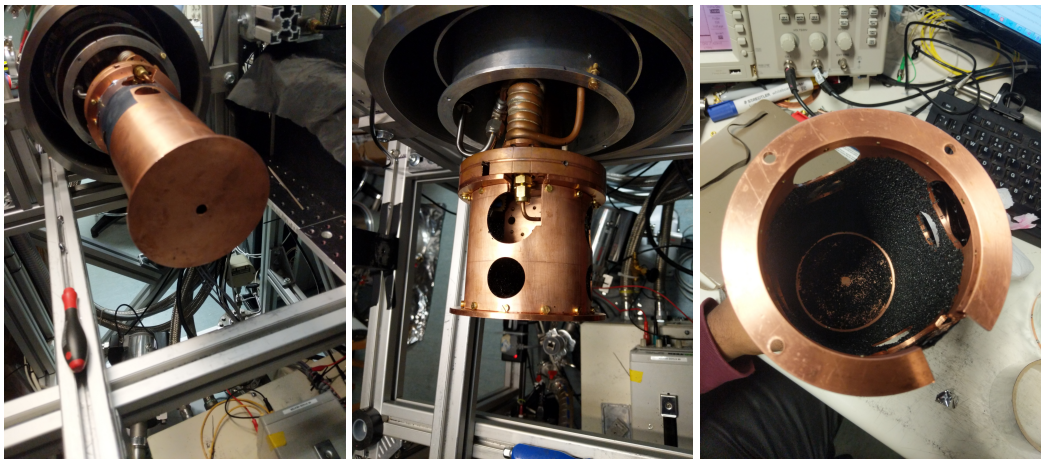

FIGURE 4.5: (left) The long 250 mm charcoal pump shown mounted in position on the 4 K cold stage. (middle) The short 120 mm charcoal pump. (right) The inside of the long pump showing the charcoal coating.

[2]sccm is 'standard cubic centimetres per minute'. This is the volumetric flow rate at standard temperature and pressure.

4.2.1 Measuring Pumping Speed

Vacuum pumps have an effective pumping speed, $\dot{V}_{\text{out}}$, usually given in litres per second, $\mathrm{l\,s^{-1}}$. The gas load, Q_{pV}, is a measure of the rate at which gas-phase molecules enter a given chamber. Gas load is usually given in units of $\mathrm{mbar\,l\,s^{-1}}$. The pressure in the chamber can be found from the ratio of gas load to pumping speed:

$$P = \frac{Q_{pV}}{\dot{V}_{\text{out}}}. \tag{4.1}$$

Turbo pumps have a maximum gas load (also called the maximum gas throughput). If the gas load of the chamber is more than the maximum gas load of the pump, the pumping speed will be reduced. Otherwise, the turbo pump will operate at its rated pumping speed. In a chamber with multiple pumps the total effective pumping speed can be found by adding the pumping speeds of pumps operating in parallel, and adding the reciprocals of the pumping speeds of pumps operating in series.

We model the CaF experiment as consisting of two pumps. The first pump, with pumping speed $\dot{V}_{\text{char}}$, is the adsorptive charcoal pump. The second, with pumping speed $\dot{V}_{\text{turb}}$, represents the overall effect of the three turbos and scroll pump. As both pumps operate on the same chamber at the same time, they can be considered to operate in parallel. Therefore, the total effective pumping speed of all pumps on the chamber is:

$$\dot{V}_{\text{out}} = \dot{V}_{\text{char}} + \dot{V}_{\text{turb}}. \tag{4.2}$$

To determine $\dot{V}_{\text{char}}$ and $\dot{V}_{\text{turb}}$, the chamber pressure, P, was measured at various helium flow rates, $\dot{V}_{\text{in}}^{\ominus}$. These data are shown in Figure 4.6. Data was taken for a vacuum chamber at room temperature where only the turbos and scroll pumps were operating (yellow), a cold chamber before the adsorptive charcoal pump had been baked (red), and a cold chamber after the charcoal pump had been baked (blue). The long charcoal pump with the lid, as shown in Figure 4.5, was used.

The gas load is related to flow rate at standard temperature and pressure by:

$$Q_{pV} = P^{\ominus} \times \dot{V}_{\text{in}}^{\ominus}, \tag{4.3}$$

where $P^{\ominus} = 1.01\,\text{bar}$ is standard pressure. From Eqn. (4.1) it can be seen that the total pumping speed is $\dot{V}_{\text{out}} = Q_{pV}/P$. Therefore, the pumping speed is the inverse of the gradient of the best fit line for the data in Figure 4.6. These best fit lines are:

$$\text{Warm (yellow)} \qquad P = (7.4 \pm 0.1) \times 10^{-4} Q_{pV} + (1.6 \pm 0.4) \times 10^{-6} \tag{4.4}$$

$$\text{Cold Unbaked (red)} \qquad P = (1.80 \pm 0.09) \times 10^{-4} Q_{pV} + (2 \pm 4) \times 10^{-7} \tag{4.5}$$

$$\text{Cold Baked (blue)} \qquad P = (8.2 \pm 0.4) \times 10^{-5} Q_{pV} + (5 \pm 2) \times 10^{-7} \tag{4.6}$$

At room temperature, $\dot{V}_{\text{char}} = 0$. Therefore, the data taken at room temperature (yellow) directly gives $\dot{V}_{\text{turb}}$:

$$\dot{V}_{\text{turb}} = (1350 \pm 20)\,\text{l}\,\text{s}^{-1}. \tag{4.7}$$

The value of $\dot{V}_{\text{char}}$ for both baked and unbaked charcoal pumps can then be found using Eqn. (4.2):

$$\dot{V}_{\text{char}}(\text{unbaked}) = (4200 \pm 300)\,\text{l}\,\text{s}^{-1} \tag{4.8}$$

$$\dot{V}_{\text{char}}(\text{baked}) = (10\,800 \pm 600)\,\text{l}\,\text{s}^{-1} \tag{4.9}$$

From this, it can be seen that the charcoal was much more effective at pumping helium in general, and it was over twice as effective when it had been baked.

4.3 The Molecular Source

The first step in many molecular science experiments is the production of a directed beam of the molecules in question [72–74]. However, typical molecular production

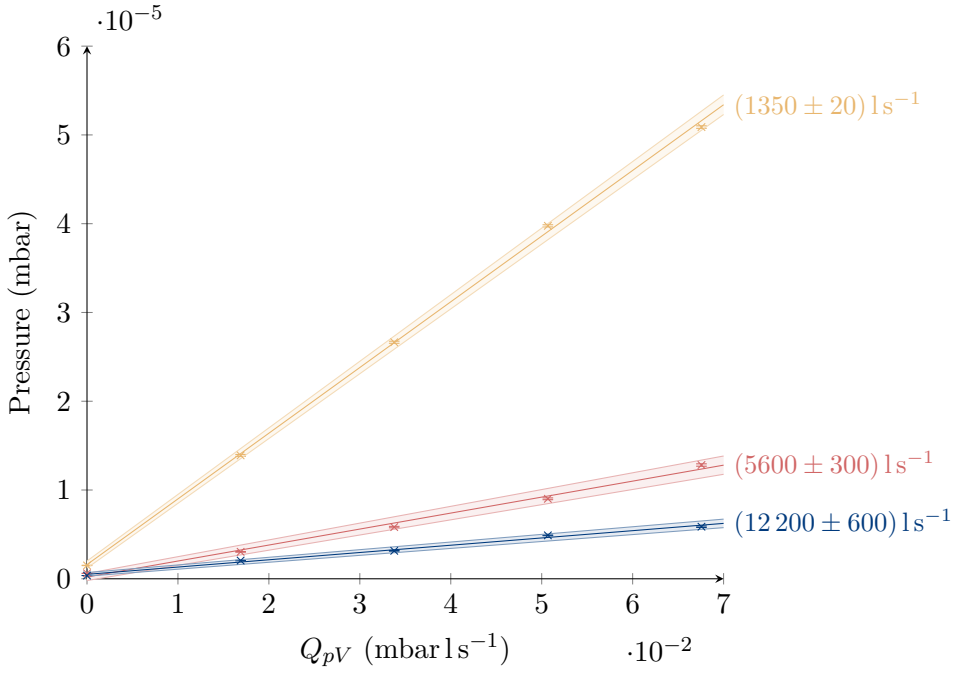

FIGURE 4.6: Chamber pressure varying with helium gas load, Q_{pV}. The chart shows data for a warm chamber (i.e., with no effective adsorptive charcoal pump) in yellow, data for a cold chamber where the adsorptive charcoal pump has not been baked in red, and data for a cold chamber where the adsorptive charcoal pump has been baked in blue. The inverse of the gradients of the best fit lines give the total effective pumping speed of the system.

methods do not naturally produce a directed beam of molecules. Supersonic expansion under vacuum is a common techinique for the production of a relatively cold beam from a pool of warm molecules. However, the resultant beam moves at a velocity exceeding the mean room temperature speed. Instead, cryogenic buffer gas sources can be a superior way to produce a relatively cold, slow-moving beam of molecules.

A buffer gas source operates under vacuum and involves the production of molecules inside a 'buffer gas cell'. The cell is a cube containing a cavity into which the molecules are introduced before thermalising with the buffer gas. The molecules of interest can be loaded into the buffer gas cell in a number of ways, including injection through a capillary, directly from a gas line, or laser ablation of an *in situ* target [75]. Great success has been had in using laser ablation to produce CaF in a buffer gas cell [12–17] and so we continued to use this method.

In this experiment, the calcium target was ablated by a 1064 nm Nd:YAG laser. The ablation occurred in an atmosphere of SF_6 and helium or neon (the 'buffer gas'), cooled to low temperatures. In the case of a helium buffer gas, the cell temperature

was around 4 K. In the case of neon, it was around 11 K. The cell was cooled by attaching it to the 4 K stage of the cryostat, with insulating spacers if necessary. A schematic of the cell is shown in Figure 4.7 and photographs are shown in Figure 4.8.

To ensure that the setup — both the cell and charcoal pump — was not radiatively heated by the outer walls of the vacuum chamber, it was surrounded by radiation shields. An aluminium radiation shield was mounted to the 40 K stage and extended out to cover both the cell and the charcoal pump. The entire setup was contained within sections S_2 and S_3 and a schematic is shown in Figure 4.9.

The setup shown in Figure 4.7 is indicative of the buffer gas cell used in our laboratory setup, with the buffer gas entering through gas inlet 1 and SF_6 entering through gas inlet 2. The Nd:YAG laser produced a calcium plasma containing a mixture of elemental calcium as well as various ions. The calcium then reacted with the SF_6 to produce a variety of compounds, including CaF (the molecule of interest). The reaction producing CaF is:

$$\mathrm{Ca} + \mathrm{SF_6} \longrightarrow \mathrm{CaF} + \mathrm{SF_5}. \tag{4.10}$$

The CaF molecules were carried out of the cell by the buffer gas in accordance with the convection-diffusion equation [76]. Details on the theory of the production and

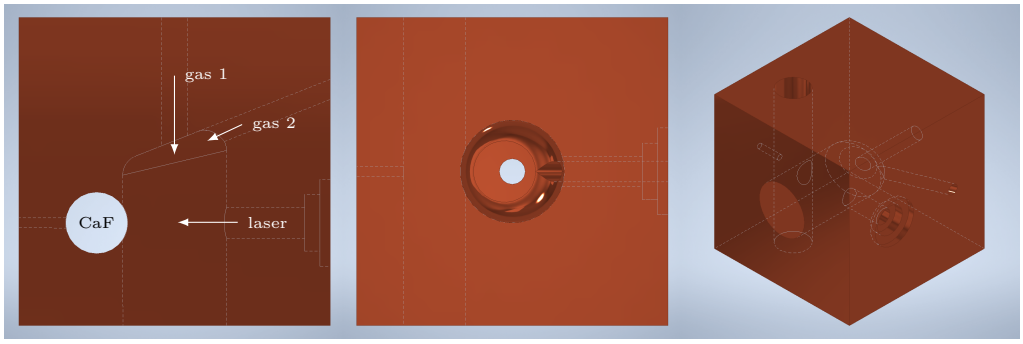

FIGURE 4.7: (to scale) CAD drawings of a buffer gas cell. Left to right: top, front, perspective. The laser enters from the right and ablates calcium on the left (black). The calcium plasma reacts with the SF_6 entering through one of the two gas inlets and thermalises with the buffer gas entering from the other gas inlet. The inlet carrying SF_6 must be specially insulated to ensure the SF_6 does not freeze before entering the cell, whilst the inlet carrying the buffer gas must be thermally connected to the cell to ensure the gas and cell are at the same temperature.

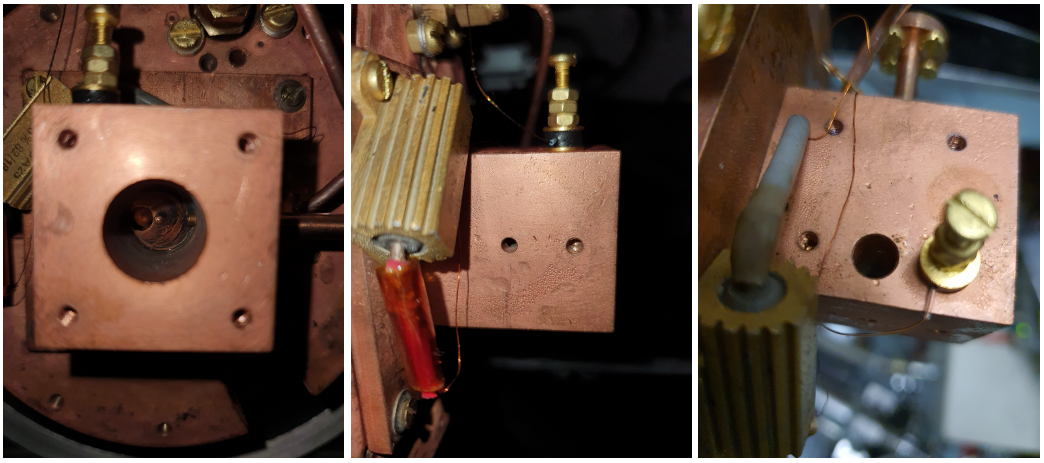

FIGURE 4.8: Photographs of the buffer gas cell showing the 22 Ω heater, diode temperature sensor, and snorkel for the Nd:YAG entry. Also shown is the slot for the calcium target and the Nd:YAG exit aperature which was used to align the laser.

extraction of CaF from the buffer gas cell, together with experimental results, are given in Chapter 5. The molecules exiting the cell were detected by laser-induced fluorescence which was captured by a PMT.

The ablation laser was a pulsed, Q-switched Quantel Big Sky Nd:YAG laser. It included both a flashlamp and a Q-switch. The delay between the operation of the flashlamp and the Q-switch, known as the flash-to-Q or F2Q, affects the output power of the laser. To characterise the laser, measurements were taken at various F2Qs on both a low-power Thorlabs power meter (with an ND filter) capable of resolving individual pulses. The measured laser pulses had a constant FWHM of 10 ns at all F2Qs. The laser power was then measured with a high-power laser power meter which measured the average power at a 2 Hz repetion rate. The results are shown in Figure 4.10.

4.4 Lasers and Detection

There were two detection points in the experiment. A schematic of them is shown in Figure 4.11. The molecular beam was produced at the exit of the cell, S, and proceeded along the z-axis. At the points D and D', which are on the z-axis, lasers in the x-z plane intersected the molecular beam. Under usual conditions, the laser's k-vector was anti-parallel to the x-axis (which we shall label $\hat{h} = -\hat{x}$), but this was

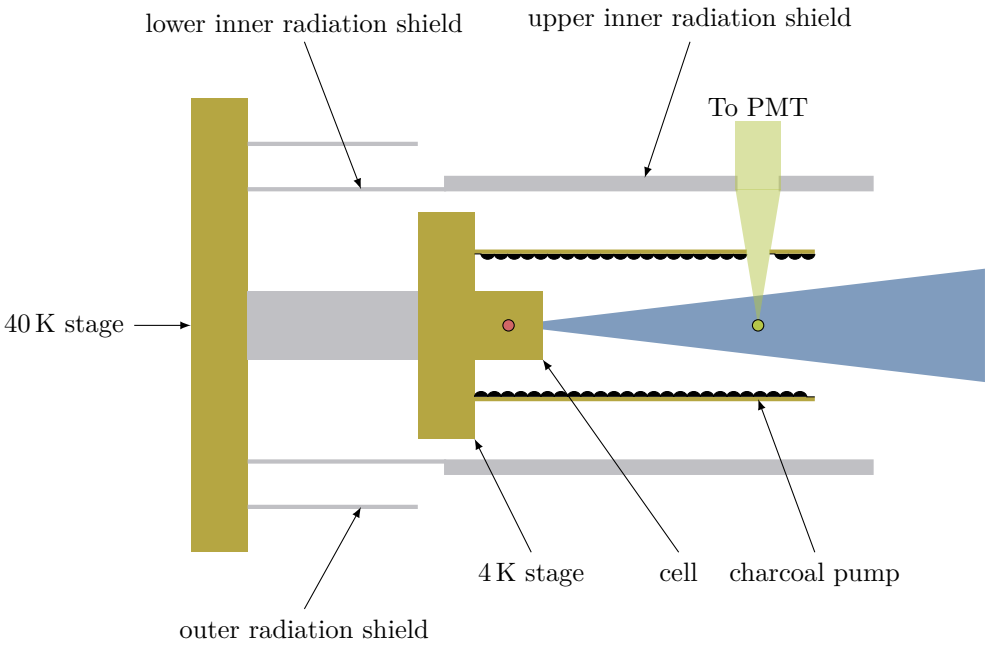

FIGURE 4.9: (not to scale; y-z plane) A schematic of the CaF source section of the chamber, showing the copper cryostat stages, cell, charcoal pump, and the aluminium radiation shields. The molecular beam is shown in blue, the 1064 nm Nd:YAG ablation laser in red, and the detection laser with the emitted fluorescence in green.

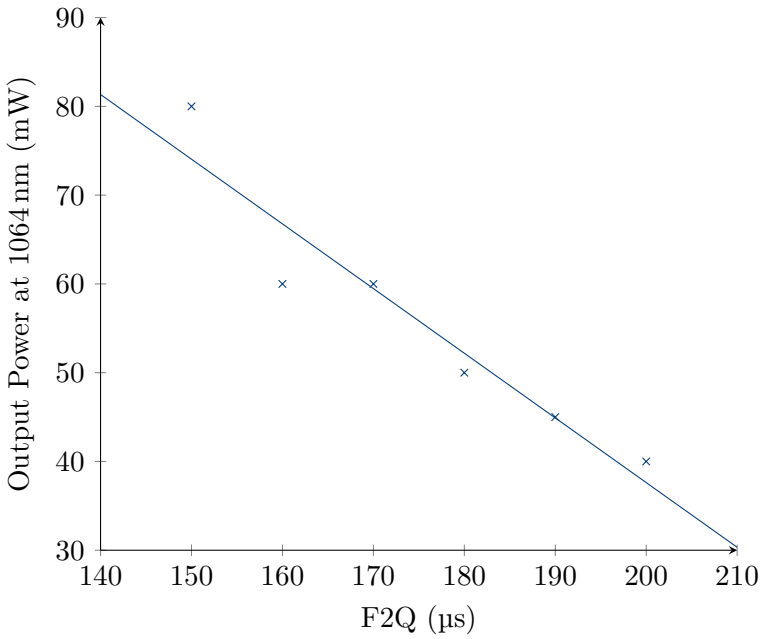

FIGURE 4.10: The time-averaged power of the Nd:YAG laser operating at a 2 Hz repetion rate. The power is shown varying with the flash lamp to Q-switch delay (flash-to-Q or F2Q). The pulse FWHM was measured to be a constant 10 ns. Therefore, the peak power is a factor of 5×10^7 higher than the average power shown here. The line of best fit given is $P = (180 \pm 20) - (0.7 \pm 0.1)\text{F2Q}$.

not the case when velocity measurements were being conducted. The laser was in the visible spectrum and was tuned to an electronic transition: either $A^2\Pi$–$X^2\Sigma$ at 606 nm or $B^2\Sigma$–$X^2\Sigma$ at 531 nm. The laser induced fluorescence which was uniformly distributed spherically[3]. This fluorescence was collected by the detection optics and directed to a PMT. Details of the PMT, including calibration at both 606 nm and 531 nm, are given in Section 4.4.3.

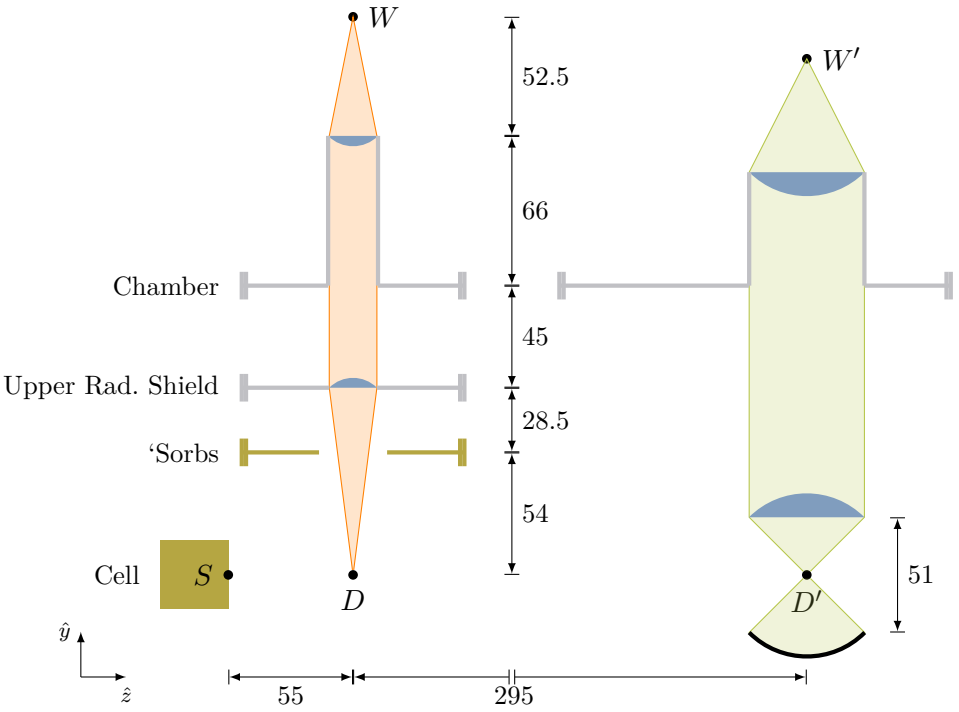

FIGURE 4.11: (mm; to scale; y-z plane) A schematic of the upstream (D) and downstream (D') CaF detection points. The upstream detector is inside the source portion of the experiment and the downstream detector is outside, beyond the charcoal pumps and radiation shields. The buffer gas cell outlet is located at S and the detection light intersects beam at D and D'. At the upstream detector, a 1 inch lens mounted to the radiation shield collimates the fluorescence and another 1 inch lens mounted to the vacuum chamber focusses it into the PMT (located at W), allowing spatial filtering by an iris. At the downstream detector a 2 inch lens and 2 inch mirror collect and collimate the fluorescence. It is focussed onto a PMT at W' by another 2 inch lens.

At the upstream detector, a portion of the fluorescence passed through a hole cut in the charcoal pump and up to a window on the upper radiation shield. At this point a 1 inch lens, whose focal length is approximately equal to its distance from D, collimated the fluorescence. The light then passed through a second window on the

[3]The distribution is dipolar per-molecule but the molecules are not spin-polarised so the overall distribution is spherically symmetric.

outer vacuum chamber before being focussed onto the surface of a PMT at W. The collection efficiency at D is given by the fraction of the sphere occupied by the cone subtended by the lens at D:

$$\eta_{\text{geo}} = \frac{1}{2}\left(1 - \sqrt{1 - \frac{r_{\text{lens}}^2}{r_{\text{lens}}^2 + l^2}}\right), \tag{4.11}$$

where r_{lens} is the radius of the lens and l is the distance from D to the lens. A complete derivation of the above for any arbitrary point inside the experiment is given in Section 5.2.1. For the upstream detector, $\eta_{\text{geo}} = 0.006$.

At the downstream detector, a 51 mm (2 inch) lens and mirror were mounted to a 51 mm lens cube such that the z-axis passed through the centre. The cube was mounted to a linear feedthrough whose vertical (y) position could be adjusted to ensure correct positioning. The upward going fluorescence was collimated by the lens and the downward going fluorescence was retro-reflected by the mirror before being collimated. The light was then focussed onto the surface of a PMT at W'. The retro-reflecting mirror doubled the geometric efficiency of the detector compared with Eqn. (4.11), giving $\eta_{\text{geo}} = 0.3$.

4.4.1 531 nm Detection Light

A frequency-doubled laser used in the neighbouring CaF MOT experiment was used to provide 531 nm light. The setup was as described in [48]. The light was locked to the CaF $B^2\Sigma(N = 1)$–$X^2\Sigma(N = 1)$ transition. Switchable 24 MHz sidebands were added with an electro-optic modulator. These could be used to address all hyperfine components of the ground state (see Figure 2.2). These were switched on when looking for time-of-flight (TOF) signals but switched off when performing velocity and molecular flux measurements. A profile of the light imaged at the entrance to the vacuum chamber is shown in Figure 4.12. The $1/e^2$ width of the central peak is (2.13 ± 0.04) mm in the z direction and (3.49 ± 0.06) mm in the y direction.

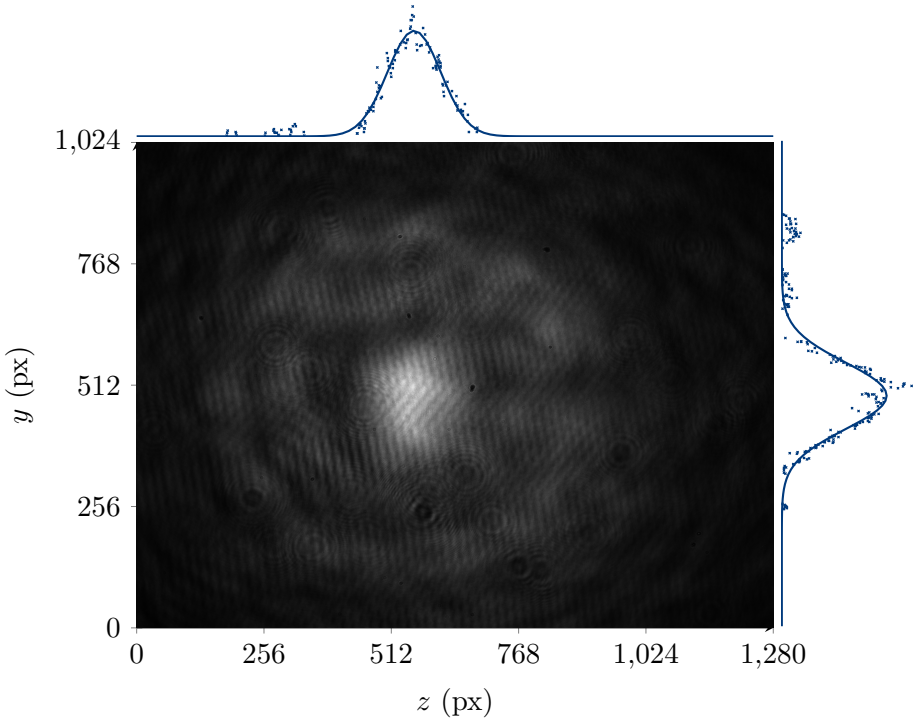

FIGURE 4.12: An image of the 531 nm detection light used, captured at the point it enters the vacuum chamber on a 1280×1024 px, 0.5 inch CCD. The $1/e^2$ width of the central peak is (2.13 ± 0.04) mm in the z direction and (3.49 ± 0.06) mm in the y direction.

4.4.2 Spectra 380 Dye Laser

The ZSD scheme requires the 606 nm pump lasers to be detuned from the transition on the order of several GHz. This requires the use of a highly tunable laser. Therefore, the principal laser light used in the experiment was a Spectra 380D ring cavity dye laser. The lasing medium of the laser was a jet of liquid Rhodamine 6G dye. The absorption and emission spectra of Rhodamine 6G are shown in Figure 4.14. It can be seen that the peak absorption is at 532 nm, and that the emission can range from 525 nm to 610 nm, thus providing the tunability. A Spectra Millenia doubled Nd:YAG laser was used to provide up to 8 W of continuous wave pump light at this wavelength. A photograph of the open cavity during lasing can be seen in Figure 4.13.

The frequency of the laser could be adjusted by changing the optical length of the laser cavity. This was adjusted by changing the angle of a birefringent crystal placed in the cavity. The mode spacing was 200 MHz. Fine adjustment of the frequency was possible using an external locking cavity which provided feedback to an etalon in the lasing cavity. The power output at a given frequency depended on the power

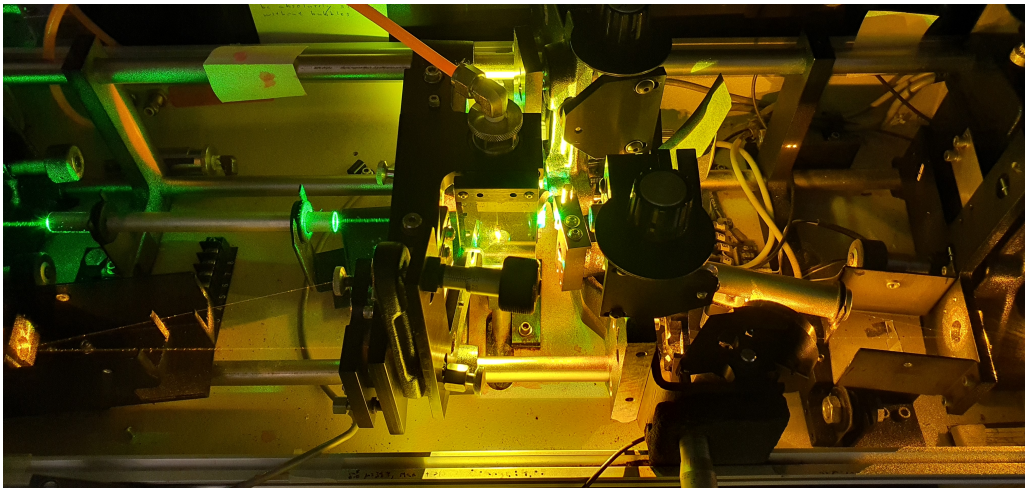

FIGURE 4.13: Photograph of the open laser cavity of the Spectra 380 dye laser.

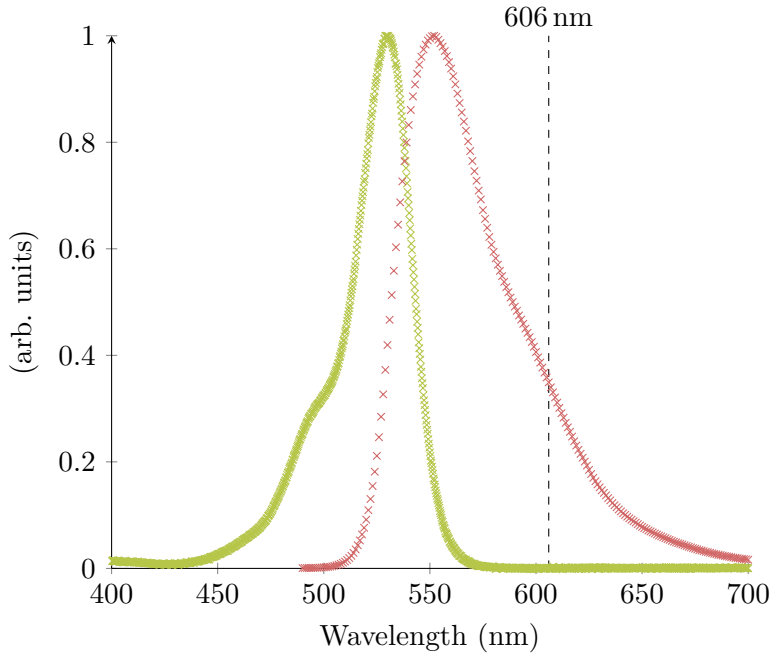

FIGURE 4.14: The absorption (green) and emission (red) spectra of Rhodamine 6G [77]. It can be seen that 606 nm is far from the peak of the emission spectrum, leading to relatively low output power.

of the pump laser and the emittance of the dye at that frequency. The calibration of pump power against output power at the peak of the emittance spectrum (553 nm) is shown in Figure 4.15. As can be seen in Figure 4.14, the emittance at 606 nm is 35% of the emittance at the peak. This lead to a reduction in output power so that, for example, at 8 W of pump power only 46 mW of 606 nm light was produced.

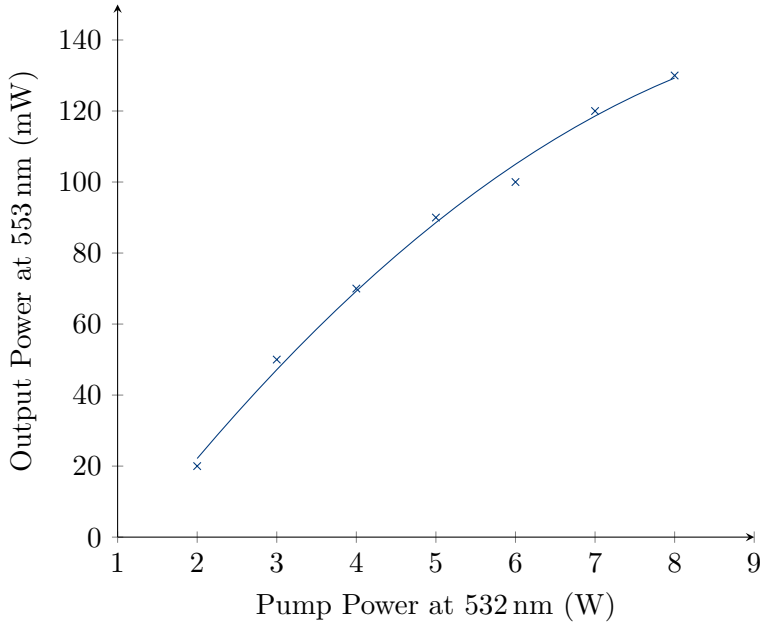

FIGURE 4.15: The output power at various pump laser powers of the Spectra 380 dye laser operating with Rhodamine 6G laser dye at the peak of the fluorescence curve (at 553 nm). It can be seen that the output power begins to saturate. The data is fitted with a quadratic best fit line, $P_{\text{out}} = -(0.036 \pm 0.008) + (0.032 \pm 0.004)P_{\text{pump}} - (0.0014 \pm 0.0004)P_{\text{pump}}^2$.

4.4.3 PMT Calibration

The PMT available for detection was a Hamamatsu R5070A with a Hamamatsu C13003-01 high-voltage power supply. The PMT outputs a time-varying current signal for each photon incident on the photocathode. In order for the PMT signal to be readable by the computer, the current signal must be converted into a voltage signal. This is achieved by feeding the current signal through an integrating transimpedence amplifier. The resulting voltage signal, Sig, is proportional to the photon count rate, Γ. We would like to know Γ in order to calculate the number of molecules passing through the detection light[4]. Therefore, we need to determine the relationship

[4]This calculation is explored in more detail in Chapter 5.

between Sig and Γ by calibrating the PMT.

The calibration was done by exposing the PMT to the detection laser under experimental conditions (i.e., *in situ* and under vacuum). The output of the PMT was switched between direct to an oscilloscope, on which individual photon detection events could be seen and counted to determine Γ, and the transimpedence amplifier to measure Sig.

Both count rate and voltage were measured as the laser power was varied. Each data point then associated a certain voltage with a certain count rate (the laser power itself being irrelevant). The data and best fit lines for both a 532 nm and a 606 nm laser are given in Figure 4.16. The final Γ–Sig calibrations are:

$$\frac{\Gamma_{532}}{\text{MHz}} = (0.11 \pm 0.03) + (4.75 \pm 0.08)\frac{\text{Sig}}{\text{V}}, \tag{4.12}$$

$$\frac{\Gamma_{606}}{\text{MHz}} = (0.07 \pm 0.03) + (5.1 \pm 0.1)\frac{\text{Sig}}{\text{V}}. \tag{4.13}$$

The number of photons incident on the photocathode, N_{ph}, can be found by first integrating the voltage signal from the PMT, Sig(t), and then rescaling according to the calibrations in Eqn. (4.12) or Eqn. (4.13).

4.5 Outlook

This chapter introduced and charactised the key aspects of the experimental setup designed for testing the CaF ZSD scheme described in Chapter 3. The next step, covered in Chapter 5, is characterising the molecular beam produced by the source described in this chapter. This is important as it will establish how the various experimental parameters affect the number of molecules in the beam and the beam velocity.

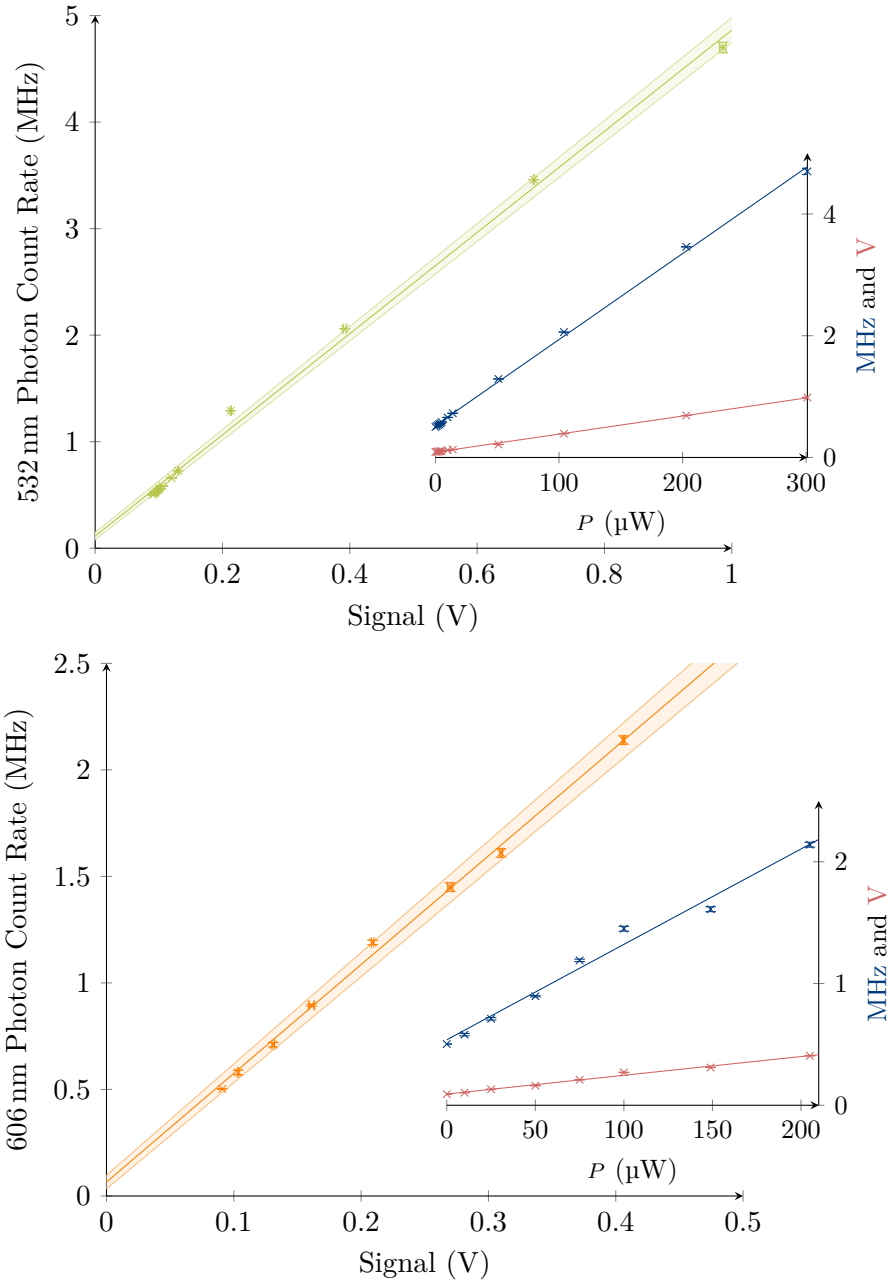

FIGURE 4.16: The calibration of the PMT used in the lab for laser light of wavelength 532 nm (top) corresponding to the CaF B–X transition and 606 nm (bottom) corresponding to the A–X transition. Inset is the raw data for count rate (blue) and voltage (red) taken at various laser powers.

Chapter 5

Beam Production in Theory & Practice

5.1 Theory of Beam Production

5.1.1 Gas Dynamics of the Buffer Gas and SF_6 in the Cell

The buffer gas cell can be treated as being held at a fixed temperature, T_{cold}, by the cryostat it is attached to. For a He buffer gas, $T_{\text{cold}} \approx 4\,\text{K}$, and for a Ne buffer gas it is somewhat higher, around 11 K. Additionally, the volume of the cavity inside the cell is a constant, V_{cell}. Hence, if the mixed gas in the cell is an ideal gas, only the total pressure, P_{cell}, or number density, n_{cell}, are required to fully describe the equilibrium conditions. The total pressure is the sum of the partial pressures contributed by the buffer gas and the SF_6, $P_{\text{cell}} = p_{\text{cell}}^{\text{Buff}} + p_{\text{cell}}^{\text{SF}_6}$ (this is Dalton's law).

For each species making up the mixed gas, with known number flow rates in and out of the cell, $\dot{N}_{\text{in}}$ and $\dot{N}_{\text{out}}$, given in molecules per second ($\text{mol}\,\text{s}^{-1}$)[1], the rate equation governing the partial pressure inside the cell is:

$$\frac{\mathrm{d}p_{\text{cell}}}{\mathrm{d}t} = \frac{\dot{N}_{\text{in}} - \dot{N}_{\text{out}}}{V_{\text{cell}}}\, k_{\text{B}} T_{\text{cold}}. \tag{5.1}$$

$\dot{N}_{\text{in}}$ can be determined from the known volumetric flow rate at standard temperature and pressure, $\dot{V}_{\text{in}}^{\ominus}$, as measured by the flow controllers: $\dot{N}_{\text{in}} = \frac{P^{\ominus}}{k_{\text{B}} T^{\ominus}} \dot{V}_{\text{in}}^{\ominus}$. $\dot{N}_{\text{out}}$ depends on both the partial pressure and the outflow velocity of the gas, v_{out} [76]:

[1] Throughtout this thesis mol is used to mean molecules, not moles.

$$\dot{N}_{\text{out}} = \frac{1}{4}\frac{p_{\text{cell}}}{k_{\text{B}}T_{\text{cold}}}\pi r_{\text{cell}}^2\, v_{\text{out}}, \tag{5.2}$$

where $r_{\text{cell}} = 2\,\text{mm}$ is the radius of the exit aperture from the cell. Since $\dot{N}_{\text{out}} \propto p_{\text{cell}}$ (Eqn. (5.2)), the solution to Eqn. (5.1) is of the form $p_{\text{cell}} \propto (1 - \exp(-\gamma t))$ and the steady state partial pressure (i.e., the constant of proportionality) is:

$$p_{\text{cell}} = \frac{4\dot{N}_{\text{in}}}{\pi r_{\text{cell}}^2\, v_{\text{out}}}\, k_{\text{B}}T_{\text{cold}}. \tag{5.3}$$

The precise outflow velocity from the cell depends on flow regime. This can be characterised by the Knudsen number or the Reynolds number, Re. Here, we shall follow the literature [76] and use the Reynolds number. The upper bound on the velocity, v_{ss}, is given by the supersonic regime ($\text{Re} \gtrapprox 100$), where the gas experiences many collisions near the exit of the cell (i.e., the mean free path is much less than the radius of the aperture). The lower bound, v_{eff}, is given by the effusive regime ($\text{Re} \lessapprox 1$), where there are almost no collisions near the exit and the velocity distribution of the particles that leave the cell is a velocity-weighted[2] sample of the velocity distribution of the particles inside the cell. Both v_{eff} and v_{ss} are given in terms of the mean thermal velocity of the particles inside the cell, v_{T} [76]:

$$v_{\text{T}} = \sqrt{\frac{8k_{\text{B}}T_{\text{cold}}}{\pi m}}, \qquad v_{\text{eff}} = \frac{3\pi}{8}v_{\text{T}}, \qquad v_{\text{ss}} = v_{\text{T}}\sqrt{\frac{5\pi}{8}}, \tag{5.4}$$

where m is the mass of the particle in question.

To get an idea of the expected flow regime in the cell, an estimate of the Reynolds number can be found by combining Eqn. (5.3) with the von Kármán relation for a gas with three degrees of freedom [76]. The von Kármán relation is:

$$v_{\text{out}} \approx \sqrt{\frac{5k_{\text{B}}T_{\text{cold}}}{96m}}\frac{\lambda}{r_{\text{cell}}}\text{Re}, \tag{5.5}$$

[2] Faster molecules have a higher chance of leaving the cell.

where $\lambda = k_B T_{cold} \left(\sum_{gases} p_{cell} \sigma \right)^{-1}$ is the mean free path and where σ is the collision cross section. Rearranging to find the Reynolds number and substituting Eqn. (5.3) and the definition of λ gives:

$$\mathrm{Re} \approx \sqrt{\frac{96m}{5k_B T_{cold}}} \frac{4v_{out}}{\pi r_{cell}} \left(\sum_{i \in gases} \frac{\dot{N}_{in}^i \sigma^i}{v_{out}^i} \right). \tag{5.6}$$

In Eqn. (5.6), v_{out} is the velocity of the gas with respect to which the Reynolds number is being calculated (i.e., whose mass is m and whose mean free path is λ). The $\{v_{out}^i\}$ are the velocities of each individual constituent gas. Hence, the Reynolds number for a particular species in a mixed gas depends on all the relative outflow velocities of every constituent gas. These are unknown (that's what we need the Reynolds number for). However, in a single species gas, only one term is included and the result is then independent of velocity:

$$\mathrm{Re} \approx \frac{4\dot{N}_{in}\sigma}{\pi r_{cell}} \sqrt{\frac{96m}{5k_B T_{cold}}}. \tag{5.7}$$

In typical operation the flow rate of the buffer gas is around 0.5 sccm to 1 sccm and the flow rate of the SF_6 is around 0.03 sccm. The kinetic radii of He, Ne, and SF_6 are 1.3 Å, 1.4 Å, and 2.8 Å respectively [78]. For helium flowing at 0.5 sccm at 4 K this gives Re = 1.4. For neon flowing at the same rate but at 11 K this gives Re = 2.2. For SF_6 flowing at 0.03 sccm at 4 K is Re = 2.3 and at 11 K is Re = 1.4. Therefore, if each gas were flowing separately the flow regime would be approximately effusive, and certainly not in the region of supersonic. Hence, we take $v_{out} = v_{eff}$ and so the partial pressure is given by:

$$p_{cell} \approx \frac{8\sqrt{2}}{3} \frac{\dot{N}_{in}}{\pi r_{cell}^2} \sqrt{\frac{m k_B T_{cold}}{\pi}}. \tag{5.8}$$

For 0.5 sccm of buffer gas and 0.03 sccm of SF_6 this gives:

Helium at 4 K**:** $P_{\text{cell}} = 3 \times 10^{-4}\,\text{mbar}$, $v_{\text{eff}}(\text{He}) = 171\,\text{m}\,\text{s}^{-1}$, and a relative abundance of He of 73%.

Neon at 11 K**:** $P_{\text{cell}} = 1 \times 10^{-3}\,\text{mbar}$, $v_{\text{eff}}(\text{Ne}) = 126\,\text{m}\,\text{s}^{-1}$, and a relative abundance of Ne of 86%.

Here, P_{cell} is the total cell pressure. It is worth noting that the relative abundances of buffer gas are lower than the 94% that would be expected from the inflow rates, as the inflow rate of each gas needs to be weighted by $\sqrt{m}$ to find the equilibrium partial pressure. Additionally, both the total pressure and the velocity are $\propto \sqrt{T_{\text{cold}}}$, but relative abundance is independent of temperature.

5.1.2 Production of a Ca Vapour

The Nd:YAG ablation laser enters through a window on one side of the cell and impacts a calcium metal target. Most of the energy of the laser is reflected; however, some is transmitted into the calcium. As calcium is opaque, it has a complex refractive index, $n + \mathrm{i}\kappa$, where κ is known as the 'extinction coefficient'. The transmitted wave takes the form of an evanescent wave [79]:

$$\epsilon(\rho, z) = E_0 \frac{4n}{(1+n)^2 + \kappa^2} \frac{\exp\left(-\frac{\rho^2}{2\sigma^2}\right)}{2\pi\sigma^2} \frac{4\pi\kappa}{\lambda} \exp\left(-\frac{4\pi\kappa z}{\lambda}\right) \tag{5.9}$$

where $\epsilon(\rho, z)$ is an energy density, E_0 and σ are the total energy and cross-sectional Gaussian width of the laser pulse, and $\lambda = 1064\,\text{nm}$ is the wavelength of the ablation laser. The energy density absorbed by the calcium is equal to the energy density of the evanescent wave at that point. The surfaces of constant energy density, ϵ, are given by the paraboloids:

$$z = a\left(r^2 - \rho^2\right), \tag{5.10}$$

$$r^2 = -2\sigma^2 \ln\left(2\pi\sigma^2 \frac{\epsilon}{E_0} \frac{\lambda}{4\pi\kappa} \frac{(1+n)^2 + \kappa^2}{4n}\right), \text{ and} \tag{5.11}$$

$$a = \frac{\lambda}{8\pi\sigma^2\kappa}. \tag{5.12}$$

These are found by taking the logarithm of both sides of Eqn. (5.9) whilst holding ϵ constant.

The energy deposited in a single calcium atom at a point where the energy density is ϵ is given by $\epsilon\frac{m_{\mathrm{Ca}}}{\rho_{\mathrm{Ca}}}$, where $\rho_{\mathrm{Ca}} = 1.55\,\mathrm{g\,cm^{-3}}$ and $m_{\mathrm{Ca}} = 6.66 \times 10^{-26}\,\mathrm{g}$ are the density of metallic calcium and atomic mass of calcium respectively [80]. The probability of a calcium atom having energy E deposited in it by the laser is proportional to the area of the constant energy density surface from Eqn. (5.10) with energy density $\epsilon = E\frac{\rho_{\mathrm{Ca}}}{m_{\mathrm{Ca}}}$. The Nd:YAG ablation laser used in our laboratory has an energy of $E_0 = 25\,\mathrm{mJ}$ at $\lambda = 1064\,\mathrm{nm}$ and a $1/\mathrm{e}^2$ width of 1.5 mm. The refractive index of calcium at this wavelength is $0.49 + 5.1\mathrm{i}$ [81]. The resulting energy distribution is shown in Figure 5.1.

Not all of the calcium atoms in the target will receive enough energy to be liberated from the rod. As found earlier, the pressure inside the cell containing the experiment is typically $3 \times 10^{-4}\,\mathrm{mbar}$ in the case of a helium buffer gas. The temperature above which the calcium vapour pressure exceeds this (i.e., the boiling point) is $(747 \pm 16)\,\mathrm{K}$ [82]. The heat of vapourisation of calcium is $4187\,\mathrm{J\,g^{-1}}$, the heat of fusion is $217.7\,\mathrm{J\,g^{-1}}$, and the specific heat capacity is $0.624\,\mathrm{J\,g^{-1}\,K^{-1}}$ [80]. Therefore, the

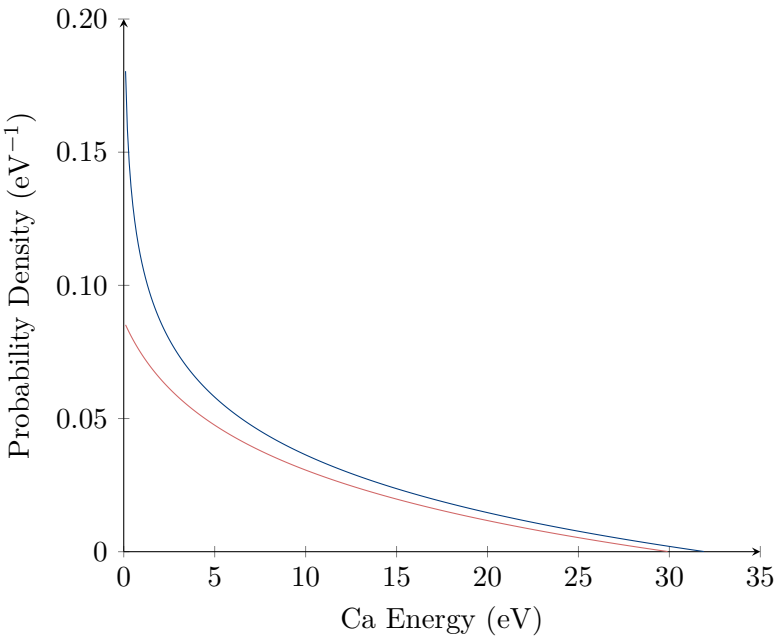

FIGURE 5.1: (Blue) The distribution of energies deposited in calcium atoms from an ablation laser of energy $E_0 = 25\,\mathrm{mJ}$ at $\lambda = 1064\,\mathrm{nm}$ and a $1/e^2$ width of 1.5 mm. (Red) The energy distribution of calcium particles in the released vapour.

minimum energy density needed to vapourise the calcium is $(7.55 \pm 0.02) \times 10^9\,\mathrm{J\,m^{-3}}$ or 2 eV per atom. Using Eqn. (5.10), we can determine that the ablation laser will melt a pool of calcium with a volume of approximately $6 \times 10^{-5}\,\mathrm{mm^3}$ and containing around 10^{15} atoms.

The plasma temperature of calcium is around 5000 K [83]. The energy in the ablation laser is more than sufficient to plasmolyse the calcium. However, if the energy (or the repetition rate of the laser) is so high that the calcium does not cool down between shots, the above energy absorption model will break down. This is because the energy required to liberate calcium ions from a plasma is higher than from a solid, since the free electrons in the plasma absorb more of the energy. This should be avoided, and so places an upper limit on the energy of the ablation laser.

5.1.3 Thermalisation of Ca and CaF

The calcium vapour will expand into a cell that already contains cold buffer gas and SF_6. The motion of the calcium particles is governed by the convection-diffusion equation. This provides two ways for calcium and CaF molecules to be lost. If the particles spread out diffusively and hit the walls of the cell then they will be lost by adsorption. If, on the other hand, the particles are carried out of the cell by advection in the buffer gas flow then they will form part of the molecular beam. If we call the loss rate by adsorption γ_{diff} and the loss rate by advection γ_{pump}, we have a system of three differential equations:

$$\begin{aligned} \frac{\mathrm{d}N_{\mathrm{beam}}}{\mathrm{d}t} &= \gamma_{\mathrm{pump}} N_{\mathrm{cell}} \\ \frac{\mathrm{d}N_{\mathrm{loss}}}{\mathrm{d}t} &= \gamma_{\mathrm{diff}} N_{\mathrm{cell}} \\ \frac{\mathrm{d}N_{\mathrm{cell}}}{\mathrm{d}t} &= -(\gamma_{\mathrm{pump}} + \gamma_{\mathrm{diff}}) N_{\mathrm{cell}} \end{aligned} \tag{5.13}$$

with boundary conditions $N_{\mathrm{cell}}(0) \neq 0$ and $N_{\mathrm{beam}}(0) = N_{\mathrm{loss}}(0) = 0$. The system has the solutions:

$$\begin{aligned} N_{\text{beam}}(t) &= \eta_{\text{beam}} N_{\text{cell}}(0)\left(1-\exp\left(-\left(\gamma_{\text{pump}}+\gamma_{\text{diff}}\right)t\right)\right) \\ N_{\text{loss}}(t) &= \eta_{\text{loss}} N_{\text{cell}}(0)\left(1-\exp\left(-\left(\gamma_{\text{pump}}+\gamma_{\text{diff}}\right)t\right)\right) \\ N_{\text{cell}}(t) &= N_{\text{cell}}(0)\exp\left(-\left(\gamma_{\text{pump}}+\gamma_{\text{diff}}\right)t\right) \end{aligned} \tag{5.14}$$

where the extraction efficiency, η_{beam}, and loss 'efficiency', η_{loss}, are given by the fraction of particles either in the beam or lost in steady state. These fractions are:

$$\eta_{\text{beam}} = \frac{\gamma_{\text{pump}}}{\gamma_{\text{pump}}+\gamma_{\text{diff}}} \tag{5.15}$$

$$\eta_{\text{loss}} = \frac{\gamma_{\text{diff}}}{\gamma_{\text{pump}}+\gamma_{\text{diff}}} \tag{5.16}$$

We can find an upper bound on the pump-out time, $\tau_{\text{pump}} = 1/\gamma_{\text{pump}}$, using Eqn. (5.1) with $\dot{N}_{\text{in}} = 0$, $\dot{N}_{\text{out}}$ given by Eqn. (5.2), and with $v_{\text{out}} = v_{\text{eff}}$ being equal to the buffer gas outflow rate. This gives [76]:

$$\tau_{\text{pump}} = \frac{4V_{\text{cell}}}{v_{\text{eff}}\pi r_{\text{cell}}^2}. \tag{5.17}$$

If we say the cell is 2 cm in linear dimension, then $V_{\text{cell}} \sim (2\,\text{cm})^3$. Then, for a helium buffer gas with $v_{\text{eff}} = 171\,\text{m}\,\text{s}^{-1}$, this gives $\tau_{\text{pump}} = 15\,\text{ms}$. For neon with $v_{\text{eff}} = 126\,\text{m}\,\text{s}^{-1}$, we have $\tau_{\text{pump}} = 20\,\text{ms}$.

For the adsorptive loss rate, we assume that all molecules which diffusively hit the walls of the cell are lost by adsorption. This is reasonable since the cell aperture is very small compared to the total surface area of the cell, and the molecules are polar radicals which are certain to be lost as soon as they hit a cold surface. Then, $\gamma_{\text{diff}} = 1/\tau_{\text{diff}}$ where τ_{diff} is the diffusion timescale. The cell cavity is around $s = 2\,\text{cm}$ in linear dimension. Under Brownian motion (i.e., diffusion) in three dimensions the diffusion timescale is $\tau_{\text{diff}} = s^2/6D$, where D is the diffusion coefficient [84]. The diffusion coefficient is given by [75]:

$$D = \frac{3\lambda}{16}\left(2\pi k_{\mathrm{B}} T_{\mathrm{s}}(\mathcal{N})\frac{m_{\mathrm{s}}+m_{\mathrm{b}}}{m_{\mathrm{s}}m_{\mathrm{b}}}\right)^{\frac{1}{2}} \tag{5.18}$$

where λ is the mean free path, T_{s} is the temperature of the species of interest (which changes with the number of collisions $\mathcal{N}$), and m_{s} and m_{b} are the masses of the species of interest and of the bulk background respectively. We take m_{b} to be the average mass of the mixture of buffer gas and SF_6, weighted by their relative abundances.

To find $T_{\mathrm{s}}(\mathcal{N})$, we must determine the number of collisions a bare calcium particle will undergo before hitting the cell wall. Given a mean thermal velocity of $v_{\mathrm{T}} = \sqrt{\frac{3k_{\mathrm{B}}T_{\mathrm{s}}(\mathcal{N})}{m_{\mathrm{s}}}}$, this is $\mathcal{N}_{\mathrm{diff}} = v_{\mathrm{T}}\tau_{\mathrm{diff}}/\lambda$:

$$\mathcal{N}_{\mathrm{diff}} = \frac{4}{9}\sqrt{\frac{6}{\pi}}\,\frac{s^2}{\lambda^2}\sqrt{\frac{m_{\mathrm{b}}}{m_{\mathrm{s}}+m_{\mathrm{b}}}}, \tag{5.19}$$

which helpfully only depends on constants and not on $T_{\mathrm{s}}(\mathcal{N})$. The temperature after $\mathcal{N}$ collisions can be calculated according to the equation [85]:

$$\frac{T_{\mathrm{s}}(\mathcal{N})}{T_{\mathrm{b}}} = 1 + \left(\frac{T_{\mathrm{s}}(0)}{T_{\mathrm{b}}} - 1\right)\exp\left(-\mathcal{N}/\nu\right), \tag{5.20}$$

where $\nu = \frac{(m_{\mathrm{s}}+m_{\mathrm{b}})^2}{2m_{\mathrm{s}}m_{\mathrm{b}}}$. Finally, the diffusion timescale, τ_{diff}, can be found by considering the mean free path and the velocity between each collision:

$$\begin{aligned}\tau_{\mathrm{diff}} &= \lambda\int_0^{\mathcal{N}_{\mathrm{diff}}}\frac{1}{v_{\mathrm{T}}(\mathcal{N})}\,\mathrm{d}\mathcal{N} \\ &= \lambda\sqrt{\frac{m_{\mathrm{s}}}{3k_{\mathrm{B}}T_{\mathrm{b}}}}\int_0^{\mathcal{N}_{\mathrm{diff}}}\left(1+\left(\frac{T_{\mathrm{s}}(0)}{T_{\mathrm{b}}}-1\right)\exp\left(-\frac{\mathcal{N}}{\nu}\right)\right)^{-\frac{1}{2}}\,\mathrm{d}\mathcal{N}\end{aligned} \tag{5.21}$$

which now depends entirely on known quantities. Using the three equations above — Eqn. (5.19), Eqn. (5.20), and Eqn. (5.21) — we can work out the time taken for a particle to travel diffusively across the cell cavity. However, both m_{s} and λ depend on whether the particle is unreacted calcium or whether it is CaF, as the mass and kinetic radius both change.

To determine the initial temperature of the calcium, $T_s(0)$, we can apply Eqn. (5.20) to the calcium immediately at the point of vapourisation. In a single species gas, $\nu = 2$ (exactly). The internal thermalisation timescale, τ, can be found from the mean free path, λ, and the mean thermal velocity, v_T, so that $\tau = \nu\frac{\lambda}{v_T}$. At the point of vapourisation, the density of the calcium vapour is equal to the density of liquid calcium, $1.376\,\mathrm{g\,cm^{-3}}$. The kinetic radius of calcium is 2.78 Å [86], which gives a mean free path of $\lambda = 2\,$Å. The average energy of Ca atoms in the vapour is 8.2 eV, which corresponds to a thermal velocity of $v_T = 6.3 \times 10^3\,\mathrm{m\,s^{-1}}$. Hence, the timescale for the calcium vapour to reach internal thermalisation is $\tau \approx 32\,$fs.

We can find bounds on τ_{diff} by considering the two extreme cases of a calcium particle reacting almost immediately after vapourisation, so that it is only CaF that diffuses through the cell, and a calcium particle proceeding through without reacting at all (despite coming into contact with SF_6). The kinetic diameter of CaF is approximated by the interatomic distance 1.97 Å plus the kinetic *radii* of calcium and fluorine [86]. The result is a kinetic diameter of 6.4 Å for CaF.

The lower bound on the diffusion timescale, τ_{diff}, is the time taken for a calcium atom to exit the cell in a straight line travelling at v_T. This gives a lower bound on τ_{diff} of 3 µs. This is eight orders of magnitude slower than the internal thermalisation timescale of 32 fs, so we can assume the calcium reaches thermal equilibrium with itself almost instantly. As the internal thermalisation is approximately adiabatic (being much quicker than the expansion of the vapour into the cell, where it can exchange energy), the mean energy does not change. Thus, the initial equilibrium energy distribution is a Maxwell-Boltzmann distribution with $\frac{3}{2}k_B T_s(0) = 8.2\,$eV, or $T_s(0) = 63\,000\,$K.

Given these parameters, the results for $\mathcal{N}_{\mathrm{diff}}$, $T_s(\mathcal{N}_{\mathrm{diff}})$, τ_{diff}, and η_{beam} are given in Table 5.1. We can see that our final values for the diffusion timescale are ten orders of magnitude greater than the calcium vapour's internal thermalisation timescale, so we are justified in approximating that process as instantaneous. Additionally, the diffusion timescale is two orders of magnitude faster than the pump-out timescale, meaning that most of the particles will be lost, and will not be in the beam. This behaviour makes sense given the low Reynolds number (recall $\mathrm{Re} \approx 2$), which implies the beam is effusive and diffusion is the dominant component of the flow.

	He				Ne			
	$\mathcal{N}_{\text{diff}}$	T_{s} (K)	τ_{diff} (µs)	η_{beam}	$\mathcal{N}_{\text{diff}}$	T_{s} (K)	τ_{diff} (µs)	η_{beam}
Ca	22	4.8	339	2.2%	26	11	346	1.7%
CaF	29	4.1	666	4.3%	33	11	562	2.7%

TABLE 5.1: Average number of collisions, $\mathcal{N}_{\text{diff}}$, required for a Ca or CaF particle to exit the buffer gas cell, its temperature, $T_{\text{s}}(\mathcal{N}_{\text{diff}})$, at that time for either a helium or neon buffer gas according to the parameters given at the end of Section 5.1.1, and the overall diffusion timescale τ_{diff}.

We know from Table 5.1 that, on average, every 3.8 collisions will be with SF_6 in a helium buffer gas, and every 7.2 in a neon buffer gas[3]. Hence, a bare calcium particle will have around six opportunities to react in helium and four in neon.

If the per-collision reaction probability is $\mathcal{P}_{\text{react}}$ then the per-molecule reaction efficiency is given by:

$$\eta_{\text{react}} = \mathcal{P}_{\text{react}} \sum_{j=1}^{N} (1 - \mathcal{P}_{\text{react}})^{j-1}, \tag{5.22}$$

where N is the number of attempts (i.e., the number of collisions with SF_6). For Ca reacting with SF_6 to produce CaF, $\mathcal{P}_{\text{react}}$ is expected to be small — well below 0.05 [87]. Taking $\mathcal{P}_{\text{react}} = 0.05$ and assuming that every Ca particle gets six opportunities to react gives an upper bound on η_{react} of 0.26.

5.1.4 Model of the CaF Molecular Beam

From Section 5.1.2 we know that around 10^{15} Ca particles are released from the calcium target by the ablation laser. They form a calcium vapour in thermal equilibrium at approximately 63 000 K almost immediately. This vapour then thermalises with the buffer gas-SF_6 mixture over the course of 20 to 30 collisions, taking around 340 µs (for helium) and 600 µs (for neon). During this time the calcium particles also react with SF_6 to form CaF with unknown efficiency, η_{react}. We are then left with a CaF vapour in the buffer gas cell containing $\eta_{\text{react}} \times 10^{15}$ particles in thermal equilibrium

[3]These numbers are the reciprocals of the relative abundances of SF_6 in each case.

with the surrounding buffer gas at T_{cold} (4 K for helium and 11 K for neon). The majority of the CaF molecules produced are adsorbed onto the walls of the cell cavity; however, 3-4% are advectively carried out of the cell, forming a molecular beam.

Since the CaF molecules are approaching thermal equilibrium with the buffer gas by the time they leave the cell, we can model the beam as initially having a Maxwell-Boltzmann distribution in velocity space. We assume a Gaussian distribution in position space, with a $1/e^2$ width[4] equal to the cell aperture, $r_{\text{cell}} = 2\,\text{mm}$, in the transverse plane and equal to the internal cell length, $L_{\text{cell}} = 2\,\text{cm}$, along the longitudinal axis. Since one-dimensional Maxwell Boltzmann distributions in velocity are simply Gaussian distributions, the six dimensional distribution in phase space is the product of six Gaussian distributions:

$$f_0(\vec{r},\vec{v}) = \left(\frac{2}{\pi}\right)^3 \frac{1}{r_{\text{cell}}^2 L_{\text{cell}}} \frac{1}{\Delta v_\perp^2\ \Delta v_z} \exp\left(-\frac{8\rho_\perp^2}{r_{\text{cell}}^2} - \frac{8z^2}{L_{\text{cell}}^2} - \frac{v_\perp^2}{2\Delta v_\perp^2} - \frac{(v_z - v_{\text{out}})^2}{2\Delta v_z^2}\right), \tag{5.23}$$

where the coordinates, r, x, y, and z, are as shown in Figure 4.2 and $\rho_\perp = \sqrt{x^2+y^2}$. The transverse velocity, $v_\perp$, is the velocity in the x–y plane, $v_\perp = v_x\hat{x} + v_y\hat{y}$, v_{out} is the outflow velocity of the CaF molecules, and $\Delta v_\perp$ and Δv_z are the widths (standard deviations) of the velocity distribution in the transverse and longitudinal directions.

Eqn. (5.23) defines the distribution at time $t = 0$. This is when half the beam has exited the cell, so the distribution is longitudinally centred on the cell aperture. Provided no forces are acting, the distribution at some later time, t, is then given by $f_t(\vec{r},\vec{v}) = f_0(\vec{r} - \vec{v}t, \vec{v})$. This causes the distribution to shear in real space at a rate equal to the velocity.

Both v_{out} and the velocity widths depend on the Reynolds number for the flow of CaF. We have already determined that the Reynolds number appropriate to the buffer gas and SF_6 flow is $\text{Re} \approx 2$. From Eqn. (5.6) we can see that the Reynolds number appropriate to small number of CaF molecules in a gas otherwise containing only buffer gas will be given by:

[4] The $1/e^2$ width is four times the standard deviation.

$$\mathrm{Re} \approx \sqrt{\frac{96 m_\mathrm{s}}{5 k_\mathrm{B} T_\mathrm{cold}}} \frac{4\dot{N}_\mathrm{in}\sigma}{\pi r_\mathrm{cell}} \frac{v_\mathrm{out}(\mathrm{CaF})}{v_\mathrm{out}(\mathrm{Buff})} \approx 17 \frac{v_\mathrm{out}(\mathrm{CaF})}{v_\mathrm{eff}(\mathrm{Buff})}, \tag{5.24}$$

where m_s is the molecular mass of CaF $\dot{N}_\mathrm{in}$ is the inflow rate of buffer gas, and σ is the collision cross section between CaF and the buffer gas. The velocity independent part of the Reynolds number is around 17 for both a helium and neon buffer gas. For $10 \lesssim \mathrm{Re} \lesssim 100$, the outflow velocity of the molecular beam is given by [76]:

$$v_\mathrm{out}(\mathrm{CaF}) = v_\mathrm{ss}(\mathrm{Buff}) \sqrt{1 - 4\mathrm{Re}^{-4/5}}, \tag{5.25}$$

and for $\mathrm{Re} > 100$, $v_\mathrm{out}(\mathrm{CaF}) \approx 0.95 v_\mathrm{ss}(\mathrm{Buff})$. Solving Eqn. (5.24) and Eqn. (5.25) together gives $v_\mathrm{out}(\mathrm{CaF}) = 145\,\mathrm{m\,s^{-1}}$ and a Reynolds number appropriate to CaF in a helium buffer gas of $\mathrm{Re} \approx 14$. The widths at 4 K for this flow regime are $\Delta v_z = \Delta v_\perp = \frac{\sqrt{\pi}}{2\sqrt{2}} v_\mathrm{T}^\mathrm{CaF} \approx 24\,\mathrm{m\,s^{-1}}$.

The distribution $f_t(\vec{r}, \vec{v})$ (Eqn. (5.23)) is a distribution in phase space and is not constant. However, it has the property that the integrated intensity profile (i.e., the distribution per steradian) is approximately constant for sufficiently large t. To see this, we first integrate out the velocity component:

$$\tilde{f}_t(\vec{r}) = \int_{-\infty}^{\infty} f_0(\vec{r} - \vec{v}t, \vec{v})\ \mathrm{d}^3 v, \tag{5.26}$$

and then transform the remainder to spherical coordinates (r, α, β) as shown in Figure 4.2:

$$\tilde{\tilde{f}}_t(\vec{r}) = r^2 \tilde{f}_t(x = r\sin\alpha\cos\beta, y = r\sin\alpha\sin\beta, z = r\cos\alpha), \tag{5.27}$$

such that $\int_0^\infty \int_0^{4\pi} \tilde{\tilde{f}}_t(\vec{r})\ \mathrm{d}r\ \mathrm{d}\Omega = 1$ with $\mathrm{d}\Omega = \sin\alpha\ \mathrm{d}\alpha\ \mathrm{d}\beta$ as the solid angle element. Integrating out the radial component leaves the molecular intensity distribution:

$$\Phi_t(\alpha, \beta) = \int_0^\infty \tilde{\tilde{f}}_t(r, \alpha, \beta)\ \mathrm{d}r. \tag{5.28}$$

Plots of the molecular intensity distribution are shown in Figure 5.2 for $t = 0\,\mu s$ to $t = 25\,\mu s$. Bearing in mind that α is the zenith angle measured from the y-axis and β is the azimuth measured anti-clockwise from the x-axis in the x–z plane, we can see that the peak molecular intensity is along the z-axis with $\alpha = \beta = \pi/2$.

Figure 5.2 shows the transition of the beam from a near field regime, where the beam's finite initial size is important, to a far field regime, where the initial distribution in space can be treated as a point. In the far field regime, the beam has a constant angular size and so has a constant intensity. As we will see in Section 5.2, it is useful to assume that the beam has a constant molecular intensity when trying to work out the number of CaF molecules produced in the lab. Hence, it is helpful to know this assumption is justified.

The transition to the far field regime can also be seen in Figure 5.3, which shows the molecular intensity along the z-axis over time. The time of the transition to the far field regime corresponds to the time at which the width of the cone containing the beam in the far field exceeds the initial size of the beam, $t \sim \frac{r_{\mathrm{cell}}}{v_{\mathrm{out}} - \Delta v_\perp} \approx 17\,\mu s$.

5.2 Beam Detection and Characterisation

In order to characterise a molecular beam in the lab, we need to measure both the number of molecules in the beam, N_{beam}, and the widths of the velocity distribution, Δv_z and $\Delta v_\perp$. These measurements were carried out at the downstream detector, D' in Figure 4.11, using a 531 nm laser in resonance with the B–X transition whose profile is shown in Figure 4.12. The distance $\overline{SD'}$ from the detector to the source is 35 cm and the distance from the beamline to the collimating lens, $\overline{D'R}$, is 1 inch $\approx$ 25 mm.

5.2.1 Time-of-Flight Measurement

The beam distribution given in Eqn. (5.26), $\tilde{f}_t(\vec{r})$, is parameterised by time and normalised over space. This means that it gives the complete, normalised, molecular distribution in space at a given time. However, a measurement of the sort described

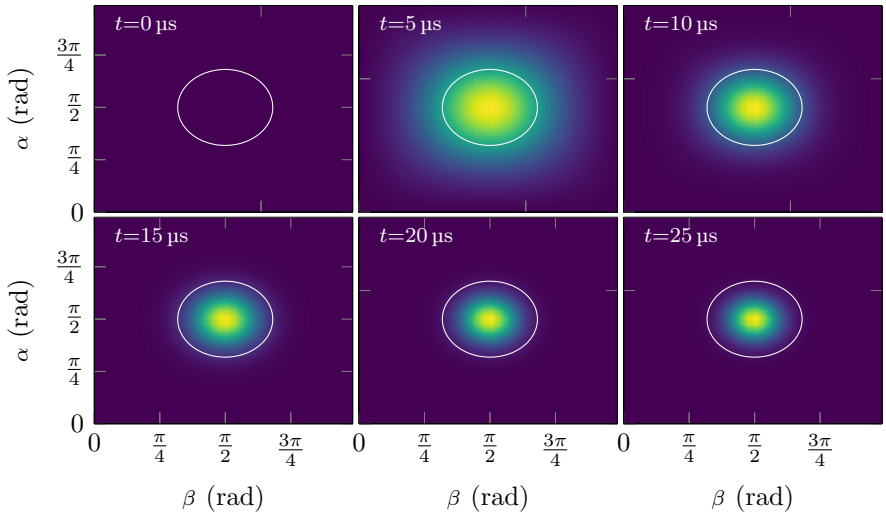

FIGURE 5.2: The modelled molecular intensity (Φ_t sr^{-1}) for a molecular beam modelled with phase space distrubtion as in Eqn. (5.23) with $v_{\text{out}} = 145\,\text{m}\,\text{s}^{-1}$, $\Delta v_\perp = \Delta v_z = 24\,\text{m}\,\text{s}^{-1}$, and spatial width $4\sigma = r_{\text{cell}} = 2\,\text{mm}$. Overlaid in white is the circle corresponding to a 1 sr cone.

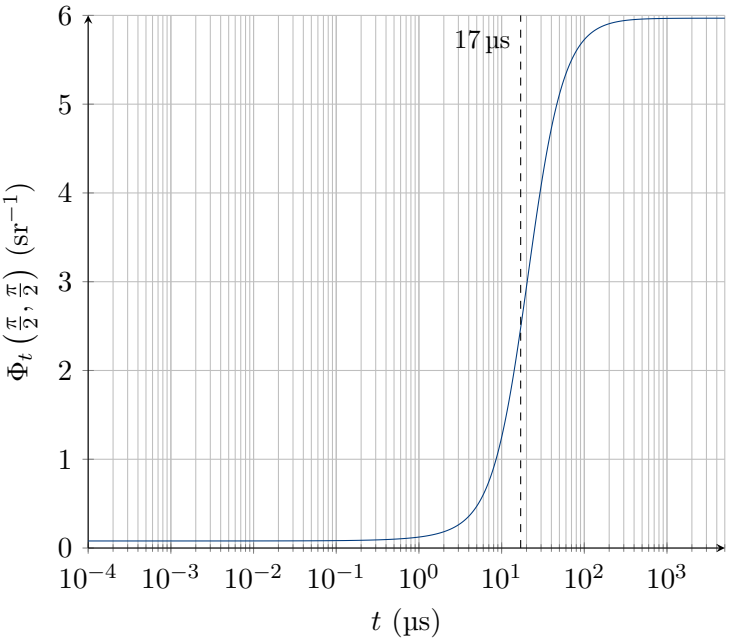

FIGURE 5.3: The modelled molecular intensity on the z-axis, $\Phi_t\left(\frac{\pi}{2}, \frac{\pi}{2}\right)$, over time for a molecular beam with phase space distribution as in Eqn. (5.23) with $v_{\text{out}} = 145\,\text{m}\,\text{s}^{-1}$, $\Delta v_\perp = \Delta v_z = 24\,\text{m}\,\text{s}^{-1}$, and spatial width $4\sigma = r_{\text{cell}} = 2\,\text{mm}$. The dashed line is $t = 17\,\mu\text{s}$, the point at which a 1 sr cone is larger than the transverse beam width.

in Figure 4.11 is not sampling this distribution. It is sampling the distribution over time in a specific plane; namely the one at $z = \overline{SD'}$. That is, z is a parameter and t is a variable over which the distribution is normalised. This requires a transformation of the volume element:

$$\tilde{f}_t(\vec{r})\ \mathrm{d}z \to \tilde{f}_t(\vec{r})\ \frac{\mathrm{d}z}{\mathrm{d}t}\mathrm{d}t, \tag{5.29}$$

$$\tilde{f}_z(x, y, t) \equiv \tilde{f}_t(\vec{r})\ v_z, \tag{5.30}$$

where $\frac{\mathrm{d}z}{\mathrm{d}t} = v_z$ is the Jacobian. This distribution is normalised such that:

$$\forall z : \int_{-\infty}^{\infty} \tilde{f}_z(x, y, t)\ \mathrm{d}x\ \mathrm{d}y\ \mathrm{d}t = 1. \tag{5.31}$$

The detection process is then equivalent to integrating over some region of the plane at z to get a purely temporal distribution. If we integrate over the entire plane (corresponding to a planar detection laser and 100% efficiency in gathering emitted photons) we get the idealised TOF (time-of-flight) distribution (using the same initial distribution as in Eqn. (5.23)):

$$\tilde{\tilde{f}}_z(t) = \int_{-\infty}^{\infty} \tilde{f}_z(x, y, t)\ \mathrm{d}x\ \mathrm{d}y \tag{5.32}$$

$$= \frac{4}{L_{\mathrm{cell}}} \frac{1}{\sqrt{2\pi}} \left[v_{\mathrm{out}} + \frac{zt}{\tau^2} \right] \left[1 + \frac{t^2}{\tau^2} \right]^{-3/2} \exp\left(-\frac{8}{L_{\mathrm{cell}}^2} \frac{(z - v_{\mathrm{out}} t)^2}{1 + \frac{t^2}{\tau^2}} \right),\ \tau = \frac{L_{\mathrm{cell}}}{4\Delta v_z}, \tag{5.33}$$

where τ is the characteristic expansion timescale of the beam (i.e., the ratio of the spatial width to the velocity width). Note that the normalisation part contains only the z-axis spatial width ($L_{\mathrm{cell}}/4$) and $\Delta v_\perp$ is not present. This is because we have integrated over the entire transverse plane, so information about transverse width of the beam is lost.

To model a line-like detection laser, we can limit the integration region to only the

$(y = 0, z = \overline{SD'})$ line. Further, if we limit the range of x to some region $x \in [-\delta x, \delta x]$ we can model the limited fraction of photons the collimating lens actually collects. However, this still does not account for the scattering rate of the laser, $R(\rho, v_h)$, the fact that the laser has a finite width, σ, or the fact that the collection efficiency, $\eta_{\text{geo}}(\vec{r})$, is not a simple top-hat function. Accounting for these, the photon count rate at the PMT is:

$$\Gamma(t) = \eta_{\text{tr}}\eta_{\text{qu}} \int_{-\infty}^{\infty} \eta_{\text{geo}}(\vec{r})\ f_t(\vec{r}, \vec{v})\ R(\rho, v_h)\ \mathrm{d}^3 r\ \mathrm{d}^3 v \tag{5.34}$$

where η_{tr} is the transmission efficiency of the optics and η_{qu} is the quantum efficiency of the PMT. $f_t(\vec{r}, \vec{v}) = f_0(\vec{r} - \vec{v}t, \vec{v})$ is the distribution normalised over phase space and parameterised by time, given in Eqn. (5.23).

If we assume that the fluorescence is emitted spherically uniformly, then the geometric efficiency, $\eta_{\text{geo}}(\vec{r})$, of the collection optics at the downstream detector is twice[5] the ratio of the solid angle subtended by the collection lens at the point $\vec{r}$ to the solid angle of a sphere (4π):

$$\eta_{\text{geo}}(\vec{r}) = 1 - \cos\left(\frac{\omega(\vec{r})}{2}\right), \tag{5.35}$$

where $\omega(\vec{r})$ is the apex angle of the cone subtended by the collection lens at the point $\vec{r}$. A diagram of this is shown in Figure 5.4. If $\vec{r} = (x, y, z)$ then the distance $\xi^2 = x^2 + (z - \overline{SD'})^2$ and the distance $l = \overline{D'R} - y$. ω is then:

$$\omega(\vec{r}) = \phi - \theta = \arctan\left(\frac{l}{\xi - r_{\text{lens}}}\right) - \arctan\left(\frac{l}{\xi + r_{\text{lens}}}\right). \tag{5.36}$$

Figure 5.5 shows the geometric efficiency for the downstream detector, as shown in Figure 4.11, with a two inch collection lens, $r_{\text{lens}} = 25.4\,\text{mm}$ (1 inch), and with $\overline{D'R} = 25.4\,\text{mm}$. In addition, we must account for the finite size of the PMT photocathode. The photocathode is 25.4 mm in diameter. If the magnification of the optics shown

[5] It is doubled due to the symmetric retro-reflecting mirror.

in Figure 4.11 is M then the corresponding detection area around D or D' is $M \times 25.4\,\text{mm}$. The magnification is the ratio of the focal length of the focussing lens, f_f, to that of the collimating lens, f_c:

$$M = \frac{f_\text{f}}{f_\text{c}}. \tag{5.37}$$

For both the upstream and downstream detection points, $f_\text{f} = 51\,\text{mm}$. For the upstream detection point, $f_\text{c}^\text{up} = 82.5\,\text{mm}$. For the downstream detection, $f_\text{c}^\text{down} = 24.5\,\text{mm}$. These give magnifications of $M_\text{up} = 0.62$ and $M_\text{down} = 2.1$ for the near and far detectors respectively. That corresponds to a detection area with a diameter of 15.7 mm around D (upstream) and 53.3 mm around D' (downstream). These detection areas are also shown in Figure 5.5. They are much smaller than the collection area of the collimating lens and provide a hard limit on the photon collection in the x-direction[6].

Turning now to the scattering rate, $R(\rho, v_h)$; this accounts for both the number of photons emitted and the finite width of the laser beam. We approximate the laser beam as Gaussian, making the scattering rate independent of the polar angle θ. It is also independent of h, since the detection light is a continuous wave beam. However, it is dependent on the CaF velocity along $\hat{h}$ due to the Doppler effect. The full form is given in Section 2.5 but the simplified version for a two-level system is:

$$R(\rho, v_h) = \frac{\gamma}{2} \frac{s(\rho)}{1 + s(\rho) + 4\left(\frac{\delta(v_h)}{\gamma}\right)^2}, \tag{5.38}$$

where γ is the excited state lifetime ($\gamma = 5.2 \times 10^7\,\text{s}^{-1}$ for the CaF $A^2\Pi$ state), $s(\rho)$ is the saturation parameter, and $\delta(v_h)$ is the frequency detuning accounting for Doppler shift. The saturation parameter is given by [69]:

[6] The detection light $1/e^2$ width is smaller than both detection areas so that is the limiting factor in the y-direction.

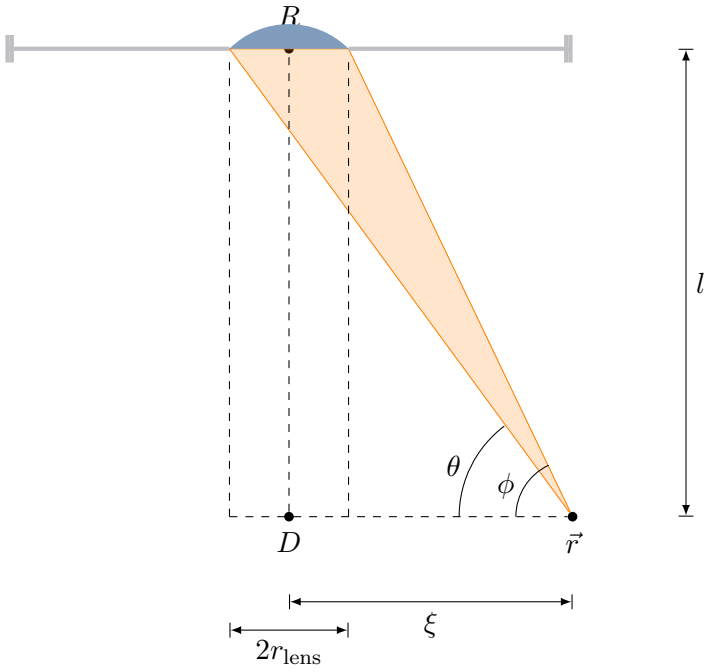

FIGURE 5.4: A detailed diagram of part of a detector as shown in Figure 4.11, showing the collimating lens and detection point D (or D'). The cone at point $\vec{r}$ subtended by the collimating lens has apex angle $\omega = \phi - \theta$, which can be calculated from the distances given.

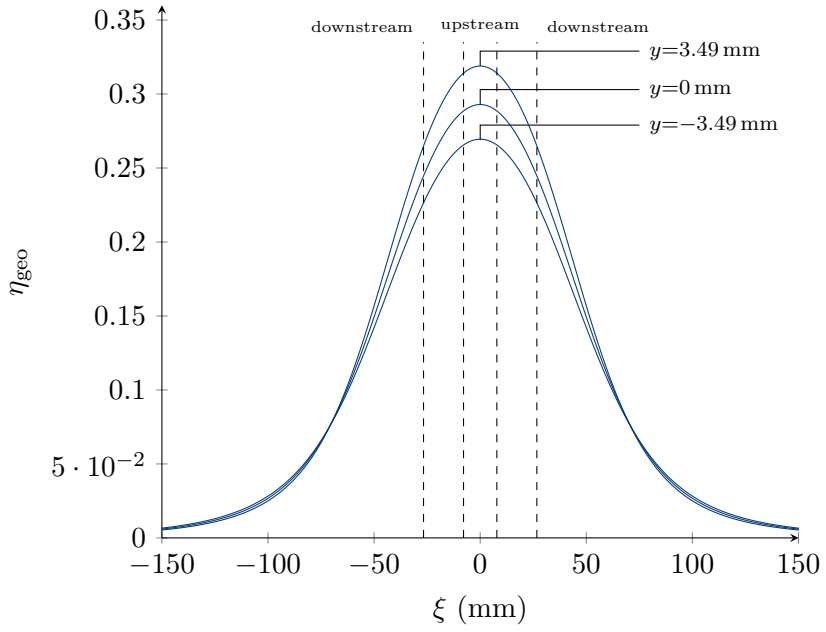

FIGURE 5.5: The geometric efficiency, $\eta_{\text{geo}}(\xi, l)$, for a collection lens with $r_{\text{lens}} = 25.4\,\text{mm}$ and $l = (25.4\,\text{mm} - y)$, together with a symmetric retro-reflecting mirror, as shown for the downstream detector in Figure 4.11. η_{geo} is shown for $y = 0\,\text{mm}$ and $y = \pm 3.49\,\text{mm}$ (i.e., the detection laser $1/e^2$ width in the y direction). The dashed lines show the size of the detection area corresponding to the magnified size of the PMT photocathode.

$$s = \frac{I}{I_s} = I(\rho)\left(\frac{\pi h c \gamma}{3\lambda^3}\right)^{-1}, \tag{5.39}$$

where $I(\rho)$ is the local laser intensity and $\lambda = 2\pi c/\omega_{\text{las}}$ is the laser wavelength. For the CaF A–X transition, $\lambda = 606\,\text{nm}$ and so $I_s = 5\,\text{mW}\,\text{cm}^{-2}$. For the B–X transition, $\lambda = 531\,\text{nm}$ and $I_s = 7\,\text{mW}\,\text{cm}^{-2}$. The detuning is given by:

$$\delta(v_h) = (1 - \beta_h)\,\omega_{\text{las}} - \omega_0, \tag{5.40}$$

where $\beta_h = v_h/c$. For detection of the molecules we would like the laser to be directly on resonance, so $\omega_{\text{las}} \approx \omega_0$, meaning that $\delta = -\beta_h \omega_{\text{las}}$. The sign is due to the fact that the transition is blue-detuned (i.e., frequency is increased) if the molecule is moving anti-parallel to the k-vector of the light. For 531 nm light and a molecule moving at $\Delta v_\perp$, $|\delta| \approx 1.5 \times 10^9\,\text{rad}\,\text{s}^{-1}$, and for 606 nm, $|\delta| \approx 1.4 \times 10^9\,\text{rad}\,\text{s}^{-1}$. A plot of the scattering rate for the CaF A–X transition can be seen in Figure 5.6.

We can now calculate $\Gamma(t)$ from Eqn. (5.34). A comparison between the complete temporal distribution, $\tilde{\tilde{f}}_z(t)$, and the photon count rate, $\Gamma(t)$ can be seen in Figure 5.7 for a molecular beam with $v_{\text{out}} = 145\,\text{m}\,\text{s}^{-1}$ and $\Delta v_z = \Delta v_\perp = 131\,\text{m}\,\text{s}^{-1}$ and scattering rates and geometric efficiencies as described above. Both distributions have been re-normalised to unit area. By doing this, it can be seen that $\Gamma(t)$ proportionally overcounts the faster molecules in the leading edge and undercounts the slower molecules in the tail. However, the overall effect on shape is minimal.

As shown in Figure 5.2, the molecular intensity distribution rapidly approaches a constant value (in time) and occupies a small cone subtended by an apex angle of only 0.8 rad. At $z = \overline{SD'} = 35\,\text{cm}$ this means the entire beam would pass through an aperture in the x-y plane greater than 15 cm in radius. The actual experimental setup has apertures in the beam line smaller than this. Therefore, the angular size of the beam is wholly determined by the angle subtended by these apertures, rather than by the natural size of the beam. The average molecular intensity over this aperture, $\langle\Phi\rangle$, is given by:

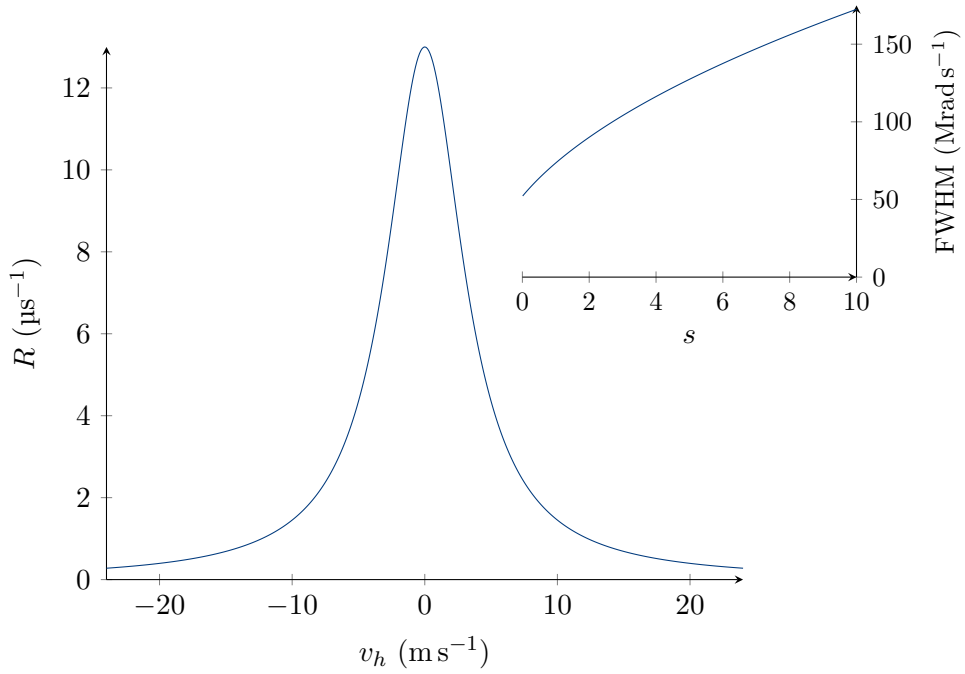

FIGURE 5.6: The scattering rate, R, as in Eqn. (5.38), at saturation intensity ($s = 1$) and for $\gamma = 5.2 \times 10^7\,\mathrm{rad\,s^{-1}}$, as for the CaF $A^2\Pi$ state. The x-axis shows the velocity along $\hat{h} = -\hat{x}$ (i.e., parallel to the laser's k-vector). The inset shows the FWHM as it varies with s (i.e., the power broadening). At $s = 1$ The FWHM is $7.35 \times 10^7\,\mathrm{s^{-1}}$ and the peak scattering rate is $R = 1.3 \times 10^7\,\mathrm{s^{-1}}$.

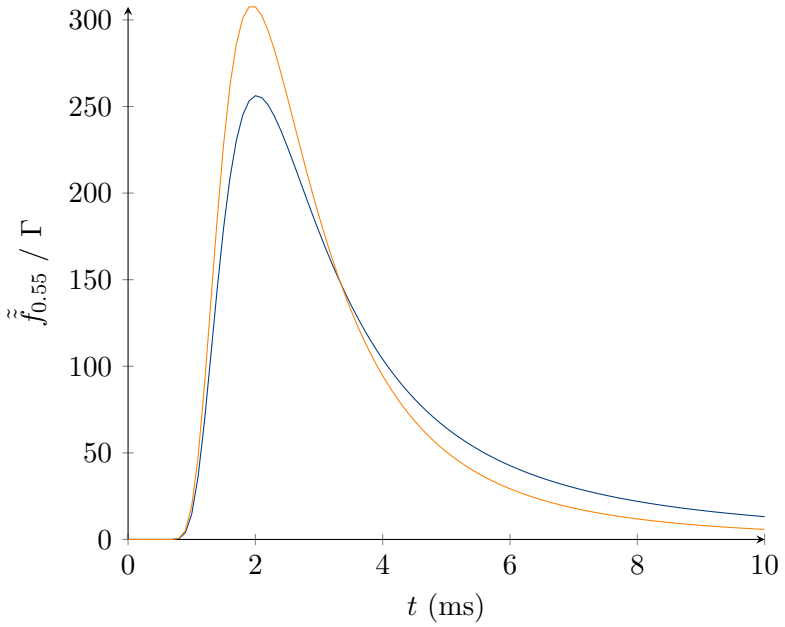

FIGURE 5.7: A comparison of $\tilde{\tilde{f}}_z(t)$ (blue, Eqn. (5.33)) and $\Gamma(t)$ (orange, Eqn. (5.34)) for a molecular beam with $v_{\mathrm{out}} = 145\,\mathrm{m\,s^{-1}}$, $\Delta v_z = \Delta v_\perp = 131\,\mathrm{m\,s^{-1}}$, and $z = 55\,\mathrm{cm}$. For $\Gamma(t)$, the collection efficiency is as in Figure 5.5 and laser pumping is on the CaF A–X transition with zero detuning. Both distribtions have been re-normalised to unit area.

$$\langle \Phi \rangle = \frac{N_{\text{beam}}}{\Omega} \int_0^{\Omega} \Phi_\infty(\Omega') \, \mathrm{d}\Omega', \tag{5.41}$$

where N_{beam} is the number of molecules in the beam, and $\Phi_\infty(\Omega')$ is the $t \to \infty$ limit of Φ_t (the total molecular intensity defined in Eqn. (5.28)) and Ω is the solid angle subtended by the smallest limiting aperture. $\langle \Phi \rangle$ has units of molecular intensity and so $\Omega \langle \Phi \rangle$ is the molecular flux, $\text{mol}\,\text{shot}^{-1}$. Since Ω is a known constant (for a given experiment), $\langle \Phi \rangle$ is also known as the flux. A measurement of $\Gamma(t)$ contains enough information to estimate $\langle \Phi \rangle$ as long as the efficiencies, scattering rates, and beam velocity are known. To see this we can modify Eqn. (5.34) to be in terms of the flux, rather than $f_t(\vec{r}, \vec{v})$, and the total photon count, $N_{\text{ph}} = \int_0^\infty \Gamma(t) \, \mathrm{d}t$:

$$N_{\text{ph}} \approx \eta_{\text{tr}} \eta_{\text{qu}} \langle \Phi \rangle \int_0^{\Omega} \int_0^{\infty} \eta_{\text{geo}}(\vec{r}) \; R(t, \rho, v_h) \; \mathrm{d}t \; \mathrm{d}\Omega', \tag{5.42}$$

where $\mathrm{d}\Omega = \sin(\alpha) \; \mathrm{d}\alpha \; \mathrm{d}\beta$. Although Eqn. (5.38) is time independent, in practice the scattering rate is time dependent. This is because the molecular transitions are not closed, and so with every scattering event there is a chance the molecule will decay to an unaddressed ground state sublevel. If the laser has a single frequency and only addresses a single ground state sublevel, then the decay to an unaddressed state will occur rapidly, reducing the scattering rate to zero. This means the number of photons emitted will approach a constant value quickly compared to the time taken for a molecule to cross the laser:

$$\int_0^t R(t', \rho, v_h) \; \mathrm{d}t' \to A(\rho, v_h) \text{ for } t \ll \frac{\sigma}{v_{\text{out}}}, \tag{5.43}$$

where $A(\rho, v_h)$ is now number of photons per molecule rather than scattering rate per molecule. Furthermore, we can approximate the transverse velocity, v_h as being:

$$v_h \approx h \left(\frac{\overline{SD'}}{v_{\text{out}}} \right)^{-1}, \tag{5.44}$$

that is, the transverse velocity needed for a molecule with average forward velocity to reach the point h along the $(y = 0, z = \overline{SD'})$ line of the detection beam. We can do this without accounting for the full convolution between $f_t(\vec{r}, \vec{v})$ and $A(\rho, v_h)$ because the molecular velocity distribution is much wider than the range of velocities with appreciable scattering rate, and so is approximately constant over the region where $A(\rho, v_h)$ is significant. Therefore, Eqn. (5.42) can be rearranged to find the molecular flux [13]:

$$\langle \Phi \rangle \approx \frac{N_{\text{ph}}}{\eta_{\text{tr}} \eta_{\text{qu}} \int_0^{\Omega} \eta_{\text{geo}}(\vec{r})\ A(\rho, v_h)\ \mathrm{d}\Omega'}. \tag{5.45}$$

Since v_h is estimated by Eqn. (5.44), the mean forward velocity, v_{out}, is needed. Therefore, we need to do a velocity measurement before we can do a molecular flux measurement.

5.2.2 Velocity & Flux Measurement

Returning to Eqn. (5.40), instead of setting $\omega_{\text{las}} = \omega_0$, we scan the laser frequency. This means that the scattering rate is now dependent on ω_{las} as well as ρ and v_h. Hence, the total photon count, N_{ph}, now depends on ω_{las} in a way that is related to the scattering rate's dependence on ω_{las}. In terms of the measured quantities, the integrated value of the PMT signal now has a frequency dependence:

$$\text{Spec}(\omega_{\text{las}}) = \int_0^{\infty} \text{Sig}(t, \omega_{\text{las}})\ \mathrm{d}t. \tag{5.46}$$

Therefore the TOF measurement can be used to perform spectroscopy on the molecule by varying the laser frequency. Figure 5.8 shows the hyperfine structure of the CaF $X^2\Sigma(N = 1)$ state obtained by varying the frequency of a laser pumping on the B–X transition. The detailed scan of the $F = 1^-$ peak shows that it follows a Lorentzian profile with a FWHM of 16 MHz.

We wish to determine the average velocity of the molecules. The detector is located a distance $\overline{SD}$ from the source aperature, S. If a molecule takes a time, t, to

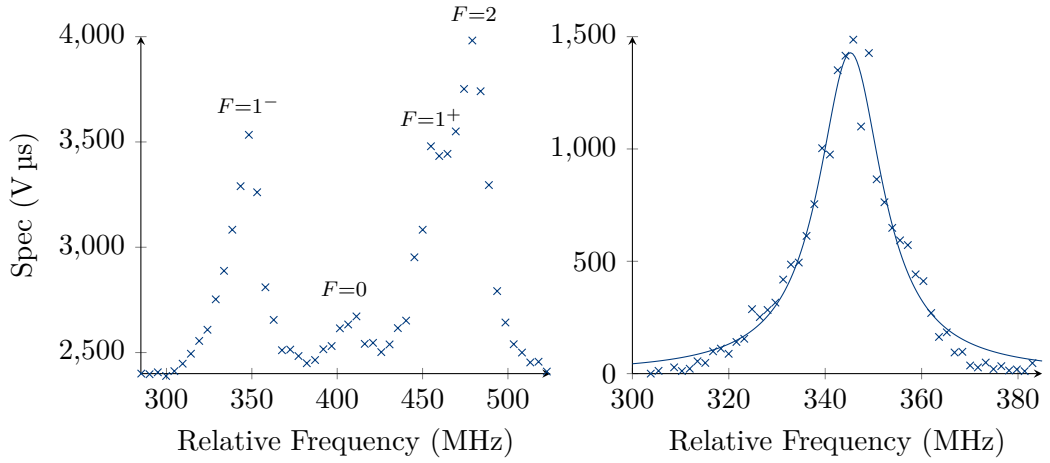

FIGURE 5.8: (left) Spectrum of the hyperfine structure of the CaF $X^2\Sigma(N=1)$ state, obtained by varying the frequency of a laser pumping on the B–X transition. (right) Detailed scan of the $F = 1^-$ peak, background subtracted and fitted to a Lorentzian profile.

arrive at the detector then the average velocity is:

$$v_{\text{out}} = \left\langle \frac{\overline{SD}}{t} \right\rangle . \tag{5.47}$$

If we consider the molecular distributions in Figure 5.7, we can find the average arrival time of the molecules at the detector, $\langle t \rangle = \int_0^\infty t \ \tilde{f}_z(t) \ \mathrm{d}t$. However, it is not true that this gives the mean z-velocity, v_{out}:

$$v_{\text{out}} \neq \frac{\overline{SD}}{\langle t \rangle}. \tag{5.48}$$

Therefore, some other method is needed to carry out a velocity measurement. We make use of spectroscopy and the Doppler effect.

In the standard detection setup described so far, the detection light is parallel to $\hat{h}$, perpendicular to the longitudinal axis of the molecular beam (i.e., $\hat{z}$). Therefore, the spectrum obtained is Doppler broadened by the velocity spread in the direction of the laser beam, but there is no overall Doppler shift. Further, the measured hyperfine spectrum contains no information about the speed in the z-direction. However, if the detection light is angled such that the $\vec{k}$ vector forms an angle β with $\hat{h}$:

$$\vec{k} = \cos(\beta)\ \hat{h} + \sin(\beta)\ \hat{z}, \tag{5.49}$$

then the Doppler shift will be:

$$\delta = \left(1 - \cos(\beta)\frac{v_h}{c} - \sin(\beta)\frac{v_z}{c}\right)\ \omega_{\text{las}} - \omega_0. \tag{5.50}$$

Averaged over all velocities in the molecular distribution, this creates a large Doppler broadening but also an overall Doppler shift of:

$$\Delta\omega = \omega_0 \left(1 - \frac{v_{\text{out}}}{c}\sin(\beta)\right), \tag{5.51}$$

where the transverse component, $\cos(\beta)v_h$ does not appear as it averages to zero. We use an experimental setup with $\beta = 30°$ pumping on the $X^2\Sigma(N = 1)$ B–X transition. The laser is scanned to obtain a spectrum of the $F = 1^-$ peak both with $\beta = 0°$ (i.e., the normal detection setup) and $\beta = 30°$. The results are shown in Figure 5.9 for a helium flow rate of 0.5 sccm. The power of laser varied with frequency in the $\beta = 30°$ scan, giving a sloping background. $\Delta\omega = (149 \pm 1)$ MHz. This gives an estimate of $v_{\text{out}} = (159 \pm 1)\,\text{m}\,\text{s}^{-1}$.

This process was repeated for buffer gas flow rates $\dot{V}_{\text{in}}^{\circ} \in \{0.3, 0.5, 0.7, 1.0\}$ sccm. The results are shown in Figure 5.10. As expected from Eqn. (5.25), v_{out} increases with flow rate. Since $\text{Re} \propto \dot{V}_{\text{in}}^{\circ}$ (see Eqn. (5.7)), the v_{out} data has been fitted with a modified form of Eqn. (5.25):

$$v_{\text{out}}(\text{CaF}) = v_{\text{ss}}(\text{Buff})\sqrt{1 - 4(m\dot{V}_{\text{in}}^{\circ} + c)^{-4/5}}. \tag{5.52}$$

The temperature in the cell was measured by a low temperature thermistor to be (5.2 ± 0.2) K. From Eqn. (5.4) we can see that this gives $v_{\text{ss}}(\text{Buff}) = (232 \pm 1)\,\text{m}\,\text{s}^{-1}$. Using this value for $v_{\text{ss}}(\text{Buff})$, the fitting gives model parameters $m = (4.3 \pm 0.6)\,\text{sccm}^{-1}$

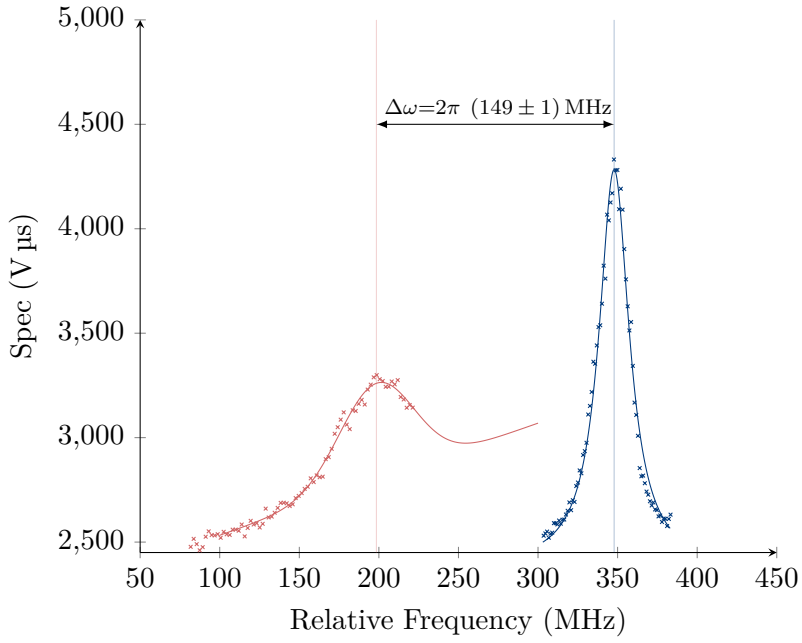

FIGURE 5.9: (blue) The stationary ($\beta = 0°$) $F = 1^-$ B–X line with a Lorentzian best fit. (red) The Doppler shifted ($\beta = 30°$) line fit with a Gaussian with a linear background in a beam produced with a He flow of 0.5 sccm. The Doppler shifted line has Gaussian Doppler broadening due to a contribution from the longitudinal velocity distribution. It can be seen that $\Delta\omega = 2\pi\ (149 \pm 1)$ MHz. Since $\omega_0 = 2\pi\ 5.9464$ THz [57], it follows from Eqn. (5.51) that the beam velocity is $(159 \pm 1)\,\mathrm{m\,s^{-1}}$.

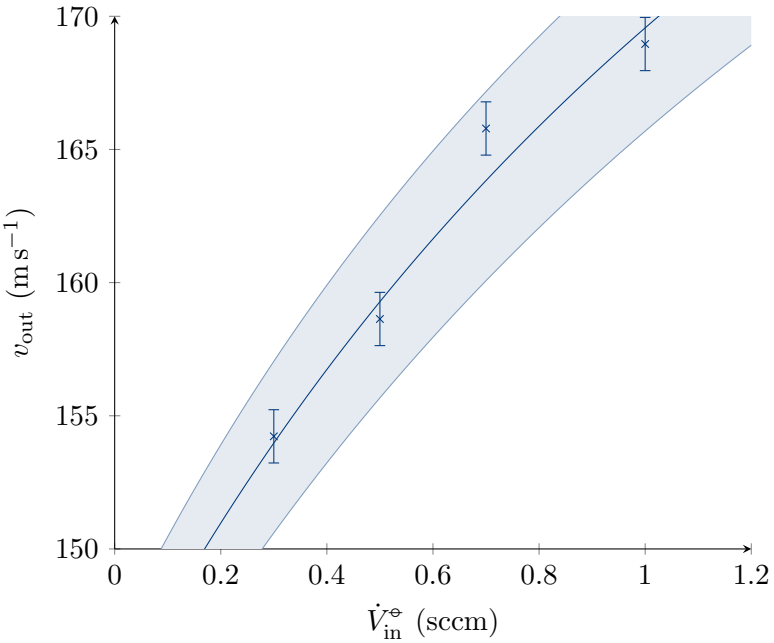

FIGURE 5.10: The beam velocity as measured using the Doppler shift of the $F = 1^-$ B–X line as it varies with bffer gas flow rate. A model of the form in Eqn. (5.52) has been fitted with $\mathrm{Re} = (4.3 \pm 0.6)\dot{V}_{\mathrm{in}}^{\circ}\ \mathrm{sccm}^{-1} + (10.4 \pm 0.3)$. The shaded band shows the error bounds of the fit.

and $c = 10.4 \pm 0.3$, meaning the Reynolds number at 0.5 sccm was 12.6 ± 0.6.

Once the average velocity of the molecules had been measured, a molecular intensity measurement for CaF was carried out. A single frequency 60 µW detection beam pumping from the $N = 1$, $F = 1^-$ hyperfine level of the $X^2\Sigma$ state to the $B^2\Sigma$ state was used. The beam profile was as in Figure 4.12. The SF_6 flow rate was 0.02 sccm. The transmission efficiency of the optics was measured to be $\eta_{\text{tr}} = 0.9$ and the quantum efficiency of the PMT is $\eta_{\text{qu}} = 0.09$ at 531 nm. Helium was used as a buffer gas and the flow rate was varied between 0.3 sccm and 2.5 sccm. The molecular flux, $\langle\Phi\rangle$, was calculated using Eqn. (5.45).

Ω was taken to be the solid angle the detection region subtends relative to the source, Ω_{det}[7]. The detection light is modelled as a Gaussian beam with a $1/e^2$ width of $4\sigma = 3$ mm. The acceptence in transverse velocity is modelled as being limited to $\Delta v_{\text{Dopp}} = 10\,\text{m}\,\text{s}^{-1}$ due to the Doppler effect. The solid angle subtended by the detection region is (by definition for small solid angles) $\Omega_{\text{det}} = A \times \left(\overline{SD'}\right)^{-2}$, where A is the area of the region in the x-y plane (i.e., perpendicular to the beamline). We take A to be the area of an ellipse with radii 2σ and $\Delta v_{\text{Dopp}} \times \left(\overline{SD'}\right)/v_{\text{out}}$, giving:

$$\Omega_{\text{det}} = \frac{2\pi\sigma\Delta v_{\text{Dopp}}}{v_{\text{out}}\overline{SD'}}. \tag{5.53}$$

The results for the flux measurement are shown in Figure 5.11. As can be seen, the flux increases non-linearly with flow rate.

These data were then fitted to the theoretical model given in Eqn. (5.41). Here, N_{beam} is the number of molecules in the beam. We can write this in terms of the number of molecules produced in the cell, $N_{\text{cell}}(0)$, and the extraction efficiency, η_{beam} (Eqn. (5.15)): $N_{\text{beam}} = N_{\text{cell}}(0)\eta_{\text{beam}}$. The integral in Eqn. (5.41) gives the fraction of the molecular intensity distribution within Ω_{det} and we label this η_{det}. Then, Eqn. (5.41) becomes:

[7] There is, additionally, a 1 inch aperture in the beamline at $z = 230$ mm (the radiation shield lid, see Chapter 4) which subtends a solid angle of $(3 \times 10^{-3})\pi$ at the source. However, Ω_{det} is smaller than this and so this aperture has no effect on $\langle\Phi\rangle$.

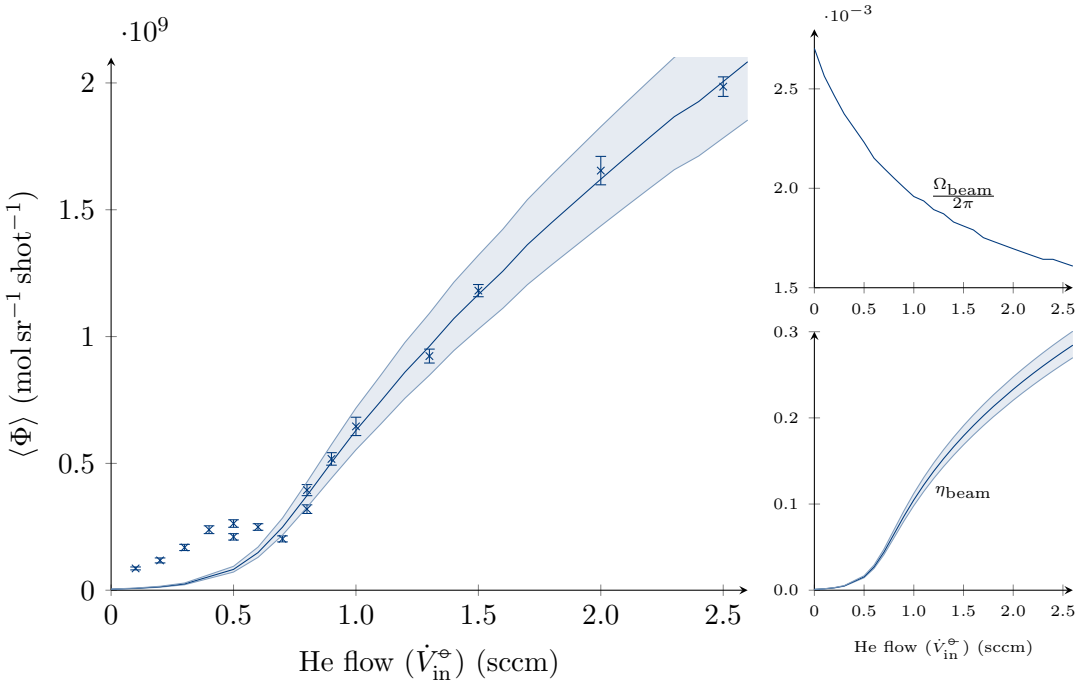

FIGURE 5.11: (left) Molecular flux, $\langle\Phi\rangle$ for various He flow rates, $\dot{V}_{\text{in}}^{\ominus}$. The data above 0.5 sccm has been fitted with the model given in Eqn. (5.54) with $N_{\text{cell}}(0) = (7.4 \pm 0.5) \times 10^7$ mol and $\tau_{\text{pump}} = (5.2 \pm 0.4)$ ms. (right) The two components for the model, Ω_{beam} and η_{beam}. Ω_{beam} is shown as the fraction of a hemisphere occupied (i.e., divided by 2π). It can be seen the η_{beam} provides the main contribution to the shape of the overall model.

$$\langle\Phi\rangle = \frac{\eta_{\text{beam}} N_{\text{cell}}(0)}{\Omega_{\text{det}}} \eta_{\text{det}}. \tag{5.54}$$

The extraction efficiency, η_{beam}, depends on the convective pump-out time, τ_{pump} (Eqn. (5.17), a constant for a given temperature and cell geometry), and τ_{diff} (Eqn. (5.21)) which depends strongly on the flow rate. For reference, we repeat all the relevant equations here, breaking them down to find their dependence on flow rate, $\dot{N}_{\text{in}}$ or $\dot{V}_{\text{in}}^{\ominus}$, or mean z-velocity, v_{out}, which depends on $\dot{V}_{\text{in}}^{\ominus}$ according to Eqn. (5.52):

$$\langle \Phi \rangle = \eta_{\text{beam}} N_{\text{cell}}(0) \frac{\eta_{\text{det}}}{\Omega_{\text{det}}} \tag{5.54}$$

$$\eta_{\text{beam}} = \frac{\tau_{\text{diff}}}{\tau_{\text{diff}} + \tau_{\text{pump}}} \tag{5.15}$$

$$\Omega_{\text{det}} = \frac{2\pi\sigma\Delta v_{\text{Dopp}}}{v_{\text{out}}\overline{SD'}} \tag{5.53}$$

$$\eta_{\text{det}} = \int_0^{\Omega_{\text{det}}} \Phi_\infty(\Omega')\, \mathrm{d}\Omega' \tag{5.41}$$

$$\tau_{\text{diff}} = \lambda\sqrt{\frac{m_{\text{CaF}}}{3k_{\text{B}}T_{\text{b}}}} \int_0^{\mathcal{N}_{\text{diff}}} \left(1 + \left(\frac{T_{\text{s}}(0)}{T_{\text{b}}} - 1\right)\exp\left(-\frac{\mathcal{N}}{\nu}\right)\right)^{-\frac{1}{2}} \mathrm{d}\mathcal{N} \tag{5.21}$$

$$\mathcal{N}_{\text{diff}} = \frac{4}{9}\sqrt{\frac{6}{\pi}}\,\frac{s^2}{\lambda^2}\sqrt{\frac{m_{\text{He}}}{m_{\text{CaF}} + m_{\text{He}}}} \tag{5.19}$$

$$\lambda = \frac{k_{\text{B}}T_{\text{b}}}{p_{\text{cell}}^{\text{Buff}}\sigma_{\text{Buff}} + p_{\text{cell}}^{\text{SF}_6}\sigma_{\text{SF}_6}}$$

$$p_{\text{cell}}^{\text{Buff}} = \frac{8\sqrt{2}}{3}\frac{\dot{N}_{\text{in}}(\text{Buff})}{\pi r_{\text{cell}}^2}\sqrt{\frac{m_{\text{He}}k_{\text{B}}T_{\text{b}}}{\pi}} \tag{5.8}$$

where ν is the ratio of the mean mass to the reduced mass, s is the diffusion length scale $\sim 2\,\text{cm}$, and σ_{Buff} and σ_{SF_6} are collision cross-sections between CaF and He and SF_6 respectively. $\Phi_t(\alpha, \beta)$ is estimated using a Gaussian beam as shown in Section 5.1.4, at a temperature of 5.2 K and with forward velocity, v_{out}, given by Eqn. (5.52). All other parameters in this model are fixed relative to the buffer gas flow rate except the convection timescale, τ_{pump}, which is known to be on the order of 15 ms (see Eqn. (5.17)), and the initial number of CaF molecules produced in the cell, $N_{\text{cell}}(0)$. τ_{pump} and $N_{\text{cell}}(0)$ are taken to be free parameters available for fitting. τ_{pump} affects the shape of the curve and $N_{\text{cell}}(0)$ gives the overall scale.

The model for τ_{diff} is valid for $\lambda \ll s$. If the mean free path is too long then the calcium will have too few collisions for the continuous approximation in Eqn. (5.20) to be valid. $\lambda \sim \frac{1}{\dot{V}_{\text{in}}^{\circ}}$ and the model is a good fit for $\dot{V}_{\text{in}}^{\circ} > 0.5\,\text{sccm}$, at which point $\lambda \sim 0.15s$. The fitted model is shown in Figure 5.11, along with all the data. The model parameters are $N_{\text{cell}}(0) = (7.4 \pm 0.5) \times 10^7$ mol and $\tau_{\text{pump}} = (5.2 \pm 0.4)$ ms.

Additionally, $\Omega_{\text{det}}/\eta_{\text{det}} \sim \Omega_{\text{beam}}$ gives the effective solid angle occupied by the beam. This can be seen by considering η_{det} to be the ratio of the detector's solid angle to the beam's solid angle, $\eta_{\text{det}} \sim \Omega_{\text{det}}/\Omega_{\text{beam}}$. A plot of Ω_{beam} is also shown in Figure 5.11. It can be seen that the effective solid angle occupied by the beam decreases with increasing flow rate, as the beam becomes more tightly confined with increasing v_{out}. Also shown is a plot of η_{beam}, which shows that this provides the main contribution to the shape of the overall model.

Finally, given that we estmate 10^{15} Ca particles are available in the cell to react and we measure $N_{\text{cell}}(0) = (7.4 \pm 0.5) \times 10^7$ mol, we get a reaction efficiency of $\eta_{\text{react}} \approx 7 \times 10^{-8}$. This is seven orders of magnitude lower than the upper bound of 0.26. Even accounting for the optimistic nature of that bound, the measured value is very low. $\langle\Phi\rangle$ is one to two orders of magnitude smaller than that which has been measured in similar sources [13]. It seems likely that the low beam intensity contributes to the experimental problems described in Chapter 6.

5.2.3 Velocity Distribution

It is also possible to get the full velocity distribution from the same spectral data collected to find the central velocity of the beam, v_{out}. Instead of integrating the PMT signal from $t = 0$ to $t = \infty$ to get the red curve in Figure 5.9, we split it up into segments:

$$\text{Spec}_i(\omega) = \int_{t_i}^{t_i+\delta t} \text{Sig}(t, \omega)\ \text{d}t. \tag{5.55}$$

This means that for each i we are only looking at the molecules that arrive between t_i and $t_i + \delta t$. For sufficiently small δt these molecules will all have the same velocity. Each $\text{Spec}_i(\omega)$ will then be Doppler shifted by a different amount. Figure 5.12 shows $\text{Spec}_i(\omega)$ for $t_i \in \{1.7, 1.9, 2.1, 2.3, 2.5, 2.7\}$ ms and $\delta t = 0.2$ ms for the same TOF measurement taken at $\beta = 30°$ and shown in Figure 5.9 in red.

Each $\text{Spec}_i(\omega)$ gives a different $\Delta\omega_i$ from which a velocity, v_i, can be calculated using Eqn. (5.51). This gives a set of data, $\{(t_i, v_i)\}$, which can be used to fit a time-velocity calibration curve. From standard kinematics it is expected that $t_i \propto 1/v_i$.

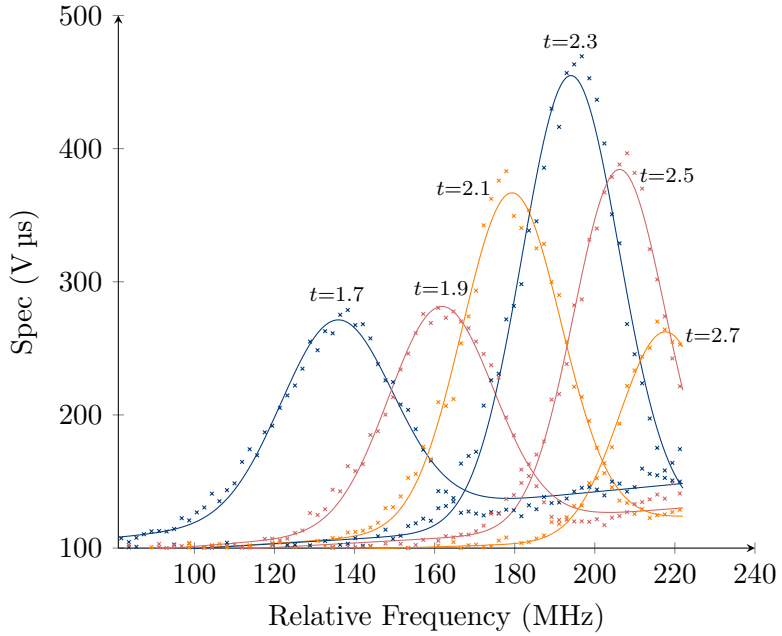

FIGURE 5.12: The same spectrum taken at $\beta = 30°$ shown in red in Figure 5.9 but now divided into time periods with $t_i \in \{1.7, 1.9, 2.1, 2.3, 2.5, 2.7\}$ ms and $\delta t = 0.2$ ms. The different Doppler shifts for the different arrival times of the molecules can clearly be seen.

This is shown in Figure 5.13, and the best fit line is:

$$t = (0.16 \pm 0.04)\,\text{ms} + \frac{(352 \pm 7)\,\text{mm}}{v}. \tag{5.56}$$

This fit accurately finds the distance from the source to the detector to be 35 cm. We interpret the 160 µs offset to be the time taken for a given molecule to emerge from the cell.

A TOF measurement, as described in Section 5.2.1, was then taken with the detection light on-resonance ($\omega_{\text{las}} = \omega_0$) with the B–X transition and orthogonal ($\beta = 0°$) to the beamline. The collected PMT signal is shown in red in Figure 5.14. Eqn. (5.56) was used to transform this into a velocity space signal, $\text{Sig}(t) \to \text{Sig}(t(v))$. This is shown in orange in Figure 5.14. The velocity space distribution clearly has non-equilibrium (i.e., non-Gaussian) features. However, it is a good fit for a double Gaussian:

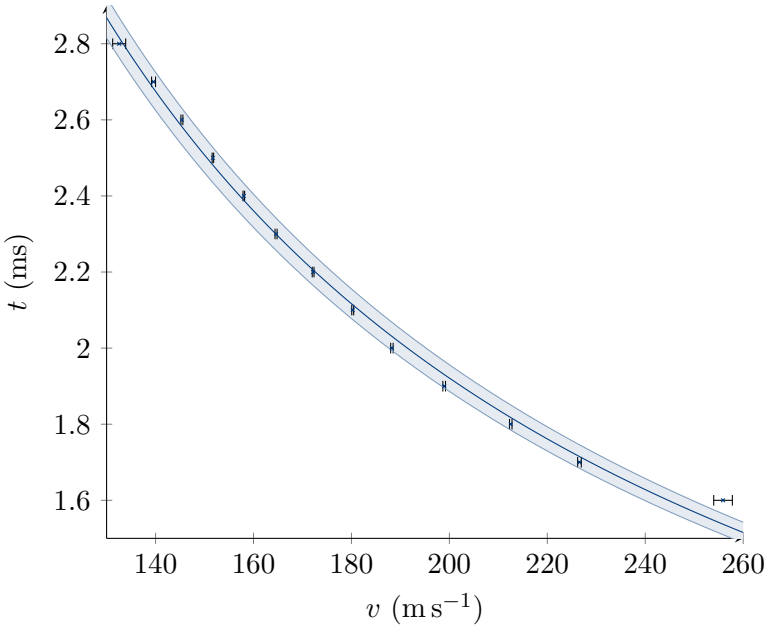

FIGURE 5.13: The velocity-time graph found from the split spectrum taken at $\beta = 30°$ shown in red in Figure 5.9 and with the split spectra shown in Figure 5.12. The best fit is $t = (0.16 \pm 0.04)\,\mathrm{ms} + \frac{(352 \pm 7)\,\mathrm{mm}}{v}$ and the error bounds are also plotted.

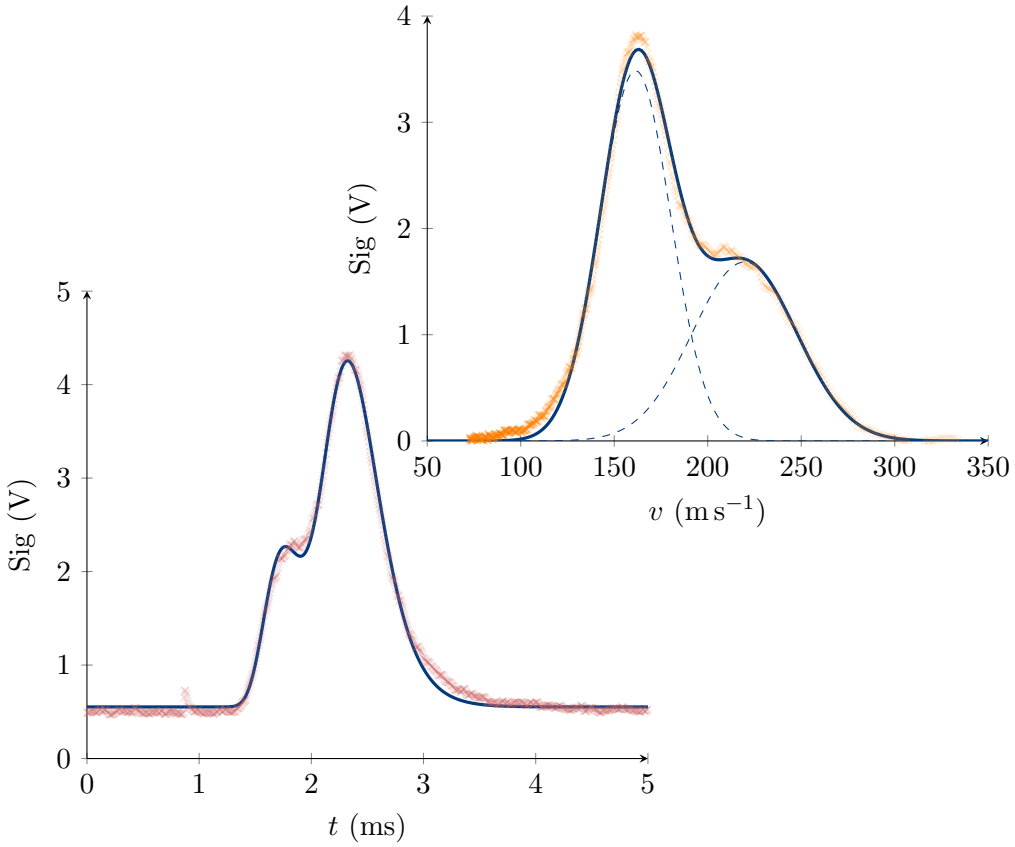

FIGURE 5.14: A TOF (red) shown fitted with Eqn. (5.59). Also shown is the data transformed into velocity-space according to Eqn. (5.56) (orange) and fitted with Eqn. (5.57).

$$G_2(v_z) = \frac{w}{\Delta v_z\sqrt{2\pi}}\exp\left(-\frac{(v_z - v_{\text{out}})^2}{2\Delta v_z^2}\right) + \frac{w'}{\Delta v_z'\sqrt{2\pi}}\exp\left(-\frac{(v_z - v_{\text{out}}')^2}{2\Delta v_z'^2}\right), \quad (5.57)$$

where w and w' are the relative weights of each component, so that the normalisation is $\int_{-\infty}^{\infty} G_2(v_z)\,\mathrm{d}v_z = w+w'$. The fit is shown in Figure 5.14. The main component has relative weighting $w/(w+w') = 0.58 \pm 0.02$ and mean velocity $v_{\text{out}} = (161 \pm 1)\,\mathrm{m\,s^{-1}}$. This agrees with the $(159 \pm 1)\,\mathrm{m\,s^{-1}}$ measured from the overall Doppler shift in Figure 5.9. The secondary component has mean $v_{\text{out}}' = (220 \pm 1)\,\mathrm{m\,s^{-1}}$. The widths are $\Delta v_z = (18.9 \pm 0.1)\,\mathrm{m\,s^{-1}}$ and $\Delta v_z' = (28 \pm 1)\,\mathrm{m\,s^{-1}}$. The predicted velocity width at 5.2 K is $27\,\mathrm{m\,s^{-1}}$ (Eqn. (5.25)), which agrees with the width of the secondary component.

We can generate a modelled TOF by modifying Eqn. (5.23) to include the double Gaussian term from Eqn. (5.57):

$$f_0(\vec{r},\vec{v}) = \left(\frac{2}{\pi}\right)^3 \frac{1}{r_{\text{cell}}^2 L_{\text{cell}}}\frac{1}{\Delta v_\perp^2}\exp\left(-\frac{8\rho_\perp^2}{r_{\text{cell}}^2} - \frac{8z^2}{L_{\text{cell}}^2} - \frac{v_\perp^2}{2\Delta v_\perp^2}\right)\sqrt{2\pi}G_2(v_z). \quad (5.58)$$

When integrated this gives a modified form of Eqn. (5.33):

$$\begin{aligned}\tilde{\tilde{f}}_z(t) = \frac{4}{L_{\text{cell}}}\frac{1}{\sqrt{2\pi}}&\left(\left[1+\frac{t^2}{\tau^2}\right]\left[1+\frac{t^2}{\tau'^2}\right]\right)^{-3/2}\Bigg\{ \\ &\times w\,\exp\left(-\frac{8}{L_{\text{cell}}^2}\frac{(z - v_{\text{out}}t)^2}{1+\frac{t^2}{\tau^2}}\right)\left[v_{\text{out}} + \frac{zt}{\tau^2}\right]\left[1+\frac{t^2}{\tau'^2}\right]^{3/2} \\ &+ w'\,\exp\left(-\frac{8}{L_{\text{cell}}^2}\frac{(z - v_{\text{out}}'t)^2}{1+\frac{t^2}{\tau'^2}}\right)\left[v_{\text{out}} + \frac{zt}{\tau'^2}\right]\left[1+\frac{t^2}{\tau^2}\right]^{3/2}\Bigg\},\end{aligned} \quad (5.59)$$

where $\tau = \frac{L_{\text{cell}}}{4\Delta v_z}$ and $\tau' = \frac{L_{\text{cell}}}{4\Delta v_z'}$. The values of v_{out}, Δv_z, v_{out}', and $\Delta v_z'$ were fixed from the $G_2(v_z)$ fit, $L_{\text{cell}} = 2\,\mathrm{cm}$, and $z = \overline{SD'} = 35\,\mathrm{cm}$. w was left as a fitting parameter, with $w' = 1 - w$ to ensure $\tilde{\tilde{f}}_z(t)$ was normalised to unity. Additionally, overall scale, S, background, B, and time offset, t_0, were added. Thus the final model fitted was $S\tilde{\tilde{f}}_z(t - t_0) + B$. The result is shown in Figure 5.14. The fitted parameters were $S = (3054 \pm 7)\,\mathrm{V\,\mu s}$, $B = (0.551 \pm 0.003)\,\mathrm{V}$, $t_0 = (227 \pm 1)\,\mu\mathrm{s}$, and

$w = 0.723 \pm 0.001$.

The analysis was repeated for buffer gas flow rates $\dot{V}_{\text{in}}^{\text{e}} \in \{0.3, 0.5, 0.7, 1.0\}$ sccm, using the same data used to produce Figure 5.10. The best fit parameters are shown in Figure 5.15. From this, it can be seen that the mean velocities of both components, v_{out} and v'_{out}, increase with $\dot{V}_{\text{in}}^{\text{e}}$, though neither agree with the modal velocity shown in Figure 5.10 and reproduced in (c) of Figure 5.15. (c) shows that the gap between the model velocity and the mean velocity of the main component, v_{out}, is decreasing as $\dot{V}_{\text{in}}^{\text{e}}$ increases.

Furthermore, (b) shows that whilst the width of the secondary component, $\Delta v'_z$, decreases with $\dot{V}_{\text{in}}^{\text{e}}$, the width of the main component, Δv_z, remains relatively constant, as predicted by theory (Eqn. (5.25)). The weight of the secondary component decreases with increasing $\dot{V}_{\text{in}}^{\text{e}}$, as shown in (a).

This indicates that the primary component (i.e., the one which provides the larger peak) is closer to the predicted equilibrium conditions, and the secondary component is a non-equilibrium contribution that diminishes with increasing $\dot{V}_{\text{in}}^{\text{e}}$. As the gas flow increases, the pressure in the cell increases. This allows the Ca and CaF particles to undergo more collisions with the buffer gas prior to leaving the cell. It takes 40–50 collisions for an ablated Ca or CaF particle to reach thermal equilibrium (Eqn. (5.20)) and this is only achieved above $\dot{V}_{\text{in}}^{\text{e}} \sim 1.2\,\text{sccm}$ (Eqn. (5.19)).

5.3 Outlook

The chapter developed a model for the mean velocity, v_{out}, and molecular flux, $\langle\Phi\rangle$, of a CaF molecular beam. The model was fitted to experimental data produced by the molecular source described in Chapter 4. The Reynolds number appropriate to the CaF molecules in the beam was found to vary with buffer gas flow rate, $\dot{V}_{\text{in}}^{\text{e}}$:

$$\text{Re}(\dot{V}_{\text{in}}^{\text{e}}) = \dot{V}_{\text{in}}^{\text{e}}(4.3 \pm 0.6)\,\text{sccm}^{-1} + (10.4 \pm 0.3),$$

and the average velocity of the beam was found to vary with Reynolds number according to Eqn. (5.52). At a buffer gas flow rate of $\dot{V}_{\text{in}}^{\text{e}} = 0.5\,\text{sccm}$, the molecular source produced a beam with $v_{\text{out}} = (159 \pm 1)\,\text{m}\,\text{s}^{-1}$ and $\text{Re} = 12.6 \pm 0.6$.

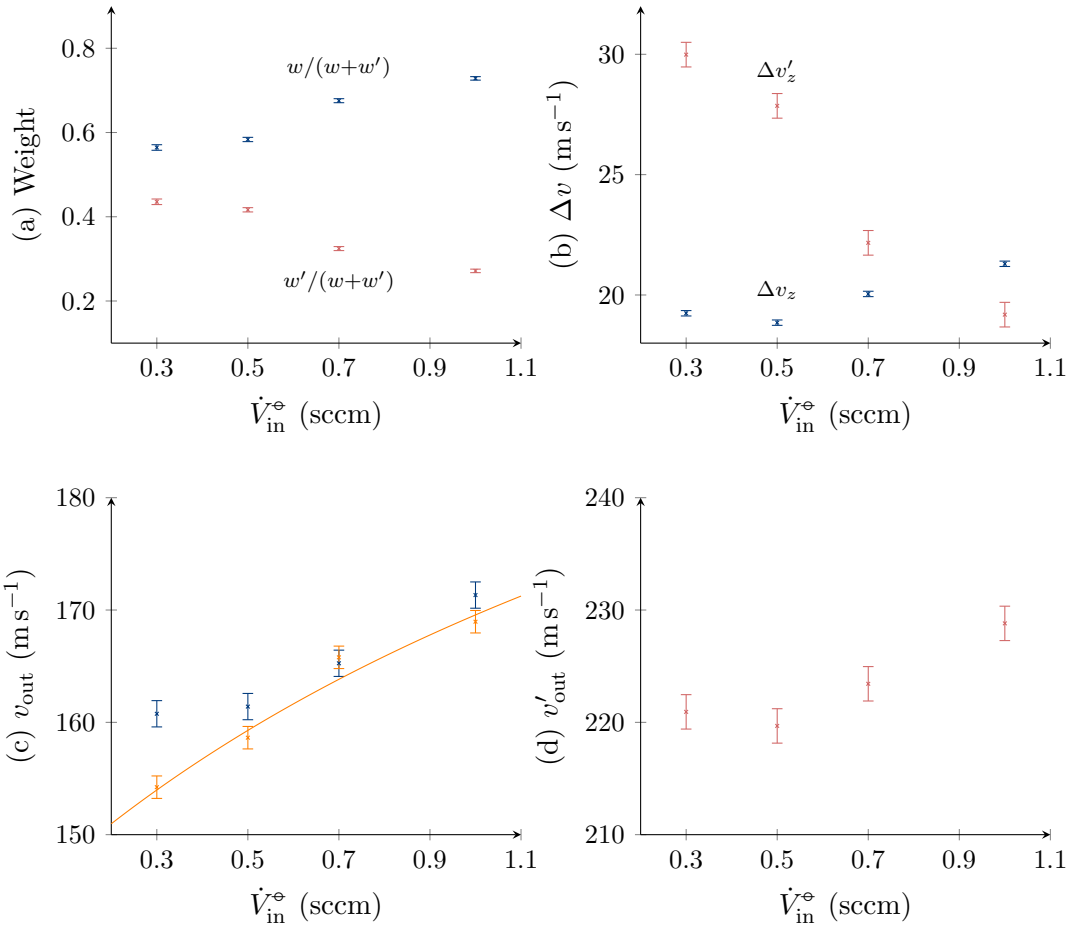

FIGURE 5.15: The variation of the fitted parameters of Eqn. (5.59) with helium flow rate, $\dot{V}_{\text{in}}^{\ominus}$. (a) shows the relative weighting of the two Gaussian components. It can be seen that the secondary component is reducing with increasing flow rate, indicating better thermalisation of the CaF. (b) shows the longitudinal velocity spread which is indicative of the temperature. It can be seen that the temperature of the secondary component approaches tht of the primary component at higher $\dot{V}_{\text{in}}^{\ominus}$, again indicating better thermalisation. (c) and (d) show the mean longitudinal velocity of the primary and secondary components respectively. It can be seen that the primary component is mostly in agreement with the modal velocity shown in Figure 5.10 and reproduced in (c) in orange, together with the fit from Eqn. (5.52).

The average molecular flux of the beam, $\langle\Phi\rangle$, was then measured. It also varied with buffer gas flow rate, but was of order $10^9\,\mathrm{mol\,sr^{-1}\,shot^{-1}}$. The beam was found to occupy a solid angle of around $10^{-2}\,\mathrm{sr}$. The convective pump-out time was measured to be $\tau_{\mathrm{pump}} = (5.2 \pm 0.4)\,\mathrm{ms}$ and number of CaF molecules in the cell was $N_{\mathrm{cell}}(0) = (7.4 \pm 0.5) \times 10^7\,\mathrm{mol}$. It was predicted that 10^{15} Ca particles would be liberated from the ablation target, giving an estimated reaction efficiency of $\eta_{\mathrm{react}} \approx 7 \times 10^{-8}$.

Finally, the velocity distribution of the molecular beam was measured. Velocity was found to be related to arrival time at the detector by:

$$t = (0.16 \pm 0.04)\,\mathrm{ms} + \frac{(352 \pm 7)\,\mathrm{mm}}{v}. \tag{5.56}$$

Further, the molecular beams were found to contain prominent non-equilibrium features. However, as buffer gas flow rate increased, these non-equilibrium features diminished.

With the beam now characterised, we can turn towards attempting to test the ZSD developed for CaF and described in Chapter 3. These attempts are described in Chapter 6.

Chapter 6

Downstream Beam Detection

In order to test the Zeeman-Sisyphus deceleration scheme, it is necessary to be able to detect the molecular beam at the exit of the decelerator, at $z = 1\,\mathrm{m}$. Then the molecular signal with and without the decelerator can be compared.

We had initial success in finding a molecular beam downstream and were able to gather some preliminary results on the guiding capabilities of the Zeeman-Sisyphus decelerator. These are presented in Section 6.1. These results were gathered using the long charcoal pump with a source-decelerator gap of 230 mm. To improve the signal at the exit of the decelerator, the decelerator was removed and the experiment modified to the form with the re-entrant radiation shield lid shown in Figure 6.2. Unfortunately, this resulted in a loss of the downstream signal which could not then be recovered. Various investigations were carried out to attempt to regain a signal downstream. None of these were successful. Nevertheless, the results from these investigations are presented in Section 6.2. Finally, a neon buffer gas source was trialled. Whilst this also failed to recover the downstream signal, the results from it are presented in Section 6.3.

6.1 Initial Success

The Zeeman-Sisyphus decelerator described in Section 3.3 was installed in the beamline, housed in vacuum chamber sections A and B with the exit in section C (see Figure 4.1). The long charcoal pump was used and the entrance of the decelerator was located 230 mm from the exit of the buffer gas cell. Experimental parameters of $\dot{V}_{\mathrm{in}}^{\circ}(\mathrm{He}) = 0.5\,\mathrm{sccm}$, $\dot{V}_{\mathrm{in}}^{\circ}(\mathrm{SF_6}) = 0.05\,\mathrm{sccm}$, and F2Q = 200 µs were used. The probe light was 531 nm light pumping on the $B^2\Sigma$–$X^2\Sigma$ transition with 24 MHz sidebands

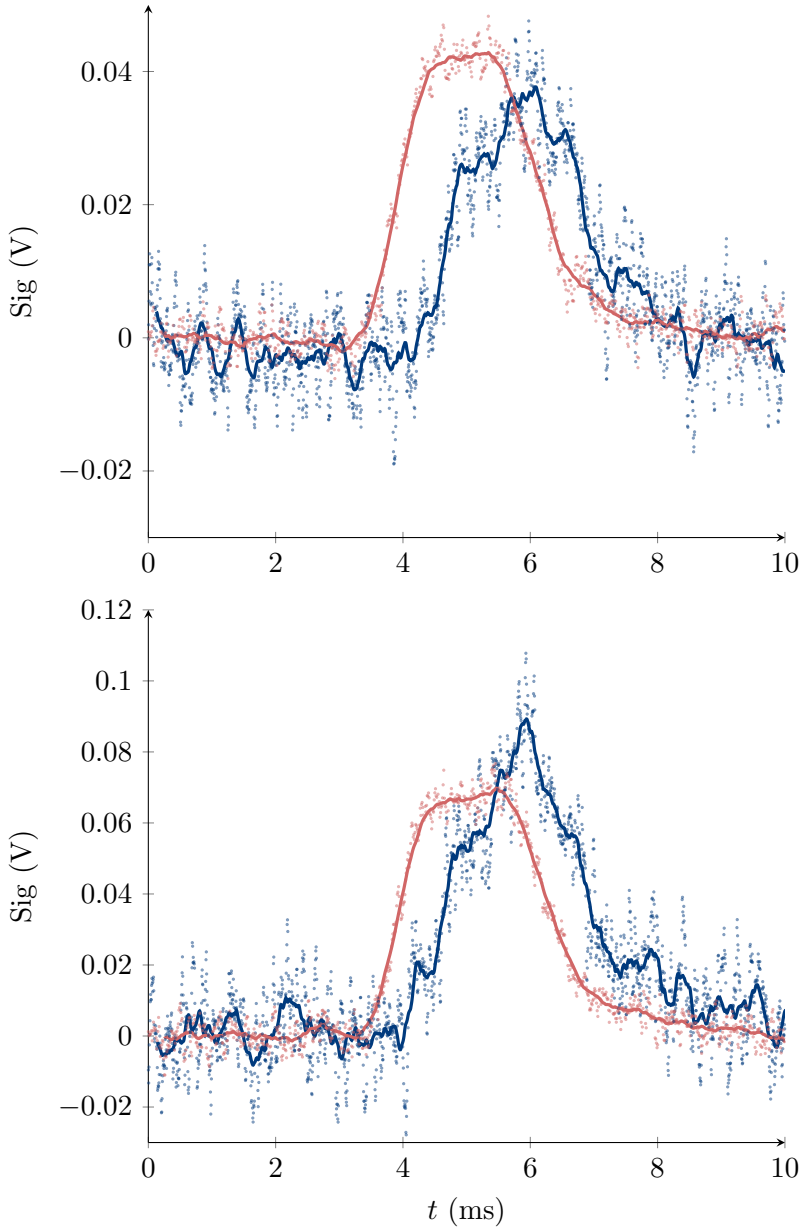

FIGURE 6.1: The background subtracted downstream TOF signal with the Zeeman-Sisyphus decelerator (blue) and without (red). 531 nm detection light was used with an intensity of $25\,\mathrm{W\,m^{-2}}$ and a $1/e^2$ width of 9 mm (top) or 15 mm (bottom). Data shown is the average of 100 shots and the lines show a 50-sample moving average. With the 15 mm probe light the total signal increases from $(166 \pm 6)\,\mathrm{V\,\mu s}$ without the decelerator to $(250 \pm 20)\,\mathrm{V\,\mu s}$ with the decelerator. With the 9 mm probe light the signal increases from $(102 \pm 3)\,\mathrm{V\,\mu s}$ to $(112 \pm 8)\,\mathrm{V\,\mu s}$.

so that all ground state hyperfine levels were addressed. A telescope was used to vary the probe beam size from a $1/e^2$ width of 3 mm to 15 mm. A constant laser intensity of 25 W m^{-2} was maintained accross all probe beam sizes.

Results of TOF measurements both with (blue) and without (red) the ZSD and with both a 9 mm and a 15 mm probe beam are shown in Figure 6.1. No ZS pump light was used so the decelerator was operating in purely guiding mode. Not shown is the mean background level, with was (2.6518 ± 0.0005) V for the 9 mm probe and (9.1551 ± 0.0009) V for the 15 mm probe. Although the 15 mm probe gave better results, the high background levels meant we were in danger of saturating the PMT. This motivated some of the investigations discussed in Section 6.2.1.

It can clearly be seen from Figure 6.1 that molecules are transmitted through the decelerator. With the 15 mm probe light the total signal increases from (166 ± 6) V µs without the decelerator to (250 ± 20) V µs with the decelerator. This is a 51% increase in total signal. However, this increase was of the same order of magnitude as the variance in the molecular signal observed across different days. Therefore, it was not possible to draw any definitive conclusions with regard to the guiding ability of the decelerator.

The simulations shown in Figure 3.15 indicate that reducing the gap between the cell and the entrance to 10 cm will result in 3× more molecules being accepted into the decelerator, and so will increase the signal at the exit. As such, it was hoped that reducing the source-decelerator gap would increase the signal at the end and provide stronger evidence for guiding. In order to achieve this, the experiment was modified to the form with the re-entrant radiation shield lid shown in Figure 6.2.

The standard charcoal pump used is 250 mm long. The upper inner radiation shield is long enough to accomodate this. However, this setup means that the entrance to the decelerator is located 230 mm from the source. The simplest way to achieve a smaller source-decelerator gap was to remove the lid of the charcoal pump and allow the entrance of the decelerator to sit inside it. However, the decelerator was in thermal contact with the room temperature walls of the vacuum chamber and so had to be radiatively separated from the charcoal. To achieve this, a top-hat shaped re-entrant radiation shield lid was used. The lid allowed the decelerator to sit inside the charcoal pump whilst being radiatively separated from it. CAD drawings of this

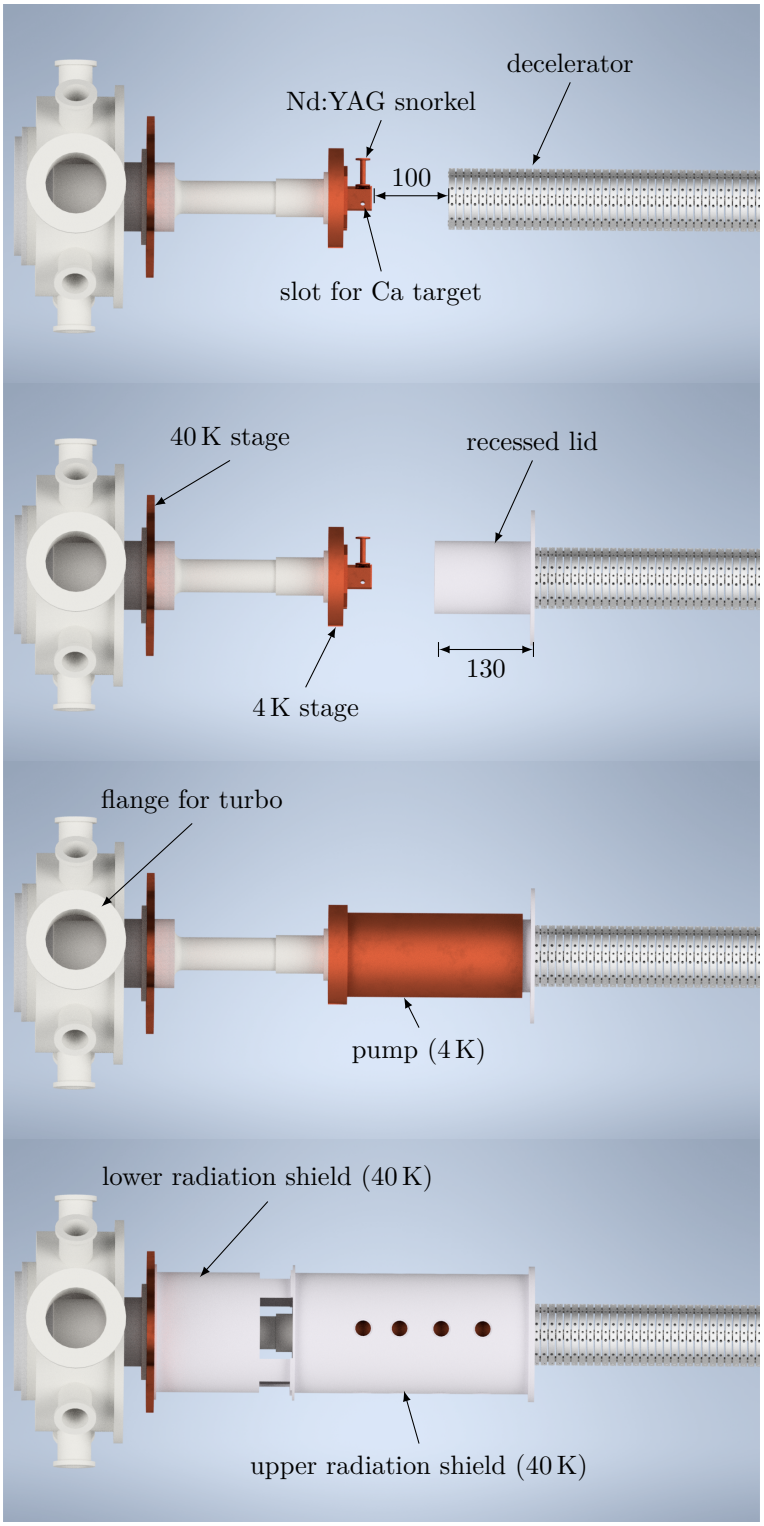

FIGURE 6.2: (mm; to scale; x-z plane) CAD models of the source portion of the CaF beamline showing (top to bottom): the cryostat, buffer gas cell, and decelerator; the addition of the recessed radiation shield lid; the charcoal pumps (optical access not shown); and the radiation shields.

setup are shown in Figure 6.2. The setup reduced the source-decelerator distance to 0.1 m.

Unfortunately, this setup resulted in a loss of the downstream signal. It was thought that the lid of the charcoal pump provided a significant fraction of the helium pumping ability and so could not be removed without compromising the effectiveness of the pump. Hence, a short, 120 mm long, charcoal pump was tried. This allowed the source-decelerator distance to be maintained at 0.1 m whilst keeping the lid of the charcoal pump. However, the reduction in charcoal surface area was found to reduce the pumping speed and the total capacity of the pump too much. The setup was therefore reverted to the standard setup with the long charcoal pump and ordinary, flat radiation shield lid.

Despite this reversion, the downstream signal was never recovered. Nonetheless, the results of various investigations carried out to attempt to recover the downstream signal are presented in Section 6.2.

6.2 Further Investigations

A series of beam detection experiments were conducted to try to recover the downstream beam seen in Section 6.1. They all utilised light from the Spectra 380 dye laser at 606 nm pumping on the $A^2\Pi_{1/2}(J = 1/2^+)$–$X^2\Sigma(N = 1)$ transition. An EOM was used to induce 24 MHz frequency sidebands on the pump light, ensuring that all ground state hyperfine components were addressed.

While none of the experiments were successful, the results of the various investigations carried out are presented in this section. Section 6.2.1 provides details on various methods used to reduce noise at the downstream detector and verifies that the theory presented in Chapter 5 indicates that a beam ought to be visible. Results from a trial of the Raman Resonance Optical Cycling (RROC) background-free imaging scheme proposed in [21] are presented in Section 6.2.2. Given the theory indicated that the beam ought to be visible, it was thought that perhaps the pressure in the chamber was too high and was reducing the mean free path of the molecules. Therefore, various different configurations of the adsorptive charcoal pumps were tried in an attempt to reduce the pressure. Details of these are given in Section 6.2.3. These

experiments were unsucessful at reducing the pressure sufficiently and so a neon buffer gas was tried, as it is easier to pump neon than helium. The setup and results from the neon buffer gas are given in Section 6.3.

6.2.1 Noise Reduction

The molecular beam expands in space as it moves through the chamber. This causes the molecular density to fall as the beam spreads out. Since the downstream detection point is at $\overline{SD'} = 1\,\text{m}$, the reduction in density presents a challenge on the face of it for detection. The predicted decay of the beam signal is shown in Figure 6.3, which has numerically calculated points from Eqn. (5.34). The data is normalised to the peak signal at the upstream detection point, with $\overline{SD'} = 55\,\text{mm}$.

Figure 6.3 shows that at $\overline{SD'} = 1\,\text{m}$ the peak signal is only 0.1% that of that peak signal at $\overline{SD'} = 55\,\text{mm}$. However, as shown in Section 4.4, the downstream detection point has a geometric efficiency 49× greater than that of the upstream detection point. Therefore, overall, we would expect the peak signal at the downstream detector to be 0.049× the signal at the upstream detector. A typical TOF measured at the upstream detector is shown in Figure 6.4. This data was taken with with $\overline{SD} = 55\,\text{mm}$, $\dot{V}^{\text{e}}_{\text{in}}(\text{He}) = 1\,\text{sccm}$, $\dot{V}^{\text{e}}_{\text{in}}(\text{SF}_6) = 0.05\,\text{sccm}$, and F2Q = 180 µs. It can be seen that the peak signal is around 0.18 V. Therefore, we would expect the peak signal at the downstream detection point to be around 8.8 mV.

In addition to the small size of the signal at the downstream detection point, the background scatter of the detection light at the downstream detector is significantly worse. This is likely due to the detector being in a shiny stainless steel vacuum chamber which can easily reflect light. On the other hand, the upstream detector is located inside the adsorptive charcoal pump, which is black. To mitigate the effect of the background scatter, Brewster angle windows with long arms were used. The angle of the windows reduced the amount of reflected light and the long arms minimised the amount of scattered light entering the main chamber. In addition, sleeves blackened with charcoal were inserted into the arms of the vacuum chamber to further reduce the amount of scattered light entering the main chamber. Finally, an iris was installed at the focal point of the focussing lens immediately in front of the PMT. This restricted the source location of detected light to a small region around D'.

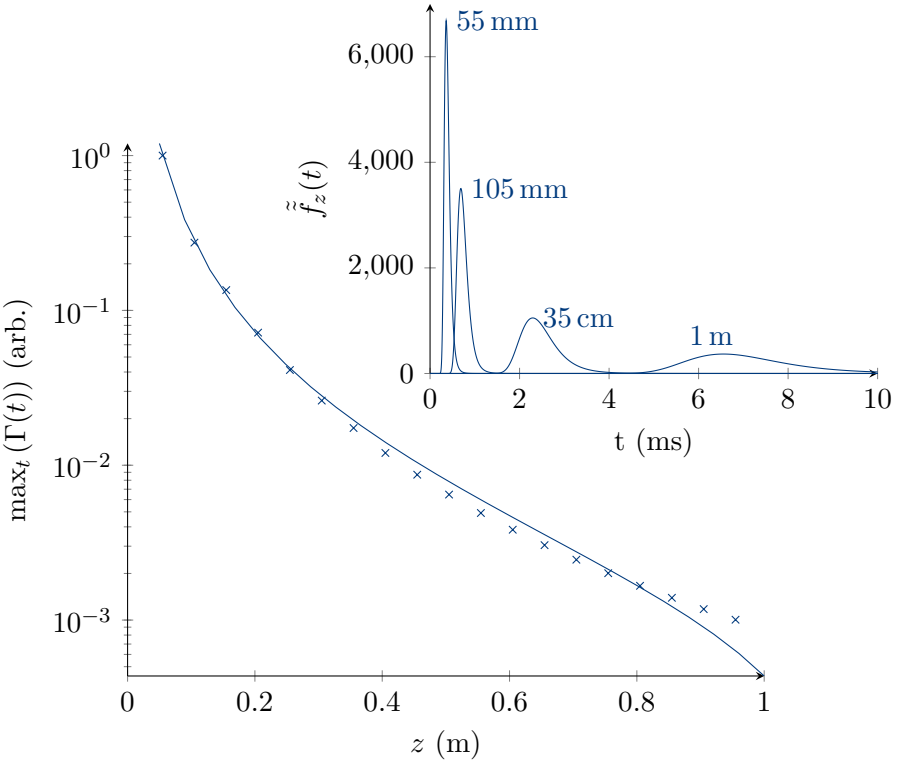

FIGURE 6.3: The peak TOF signal ($\max_t(\Gamma(t))$) against distance for a molecular beam with $v_{\text{out}} = 145\,\text{m}\,\text{s}^{-1}$ and $\Delta v_z = \Delta v_\perp = 24\,\text{m}\,\text{s}^{-1}$. Calculated from Eqn. (5.34) and normalised to unity at $\overline{SD} = 55\,\text{mm}$. The points are numerically calculated and the best fit line is $\max_t(\Gamma(t)) = -\frac{2.6\times10^{-5}\,\text{mm}^3}{z^3} + \frac{3.7\times10^{-3}\,\text{mm}^2}{z^2} - \frac{3.2\times10^{-3}\,\text{mm}}{z}$. The inset shows $\tilde{\tilde{f}}_z(t)$ calculated for $z = 55\,\text{mm}$, $z = 105\,\text{mm}$, $z = 35\,\text{cm}$, and $z = 1\,\text{m}$.

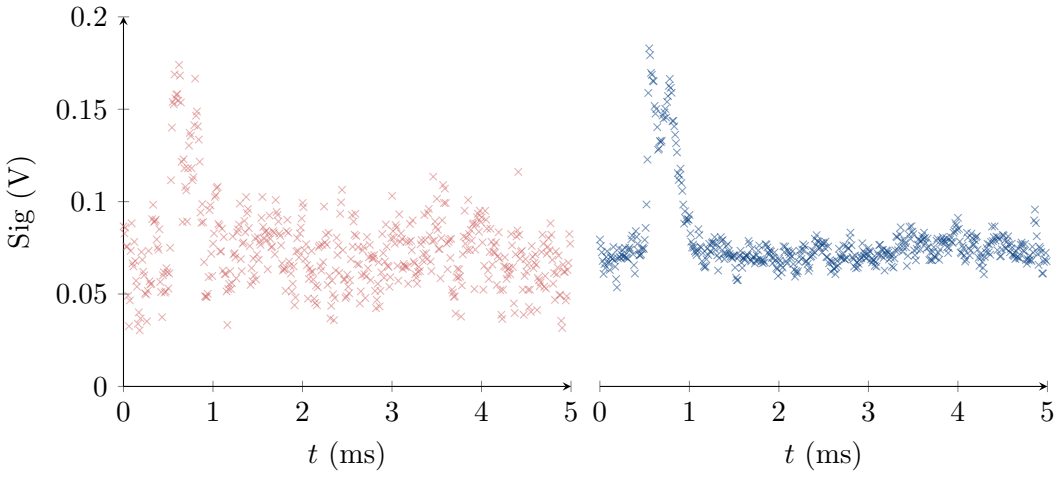

FIGURE 6.4: A typical TOF measured at the upstream detection point with $\overline{SD} = 55\,\text{mm}$, $\dot{V}_{\text{in}}^{\text{e}}(\text{He}) = 1\,\text{sccm}$, $\dot{V}_{\text{in}}^{\text{e}}(\text{SF}_6) = 0.05\,\text{sccm}$, and F2Q $= 180\,\mu\text{s}$. The data from 10 shots of the Nd:YAG laser was collected. The average noise (standard deviation of the background) was $\sigma = (0.0169 \pm 0.0005)\,\text{V}$. (left, red) An example of a single-shot TOF. (right, blue) The average of all 10 shots, showing a peak signal of 0.18 V and a much reduced noise of 0.006 V. This is slightly more than the Poisson-limited $\sigma 10^{-1/2}$.

These scatter reduction methods succeeded in reducing the background to a level comparable to (though still higher than) the upstream detector, as can be seen in Figure 6.5. However, in order to distinguish the molecular signal, it must be larger than the noise — not the mean background. One measure of the noise is the standard deviation of the background.

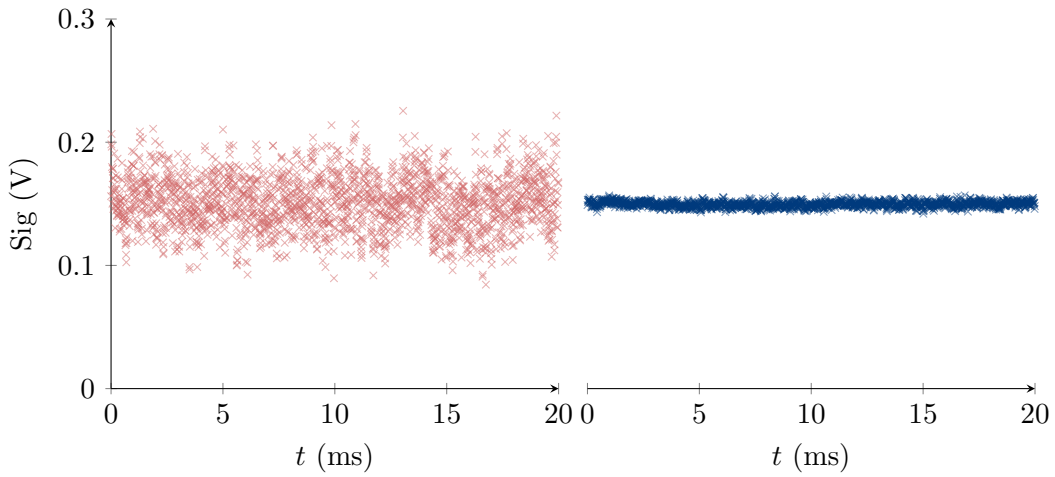

FIGURE 6.5: 100-shot TOF measured at the downstream detection point with $\overline{SD} = 1\,\mathrm{m}$, $\dot{V}_{\mathrm{in}}^{\mathrm{e}}(\mathrm{He}) = 1\,\mathrm{sccm}$, $\dot{V}_{\mathrm{in}}^{\mathrm{e}}(\mathrm{SF_6}) = 0.05\,\mathrm{sccm}$, and F2Q = 180 µs. (left, red) A single shot showing a noise level of $\sigma = (0.0227 \pm 0.0008)\,\mathrm{V}$. (right, blue) The average signal from 100 shots with a noise level of $\sigma = 0.0023\,\mathrm{V}$, which is in accordance with Poisson noise. As can be seen, there is no visible signal from the CaF beam, despite the peak signal being expected to be 0.49 V.

The Poisson shot-noise limit provides a fundamental limit on the noise from laser light. A laser emitting photons at a rate R is, in reality, randomly emitting photons in a Poissonian process with mean rate R:

$$\mathrm{P}\left(N_{\mathrm{ph}}, t\right) = \frac{(Rt)^{N_{\mathrm{ph}}} \exp\left(-Rt\right)}{N_{\mathrm{ph}}!}, \tag{6.1}$$

where $\mathrm{P}\left(N_{\mathrm{ph}}, t\right)$ is the probability of the laser emitting N_{ph} photons in a time t. As with any Poisson process, the mean and standard deviation are Rt and $\sqrt{Rt}$ respectively.

The signal measured by the PMT is related to the number of photons per unit time:

$$\mathrm{Sig} = \frac{\eta}{mt} N_{\mathrm{ph}}, \tag{6.2}$$

where η is the total efficiency of the detection (including geometric and quantum efficiency), m is the PMT calibration factor given in Section 4.4.3, and t is the integration time of the transimpedence amplifier used to convert the PMT current signal into a voltage signal. For 606 nm light, $m = (5.1 \pm 0.1)\,\mathrm{MHz\,V^{-1}}$ (Eqn. (4.13)). This results in the detected signal being a scaled Poisson process, so that:

$$\mathrm{P}\left(\mathrm{Sig}, t\right) = \frac{(Rt)^{\frac{mt\ \mathrm{Sig}}{\eta}} \exp\left(-Rt\right)}{\Gamma\left(\frac{mt\ \mathrm{Sig}}{\eta} + 1\right)}, \tag{6.3}$$

where $\Gamma(x+1) = x!$ is the Gamma function. The mean and variance of the scaled Poisson process are given by:

$$\mathrm{E[Sig]} = \frac{\eta R}{m}, \tag{6.4}$$

$$\mathrm{Var[Sig]} = \frac{\eta^2 R}{m^2 t}, \tag{6.5}$$

$$\mathrm{Var[Sig]} = \frac{\eta}{mt}\mathrm{E[Sig]}. \tag{6.6}$$

Therefore, if the background of the measured signal is Poisson-limited, we would expect the mean to be proportional to the variance. To test this, data was taken at a series of increasing laser powers under vacuum at the downstream detector, but with no molecules present and no gas flowing. A higher laser power resulted in a higher mean background level. Ten 40 ms shots were taken at each laser power and the mean and variance of each shot was calculated. The data is shown in Figure 6.6. As can be seen, the data indicates that the background is a Poisson-limited process, with:

$$\frac{\eta}{mt} = (0.0099 \pm 0.0002)\,\mathrm{V}. \tag{6.7}$$

The detection efficiency can be broken down into constituent parts, $\eta = \eta_{\text{geo}}\eta_{\text{tr}}\eta_{\text{qu}}$, whose values are given in Section 4.4 and Section 5.2.2 such that $\eta = 0.0243$. From Eqn. (4.13) we know that $m = (5.1 \pm 0.1)\,\text{MHz}\,\text{V}^{-1}$. Therefore, $t = (480 \pm 10)\,\text{ns}$.

It can be seen in Figure 6.5 that the single-shot noise at the downstream detector is $(0.0227 \pm 0.0008)\,\text{V}$. In a Poisson-limited process, the noise will scale as $1/\sqrt{N}$ for N trials averaged together. This is because averaging N trials together is equivalent to replacing t with Nt in Eqn. (6.6). On the other hand, any constant molecular signal will remain constant when averaged. This can be seen in Figure 6.4 for the upstream detector, where the single-shot noise of $(0.0169 \pm 0.0005)\,\text{V}$ is reduced to 0.006 V when 10 shots are averaged, while the peak signal remains constant at 0.18 V. It can also be seen in Figure 6.5 for the downstream detector, where the noise on the 100-shot TOF is reduced to 2.3 mV. We expect the molecular signal at the downstream detector to be 8.8 mV. This analysis indicates that if 7 or more shots are averaged together the

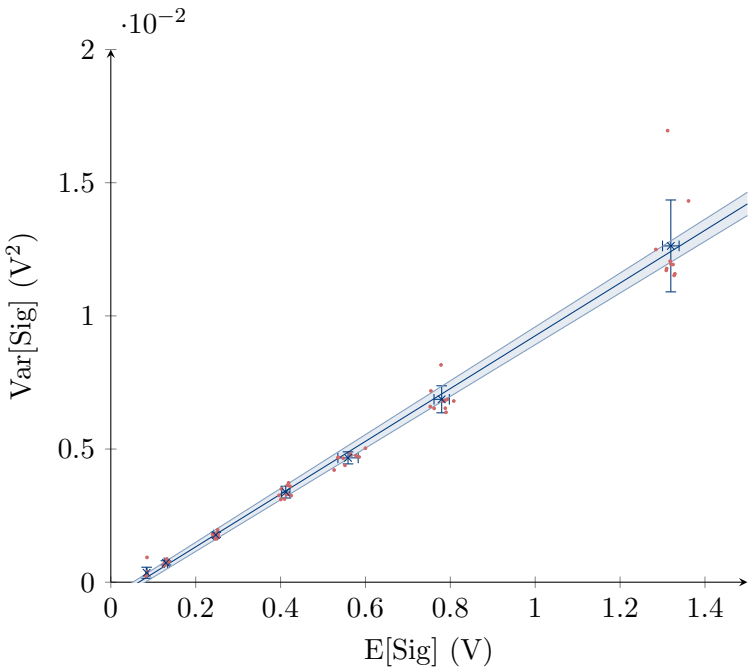

FIGURE 6.6: The mean and variance of the background noise at the downstream detection point after noise reduction efforts. Ten shots of data were taken at seven different laser intensities. Each shot consists of 40 ms of data taken at a 0.1 MHz sample rate. The red marks show the mean and variance of each shot. The blue marks show the mean and variance across the entire set of ten shots for each laser intensity, with error bars showing the spread of the underlying data (i.e., the red marks). The line of best fit gives $\text{Var[Sig]} = \text{E[Sig]}(0.0099 \pm 0.0002)\,\text{V} - (0.0007 \pm 0.0001)\,\text{V}^2$. This is consistent with noise arising from a scaled Poisson distribution with scale factor $(0.0099 \pm 0.0002)\,\text{V}$.

signal should be visible over the noise.

Once it was established that a signal of 8.8 mV ought to be visible at the downstream detection point, data was taken in an attempt to locate the molecular beam. The measured TOF is shown in Figure 6.5. The experimental parameters were $\overline{SD} = 1\,\mathrm{m}$, $\dot{V}_{\mathrm{in}}^{\ominus}(\mathrm{He}) = 1\,\mathrm{sccm}$, $\dot{V}_{\mathrm{in}}^{\ominus}(\mathrm{SF_6}) = 0.05\,\mathrm{sccm}$, and F2Q = 180 µs, as for the data taken at the upstream detector and shown in Figure 6.4. 100 shots were taken and averaged together to produce the final TOF. The noise is reduced by a factor 10 over the single-shot noise, as expected. However, no molecules are visible. The analysis in this section indicates that the problem is not merely one of detection. Therefore, there must be an unaccounted-for process which is disrupting the molecular beam and preventing molecules from arriving at the downstream detector.

6.2.2 Background-Free Imaging

Another technique attempted to further reduce the background noise was Raman Resonance Optical Cycling (RROC). This was proposed for CaF in [21] and trialled on this experiment.

Instead of pumping the CaF $A^2\Pi_{1/2}(J = 1/2^+)$–$X^2\Sigma(N = 1)$ transition within a single vibrational level (typically $v = 0$), RROC involves pumping molecules on two off-diagonal vibrational transitions. In particular, on the transitions:

$$A^2\Pi_{1/2}(v' = 1, J = 1/2^+) - X^2\Sigma(v = 0, N = 1) \text{ at } 585\,\mathrm{nm} \tag{6.8}$$

$$A^2\Pi_{1/2}(v' = 0, J = 1/2^+) - X^2\Sigma(v = 1, N = 1) \text{ at } 628\,\mathrm{nm} \tag{6.9}$$

Molecules pumped to the $A^2\Pi(v = 0)$ state will decay to the $X^2\Sigma(v = 0)$ state, and likewise for $v = 1$. This means that the pump light wavelength is offset from the fluorescence wavelength. Whilst the pump lasers are at 585 nm and 628 nm, the fluorescence occurs at the usual 606 nm. The difference in wavelength between the pump and emitted light means that a bandpass filter can be used to filter out the pump light and prevent it from reaching the PMT.

The experiment was set up using a Semrock FF01-605/15-25 bandpass filter. This allows light in the range 590 nm to 620 nm to pass through with transmission efficiency

$\eta_{\mathrm{tr}} = 0.95$. The Spectra 380 dye laser was used to provide 3.6 mW of 585 nm light and 6.5 mW of 628 nm light was borrowed from a neighbouring experiment. The relevant Franck-Condon factors in CaF are, $\langle v'|v\rangle$:

$$|\langle 0|1\rangle|^2 = 0.015 \tag{6.10}$$

$$|\langle 1|0\rangle|^2 = 0.03 \tag{6.11}$$

$$|\langle 0|0\rangle|^2 \approx |\langle 1|1\rangle|^2 \approx 1 \tag{6.12}$$

The lower Franck-Condon factors mean that the saturation intensity of the off-diagonal transitions is higher by a factor of ~ 100 compared with the vibrationally diagonal transitions. We did not have access to enough laser power to fully saturate both transitions but the method was trialled as a proof-of-concept. The experiment was run using the neon buffer gas source described more fully in Section 6.3 at the upstream detection point with experimental parameters $\dot{V}_{\mathrm{in}}^{\ominus}(\mathrm{Ne}) = 30\,\mathrm{sccm}$, $\dot{V}_{\mathrm{in}}^{\ominus}(\mathrm{SF_6}) = 0.09\,\mathrm{sccm}$, and F2Q $= 150\,\mu\mathrm{s}$. The results are shown in Figure 6.7. There is a 33% (0.0025 V) increase in signal when dual frequency light at 585 nm and 628 nm is used (blue) over single frequency 585 nm light (red), showing the effect of the RROC.

The single-shot noise[1] using the dual frequency light with the bandpass filter is (0.02 ± 0.03) V. When using 606 nm light without the filter the noise is (0.02 ± 0.02) V. This is despite the background levels being 0.015 V lower with the filter in place. The limited laser power available meant we were not able to saturate the transitions, so the the signal-to-noise for the dual frequency setup over 100 shots is 3. For direct imaging using 606 nm light over 100 shots a typical signal-to-noise is 13. There were no molecules visible at the downstream detector so it was not possible to try RROC in a situation where the noise was higher.

6.2.3 Charcoal Experiments

The second assumption that requires investigation is that the CaF molecules are moving freely in the vacuum chamber. For our purposes, 'free movement' means the

[1] Standard deviation of the background.

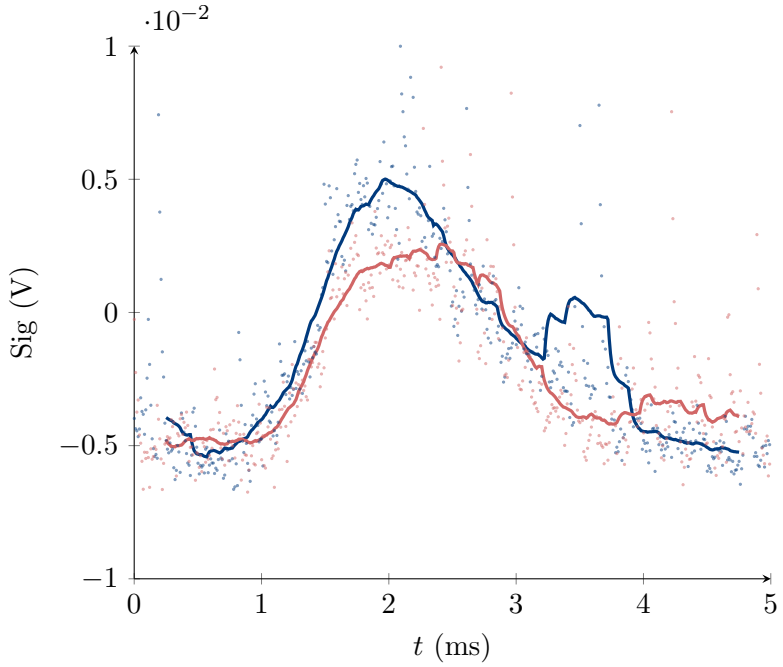

FIGURE 6.7: TOFs with single frequency 585 nm light (red) and dual frequency 585 nm and 628 nm light (blue). Taken at the upstream detection point with a neon buffer gas source (see Section 6.3) and experimental parameters $\dot{V}_{\text{in}}^{\text{e}}(\text{Ne}) = 30\,\text{sccm}$, $\dot{V}_{\text{in}}^{\text{e}}(\text{SF}_6) = 0.09\,\text{sccm}$, and F2Q = 150 µs. Each TOF shown is the average of 100 shots. Lines show a moving average over 50 samples (0.5 ms). An increase in signal of 33% (0.0025 V) can be seen with dual frequency light.

mean free path of the molecules is larger than the relevant distance scale of 1 m. The mean free path of a CaF molecule in the beam moving through a gas in thermal equilibrium is:

$$\lambda = \frac{\langle v_{\text{rel}} \rangle}{\sigma n \langle v_{\text{CaF}} \rangle}, \tag{6.13}$$

where $\langle v_{\text{rel}} \rangle$ is the mean relative velocity between the particle and a particle of the background gas, $\langle v_{\text{CaF}} \rangle$ is the mean velocity of the CaF in the beam, σ is the collision cross-section, and n is the number density of the background gas. The mean relative velocity of two particles moving independently is the quadrature sum of their individual mean velocities:

$$\langle v_{\text{rel}} \rangle = \sqrt{\langle v_{\text{CaF}}^2 \rangle + v_{\text{T}}^2}, \tag{6.14}$$

where v_{T} is the thermal velocity of the background gas. The mean-square velocity of a Gaussian CaF beam with beam velocity v_{out} and velocity width $\Delta v_{\perp} = \Delta v_z$ is (see Eqn. (5.23)):

$$\left\langle v_{\mathrm{CaF}}^2 \right\rangle = v_{\mathrm{out}}^2 + 3\Delta v_z^2, \tag{6.15}$$

and $n = P/(k_{\mathrm{B}}T)$. Therefore, the mean free path is:

$$\lambda = \frac{k_{\mathrm{B}}T}{\sigma P}\sqrt{1 + \frac{v_{\mathrm{T}}^2}{v_{\mathrm{out}}^2 + 3\Delta v_z^2}}. \tag{6.16}$$

The kinetic radius of CaF was found to be 3.2 Å in Section 5.1.3. We first work out the mean free path of CaF assuming completely effective helium pumping, so the background gas is the residual air remaining in the chamber at 5×10^{-7} mbar (see Section 4.2.1). We take the kinetic radius of nitrogen gas, 1.9 Å, to be representative of air. The background gas in the vacuum chamber is in thermal equilibrium with the outer wall of the vacuum chamber, which is in turn in thermal equilibrium with the room. Therefore, $T = 293\,\mathrm{K}$. This gives an upper bound on the mean free path of $\lambda = 130\,\mathrm{m}$. This is much larger than our length scale of 1 m, so under these conditions (perfect helium pumping), we would be able to consider the CaF beam to be moving freely.

In Section 4.2.1, we measure the pressure of helium at various flow rates. In the best helium pumping conditions, the partial pressure of helium when flowing at 1 sccm ($0.017\,\mathrm{mbar\,l\,s^{-1}}$) is 1.4×10^{-6} mbar. By the time the helium arrives at the pressure gauge, it will be at room temperature, 293 K. Therefore, the density of helium is an order of magnitude greater than air in the chamber, and so we ignore the contribution of air. The kinetic radius of helium is 1.3 Å (Section 5.1.3). Under these conditions, the mean free path of CaF is 0.3 m. Over the course of 1 m, a CaF particle will undergo on average five collisions with the helium gas. Ensuring $\lambda > 1\,\mathrm{m}$ requires reducing the pressure of helium by an order of magnitude.

Whilst the pumping speed of the turbos, $\dot{V}_{\mathrm{turb}}$, is a fixed property of the individual

pumps, the pumping speed of the adsorptive charcoal pump, $\dot{V}_{\text{char}}$, is related to the surface area of charcoal exposed to the helium gas. It is well known [48, 88] that the charcoal pumps have a maximum helium capacity and need to be periodically 'cleared' by allowing them to warm up so that trapped helium can escape. If we take the maximum helium capacity of the pump to be N_0 particles then we can model the pumping rate in molecules per unit time as:

$$\frac{\mathrm{d}N}{\mathrm{d}t} = k(N_0 - N) \tag{6.17}$$

$$= N_0 k \exp(-kt), \tag{6.18}$$

where N is the number of helium particles adsorbed by the charcoal and k is the adsorption rate. For any fixed reference temperature, T_R, and pressure, P_R, this translates directly into a pumping speed:

$$\dot{V}_{\text{char}}(t) = V_0 k \exp(-kt), \tag{6.19}$$

where $V_0 = (N_0 k_{\text{B}} T_R)/P_R$ and $\dot{V}_{\text{char}}(t=0) = V_0 k$. Recall Eqn. (4.1), where $\dot{V}_{\text{out}} = \dot{V}_{\text{turb}} + \dot{V}_{\text{char}}$. Therefore, from Eqn. (6.19) we have:

$$P(t) = \frac{Q_{pV}(\text{He})}{\dot{V}_{\text{turb}} + V_0 k \exp(-kt)}. \tag{6.20}$$

The form of this model is a logistic curve. The pressure in the chamber is predicted to increase exponentially at first, as the charcoal pump fills with helium, and then reach an asymptotic pressure equal to $Q_{pV}(\text{He})/\dot{V}_{\text{turb}}$ once the charcoal is full. This suggests that the above mean free path of 0.3 m is the best case scenario which is only achieved immediately after the helium flow is switched on.

The model was fitted to pressure over time data with $\dot{V}_{\text{in}}^{\ominus}(\text{He}) = 3.4\,\text{sccm}$, a plot of which is shown in Figure 6.8. The fitted parameters are $\dot{V}_{\text{turb}} = (870 \pm 90)\,\text{l}\,\text{s}^{-1}$, $k = (0.474 \pm 0.009)\,\text{h}^{-1}$, and $V_0 k = (11\,380 \pm 60)\,\text{l}\,\text{s}^{-1}$. The initial charcoal pumping speed ($V_0 k$) measured here is in agreement with the $(10\,800 \pm 600)\,\text{l}\,\text{s}^{-1}$ measured in

Section 4.2.1. $\dot{V}_{\text{turb}}$ is lower than that measured in Section 4.2.1. The difference is due to a different pump being used here while one of the regular pumps was being serviced. The helium pressure measured after three hours was 3.5×10^{-5} mbar, which gives $\lambda = 12$ mm. This cannot be considered free motion over a 1 m scale.

V_0 gives the total maximum volume of helium the charcoal pump can adsorb, measured at $P(t = 0)$ and $T = 4$ K. From the measured $V_0 k$ and k we calculate this to be $V_0 = (24\,000 \pm 500)$ l. This translates into a volumetric capacity of (0.0164 ± 0.0003) l of helium at STP or a molecular capacity of $N_0 = (4.34 \pm 0.06) \times 10^{21}$ mol. It is equivalent to flowing 5 sccm of helium for just over 30 minutes, though the charcoal pump takes longer than this to fill up as its adsorption rate is limited by k.

Since the initial pumping speed is given by $V_0 k$, it can be increased by increasing the carrying capacity of the pump, even if the adsorption rate k remains constant. The most straightforward way to increase the capacity of the pump is to increase the surface area of charcoal exposed to the helium. To achieve this, the charcoal

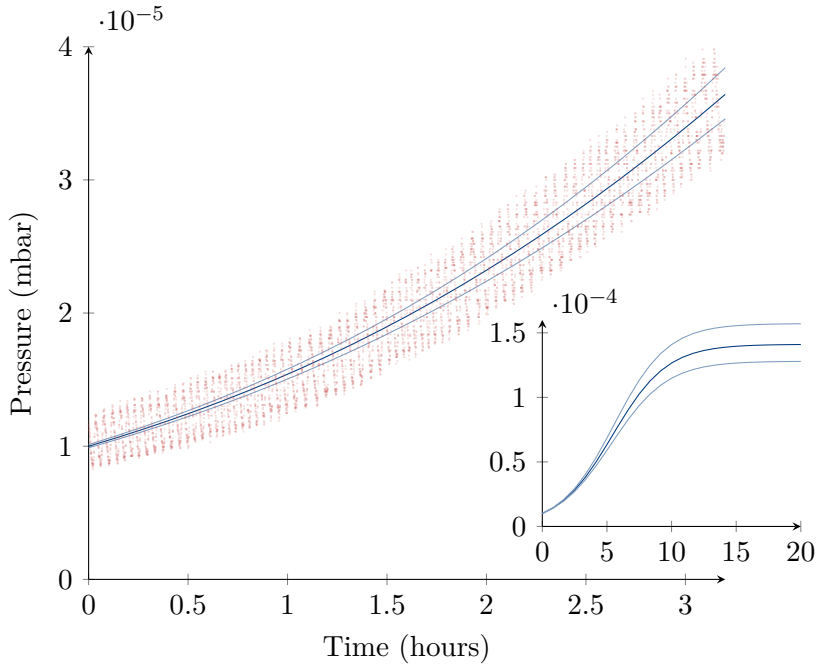

FIGURE 6.8: Vacuum chamber pressure data (red) taken with a constant helium flow rate of 3.4 sccm, equivalent to a gas load of $Q_{pV}(\text{He}) = 0.12\,\text{mbar}\,\text{l}\,\text{s}^{-1}$. The background pressure with no helium flow of $(2.09 \pm 0.01) \times 10^{-7}$ mbar has been subtracted. The data has been fitted with the model of Eqn. (6.20) (blue) where $Q_{pV}(\text{He})$ was fixed. The fitted parameters are $\dot{V}_{\text{turb}} = (870 \pm 90)\,\text{l}\,\text{s}^{-1}$, $k = (0.474 \pm 0.009)\,\text{h}^{-1}$, and $V_0 k = (11\,380 \pm 60)\,\text{l}\,\text{s}^{-1}$. The inset shows the extrapolated model with the pressure reaching the no-charcoal limit of $Q_{pV}/\dot{V}_{\text{turb}}$ after around 10 hours.

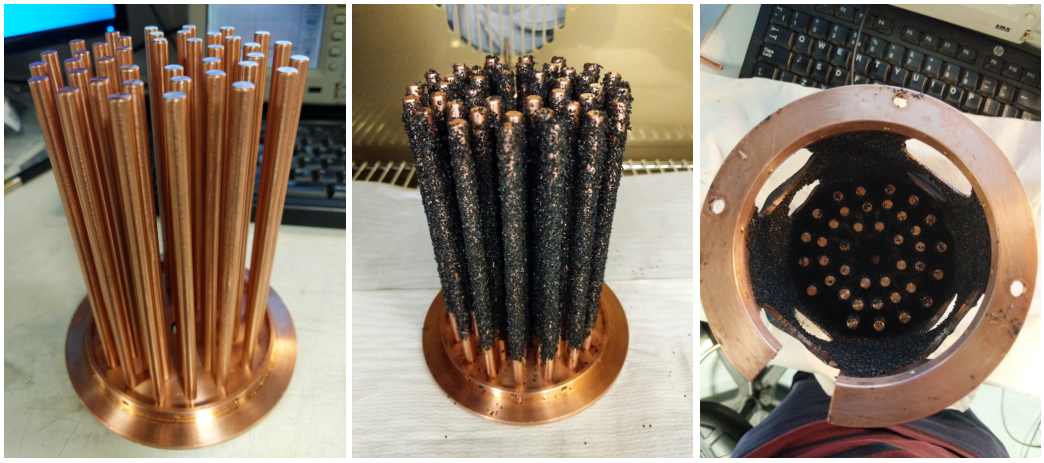

FIGURE 6.9: Photograph of a modified adsorptive charcoal pump with 39 rods 10 cm in length coated with charcoal. The aim is to increase the total charcoal surface area and so pump more helium. In the event this was too much thermal mass for the cryostat to cool and the setup never reached a low enough temperature for the pump to be effective.

pump was modified to include 39 10 cm long rods which were coated in charcoal. A photograph of this pump can be seen in Figure 6.9.

Unfortunately, this method of increasing the surface significantly increased the mass of the charcoal shield. The cyrostat has a maximum cooling power and if the thermal mass is too high it will take too long to cool down. The temperature was monitored whilst the new charcoal pumps were cooling down. An hour after the cold stage normally reaches 4 K the temperature of the pump had still not fallen below 40 K. Upon inspection, helium pump in the cryostat was found to be operating outside its normal conditions and so the cool-down was stopped and the charcoal pump was replace with the standard long cylinder pump.

6.3 Neon Buffer Gas

Although helium is the most common choice of buffer gas in cold molecular sources, neon has also been used [89]. Neon has the advantage that it can be pumped more rapidly by adsorptive pumps, leading to a lower chamber pressure for a given flow rate. As shown in Section 6.2.3, the relatively high chamber pressure was a key concern in relation to the inability to see a downstream CaF signal. Therefore, we decided to try a neon buffer gas source.

Neon has a higher freezing point than helium. Therefore, a higher cell temperature was necessary to prevent the neon from freezing. The experimental setup was modified to allow the buffer gas cell temperature to be adjusted independently. The plate on which the cell was mounted was stood off from the 4 K stage of the cryostat by two steel washers at each of the four corner bolts. The 21 Ω cell heater was then used to adjust the cell temperature. Data on the cell temperature as it varied with heater power is shown in Figure 6.10.

The integrated TOF signal[2], Spec, was measured at various cell temperatures in order to find the optimum temperature. The results are shown in Figure 6.11. In general, the signal increases with decreasing temperature. However, below 13 K the signal falls significantly. This is likely due to the neon freezing. Therefore, the optimum cell temperature is around 13 K.

Once the optimum temperature had been found a pressure test analogous to that shown in Figure 4.6 was carried out for neon. The results are shown in Figure 6.12 with the data for neon pumping in a warm chamber (i.e., with no adsorptive pumping) shown in yellow and in a cold chamber with the cell heater at 2 W shown in red. Also shown in blue is the cold helium pumping data from Figure 4.6. The pressure response for neon below around 10 sccm (0.17 mbar l s^{-1}) was very non-linear. Above this, in the linear regime, it was found that $\dot{V}_{\mathrm{char}}(\mathrm{Ne}) = (3.4 \pm 0.5) \times 10^5\,\mathrm{l\,s^{-1}}$. This is an order of magnitude higher than the best helium pumping speed achieved.

Given that a higher buffer gas flow rate leads to greater extraction efficiency (i.e., a larger η_{beam}), it is preferable to run at as high a flow rate as possible whilst ensuring the pressure remains low enough. As discussed in Section 6.2.3, the mean free path of the CaF molecules is the main limiting factor. The other limiting factor is the maximum flow rate of the flow controller, which is 32 sccm. At a neon flow rate of 30 sccm (0.51 mbar l s^{-1}), the chamber pressure was $(4.5 \pm 0.2) \times 10^{-6}$ mbar. This is comparable to the chamber pressure at a helium flow rate of 1 sccm at 4 K. A proper velocity measurement was not carried out for neon, but Eqn. (5.24) and Eqn. (5.25) predict $v_{\mathrm{out}} = 162\,\mathrm{m\,s^{-1}}$ and $\Delta v_z = \Delta v_\perp = 43\,\mathrm{m\,s^{-1}}$. This provides a mean free path according to Eqn. (6.16) of 0.81 m. This is approximately the length of the beamline,

[2] Spec $= \int_0^\infty \mathrm{Sig}(t)\,\mathrm{d}t$, which is related to $\langle\Phi\rangle$ by Eqn. (4.13) (the PMT calibration) and Eqn. (5.45).

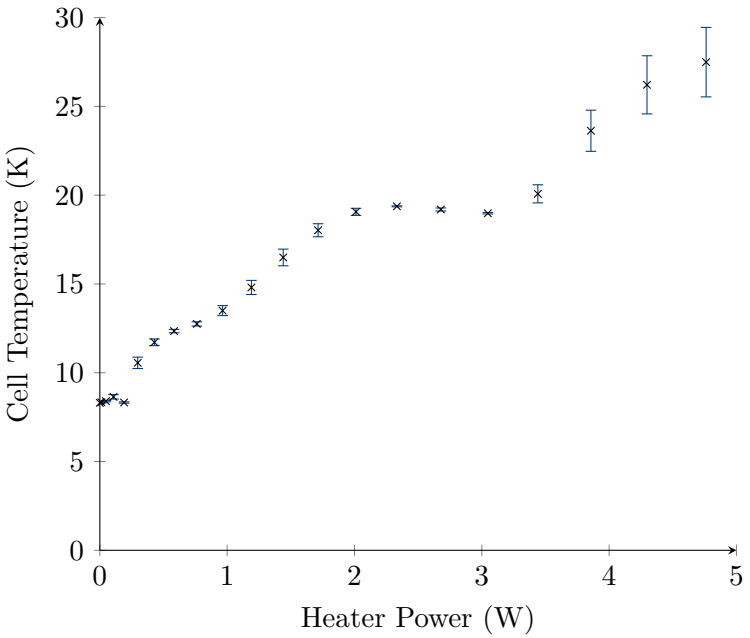

FIGURE 6.10: The temperature of the buffer gas cell as the heater power was varied. Heater power was calculated from the applied voltage and heater resistance of 21 Ω which was measured at 8 K. As can be seen, the response is highly non-linear. Nevertheless, the temperature response was repeatable. Therefore, the data was used to inform the choice of heater power.

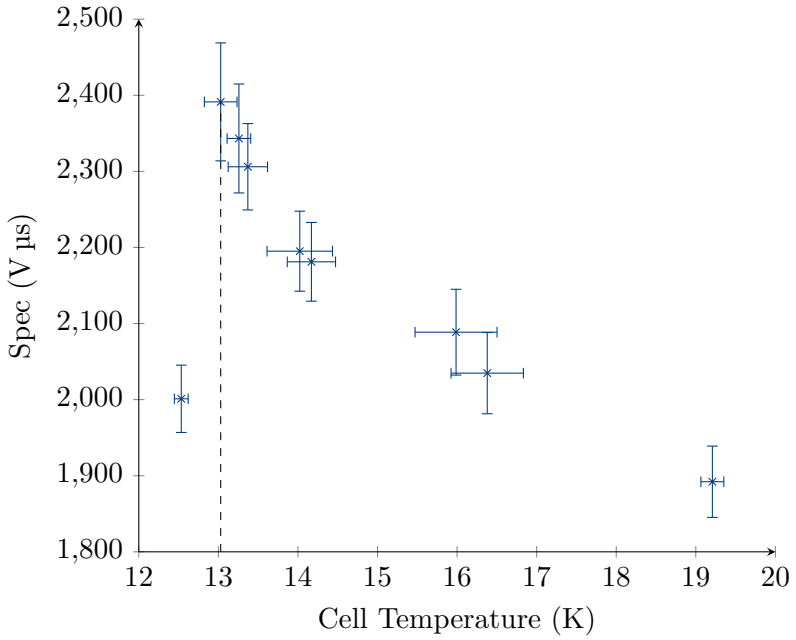

FIGURE 6.11: The integrated TOF signal, $\int_0^\infty \mathrm{Sig}(t)\ \mathrm{d}t$, taken at the upstream detection point with experimental parameters $\overline{SD} = 55\,\mathrm{mm}$, $\dot{V}_{\mathrm{in}}^{\mathrm{e}}(\mathrm{Ne}) = 10\,\mathrm{sccm}$, $\dot{V}_{\mathrm{in}}^{\mathrm{e}}(\mathrm{SF_6}) = 0.05\,\mathrm{sccm}$, and F2Q = 150 µs. Error bars show the standard deviation over 100 shots. The threshold below which the neon freezes in the gas line, thus reducing the buffer gas flow and hence the signal, can clearly be seen at 13 K.

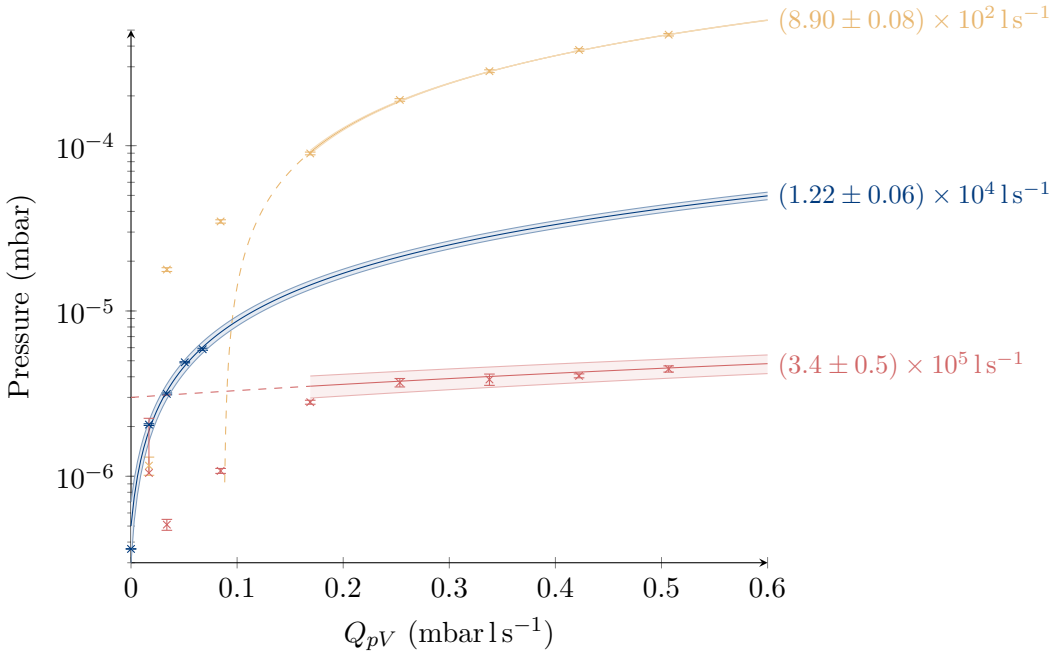

FIGURE 6.12: Chamber pressure varying with buffer gas load, Q_{pV}. Data are shown for a warm chamber with neon flow (yellow), a cold chamber with helium (blue), and a cold chamber with neon (red). The neon pressure response is non-linear below $0.17\,\mathrm{mbar\,l\,s^{-1}}$. Best fit lines for neon were fit to data above this flow rate and extrapolations below this are shown with dashed lines. It can be seen that at high flow rates the cold neon pumping speed is an order of magnitude higher than the cold helium pumping speed.

but still not large enough that we can consider the CaF molecules' motion to be fully free.

Once it was established that the experiment could be run with up to 30 sccm of neon buffer gas, data was collected on signal size as it varied with neon flow rate. This is shown in Figure 6.13. It can be seen that the general shape of the signal-flow rate matches that found for helium (see Figure 5.11). Recall from Section 5.2.2 that increasing buffer gas flow rate increases both the extraction efficiency, η_{beam}, and reduces the divergence of the beam, Ω_{beam}. Therefore, the signal strength increases with flow rate. The only limiting factor is the pressure in the vacuum chamber. The high pumping speed for neon therefore allows us to operate in the high flow regime, which is > 5 sccm for neon[3].

The upstream TOF taken at 30 sccm is shown in Figure 6.14. Measurements were also taken at the downstream detection point with the same experimental parameters.

[3]Recall for helium the high flow regime is > 0.5 sccm.

This TOF is also shown in Figure 6.14. No molecules were seen at the downstream detection point.

6.4 Outlook

Initial results presented here show that the ZSD designed for CaF is capable of transmitting molecules along its length. In order to improve the acceptance of molecules into the decelerator, the experimental setup was modified to reduce the gap between the molecular source and the decelerator entrance. This resulted in the loss of the downstream signal, which is required in order to carry out tests of the decelerator.

Despite extensive investigations into the noise associated with the detection light, chamber pressure, and trialling neon as a buffer gas and RROC imaging, it was not possible to recover a CaF signal at the downstream detection point at $\overline{SD} = 1\,\mathrm{m}$. This was extremely frustrating and meant that it was not possible to further test the Zeeman-Sisyphus decelerator with the present apparatus, despite often obtaining strong molecular beam signals at the upstream detector.

The next possible line of investigation would be the gas flows within the buffer gas cell, with a view to resolving the low reaction efficiency identified in Section 5.2.2. It was thought that the configuration with the SF_6 line parallel to the beam axis and the buffer gas line perpendicular was not optimal and the reverse configuration might be preferable. This would have required a re-design of the buffer gas cell and re-construction of the gas lines. As significant time had been lost due to the Covid-19 pandemic, it was decided to focus on further simulations of Zeeman-Sisyphus deceleration instead, and in particular on ZSD of YbF. These simulations are presented in Chapter 7.

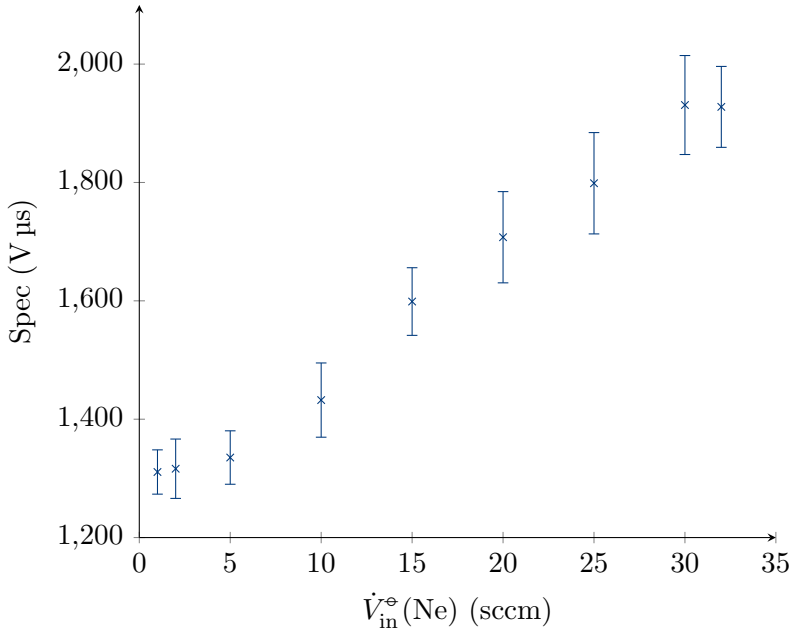

FIGURE 6.13: The integrated TOF signal, Spec $= \int_0^\infty \text{Sig}(t)\ \text{d}t$, as it varies with neon buffer gas flow rate, $\dot{V}_{\text{in}}^{\ominus}(\text{Ne})$. Data was taken at the upstream detection point with experimental parameters $\overline{SD} = 55\,\text{mm}$, $\dot{V}_{\text{in}}^{\ominus}(\text{SF}_6) = 0.05\,\text{sccm}$, and F2Q $= 150\,\mu\text{s}$. Error bars show standard deviation over 100 shots.

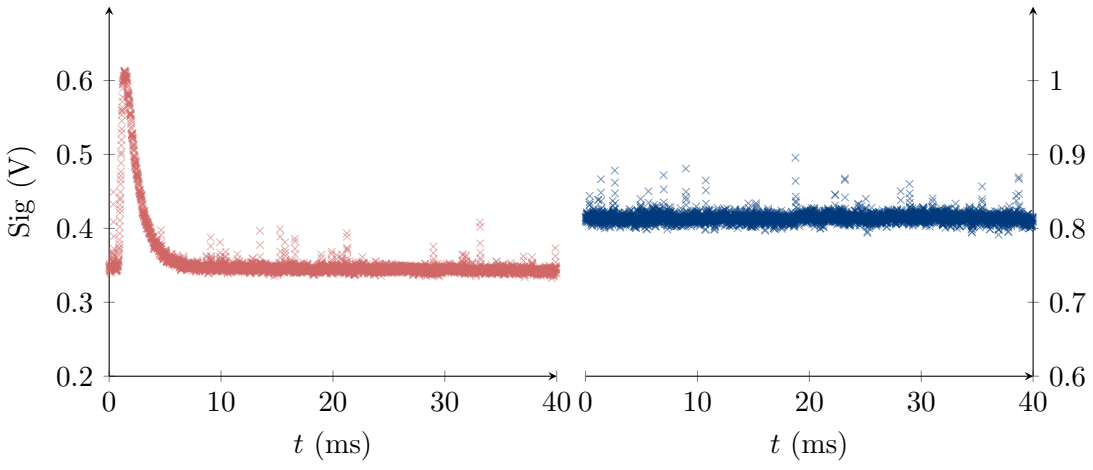

FIGURE 6.14: TOFs measured at the upstream (left, red) and downstream (right, blue) detection points with experimental parameters $\dot{V}_{\text{in}}^{\ominus}(\text{Ne}) = 30\,\text{sccm}$, $\dot{V}_{\text{in}}^{\ominus}(\text{SF}_6) = 0.05\,\text{sccm}$, and F2Q $= 150\,\mu\text{s}$. Each TOF shown is the average of 100 shots. No beam is visible at the downstream detection point despite the lower pressure achieved with a neon buffer gas.

Chapter 7

Simulating Zeeman-Sisyphus Deceleration of YbF

Although Zeeman-Sisyphus deceleration was first proposed for CaF molecular beams, its great advantage is in decelerating molecules that are much heavier and do not have closed laser cooling cycles. A good example of such a molecule is ytterbium monofluoride, YbF. YbF is used in experiments to measure the electron's electric dipole moment. As covered in Section 1.2, the accuracy of the measurement improves with longer interaction times. This interaction time can be improved with a 'fountain' experiment [46] or with a magneto-optical trap [90]. Both experiments require the YbF beam to be slowed prior to trapping. YbF is 3.3 times heavier than CaF and has significantly less favourable Franck-Condon factors [28], meaning that optical pumping cycles are less closed. Therefore, there is a significant advantage to be gained from the fewer photons scattered by a ZSD cooling scheme.

7.1 The ZS Cooling Cycle in YbF

The YbF $A^2\Pi_{1/2}$ state has a more complex structure than that of CaF. This can be seen in Figure 7.1. In CaF, the Zeeman splitting of the $A^2\Pi_{1/2}$ state was only $0.29\,\mathrm{GHz\,T^{-1}}$. On the other hand, in YbF, the $A^2\Pi_{1/2}$ state has a splitting of $4.2\,\mathrm{GHz\,T^{-1}}$. The YbF $X^2\Sigma$ state has a splitting of $14\,\mathrm{GHz\,T^{-1}}$. There is, additionally, an avoided crossing between the $A^2\Pi_{1/2}(J = 1/2^+, F = 1, M_F = 1, 0)$ state and the $A^2\Pi_{1/2}(J = 3/2^+, F = 1, M_F = 0)$ state at $0.7\,\mathrm{T}$. This means that the

$A^2\Pi_{1/2}(J = 1/2^+, F = 1, M_F = 1, 0)$ states are SFS at very high magnetic field, despite being initially WFS. These states are marked in black in Figure 7.1.

Due to the large Zeeman splitting in the excited state, there are many more resonances to consider than with CaF. For example, at 0.155 T, the energy gap between the WFS and SFS ground states is equal to the 4.4 GHz gap between the $A^2\Pi_{1/2}(J = 1/2^+, F = 1, M_F = -1, 0)$ state and the $A^2\Pi_{1/2}(J = 3/2^+, F = 2, M_F = 2)$ state. This means the s2w laser resonant with the $A^2\Pi_{1/2}(J = 1/2^+, F = 1, M_F = -1, 0)$–$X^2\Sigma(N = 1, \text{SFS})$ P-branch transition at 0.155 T will also be resonant with the $A^2\Pi_{1/2}(J = 3/2^+, F = 2, M_F = 2)$–$X^2\Sigma(N = 1, \text{WFS})$ Q-branch transition. There are several similar resonances in the region between 0.11 T and 0.23 T in YbF. They are shown in Figure 7.2.

These resonances present an issue if we consider implementing the ZSD scheme in Figure 7.1 with the same longitudinal laser setup used for CaF. In this scheme, molecules in SFS states will be pumped to WFS states at, for example, 0.05 T by the s2w laser. They will then move through a region of increasing magnetic field. When the field is between 0.11 T and 0.23 T the molecules will once again be in resonance with the s2w laser, except this laser will now pump them to the $A^2\Pi_{1/2}(J = 3/2^+)$ states. From here the molecules may decay to $X^2\Sigma(N = 3)$ and be lost. To avoid this, a transverse laser configuration may be used. In this configuration, the laser beams are perpendicular to the beamline. This means that multiple beams are required (two per half-cycle of the magnetic field). However, since they only have significant intensity at certain z-positions, and so at certain magnetic field strengths, the lasers do not come into resonance with stray transitions at different magnetic field strengths.

7.2 The Magnetic Field

Zeeman-Sisyphus deceleration with transverse laser beams has been demonstrated with beams of CaOH [5]. In [5], superconducting solenoids were used to provide the magnetic field, rather than arrays of permanent magnets. Solenoids allow for high magnetic fields to be achieved over a larger central bore through which the molecules can move, on the order of centimetres rather than millimetres. We carry out the simulations in this chapter using a similar setup.

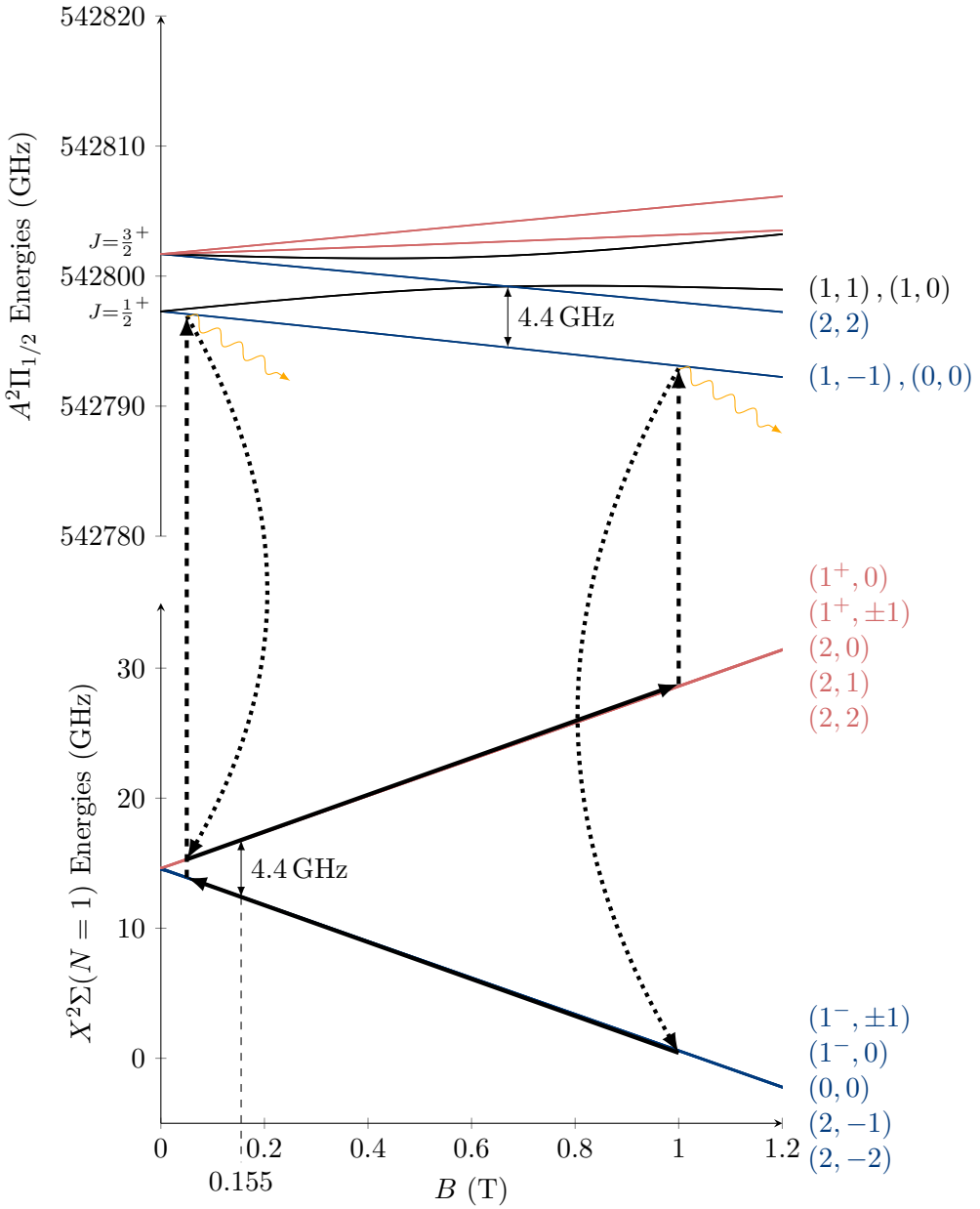

FIGURE 7.1: The energy level diagram for the YbF A–X transition against magnetic field strength. From top to bottom the diagram shows the four $A^2\Pi_{1/2}(J = 3/2^+)$ levels, the two $A^2\Pi_{1/2}(J = 1/2^+)$ levels, the $X^2\Sigma(N = 1, \text{WFS})$ levels, and the $X^2\Sigma(N = 1, \text{SFS})$ levels. The $X^2\Sigma(N = 1)$ states and $A^2\Pi_{1/2}$ states are labelled with their (F, M_F) quantum numbers. WFS states are coloured in red and SFS states are coloured in blue.

Overlaid is an example ZSD optical pumping scheme with a 'weak-to-strong' laser pumping the $A^2\Pi_{1/2}(J = 1/2^+, F = 1, M_F = -1, 0) - X^2\Sigma(N = 1, \text{WFS})$ transition at $B = 1\,\text{T}$ and a 'strong-to-weak' laser pumping the $A^2\Pi_{1/2}(J = 1/2^+, F = 1, M_F = -1, 0) - X^2\Sigma(N = 1, \text{SFS})$ transition at $B = 0.05\,\text{T}$. The arrows show the path of the molecule. At $0.155\,\text{T}$ the WFS − SFS gap and the $A^2\Pi_{1/2}(J = 1/2^+, F = 1, M_F = -1, 0) - A^2\Pi_{1/2}(J = 3/2^+, F = 2, M_F = 2)$ gap are equal.

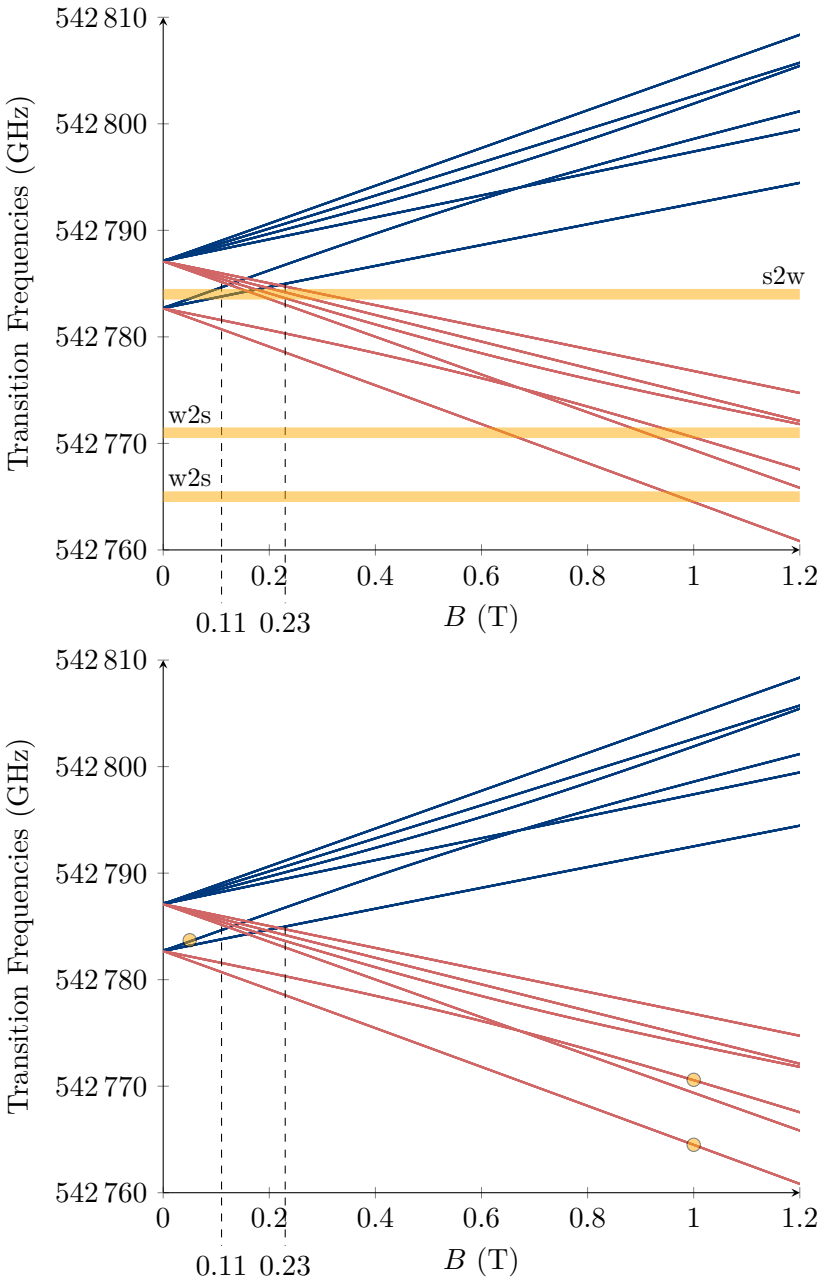

FIGURE 7.2: Transition frequencies for YbF $A^2\Pi_{1/2}$–$X^2\Sigma(N = 1)$. States are coloured according to whether the ground state ($X^2\Sigma$) is WFS (red) or SFS (blue). Overlaid are the 'strong-to-weak' (s2w) and 'weak-to-strong' (w2s) lasers for the ZSD scheme shown in Figure 7.1. (top) The laser in the longitudinal configuration, with non-negligible intensity at all magnetic field strengths. (bottom) To avoid optically pumping unwanted transitions a transverse laser configuration may be used. Here the lasers only have significant intensity at certain z-positions or magnetic field strengths.

A thin cylindrical solenoid of finite length produces a cylindrically symmetric magnetic field [91]:

$$
\begin{aligned}
B_{\rho_\perp} &= \frac{B_0}{\rho_\perp}\left[\sqrt{\frac{4R\rho_\perp}{m}}\left((m-2)K(m)+2E(m)\right)\right]_{\zeta_-}^{\zeta_+} \\
B_z &= 2B_0\left[\sqrt{\zeta\frac{4R\rho_\perp}{m}}\left(K(m)+\frac{R-\rho_\perp}{R+\rho_\perp}\Pi(n,m)\right)\right]_{\zeta_-}^{\zeta_+} \\
B_0 &= \frac{\mu_B I}{4\pi l} \\
m &= \frac{4R\rho_\perp}{(R+\rho_\perp)^2+\zeta^2} \\
n &= \frac{4R\rho_\perp}{(R+\rho_\perp)^2} \\
\zeta_\pm &= z \pm \frac{l}{2}
\end{aligned}
\tag{7.1}
$$

where $\rho_\perp = \sqrt{x^2+y^2}$, I is the current, l is the length of the solenoid, R is its radius, and the coordinates are as in Figure 4.2. $K(m)$, $E(m)$, and $\Pi(n,m)$ are the complete elliptic integrals of the first, second, and third kind respectively.

We simulate a magnetic field of twenty ring solenoids, each 2.5 cm in radius and 1 mm thick (i.e., $l = 1$ mm). A current of 100 kA was chosen in order to provide a peak on-axis magnetic field of approximately 1 T. Alternate solenoids have their current directions reversed. This creates a periodic field, with the field reaching zero midway between two solenoids. A solenoid spacing of 5 cm provides a transverse magnetic field with positive curvature in the weak field regions, so as to facilitate guiding. The initial and final peaks in field strength are higher than in the middle of the decelerator. The typical peak field on-axis is 1.06 T. The magnetic field is shown in Figure 7.3. Unlike the CaF ZSD field, this field is cylindrically symmetric. It can be seen in Figure 7.3(d) that the strong field regions also have a positive transverse curvature. This means that molecules in SFS states will be anti-guided. This is explored more in Section 7.4.

Laser beams are arranged so that there are two per stage. The w2s laser, to pump molecules from WFS states to SFS states, is at the peak magnetic field at the center of a solenoid. The s2w laser, to pump from SFS to WFS, is offset from a magnetic field minimum. Each beam is simulated as comprising six lasers — one for each of the

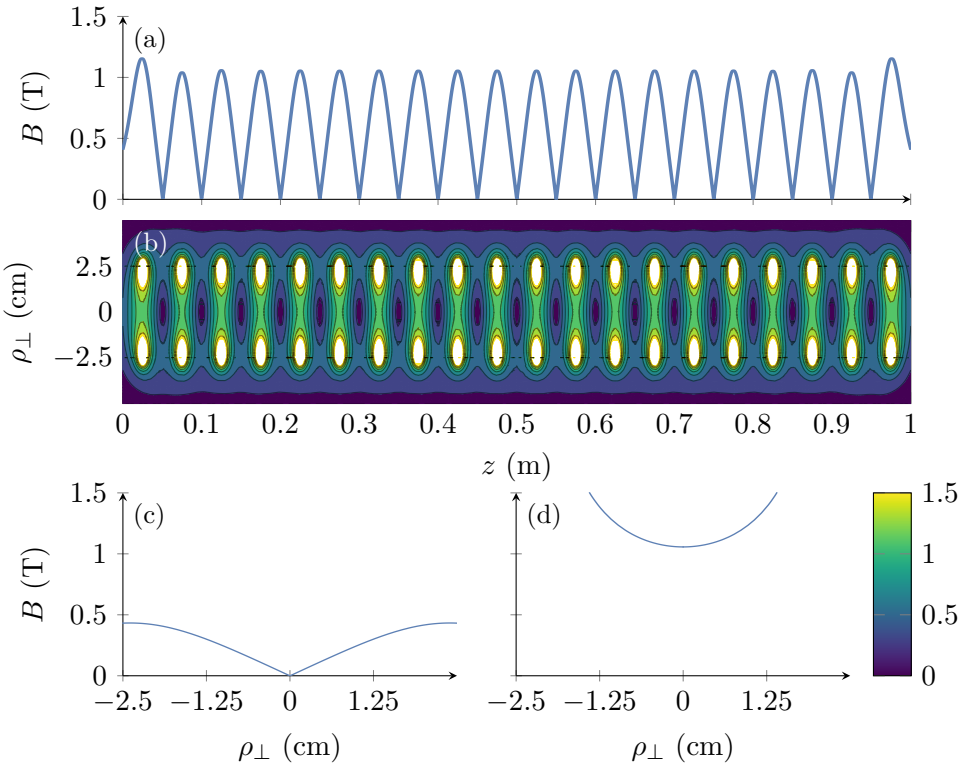

FIGURE 7.3: The magnetic field of a ZSD consisting of twenty solenoids evenly spaced over 1 m. Each solenoid is 2.5 cm in radius, 1 mm long, and runs a current of 100 kA. Neighbouring solenoids have reversed current directions. (a) shows the field along the z with $x, y = 0$. (b) shows the field in the $\rho_\perp$-z plane ($\rho_\perp = \sqrt{x^2 + y^2}$). The solenoids are the singularities at $x, y = \pm 0.025$ m. (c) and (d) show the field at $z = 0.200$ m (c, minimum) and $z = 0.224$ m (d, maximum) respectively.

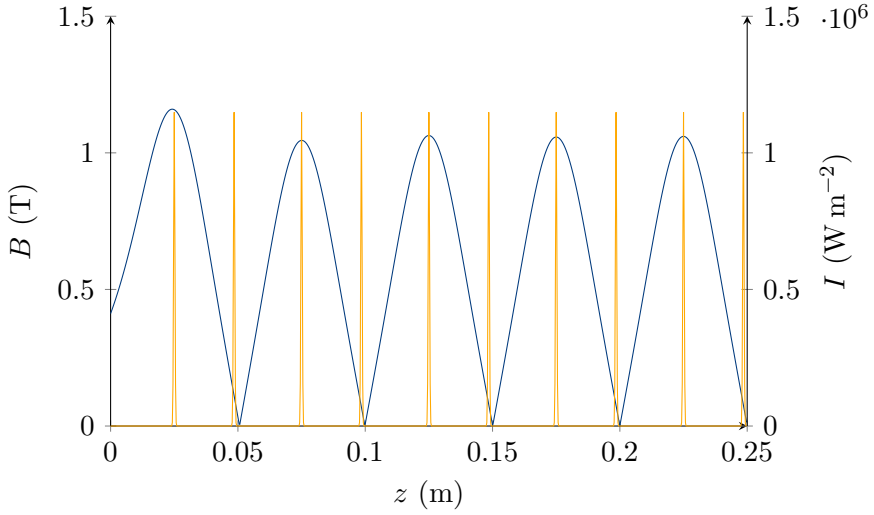

FIGURE 7.4: The first 0.5 m of the on-axis ($x = 0$, $y = 0$) magnetic field (blue) shown in Figure 7.3 overlaid with the laser intensities (orange) showing the transverse configuration with beams only present at specific longitudinal positions.

SFS/WFS hyperfine sub-levels. The frequencies are set to account for the Zeeman effect at $\rho_\perp = 0$ at the z-position of the laser. Figure 7.4 shows the first 0.25 m of the decelerator with the laser intensities overlaid for 75 mW beams with a $1/e^2$ width of 1 mm. The s2w lasers are offset from the field minima by 1.5 mm. This corresponds to a magnetic field of 0.076 T at the beam centre, ensuring that the Q-branch transitions will not come into resonance with the laser.

7.3 Spin Flip Probability

A key requirement for a Zeeman-Sisyphus deceleration scheme is a high probability of spin flip (spin flip probability, SFP) from all WFS states to any SFS state, and vice versa, at the appropriate magnetic field strength. To see if all ground hyperfine levels in YbF have a high SFP we examine the transition intensities and the branching ratios. These were calculated using the equations given in Section 2.5.

Calculating the matrix elements for electromagnetic transitions requires specifying a polarisation in the basis where the z-axis is parallel to the local magnetic field. If the k-vector of the light is parallel to the B field, the polarisation is in the plane perpendicular to both. This means that the system is cylindically symmetric about the B field. Hence, the angle of polarisation (for linearly polarised light) does not affect the transition intensity.

In the setup simulated here, however, the k-vectors of the lasers are along the x-axis and the magnetic field at $\rho_\perp = 0$ is parallel to the z-axis. Hence, the light is polarised in the y-z plane. The angle of polarisation is therefore an angle relative to the local magnetic field. This means that the polarisation will affect the transition intensities. This can be seen in Figure 7.5. The figure shows the transition intensities for two example YbF transitions, with the laser in the transverse (blue) and longitudinal (red) configurations. A polarisation angle of $\theta = \pi/2$ corresponds to polarisation parallel to the y-axis.

Figure 7.6 shows the transition intensities in weak field and strong field at the best polarisation (also shown) for each transition. There is appreciable transition intensity for all ground sub-states, though the intensity is small at high field for the $(2, 1)$ and $(2, 2)$ ground states. Figure 7.7 shows the total branching ratio from each of the four

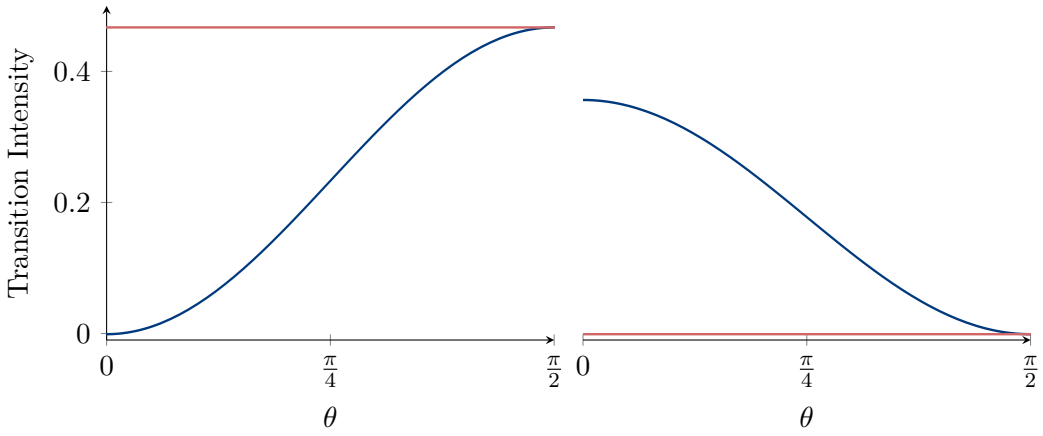

FIGURE 7.5: The transition intensity varies with polarisation angle θ if the k-vector of the light is perpendicular to the B-field (blue) but does not vary if the k-vector is parallel to the B-field (red). The transition intensities are for a B-field parallel to the z-axis. (blue) Transverse configuration with laser parallel to the x-axis and θ as in Figure 4.2. (red) Longitudinal configuration with laser parallel to the z-axis. (left) Shows $A^2\Pi_{1/2}(J = 1/2^+, F = 0, M_F = 0)$–$X^2\Sigma(N = 1, F = 1^-, M_F = 1)$. (right) Shows $A^2\Pi_{1/2}(J = 1/2^+, F = 1, M_F = -1)$–$X^2\Sigma(N = 1, F = 1^+, M_F = -1)$.

$A^2\Pi_{1/2}(J = 1/2^+)$ states to $X^2\Sigma(N = 1, \mathrm{SFS})$ (blue), $X^2\Sigma(N = 1, \mathrm{WFS})$ (red), and $X^2\Sigma(N \neq 1)$ (black). It can be seen that the $A^2\Pi_{1/2}(J = 1/2^+, F = 1, M_F = 0, 1)$ states have a particularly high probability of decay to an $N \neq 1$ state. This is due to the avoided crossing which causes these states become mixed with $J = 3/2^+$ components at higher magnetic field strengths. Molecules that decay to an $N \neq 1$ state are lost. In order to avoid decay to $X^2\Sigma(N \neq 1)$ states, it is important to minimise excitations to the $A^2\Pi_{1/2}(J = 1/2^+, F = 1, M_F = 0, 1)$ states. From Figure 7.6 it can be seen that the $(1^-, 0)$, $(2, -1)$, $(2, 1)$, and $(2, 2)$ ground states can only be excited to the $A^2\Pi_{1/2}(J = 1/2^+, F = 1, M_F = 0, 1)$ states. This means that some loss due to non-closed optical pumping cycles is inevitable.

In order to determine the overall SFP, 50 molecules beginning in each WFS state were simulated moving from $z = 0.11\,\mathrm{m}$ to $z = 0.14\,\mathrm{m}$, through the w2s laser beam at $z = 0.125\,\mathrm{m}$. The laser contained frequency components addressing each WFS ground state and polarisations were chosen so as to select the excited state with maximium transition intensity (see Figure 7.6). Similarly, 50 molecules beginning in each SFS state were simulated between $z = 0.14\,\mathrm{m}$ and $z = 0.16\,\mathrm{m}$, moving through the s2w laser beam at $z = 0.15\,\mathrm{m}$. The s2w laser similarly contained frequency components addressing each SFS ground state and polarisations were chosen so as to select the

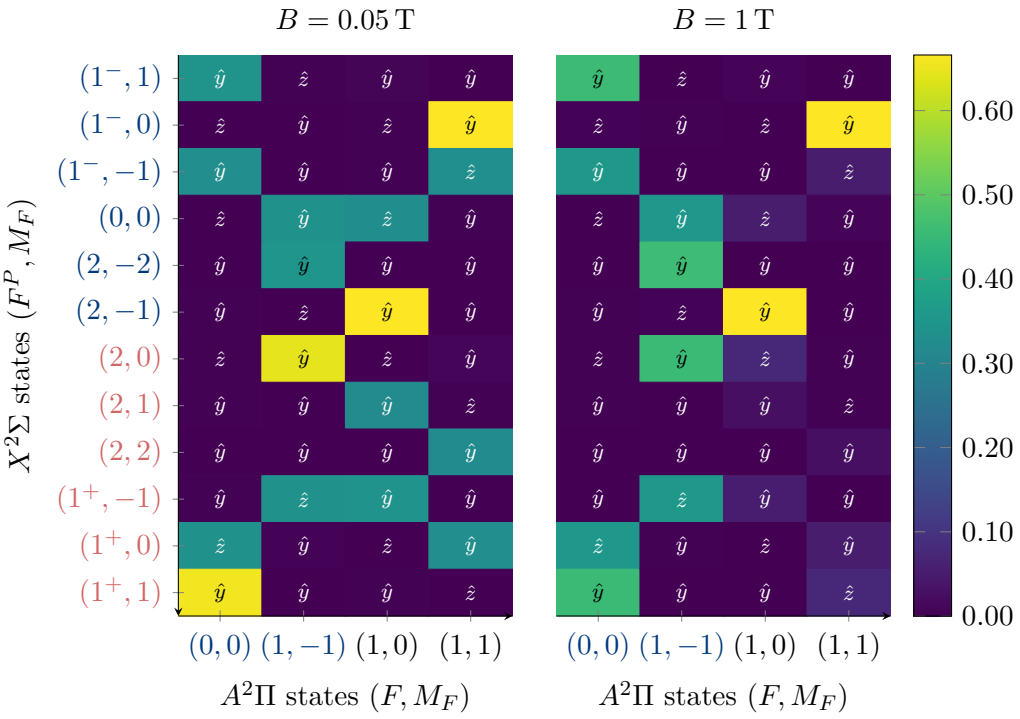

FIGURE 7.6: The transition intensities at 0.05 T and 1 T for the hyperfine sub-states of the $A^2\Pi_{1/2}(J = 1/2^+)$–$X^2\Sigma(N = 1)$ transitions in YbF. The polarisation giving the maximum intensity was used (and is shown). Colour coding is as in Figure 7.1.

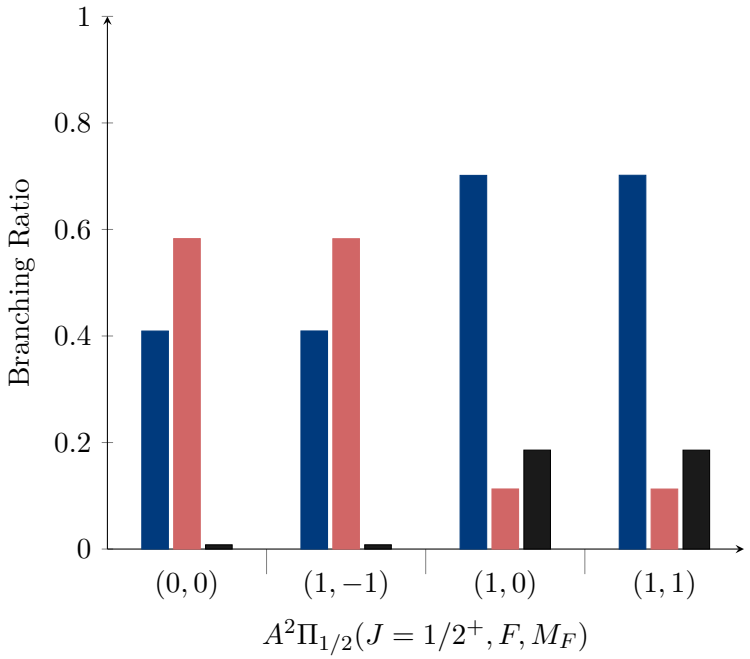

FIGURE 7.7: The total branching ratios from each of the four $A^2\Pi_{1/2}(J = 1/2^+)$ states to $X^2\Sigma(N = 1, \mathrm{SFS})$ (blue), $X^2\Sigma(N = 1, \mathrm{WFS})$ (red), and $X^2\Sigma(N \neq 1)$ (black). Molecules that decay to an $N \neq 1$ state are lost. It can be seen that the $A^2\Pi_{1/2}(J = 1/2^+, F = 1, M_F = 0, 1)$ states have a particularly high probability of decay to an $N \neq 1$ state. Hence, it is important to avoid exciting molecules to these states if at all possible.

excited state with maximium transition intensity.

The SFPs and loss probabilities for each initial state are shown in Figure 7.8. The SFP is ≥ 0.94 for all states except $(2,1)$ and $(2,2)$, which have SFPs of 0.72 and 0.78 respectively. The lower SFPs for these states is due to the increased loss probability and significantly lower transition intensity.

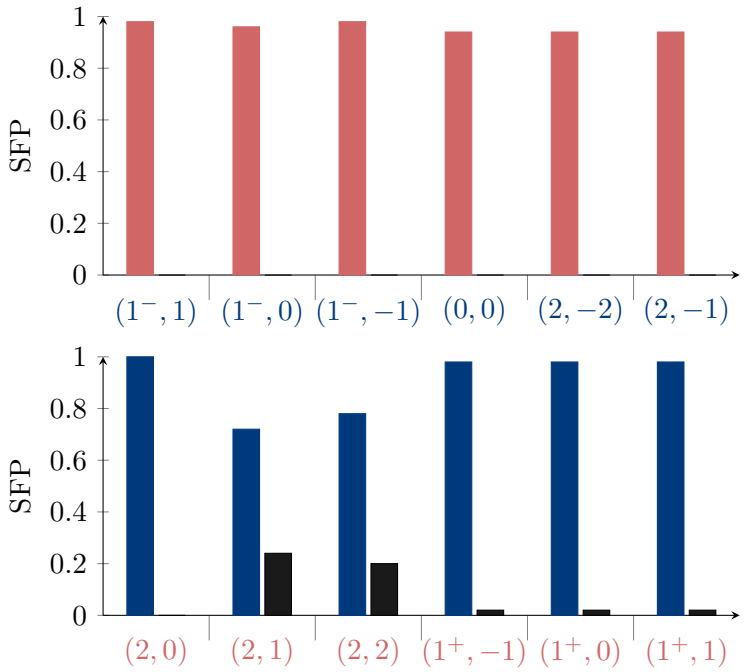

FIGURE 7.8: The spin flip probabilities (red, blue) and loss probabilities (black) of molecules initially in SFS (a) and WFS (b) states. Molecules were simulated moving between 0.400 m and 0.525 m of the field and lasers shown in Figure 7.4. The lasers had 200 mW of power and a $1/e^2$ width of 1.7 mm. The s2w laser was offset from the field minimum at 0.5 m by -3 mm, giving a detuning of $\Delta_{\mathrm{s2w}} = 1$ GHz. The w2s laser was offset from the field maximum by 5 mm (b) giving a detuning of $\Delta_{\mathrm{w2s}} = -16.3$ GHz.

7.4 Dynamics in the Decelerator

As with CaF, molecules in a WFS state travelling through the decelerator experience a transverse force due to the positive curvature of the magnetic field in the transverse plane. This causes them to oscillate radially. In the harmonic model for the CaF decelerator, Eqn. (3.10) gave the angular frequency of this oscillation. In this solenoid-based YbF decelerator, the positive curvature exists throughout the length of the decelerator. This means there is an extra factor of 2 compared with Eqn. (3.10), giving:

$$\omega = 2\sqrt{\frac{\mu_B B_1^{\mathrm{wk}}}{m_{\mathrm{YbF}} R^2}}. \tag{7.2}$$

For this decelerator, we have $B_1^{\mathrm{wk}} = 0.45\,\mathrm{T}$ and $R = 0.025\,\mathrm{m}$. This gives $\omega = 289\,\mathrm{rad\,s^{-1}}$, or an oscillation period of 22 ms. On the other hand, if the molecule is in a SFS state, the same positive curvature magnetic field has an anti-guiding effect. This accelerates molecules away from the centre of the decelerator.

Time-stepped simulations were carried out as described in Section 3.4.2, with YbF molecules moving through a magnetic field as described in Section 7.2. Since the magnetic field can be calculated analytically from Eqn. (7.1), this calculation was used rather than generating a numerically calculated field. An example of the molecular motion for a YbF molecule in a WFS state (red) and SFS state (blue) is shown in Figure 7.9.

Under the deceleration scheme, YbF molecules are expected to be in a WFS state approximately half the time, and in a SFS state the other half. Therefore,

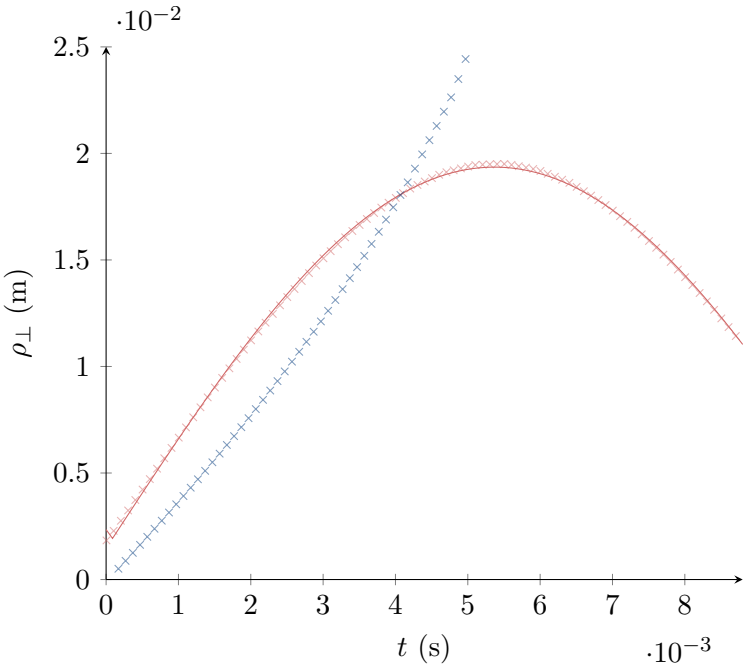

FIGURE 7.9: (red) Simulated motion of a YbF molecule in a WFS state in a decelerator with no optical pumping. The trajectory is fitted with a function of the form $|\sin(\omega t + \phi)|$ to determine the effective oscillation frequency of $\omega = 297\,\mathrm{rad\,s^{-1}}$. (blue) The same for a YbF molecule in a SFS state, showing the anti-guiding effect of the magnetic field.

it is expected that in this magnetic field, molecules will experience no net guiding or anti-guiding. This means that molecules with non-zero transverse velocity are expected to move linearly away from the centre of the decelerator, as if through free space. Therefore, the phase space acceptance with the optical pumping and perfect spin-flips is given by the cone of transverse velocities defined by the length of the decelerator and the radius of the central bore:

$$\max\left(v_{\perp}\right) = \frac{(R-\rho_{\perp})v_z}{\mathcal{L}}, \tag{7.3}$$

where $\mathcal{L}$ is the length of the decelerator and R is the radius of the central bore. For the setup described here, this gives $\max\left(v_{\perp}\right) = 3.6\,\mathrm{m\,s^{-1}}$ for a molecule with $\rho_{\perp} = 0$ and $\max\left(v_{\perp}\right) = 7.2\,\mathrm{m\,s^{-1}}$ for a molecule with $\rho_{\perp} = R$.

However, the transverse setup of the optical pumping light presents an additional problem. The light is tuned to be resonant with molecules seeing the magnetic field at the centre of the decelerator. This means that as molecules move away from the centre, so seeing higher magnetic fields, they are increasingly off-resonance. In the longitudinal optical pumping setup, this simply moves the longitudinal position of the resonance. However, in the transverse setup, this means molecules off-centre will never be optically pumped and will not spin-flip. The scattering rates against transverse position for both the w2s and s2w lasers can be seen in Figure 7.10.

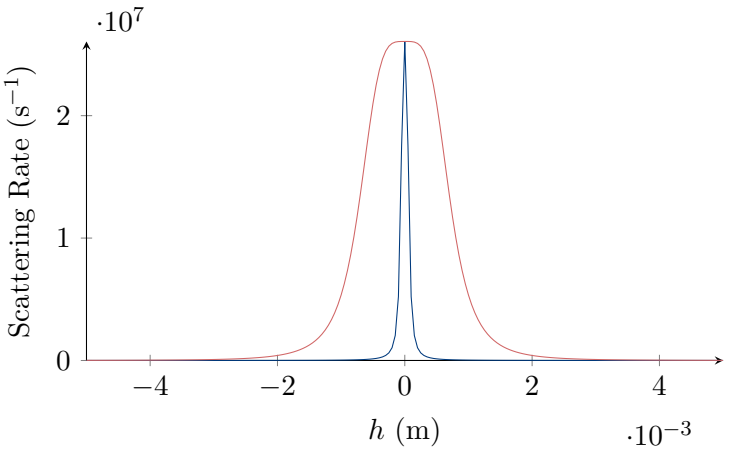

FIGURE 7.10: The scattering rates for the w2s laser (red) and s2w laser (blue) varying with transverse position. The lasers are modelled at being at saturation intensity and on-resonance with the transition at the centre, $\rho_{\perp} = 0$.

The upshot of this is to reduce the effective radius, $\tilde{R}$, of the decelerator to a few millimetres. Within this effective radius, molecules have high spin-flip probability and can be decelerated, whereas outside it they can only be guided. Therefore, although the solenoid setup allows for a larger central bore, the transverse optical pumping scheme reduces the effective radius to a similar size as with the permanent magnet setup shown in Chapter 3.

Further, the lack of net guiding effect combined with the smaller effective radius reduces the phase space acceptance in transverse velocity. For a molecule initially at $\rho_\perp = 0$, and taking $\tilde{R} = 0.002\,\mathrm{m}$, this 'soft' phase space acceptance has $\max(v_\perp) \sim 0.3\,\mathrm{m\,s^{-1}}$. In order to maximise the fraction of molecules accepted we can consider this to be the maximum width of the transverse velocity distribution of the molecules. This then corresponds to a beam temperature of 2 mK. More detail on this is given in Section 7.5.

An example trajectory of a YbF molecule with optical pumping is shown in Figure 7.11. The s2w laser beams are offset from the field minima by 1.5 mm. The laser power is 75 mW and the $1/e^2$ width of the beams is 1 mm. The molecule has an initial transverse velocity of $0.96\,\mathrm{m\,s^{-1}}$. The figure also shows the theoretical trajectory calculated from Eqn. (3.28). For this decelerator, $L = 0.1\,\mathrm{m}$ and $\Delta\epsilon = -1.8 \times 10^{-23}\,\mathrm{J}$. The molecule spin-flips regularly and has the expected linear transverse trajectory until $z = 0.75\,\mathrm{m}$. At this point, $\rho_\perp = 5\,\mathrm{mm}$ and the molecule is no longer resonant with the laser and stops spin-flipping. It remains in a WFS state and the guiding effect of the magnetic field can be seen in the final 0.25 m.

7.5 Deceleration

In order to maximise the number of YbF molecules accepted into this configuration of ZS decelerator, the transverse beam temperature should be around 2 mK. This is significantly colder than beams produced by most buffer gas sources. However, it has been shown that it is possible to transversely cool YbF in two dimensions to temperatures below 200 µK [92]. In this section we present the results of a series of deceleration simulations which were run with YbF molecular beams having transverse

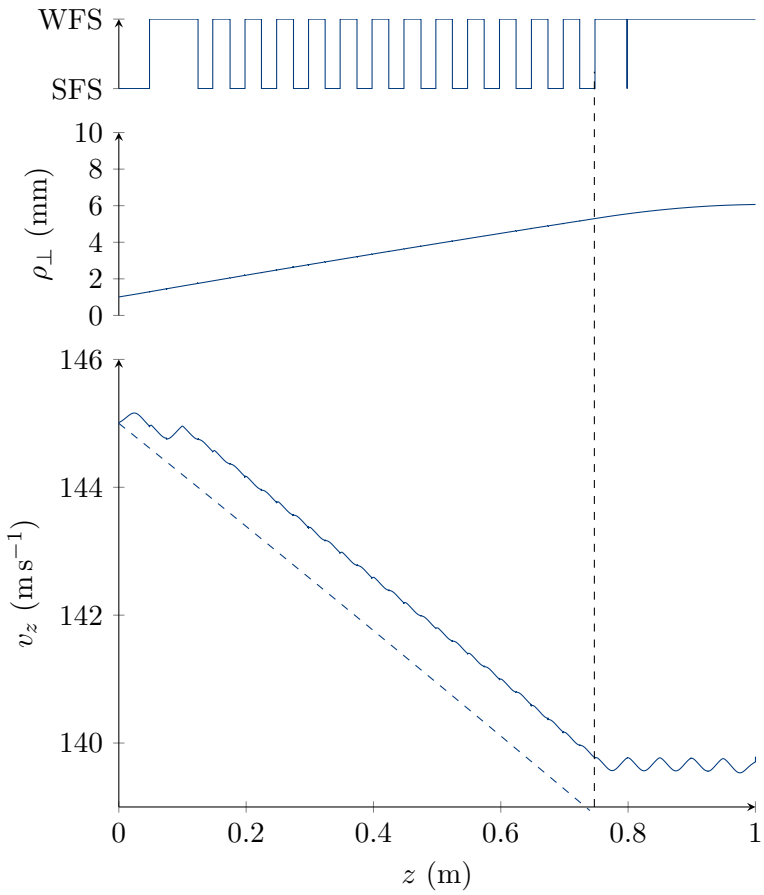

FIGURE 7.11: The trajectory through the z–v_z phase space of a single YbF molecule, together with a plot of the molecule's state (top) and its transverse position, $\rho_\perp$. The dashed line shows the theoretical trajectory calculated from Eqn. (3.28), which assumes perfect spin flipping. The dashed black line shows $z = 0.75\,\mathrm{m}$, when $\rho_\perp = 5\,\mathrm{mm}$. After this point the molecule is too far off-resonance to spin-flip and remains in a WFS state.

temperatures between 100 µK and 10 mK. The beams had $\Delta v_z = 24\,\mathrm{m\,s^{-1}}$ and $v_{\mathrm{out}} = 145\,\mathrm{m\,s^{-1}}$.

Molecules at 10 mK have $\Delta v_\perp = 0.64\,\mathrm{m\,s^{-1}}$. This is well within the 'hard' acceptance of the decelerator. Therefore, it is not expected that a significant number of molecules will hit the walls of the decelerator. However, molecules with higher transverse velocities will move away from the centre and so at some point will undergo a final spin-flip, after which they will no longer be resonant with the lasers. This means that the molecules will no longer undergo deceleration. Therefore, the average reduction in velocity across the whole beam will decrease at higher temperatures, as more molecules fall outside the spin-flippable 'soft' acceptance region. This can be seen in Figure 7.12.

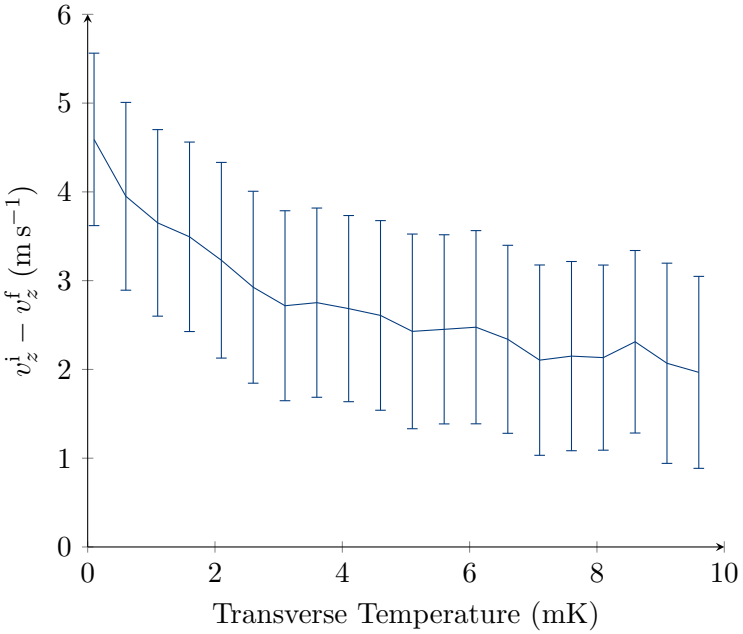

FIGURE 7.12: The simulated mean change in v_z for beams of YbF molecules at varying transverse temperatures. Each point is the mean of 1×10^3 molecules. Error bars show the standard error of the mean. The maximum deceleration under ideal conditions (see Eqn. (3.28)) is $9\,\mathrm{m\,s^{-1}}$.

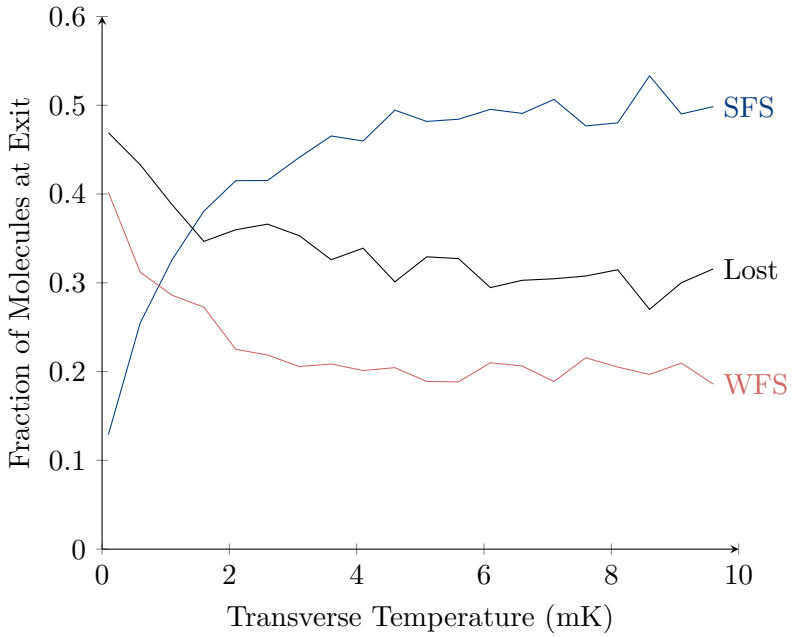

FIGURE 7.13: The simulated state populations at the exit of the decelerator, shown as a fraction of accepted molecules. It can be seen that there is significant loss to $X^2\Sigma(N \neq 1)$ states (black), as expected from the branching ratios (see Figure 7.7).

From Figure 7.10 it can be seen that the w2s laser has significant scattering rate at larger transverse positions than the s2w laser. Therefore, it is more likely that the final spin flip will be weak-to-strong, rather than strong-to-weak. On the other hand, for molecules which are always on-axis, the final laser beam is s2w, so we would expect them to finish in a WFS state. Hence, we would expect to see very few molecules exiting the decelerator in SFS states at low temperatures, and an increasing number at higher temperatures as fewer molecules are resonant with the final s2w laser. This can be seen in Figure 7.13. The figure also shows the high loss rate of molecules which decay to $X^2\Sigma(N \neq 1)$ states, as expected from the branching ratios (see Figure 7.7).

Finally, molecules which fall outside the spin-flip region and are in a SFS state continue to move away from the centre. Molecules in a WFS state will be guided back towards the centre and any molecules near the centre will finish in a WFS state due to the final s2w laser. Since there is a higher chance of molecules leaving the soft acceptance region in a SFS state we would expect the number of soft accepted molecules to fall to just below 50% at higher temperatures. This can be seen in

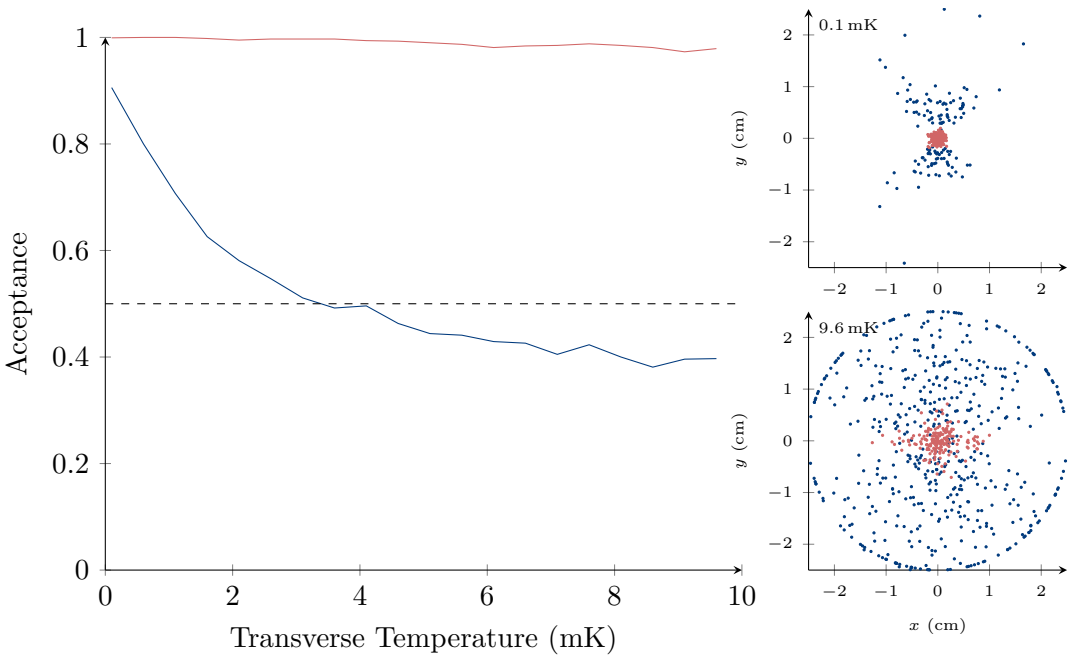

FIGURE 7.14: (left) Hard (red) and soft (blue) phase space acceptance. The soft acceptance has a radial threshold of $\rho_\perp = 5\,\text{mm}$. As the temperature increases more molecules fall outside the soft acceptance. The dashed line shows 50%. (right) The transverse distribution of molecules exiting the decelerator for a transverse temperature of 1 mK and 9.6 mK. WFS molecules are shown in red and SFS in blue. The effect of the anti-guiding of SFS molecules can be clearly seen in the 9.6 mK distribution.

Figure 7.14. Additionally, SFS molecules are anti-guided and so we expect to see all molecules which leave the decelerator in a SFS state to move away from the centre. This can also be seen in the figure.

7.6 Outlook

ZSD of heavy molecules and those with unfavourable vibrational branching ratios is a promising area of research. The simulations presented in this chapter represent progress towards developing a scheme for YbF.

Although a solenoid type magnetic field was chosen as a way to increase the phase space acceptance of the ZSD, it is clear from these simulations that it has some drawbacks. Firstly, there is a relatively high loss rate due to the structure of the molecule. 30-40% of molecules decaying to $N \neq 1$ states should be expected if the optical pumping is to occur on the A–X transition.

Secondly, there is a positive curvature in the magnetic field in the transverse plane in the strong field sections as well as the weak field sections. This leads to molecules necessarily being anti-guided when they are in SFS states, as the timing of the pumping to SFS states cannot be conincided with magnetic field regions without curvature (as in the CaF scheme). With the laser positions chosen here, this leads to no net guiding or anti-guiding effects, meaning the molecules move as if through free space while they are being regularly spin-flipped.

Thirdly, curvature of the solenoid field coupled with the transverse optical pumping setup required by the structure of the YbF molecule, results in molecules only being on resonance with each laser within a very small transverse area. For the field used in this simulation, this region is $\rho_\perp < 5\,\text{mm}$. Molecules which are outside this region do not get optically pumped and so stop spin-flipping.

Taken together, the latter two effects lead to the phase space acceptance being reduced to close to that of a cylinder of radius 5 mm in free space. This occurs because molecules within this region move in straight lines as if through free space, due to the second effect. If their transverse velocity is such that they leave this region, they will stop being spin-flipped due to the third effect, and will have a 50% chance of being stuck in an SFS state. They are then anti-guided and lost. There are a few possible

lines of investigation which can mitigate these effects. Firstly, the positions of the w2s and s2w lasers could be adjusted to increase the amount of time molecules spend in WFS states, albeit at the cost of reduced deceleration per half-cycle. Secondly, the lasers could be arranged such that molecules spend every other half-cycle completely in a WFS state, though again this comes at the cost of reduced deceleration. Thirdly, whilst short solenoids (loops, really) were chosen to minimise the overall length of the decelerator here, longer solenoids would provide a more uniform magnetic field at the centre (though there will still be large curvature at the edges), reducing the anti-guiding effect in strong field regions.

The impact of the second and third effects is minimised if the beam is transversely cooled before entering the ZSD. Since ZSD does not transversely cool molecules, only confines them (subject to the above discussion regarding spin-flipping and anti-guiding), separate transverse cooling is necessary anyway if the number of molecules accepted into a magneto-optical trap is to be increased. Transverse cooling of YbF has already been demonstrated [92]. ZSD in combination with transverse cooling would provide the additional benefit of slowing the beam, increasing the number of molecules below the capture velocity of a MOT, while minimising the number of photons scattered.

Chapter 8

Conclusions

This thesis has presented theoretical analysis and work towards experimental implementation of a proposed method for slowing polar molecules: Zeeman-Sisyphus deceleration (ZSD). ZSD is a promising experimental technique for slowing molecular beams, and has recently been demonstrated experimentally with a beam of CaOH molecules [5]. The work presented here developed the scheme from its initial proposal [1], prepared and characterised an experiment for testing a CaF ZSD, and developed a YbF ZSD scheme.

In order to inform the design of an experiment for testing the ZSD scheme for CaF, the phase space acceptance of the decelerator was calculated. The overlap between the distribution of molecules in phase space and the acceptance of the ZSD was found to decrease significantly as the gap between the molecular source and the decelerator increased. The means it is advantageous to design an experiment including this ZSD with this gap being as small as possible. Additionally, trajectory simulations were carried out to determine the spin-flip probability (SFP) accross a range of laser detunings and powers. This showed that the optimum detunings for maximising SFP coincided with the optimum detunings for maximising the deceleration effect. This work was presented in Chapter 3.

A molecular beam source was then developed in Chapter 4, with a view to using it to test the CaF ZS decelerator. The source produced beams with a molecular flux of $(2.6 \pm 0.1) \times 10^8\,\mathrm{mol\,sr^{-1}\,shot^{-1}}$ and occupying a solid angle of $0.014\,\mathrm{sr}$ at a helium buffer gas flow rate of $0.5\,\mathrm{sccm}$. The average beam velocity at this flow rate was $(159 \pm 1)\,\mathrm{m\,s^{-1}}$. The beams produced had clear non-equilibrium features at low buffer gas flow rates. As the flow rates increased, these non-equilibrium features

diminished. However, the flow rate was practically limited to 0.5 sccm by the capacity of the charcoal pumps used to pump the helium. This work characterising the source was presented in Chapter 5.

The molecular source was used to test the decelerator, and it was found that molecules were able to be transmitted through the decelerator in Chapter 6. This initial test had a source-decelerator gap of 23 cm. From the simulations carried out, it was known that this resulted in significant loss of molecules due to the phase space acceptance of the decelerator. Therefore, steps were taken to reduce this gap to 10 cm. Unfortunately, this resulted in the loss of the downstream molecular signal, without which the decelerator could not be tested.

As part of the attempts to recover the downstream signal, a neon (rather than helium) buffer gas source was trialled. It was found that the pumping speed of the charcoal pumps was one order of magnitude higher for neon than for helium: $(3.4 \pm 0.5) \times 10^5\,\mathrm{l\,s^{-1}}$ for neon versus $(1.22 \pm 0.06) \times 10^4\,\mathrm{l\,s^{-1}}$ for helium. Therefore, it was thought that the resulting reduced pressure would increase the mean free path of the CaF through the chamber, or allow for operation in the high buffer gas flow rate regime, or both. It was possible to operate at up to 30 sccm of neon with a CaF mean free path of 0.81 m. However, no downstream signal was recovered.

Efforts were also made to reduce the background noise at the downstream detection point, so as to better distinguish a weak molecular signal. As part of this, a Raman resonance optical cycling (RROC) technique, proposed for CaF in [21], was tested. RROC involves pumping two off-diagonal vibrational transitions and results in the pump light and emitted light being at different wavelengths. Therefore, the pump light can be filtered out by a bandpass filter, resulting in reduced background noise. Although there was not enough laser power to see the full benefit of the scheme, it was tested as a proof-of-concept. The use of the dual frequency light, giving a closed cycle, resulted in a 33% increase in signal over pumping only a single vibrational transition. It is expected that this will increase further if both transitions are fully saturated.

Despite extensive investigations, it was not possible to recover a downstream beam signal. Efforts turned instead towards developing a ZSD scheme for YbF in Chapter 7. It was found that YbF's more complex energy level structure meant that there were

many stray transitions which could come into resonance with the w2s and s2w lasers at unindented magnetic field strengths. Therefore, it is beneficial to arrange the lasers perpendicular to the axis of the decelerator, so there was only appreciable intensity at certain chosen magnetic field strengths.

As simulations for CaF indicated that the small phase space acceptance may pose some problems, the simulations for YbF explored a decelerator with a larger central bore. To achieve this, superconducting solenoids can be used [5]. However, the use of a solenoid magnetic field results in significant positive curvature in the magnetic field in the transverse plane in strong field regions. Molecules in SFS states are anti-guided by such a field and so, for the detunings examined in the simulations, there was no net guiding effect. This could be mitigated by changing the laser detunings or skipping spin-flips every other half-cycle, at the expense of deceleration, or by increasing the length of the solenoids to make the field more uniform at the centre, at the expense of physical size.

Heavy polar molecules in particular, and ultracold molecules in general, continue to be an exciting and promising area of research. They have applications in fields from fundamental physics to quantum computation. The complex electronic and ro-vibrational structure of these molecules makes it difficult to find optical pumping cycles that are sufficiently closed to allow for laser cooling. Therefore, there is a need to provide novel slowing methods that can reduce the speed of a molecular beam to within the capture velocity of a magneto-optical trap. It is hoped that the work presented in this thesis represents a step towards an implementation of one such slowing method, Zeeman-Sisyphus deceleration, for beams of CaF and YbF molecules.

FIGURE 8.1: BL0015, Blackett Laboratory, 12 March 2021

Appendix A

Simulation Code

The simulations whose results are presented in Chapter 3 and Chapter 7 were written in C++ and analysed in Mathematica. The source code is available at [93].

Bibliography

[1] N. J. Fitch and M. R. Tarbutt, Chemphyschem **17**, 3609 (2016), ISSN 1439-7641, 27629547[pmid], URL https://www.ncbi.nlm.nih.gov/pubmed/27629547.

[2] L. D. Carr, D. DeMille, R. V. Krems, and J. Ye, New Journal of Physics **11**, 055049 (2009).

[3] M. Di Rosa, The European Physical Journal D-Atomic, Molecular, Optical and Plasma Physics **31**, 395 (2004).

[4] M. R. Tarbutt, Contemporary Physics **59**, 356 (2018), URL https://doi.org/10.1080/00107514.2018.1576338.

[5] B. L. Augenbraun, A. Frenett, H. Sawaoka, C. Hallas, N. B. Vilas, A. Nasir, Z. D. Lasner, and J. M. Doyle, Physical Review Letters **127**, 263002 (2021).

[6] J. A. Blackmore, L. Caldwell, P. D. Gregory, E. M. Bridge, R. Sawant, J. Aldegunde, J. Mur-Petit, D. Jaksch, J. M. Hutson, B. E. Sauer, et al., Quantum Science and Technology **4**, 014010 (2018).

[7] R. Sawant, J. A. Blackmore, P. D. Gregory, J. Mur-Petit, D. Jaksch, J. Aldegunde, J. M. Hutson, M. Tarbutt, and S. L. Cornish, New Journal of Physics **22**, 013027 (2020).

[8] C. Zhang and M. Tarbutt, PRX Quantum **3**, 030340 (2022).

[9] G. Barontini, L. Blackburn, V. Boyer, F. Butuc-Mayer, X. Calmet, J. R. Crespo López-Urrutia, E. A. Curtis, B. Darquié, J. Dunningham, N. J. Fitch, et al., EPJ Quantum Technology **9**, 12 (2022), ISSN 2196-0763, URL https://doi.org/10.1140/epjqt/s40507-022-00130-5.

[10] T. E. Wall, J. F. Kanem, J. J. Hudson, B. E. Sauer, D. Cho, M. G. Boshier, E. A. Hinds, and M. R. Tarbutt, Phys. Rev. A **78**, 062509 (2008), URL https://link.aps.org/doi/10.1103/PhysRevA.78.062509.

[11] T. E. Wall, J. F. Kanem, J. M. Dyne, J. J. Hudson, B. E. Sauer, E. A. Hinds, and M. R. Tarbutt, Physical Chemistry Chemical Physics **13**, 18991 (2011).

[12] V. Zhelyazkova, A. Cournol, T. E. Wall, A. Matsushima, J. J. Hudson, E. A. Hinds, M. R. Tarbutt, and B. E. Sauer, Phys. Rev. A **89**, 053416 (2014), URL https://link.aps.org/doi/10.1103/PhysRevA.89.053416.

[13] S. Truppe, M. Hambach, S. M. Skoff, N. E. Bulleid, J. S. Bumby, R. J. Hendricks, E. A. Hinds, B. E. Sauer, and M. R. Tarbutt, Journal of Modern Optics **65**, 648 (2018), URL https://doi.org/10.1080/09500340.2017.1384516.

[14] S. Truppe, H. J. Williams, N. J. Fitch, M. Hambach, T. E. Wall, E. A. Hinds, B. E. Sauer, and M. R. Tarbutt, New Journal of Physics **19**, 022001 (2017), URL https://doi.org/10.1088%2F1367-2630%2Faa5ca2.

[15] S. Truppe, H. J. Williams, M. Hambach, L. Caldwell, N. J. Fitch, E. A. Hinds, B. E. Sauer, and M. R. Tarbutt, Nature Physics **13**, 1173 EP (2017), URL https://doi.org/10.1038/nphys4241.

[16] H. J. Williams, S. Truppe, M. Hambach, L. Caldwell, N. J. Fitch, E. A. Hinds, B. E. Sauer, and M. R. Tarbutt, New Journal of Physics **19**, 113035 (2017), URL https://doi.org/10.1088%2F1367-2630%2Faa8e52.

[17] H. J. Williams, L. Caldwell, N. J. Fitch, S. Truppe, J. Rodewald, E. A. Hinds, B. E. Sauer, and M. R. Tarbutt, Phys. Rev. Lett. **120**, 163201 (2018), URL https://link.aps.org/doi/10.1103/PhysRevLett.120.163201.

[18] L. Caldwell, H. Williams, N. Fitch, J. Aldegunde, J. M. Hutson, B. Sauer, and M. Tarbutt, Physical Review Letters **124**, 063001 (2020).

[19] S. Jurgilas, A. Chakraborty, C. Rich, B. Sauer, M. D. Frye, J. M. Hutson, and M. Tarbutt, New Journal of Physics **23**, 075004 (2021).

[20] S. Jurgilas, A. Chakraborty, C. Rich, L. Caldwell, H. Williams, N. Fitch, B. Sauer, M. D. Frye, J. M. Hutson, and M. Tarbutt, Physical Review Letters **126**, 153401 (2021).

[21] C. McGarry, Ph.D. thesis, Imperial College London (2022).

[22] J. Hudson, B. Sauer, M. Tarbutt, and E. Hinds, Physical review letters **89**, 023003 (2002).

[23] J. J. Hudson, D. M. Kara, I. Smallman, B. E. Sauer, M. R. Tarbutt, and E. A. Hinds, Nature **473**, 493 (2011).

[24] M. Tarbutt, J. Hudson, B. Sauer, E. Hinds, V. Ryzhov, V. Ryabov, and V. Ezhov, Journal of Physics B: Atomic, Molecular and Optical Physics **35**, 5013 (2002).

[25] N. J. Fitch, J. Lim, E. A. Hinds, B. E. Sauer, and M. R. Tarbutt, Quantum Science and Technology **6**, 014006 (2020), URL https://dx.doi.org/10.1088/2058-9565/abc931.

[26] N. E. Bulleid, S. M. Skoff, R. J. Hendricks, B. E. Sauer, E. A. Hinds, and M. R. Tarbutt, Phys. Chem. Chem. Phys. **15**, 12299 (2013), URL http://dx.doi.org/10.1039/C3CP51553B.

[27] J. Lim, J. R. Almond, M. A. Trigatzis, J. A. Devlin, N. J. Fitch, B. E. Sauer, M. R. Tarbutt, and E. A. Hinds, Phys. Rev. Lett. **120**, 123201 (2018), URL https://link.aps.org/doi/10.1103/PhysRevLett.120.123201.

[28] X. Zhuang, A. Le, T. C. Steimle, N. Bulleid, I. Smallman, R. Hendricks, S. Skoff, J. Hudson, B. Sauer, E. Hinds, et al., Physical Chemistry Chemical Physics **13**, 19013 (2011).

[29] P. D. Group, P. A. Zyla, R. M. Barnett, J. Beringer, O. Dahl, D. A. Dwyer, D. E. Groom, C. J. Lin, K. S. Lugovsky, E. Pianori, et al., Progress of Theoretical and Experimental Physics **2020** (2020), ISSN 2050-3911, 083C01, https://academic.oup.com/ptep/article-pdf/2020/8/083C01/34673740/rpp2020-vol2-2015-2092_18.pdf, URL https://doi.org/10.1093/ptep/ptaa104.

[30] G. R. Bengochea, G. León, E. Okon, and D. Sudarsky, The European Physical Journal C **80**, 1 (2020).

[31] R. McEvoy and J. Betts, *Harrison Decoded: Towards A Perfect Pendulum Clock* (Oxford University Press, 2020).

[32] D. Ziemkiewicz, Phys. Rev. E **103**, 062208 (2021), URL https://link.aps.org/doi/10.1103/PhysRevE.103.062208.

[33] M. Kajita, Journal of the Physical Society of Japan **87**, 104301 (2018), https://doi.org/10.7566/JPSJ.87.104301, URL https://doi.org/10.7566/JPSJ.87.104301.

[34] E. Purcell and N. Ramsey, Physical Review **78**, 807 (1950).

[35] E. D. Commins, in *Advances in Atomic, Molecular, and Optical Physics* (Elsevier, 1999), vol. 40, pp. 1–55.

[36] A. C. A. V. . . A. D. . D. D. acme@ physics. harvard. edu 2 d Doyle JM 1 Gabrielse G. 1 3 Haefner J. 1 Hutzler NR 1 4 Lasner Z. 2 Meisenhelder C. 1 OLeary BR 2 Panda CD 1 West AD 2 6 West EP 1 6 Wu X. 1 2, Nature **562**, 355 (2018).

[37] W. B. Cairncross, D. N. Gresh, M. Grau, K. C. Cossel, T. S. Roussy, Y. Ni, Y. Zhou, J. Ye, and E. A. Cornell, Physical review letters **119**, 153001 (2017).

[38] T. S. Roussy, L. Caldwell, T. Wright, W. B. Cairncross, Y. Shagam, K. B. Ng, N. Schlossberger, S. Y. Park, A. Wang, J. Ye, et al., *A new bound on the electron's electric dipole moment* (2022), 2212.11841.

[39] S. Lloyd, Science **273**, 1073 (1996).

[40] R. Blatt and C. F. Roos, Nature Physics **8**, 277 (2012).

[41] C. Gross and I. Bloch, Science **357**, 995 (2017).

[42] A. Muthukrishnan and C. R. Stroud Jr, Physical review A **62**, 052309 (2000).

[43] M. A. Joffe, W. Ketterle, A. Martin, and D. E. Pritchard, JOSA B **10**, 2257 (1993).

[44] E. S. Shuman, J. F. Barry, and D. DeMille, Nature **467**, 820 EP (2010), URL https://doi.org/10.1038/nature09443.

[45] M. R. Tarbutt, New Journal of Physics **17**, 015007 (2015), URL https://doi.org/10.1088%2F1367-2630%2F17%2F1%2F015007.

[46] M. Tarbutt, B. Sauer, J. Hudson, and E. Hinds, New Journal of Physics **15**, 053034 (2013).

[47] E. B. Norrgard, D. J. McCarron, M. H. Steinecker, M. R. Tarbutt, and D. DeMille, Phys. Rev. Lett. **116**, 063004 (2016), URL https://link.aps.org/doi/10.1103/PhysRevLett.116.063004.

[48] H. Williams, Ph.D. thesis, Imperial College London (2018), URL http://hdl.handle.net/10044/1/62635.

[49] J. F. Barry, D. J. McCarron, E. B. Norrgard, M. H. Steinecker, and D. DeMille, Nature **512**, 286 EP (2014), URL https://doi.org/10.1038/nature13634.

[50] B. Hemmerling, E. Chae, A. Ravi, L. Anderegg, G. K. Drayna, N. R. Hutzler, A. L. Collopy, J. Ye, W. Ketterle, and J. M. Doyle, Journal of Physics B: Atomic, Molecular and Optical Physics **49**, 174001 (2016), URL https://doi.org/10.1088%2F0953-4075%2F49%2F17%2F174001.

[51] J. Kawanaka, K. Shimizu, and H. Takuma, Applied Physics B **57**, 113 (1993).

[52] U. Schünemann, H. Engler, M. Zielonkowski, M. Weidemüller, and R. Grimm, Optics Communications **158**, 263 (1998).

[53] Z. Lin, K. Shimizu, M. Zhan, F. Shimizu, and H. T. H. Takuma, Japanese Journal of Applied Physics **30**, L1324 (1991).

[54] J. Stack, Ph.D. thesis, Imperial College London (2010).

[55] H. L. Bethlem, G. Berden, and G. Meijer, Physical Review Letters **83**, 1558 (1999).

[56] S. Tokunaga, J. Stack, J. Hudson, B. Sauer, E. Hinds, and M. Tarbutt, The Journal of chemical physics **126**, 124314 (2007).

[57] K. P. Huber and G. H. Herzberg, *NIST Chemistry WebBook, NIST Standard Reference Database Number 69* (National Institute of Standards and Technology, ????), chap. Constants of Diatomic Molecules.

[58] W. M. Haynes, *Spectroscopic constants of diatomic molecules* (2014).

[59] B. H. Bransden and C. J. Joachain, *Physics of Atoms and Molecules* (Prentice Hall, 2003), ISBN 058235692X, URL https://www.ebook.de/de/product/3262054/brian_h_bransden_charles_jean_joachain_physics_of_atoms_and_molecules.html.

[60] J. P. Dahl and M. Springborg, The Journal of chemical physics **88**, 4535 (1988).

[61] J. M. Brown, J. M. Brown, and A. Carrington, *Rotational spectroscopy of diatomic molecules* (Cambridge university press, 2003).

[62] A. R. Edmonds, *Angular momentum in quantum mechanics* (Princeton university press, 1996).

[63] R. W. Field, D. O. Harris, and T. Tanaka, Journal of molecular spectroscopy **57**, 107 (1975).

[64] J. Devlin, M. Tarbutt, D. Kokkin, and T. Steimle, Journal of Molecular Spectroscopy **317**, 1 (2015).

[65] T. C. Steimle, T. Ma, and C. Linton, The Journal of chemical physics **127**, 234316 (2007).

[66] K. Dunfield, C. Linton, T. Clarke, J. McBride, A. Adam, and J. Peers, Journal of Molecular Spectroscopy **174**, 433 (1995).

[67] T. Ma, C. Butler, J. M. Brown, C. Linton, and T. C. Steimle, The Journal of Physical Chemistry A **113**, 8038 (2009).

[68] R. Loudon, *The Quantum Theory of Light* (Oxford University Press, 2000), ISBN 0198501765, URL https://www.ebook.de/de/product/3256690/rodney_loudon_the_quantum_theory_of_light.html.

[69] N. Fitch and M. Tarbutt (Academic Press, 2021), vol. 70 of *Advances In Atomic, Molecular, and Optical Physics*, pp. 157–262, URL https://www.sciencedirect.com/science/article/pii/S1049250X21000033.

[70] J. Brown and B. Howard, Molecular Physics **31**, 1517 (1976).

[71] K. Halbach, Nuclear instruments and methods **169**, 1 (1980).

[72] N. F. Ramsey, *Molecular Beams* (Oxford University Press, 1990), ISBN 9780198520214, URL https://www.amazon.com/Molecular-Oxford-Classic-Physical-Sciences/dp/0198520212?SubscriptionId=AKIAIOBINVZYXZQZ2U3A&tag=chimbori05-20&linkCode=xm2&camp=2025&creative=165953&creativeASIN=0198520212.

[73] G. Scoles, *Atomic and molecular beam methods* (Oxford University Press, 1988), ISBN 9780195042801.

[74] D. H. Levy, L. Wharton, and R. E. Smalley, *Chemical and Biochemical Applications of Lasers* (Academic Press, 1977), chap. 1.

[75] S. M. Skoff, R. J. Hendricks, C. D. J. Sinclair, J. J. Hudson, D. M. Segal, B. E. Sauer, E. A. Hinds, and M. R. Tarbutt, Phys. Rev. A **83**, 023418 (2011), URL https://link.aps.org/doi/10.1103/PhysRevA.83.023418.

[76] N. R. Hutzler, H.-I. Lu, and J. M. Doyle, Chemical Reviews **112**, 4803 (2012), URL https://doi.org/10.1021/cr200362u.

[77] J. M. Dixon, M. Taniguchi, and J. S. Lindsey, Photochemistry and photobiology **81**, 212 (2005).

[78] D. W. Breck, *8.3.1 the kinetic diameter* (1974), URL https://app.knovel.com/hotlink/khtml/id:kt011I1LX1/zeolite-molecular-sieves/the-kinetic-diameter.

[79] E. Hecht, *Optics, Global Edition* (Pearson Education, London, England, 2016), 5th ed.

[80] S. E. Hluchan and K. Pomerantz, *Calcium and calcium alloys* (2006), URL https://onlinelibrary.wiley.com/doi/abs/10.1002/14356007.a04_515.pub2.

[81] A. G. Mathewson and H. P. Myers, Physica Scripta **4**, 291 (1971), URL https://doi.org/10.1088/0031-8949/4/6/009.

[82] G. De Maria and V. Piacente, The Journal of Chemical Thermodynamics **6**, 1 (1974), ISSN 0021-9614, URL https://www.sciencedirect.com/science/article/pii/0021961474902006.

[83] H. Pauna, M. Aula, J. Seehausen, J.-S. Klung, M. Huttula, and T. Fabritius, steel research international **91**, 2000051 (2020), ISSN 1869-344X, _eprint: https://onlinelibrary.wiley.com/doi/pdf/10.1002/srin.202000051, URL https://onlinelibrary.wiley.com/doi/abs/10.1002/srin.202000051.

[84] A. Einstein, *Investigations on the Theory of the Brownian Movement* (Courier Corporation, 1956).

[85] R. deCarvalho, J. M. Doyle, B. Friedrich, T. Guillet, J. Kim, D. Patterson, and J. D. Weinstein, The European Physical Journal D - Atomic, Molecular, Optical and Plasma Physics **7**, 289 (1999), ISSN 1434-6079, URL https://doi.org/10.1007/s100530050572.

[86] S. S. Batsanov, Inorganic materials **37**, 871 (2001).

[87] X. Liu, W. Wang, S. Wright, M. Doppelbauer, G. Meijer, S. Truppe, and J. Pérez-Ríos, The Journal of Chemical Physics **157**, 074305 (2022).

[88] J. Bieniewska, Ph.D. thesis, Imperial College London (2021).

[89] D. Patterson, J. Rasmussen, and J. M. Doyle, New Journal of Physics **11**, 055018 (2009), URL https://doi.org/10.1088%2F1367-2630%2F11%2F5%2F055018.

[90] N. Fitch, J. Lim, E. Hinds, B. Sauer, and M. Tarbutt, Quantum Science and Technology **6**, 014006 (2020).

[91] E. E. Callaghan, *The magnetic field of a finite solenoid*, vol. 465 (National Aeronautics and Space Administration, 1960).

[92] X. Alauze, J. Lim, M. Trigatzis, S. Swarbrick, F. Collings, N. Fitch, B. Sauer, and M. Tarbutt, Quantum Science and Technology **6**, 044005 (2021).

[93] G. Kambhampati, N. Fitch, and M. Tarbutt, *Zeeman-sisyphus simulator*, URL https://github.com/coldmatter.